Characterisation of FePt Nanoparticles using X-ray, Neutron, and Electron Analytical Probes

Marianne Monteforte

Supervisor
Prof. Ian K. Robinson

London Centre for Nanotechnology
University College London

Submitted in partial fulfilment of the requirements
for the degree of Doctor of Engineering
at the University College London

April 19, 2017

I, Marianne Monteforte, confirm that the work presented in this thesis is my own.

Where information has been derived from other sources, I confirm that this has been indicated in the thesis.

Abstract

Nanoparticles are the simplest form of crystal structures and are defined as such when they exhibit one dimension in the size range below 100 nm. Michael Faraday's pioneering discovery of the unique optical properties of colloidal gold in the 18th century triggered a rapid uprise in nanoparticle synthesis research. As a result, increasing academic and industrial interest in alloy nanoparticles has resulted in this field becoming one of the most active and advancing research areas in nanotechnology to date.

Bimetallic nanoparticle alloys can be synthesised to pertain many different chemical and physical properties which drastically influence their behaviour and thus application. For example, FePt nanoparticles in cubic form are prime candidates for exploitation in high-density magnetic data storage, FePt@Fe_3O_4 core-shell nanoparticles and functionalised ultra-fine FePt nanoparticles lend themselves particularly well to biomedical applications, and the large surface area of FePt octapods makes them ideally suited to catalytic applications. Within this study synthetic strategies were designed and conducted at the Healthcare Biomagnetics and Nanomaterials Laboratory (at the Royal Institution of Great Britain) to fabricate these FePt nanoparticles (with a diameter $<$ 20 nm and capped with oleic acid and olelyamine surfactants).

The small size of the nanoparticles is of importance for many applications however it typically confines the analysis of their properties to conventional laboratory-based techniques, which can be limited in the degree of information they are able to provide. Consequently, the motivation behind the investigations conducted within this thesis was a desire to design and develop advanced nano-characterisation techniques using electrons, neutrons, and X-rays as analytical probes, respectively for the comprehensive study of small alloy nanoparticles.

Qualitative and quantitative investigations of the FePt nanoparticles were conducted utilising high-resolution electron microscopes and large-scale synchrotron and neutron facilities. Advanced nano-characterisation methods were used through access to state-of-the-art electron microscopy facilities at the Japan Advanced Institute for Science and Technology to conduct a comprehensive study of the FePt nanoparticles crystallographic structure, compositional distribution, 3D morphology, and 2D strain distribution. The 2D strain gradients were resolved using a

geometric phase analysis method utilising an in-house software program.

Bragg coherent X-ray diffraction imaging (BCDI) measurements of FePt nanoparticles and AuPd nanoparticles were conducted at beamline 34-ID-C of the Advanced Photon Source, Argonne National Laboratory, to quantitatively reconstruct the nanoparticles' 3D morphology and strain distribution. In this study, novel stabilisation methodologies were developed to resolve the size limitations of the BCDI technique; extending the size regime for other synchrotron users.

High-energy neutron powder diffraction measurements of isotopic substitutions of FePt nanoparticles in solution were conducted at the Nimrod beamline at the Rutherford Appleton Neutron Facility. Neutron pair distribution function (PDF) analysis enabled the structural properties of the surfactant layer to be extracted and analysed. Complementary high-energy X-ray powder diffraction measurements were conducted at beamline I15 of the Diamond Light Source to enable the structural properties of the FePt nanoparticle to be extracted from X-ray PDF analysis. Also, a 3D reconstruction of an FePt nanoparticle and the surrounding surfactant layer was built using a nanoparticle modelling software program that can find use in future refinement analysis.

The progressive steps detailed in the investigations and results presented within this thesis, demonstrate the capabilities and potential of current and new characterisation and analysis techniques, respectively. These investigations constitute a multidisciplinary approach in the analysis of chemically synthesised nanoparticles, which is essential for device development.

Acknowledgements

First and foremost I would like to express my extreme gratitude to my supervisor Professor Ian K. Robinson for his continued guidance and invaluable advise throughout the course of my EngD. Ian's dedication and vast expertise in a range of disciplines has taught me valuable skills which I will apply in future life. I would like to acknowledge the UCL's industrial training centre in Molecular Modelling and Material's Science, the EPSRC, and my industrial sponsor—Diamond Light Source—for funding me throughout my EngD and express my gratitude to the Japanese Society for the Promotion of Science scheme for providing me with a scholarship that enabled me the opportunity to build a strong research collaboration and gain an unforgettable experience at the Japanese Advanced Institute for Science and Technology.

I would also like to express my thanks to the members of Ian's group, in particular; Ana for many enjoyable beamtimes spent together, Laura for her insightful conversations and input and also Bo for introducing me to the nanoparticle software package. I would to express my gratitude my second supervisor Nguyen Thanh for enabling access to the UCL Health Biomagnetics and Nanomaterials Laboratory at the Royal Institution and to Luke for introducing me to the complexities of nanoparticle synthesis. In addition, thanks to the beamline staff Dr Tristan Young and also Dr David Keen for their guidance in running experiments. Thanks also to my committee members Professor Sankar and Dr Chris (who were on my qualifying committee) for their valuable input.

Thank you also to Shinya Maenonoso sensei for welcoming me into his group and to Derrick Mott sensei, Shoko Kobayahi san, and Koichi Higashimine san for taking the time to introduce me to a range of nano-characterisation techniques. I would also like to extend my thanks to Samantha and Alice for their friendship and support during the years at the labs and at the LCN, respectively. Above all, I owe a special thanks to my family especially my parents, Jim and Annemarie for their intellectual disucssions, encouragement, and unwavering support throughout what has been a very enjoyable and insightful period of my life which will remain with me throughout my profession.

Publications

Quantitative 2D Elemental Strain Mapping and 3D Segmentation of Core-Shell $FePt@Fe_3O_4$ Nanoparticles, **Marianne Monteforte**, Shinya Maenosono, Shoko Kobayashi, Koichi Higashimine, Derrick M. Mott, Nguyen T. K. Thanh, and Ian K. Robinson *New Journal of Physics, Institute of Physics.* 2016.

A Novel Silica Stabilisation Method for the Analysis of Fine Nanoparticles using Coherent X-ray Diffraction Imaging, **Marianne Monte, iforte**, Michael Huang, Bo Chen, Ross Harder, Ana K. Estandarte, Ian K. Robinson *International Union of Crystallography, Journal of Synchrotron Techniques*, 2016.

Contents

List of Figures

List of Tables

Chapter 1

Prelude

Bimetalic FePt nanoparticles are preferred over their pure metal counterparts for their enhanced properties such as a high chemical stability, catalytic activity, and tuneable magnetic properties. FePt nanoparticles are studied in this thesis as they offer themselves as model alloys that can be fabricated and engineered for a range of different applications. Subsequent nano-characterisation technques developed in the Chapters in this thesis enables their chemical and physical properties to be defined.

Chapter 2: Neutrons, high energy X-rays and electrons were utilised as analytical probes to elucidate the crystallographic, compositional distribution, 3D morphology and distribution, internal strain and surface functionalisation behaviour of FePt nanoparticles. The importance of determining these different chemical and physical properties of the FePt nanoparticles and their potential applications are detailed within this Chapter. The generation of synchrotron, neutron and electon radiation is detailed and their interaction with matter is described. The basic principals of diffraction are also detailed providing a knowledge platform for the techniques used within this thesis.

Chapter 3: The fundamentals behind a range of solvothermal synthetic strategies that are typically adopted in the fabrication of FePt nanoparticles are outlined and the nanoparticle formation mechanism is proposed. Well-defined synthetic strategies were adopted (by adjusting the reaction parameters) to fabricate the following model FePt nanoparticle systems—nanocubes of diameter 8.41 $\pm$ 0.56

nm to, $FeP@Fe_3O_4$ core-shell nanoparticles of diameter 8.71 $\pm$ 0.44 nm, and octapods of diameter 17.0 $\pm$ 2.01 nm. Also, a specialised deuterated synthesis was conducted in the fabrication of spherical ultrafine 2 nm FePt nanoparticles with isotopic substitutions of surfactants (for neutron diffraction analysis).

Chapter 4: The award of a Japan Society for the Promotion of Science (JSPS) scholarship enabled nano-characterisation of the FePt nanoparticles, of different shapes and size, through access to state-of-the-art electron microscopy facilities at Japan Institute for Science and Technology (JAIST), Japan. The range of nano-characterisation techniques that were adopted to conduct a comprehensive study of the FePt nanoaprticles are described and include; Fourier Transform infrared spectroscopy (FTIR), powder X-ray diffraction, TEM imaging modes, electron tomography, high resolution TEM (HRTEM), aberration corrected scanning TEM(STEM)-HAADF, and STEM-energy dispersive spectroscopy(EDS).

Chapter 5: The results from the range of nano-characterisation methods utilised at JAIST are presented within this Chapter. This study enabled a comprehensive analysis of the compositional, morphological, and, strain distribution in the FePt nanoparticles, which is of fundamental interest in the fine-tuning of these nanoparticle materials for applications. Strain analysis of the high resolution TEM images was conducted through the design and implementation of a gradient phase analysis (GPA) program built using a MatLab script. The resultant 2D strain maps, acquired using the Matlab GPA code enable strained regions to be qualitatively mapped and strain decay behaviours to be analysed.

Chapter 6: Bragg coherent X-ray diffraction imaging (BCDI) investigations were conducted at 34-ID-C beamline at the Argonne Photon Source, USA and a novel one-step silica stabilisation method was developed and optimised. These stabilisation methods were developed as a prompt and efficient approach in resolving the limitations of the BCDI, extending the accessible size regime. CDI investigations were conducted at the Argonne Photon Source 34-ID-C beamline on chemically synthesised 17 nm FePt octapods, and 60 nm - 120 nm AuPd nanoparticles stabilised in a silica matrix. The results show that it is possible to overcome the size limits of the BCDI technique through the use of this novel silica stabilisation method. Thus, on implementation of this method the strain and morphology of smaller nanoparticles can be probed furthering the knowledge and understanding of the fundamental properties of the nanoparticles and enabling key applications

in medicine, catalysis and information technologies. The results of this extensive study are published in the International Union of Crystallography, Journal of Synchrotron Techniques (2016). The nanoparticle stabilisation method enables members of the CDI community to adopt and develop this approach as an effective method to analyse small nanoparticles.

Chapter 7: A novel characterisation approach was designed to probe the whole FePt nanoparticle-surfactant system using a pair distribution function (PDF) analytical technique (using both neutrons and high energy X-rays as analytical probes). The investigations were conducted at the near intermediate range order diffraction (Nimrod) beamline, housed at the ISIS neutron facility at the Rutherford Appleton Laboratories (Oxfordshire, UK), utilising neutrons as an analytical probe. A novel neutron diffraction flow cell experiment was developed at the Nimrod beamline and the isotopic substitutions, experimental design, and instrumental set-up was optimised enabling structural information to be obtained from the surfactant shell. Complementary X-ray PDF investigations enabled structural information from the FePt nanoparticle core to be extracted. The disordered systems modelling program, DISCUS, was used to build a 3D model of the FePt alloy. The model was refined aogainst the experimental PDF data using a Reverse Monte Carlo progarm.

Chapter 2

Introduction

2.1 Introduction to FePt Nanoparticles

2.1.1 Nanoparticle Characteristics

2.1.1.1 Nanoparticle Phases

FePt nanoparticles can exist in three different phases as detailed in Fig.2.1a-b. The A1 phase is typically obtained from the as-prepared chemical synthesis of the

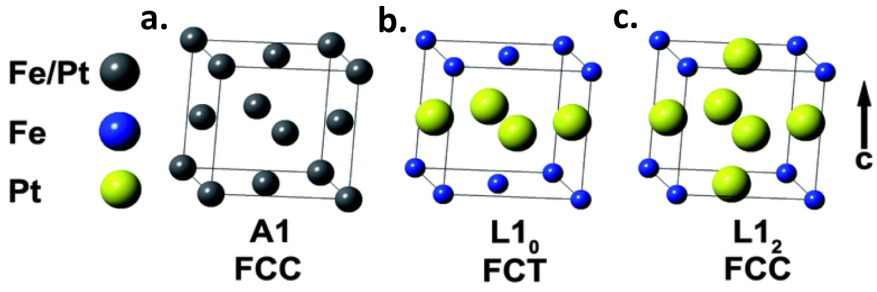

Figure 2.1: *Models of the unit cells of different phases of FePt alloys: (a) A1 alloy, face-centered cubic phase, (b) $L1_0$ FePt intermetallic, face-centered tetragonal phase, and (c) $L1_2$ $FePt_3$ intermetallic, face-centered cubic phase. Reprinted with permissions from [REF].*

nanoparticles. The face-cantered cubic (fcc) structure has a randomly ordered

arrangement of Fe and Pt atoms as shown in Fig.2.1a. FePt nanoparticles in this phase typically exhibit superparamagnetic behaviour, and are termed as 'soft magnets' (only magnetized in the presence of an external magnetic field). Thermal annealing of the initial A1 phase with an equimolar stoichometry of Fe_xPt_{1-x} where x is within the range of $0.4 \leq x \leq 0.6$ [Nguyen et al., 2006] will convert the alloy into the $L1_0$ face-centered tetragonal (fct) phase. This fct phase has an ordered sequential arrangement of Fe and Pt layers as illustrated in Fig. 2.1b compressed the difference between the radii of the Fe and Pt forces the compression of the c-axis. FePt nanoparticles in this phase exhibit ferromagnetic behaviour with a high saturation magnetisation and are termed as 'hard magnets' (remains magnetized after the external magnetic field, has been removed). In this investigation nanoparticles were analysed in the as-synthesised FePt A1 phase.

2.1.1.2 Compositional Distribution and Morphology

Bimetallic nanoparticles can exhibit unique behaviours which are different from the bulk this is expecte to be a result of large surface segregation effects that can dominant the structure. Therefore the structure, composition and phase properties of these bimetallic nanoparticles are critical in tuning their behaviour for their desired applications. The atomic arrangement of Fe and Pt atoms in alloy nanoparticles can exhibit random, clustered or short-range or long range ordered arrangements and is dependent on factors in the synthetic strategy. Elucidation of the internal structure of alloy nanoaparticles is an important pre-requisite to determine the functionality of nanoparticles and to tune the synthetic schemes. Thus, the two-dimensional (2D) composition of the FePt nanoparticles and 3D morphology of FePt were investigated in Chapter 5 using electrons as an analytical probe. Additionally, the 3D compositional distribution of the FePt nanoparticles was investigated in Chapter 7 using neutrons and X-rays as analytical probe.

2.1.1.3 Strain Distribution

Deviations in lattice fringe positions from the perfect crystal structure are the evidence of any strain fields in the lattice. Elucidation of the presence of any strain in nanoparticles can reveal factors that induce strain in nanoparticles as

shown in Fig.2.2. For example, surface relaxation (expansion) or tension (compression) of the lattice as a result of the shape of the nanoparticles will cause the lattice fringe positions to deviate. It can also reveal the presence of defects (such as stacking faults, dislocation loops, twin boundaries) in nanoparticles. Therefore, mapping the presence/absence of this strain is useful in the develop-

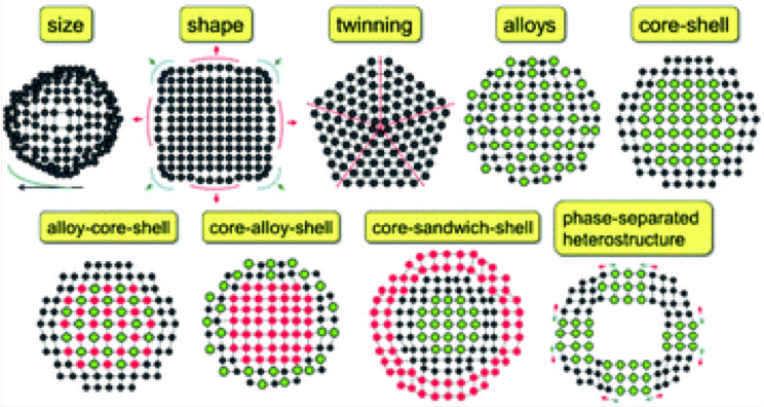

Figure 2.2: *Different physical factors that can induce strain in nanoparticles. Image reprinted with permissions from [REF] [Sneed et al., 2015]*

ment of these functional nanoparticle materials. For example, it could be used in the design of electromagnetic devices [Carpenter et al., 2003], nano-catalytic devices [Wang and Xia, 2004] and permanent magnetic data storage mediums. Strain mapping is therefore essential in the development of these nanoparticles for their desired applications. In the investigations conducted within Chapter 5 electrons were utilsed as an analytical probe to gain crystallographic images of the nanoparticle structures and simple method to map the presence of strain in the nanoparticles was designed.

2.1.1.4 Surfactant Layer

The functionalization of magnetic nanoparticles can be achieved by adsorbing organic surfactants—or ligands—on to the surface of the nanoparticle via their ionic functional head groups. Surfactants adsorb on to a particle surface either by electrostatic interactions or by chemical interactions (where the latter interaction is most common in colloidal nanoparticle solutions). They form a surfactant layer on the surface on the nanoparticle and play synergistic roles including:

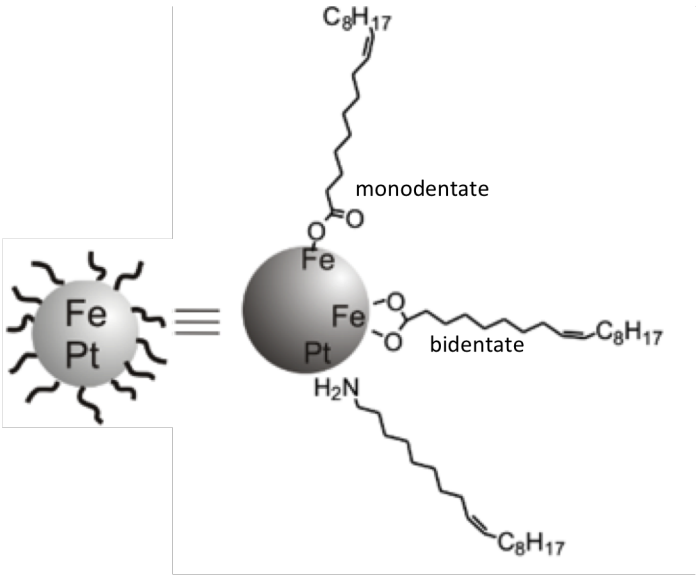

Figure 2.3: *Schematic of an FePt nanoparticle with oleic acid and oleylamine surfactants bonded to the surface [van Ewijk et al., 2002]. Reprinted with permissions from [REF].*

- Facilitating the nucleation and growth of the nanoparticles and the resultant morphology of the nanoparticles.
- Stabilising the precursors and the formed nanoparticles in a colloidal dispersion thus enhancing their chemical stability.
- Enhancing the compatibility of nanoparticles e.g. to create bio-solutions or nanoparticles suitable for exposure in tissue environments.
- Influencing the self-assembly of the nanoparticles on a substrate.

Oleylamine (OLA), $C_{18}H_{35}NH_2$, and oleic acid (OA),$C_{18}H_{34}O_2$, are the most commonly used surfactants in partnership with FePt nanoparticles. The extended surfactant length of OLA and OA is 2.06 and 2.08 nm, respectively [van Ewijk et al., 2002]. It is proposed that the carboxylic acid moiety of the OA surfactant has a specific bonding affinity to the Fe atoms on the nanoparticle surface and the amine moiety of the OLA surfactant has a specific bonding affinity to the Pt atoms on the FePt nanoparticle surface [Sebt et al., 2009], as illustrated in the schematic in Fig.2.3 [van Ewijk et al., 2002]. The interaction between the carboxylate moiety of the OA and the metal Fe atom of the nanoparticle depends on the OA content and could take one of three forms; monodentate, bridging bidentate or chelating bidentate.

The structural properties and bonding speciation of the organic surfactant layer is of specific interest in biomedical applications. Yet very few methods have been used to quantitatively probe these properties. Thus, neutron investigations were developed in Chapter with the intention to probe the structure and speciation of the surfactant layer 7.

2.1.2 Potential Applications

2.1.2.1 High Density Data Storage

The ongoing endeavour to increase storage capacity of devices has lead to the increasing use of nanoparticles in the design of next generation recording media. Data storage devices typically consist of patterned media which comprise arrays of magnetic islands arranged in a nonmagnetic matrix. For this application (Figure2.4) it is required that each nanoparticle array consists of perpendicular magnetic domain which can be magnetically manipulated using a 'monopole' writing element, to retain data (bit), until it is wiped [Soichiro Saita, 2005]. The nanoparticles are required to be of a highly monodisperse size distribution and packed into dense two-dimensional superlattice arrays in order to define magnetic boundaries and prevent 'jitter' (which effectively weakens the ability of the nanoparticle to hold the magnetic data). FePt nanoparticles in the $L1_0$ phase are of particular interest for this application as they exhibit a high magnetocrystalline anisotropy $7 \times 10^7 erg/cm^3$ and are chemically stable (down to 3 nm in size). Therefore FePt nanoparticles can maintain a stable magnetisation [Shukla et al., 2006], making them potential candidates for ultra high density patterned media devices. Two-dimensional superlattice arrays of FePt nanoparticles were first identified by the IBM group (at the Thomas J. Watson Research Center) as a promising candidate for the application to patterned media recording systems [Chen et al., 2004]. Seagate Technology are currently investigating the use of 4-10 nm FePt nanocubes for application in heat assisted magnetic recording devices and ultimately deliver storage densities of 50 Terabit per inch^2.

Nanocubes exhibit the most preferred shape for magnetic data storage applications as during deposition onto a substrate they typicallly align with one facet flat on the plane their [100] axis along the surface normal. This [100] axis is

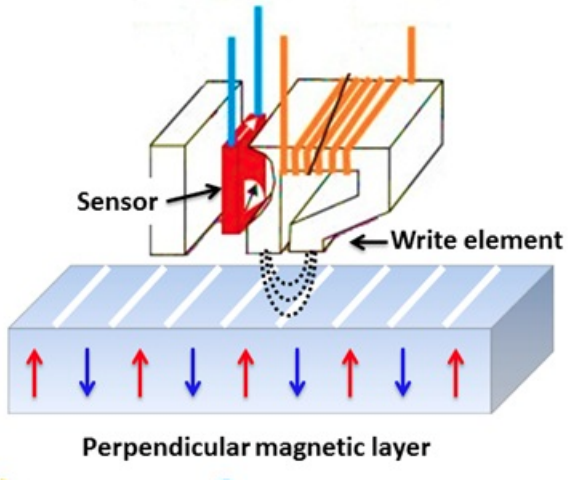

Figure 2.4: *2D supperlattice arrays of nanoparticles with magnetic read head for data storage applications.Reprinted with permission from [Matsui et al., 2011]. Copyright 2016, AIP Publishing LLC.*

termed as the c-axis or the magnetic easy axis and is the direction in which the magnetic domains can be most readily manipulated. Comparatively the magnetic easy axes of spherical nanoparticles is more difficult to align resulting in a low magnetic moment per unit area [Chen et al., 2006]. Therefore in this investigation $FePt@Fe$ $(core@shell)$ nanocubes were fabricated and act as a model system for data storage applications (prior to phase transformation).

2.1.2.2 Therapeutic and Diagnostic Devices

FePt nanoparticles in the fcc phase are magnetically 'soft' and are attractive candidates for therapeutical and diagnostic applications as they retain magnetic behaviour in colloidal dispersions and are stable in physiological conditions [Pankhurst et al., 200
Also, nanocomposites such as FePt@Fe oxide (core@shell) nanoparticles can be tuned by altering the composition, core size, and shell thickness. Biomedical applications of these nanocomposites include; magnetic resonance imaging (MRI) contrast agents, magnetic hyperthermia, and targeted drug delivery.

Spherical $FePt@Fe_3O_4$ nanoparticles exhibit minimal levels of drag in the body and the biocompatible layer removes the concerns over toxicity. $FePt@Fe_3O_4$ nanoparticles as MRI contrast agents function by accentuating the magnetic-

response, of MRI enabling differences in soft tissue and hard tissue to be distinguishable. The high magnetic coercivity of FePt also enables it to be tracked in the body. For example, FePt nanoparticles functionalised with L-cysteine behave as a superior contrast agent for MRI/CT imaging in the diagnosis of brain malignant tumours [Liang et al., 2015]. FePt nanoparticles have also been identified to exhibit superior magnetic behaviour for application as MRI contrast agents in comparison to magnetic iron oxide nanoparticles [Jha et al., 2015].

$FePt@Feoxide$ nanoparticles are also being investigated for therapeutic magnetic hyperthermia for cancer therapy applications. Magnetic hyperthermia involves the injection of magnetic nanoparticles into a tumour which is then exposed to an alternating current (AC) magnetic field, causing the magnetic spin of the magnetically active nanoparticle to flip, resulting in radio frequency induced heat destruction of the cell [Hergt et al., 2006]. Therefore, as a model system for MRI contrast agents

In addition, FePt cationic polyelectrolyte nano-hybrids have been realised for their enhanced capacity to carry medical drugs and genes (by acting as magnetic drug carriers these 'loaded' nanoparticles can be guided by a magnetic field to an affected region in the body for treatment) [Fuchigami et al., 2011]. This form of targeted drug delivery enables a drug (such as a chemotherapy drug) to be attached to the nanoparticle surface creating a delivery system that localises drug delivery to only the malignant cells. This approach can effectively reduce drug dosage and the extent of chemotherapy side effects in comparison to conventional chemotherapy treatments.

The accessible surface for surfactant attachment is of particular interest in order to develop the understanding of the functionality of the nanoparticle. The surfactants on the FePt nanoparticles can be tailored through exchange with particular ligands. The exchange allows for surface conjugation, via the ligand, with various peptides, proteins, antibodies and other biomolecules. Nanoparticles are therefore readily amenable to bio-conjugation and bio-modification. Small FePt nanospheres are of commercial importance because they have a large surface to volume ratio available for surface functionalisation, and therefore these nanoparticles were fabricated as model systems for the investigations within.

2.1.2.3 Nano-Catalytic Devices

Pure Pt nanoparticles are vital for catalytic applications such as oxygen reduction reactions (ORR) in for example, fuel cells where the nanoparticle surface acts as a site for conversion of oxygen and hydrogen into electricity and water. However, bimetallic nanoparticle alloys are becoming increasingly sought after as catalyst supports. For example, an alloy of magnetic Fe with catalytic Pt is attractive for catalytic applications and enables recovery of the catalyst by magnetic separation [Akbarzadeh et al., 2012] and is a more economically viable alternative to their expensive pure metal Pt. Also, the alloy has been reported to exhibit a higher catalytic activity and to be a more durable catalyst (for ORRs) in comparison to pure commercial Pt nanoparticles [Guo and Sun, 2012]. The shape of the nanoparticle has also been identified to influence electro-catalytic activity and FePt nanoparticles with high index facets such as, FePt nanodentrites [Wang et al., 2015] reported to enhance electro-catalytic activity. Also, FePt octapods have a large surface area and thus were fabricated to act as a model system for catalytic applications and to test stabilisation methods for the CDI investigations.

2.1.2.4 Commercial Implications

FePt nanoparticles offer an array of potential application to a range of industry sectors. However, the industry must first face the difficulties that remain in quantifying the long-term efficacy, toxicity, and metabolism of FePt nanoparticles. Most in-vitro studies into the cytotoxicity of FePt nanoparticles remain in the laboratory phase and still require further exploration. Also, the environmental impact of nanoparticles on the global diversity remains unknown. Regulatory bodies are restricted from categorising nanoparticles owing to the fact nanoparticles exhibit inherent properties that can be unique to their size and shape. Therefore, it is essential that nanoparticle research continues to push the boundaries of analytical methods in order to distinguish and correlate the impact of physical properties. These techniques will not only contribute towards scientific contributions to knowledge but also enable regulatory bodies to efficiently define and categorise nanoparticles furthering their potential applications. In addition the application of analytical techniques are especially required for the analysis of small nanopar-

ticles of diameter less than 20 nm as this is the size in which conventional approaches can fail.

2.2 Introduction to Synchrotron Radiation

2.2.1 Electromagnetic Spectrum

Part of the fundamental principle of physics is that when charged particles are accelerated they emit electromagnetic (EM) radiation. Max Planck deduced the quantum relationship between energy and frequency of EM radiation in 1901 stating that an oscillation of frequency, v, can be categorised into a discrete quanta of energy, given by hv, where h is a universal constant now termed as Planck's constant. This determined Planck's equation where the energy of EM radiation is related to the wavelength λ by:

$$E = \frac{hc}{\lambda} \tag{2.1}$$

where h is Planck's constant $6.626x10^{-34}\ Js^{-1}$, and λ is the wavelength of the EM radiation. In order to utilise this radiation to probe an object the wavelength of the radiation must be comparable to, or smaller than the size of the object, as detailed in the electromagnetic (EM) spectrum in Fig.2.5. X-rays have a much shorter

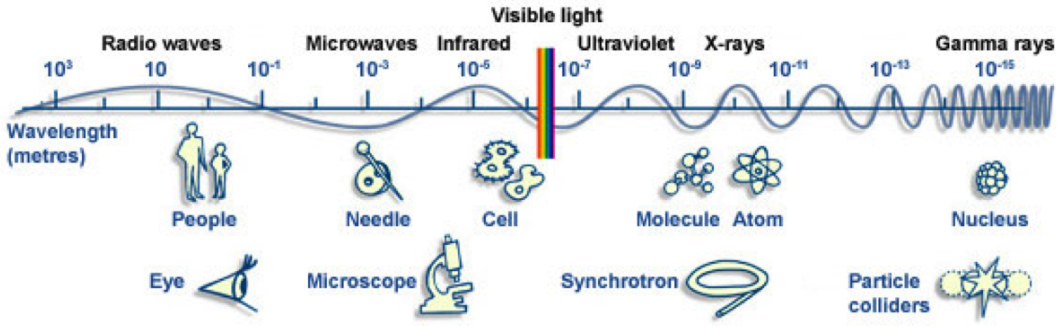

Figure 2.5: *Electromagnetic spectrum from low E, high λ to high E, short $lambda$ capable of probing the corresponding objects [REF].*

wavelength than visible light thus allows structures to be resolved with higher spatial resolution. In the EM spectrum in Fig.2.5 it shows that the wavelength of hard X-rays is comparable to atomic scale distances. These X-rays are generated

using synchrotron radiation. Synchrotron radiation facilities use powerful bending electromagnets to accelerate electron bunches close to relativistic speeds, and strong magnetic fields to force the bunches to travel in a closed trajectory, in the process emitting synchrotron radiation which can span a wide frequency range, from infrared up to the highest-energy X-rays. Researchers at academic and industrial institutions alike utilise these different energies of emitted synchrotron radiation to conduct a range of studies including, diffraction, absorption, transmission, spectroscopy, and scattering investigations enabling dedicated studies a numerous array of sample types from biological to condensed matter. The exceptional intensity and brightness of synchrotron radiation supports a range of scientific disciplines, including life sciences, engineering, cultural heritage, environmental science, radiography, and materials science.

2.2.2 Synchrotron Facilities

One of the most significant developments in synchrotron light generation took place in 1981 when the first dedicated radiation source became operational in the UK at the Daresbury Synchrotron Radiation Source. Since then the number of facilities dedicated to synchrotron radiation expanded rapidly leading to pioneering advances to increase the spectral brightness of the sources.

Synchrotron radiation is characterised by a high spectral brightness that is many orders of magnitude brighter than conventional sources; it is highly polarised, tunable, collimated, and concentrated over a small area. Spectral brightness is an important parameter used to characterise the quality of the radiation source, and is a measure designed to compare synchrotron radiation sources in terms of the quality of the beam produced. It combines several aspects and is defined as:

$$B = \frac{\text{Photons per second}}{(\text{beam divergence mrad})^2(\text{source area mm})^2(0.1\ \%\ \text{energy bandwidth})} \tag{2.2}$$

The development of insertion devices (ID) which consist of periodic arrays of magnets forming a magnetic multipole structure has enabled the emergence of synchrotron devices with higher brilliance. 2nd generation synchrotrons were retro fitted with IDs and 3rd generation synchrotrons were initially installed with them

enabling them to produce synchrotron radiation of even higher spectral brightness. The first 3rd generation synchrotrons emerged in the 1990s; European Synchrotron Radiation Source in 1994 (Grenoble, France), the Advanced Photon Source (Illinois, USA) in 1996 and Spring8 (Hyogo, Japan) in 1998. The exceptional coherence properties and brightness of synchrotron radiation over the past 30 years has paved the way for the emergence of modern X-ray imaging techniques [Als-Nielsen and McMorrow, 2011] that were not previously achievable, such as coherent x-ray diffraction (as discussed in Chapter6).

In this section the fundamentals behind the synchrotron light generation is demonstrated using the DLS located at the Harwell Science and Innovation Campus in Oxfordshire, as an example. The numbered points in Fig.2.6 are described as follows:

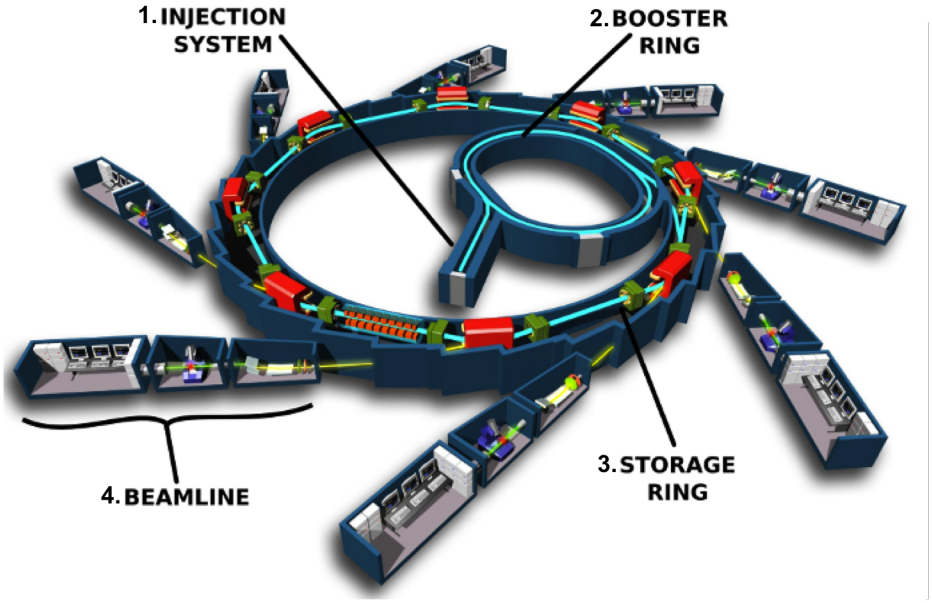

Figure 2.6: *Synchrotron light generation with labelled points of interest 1. Electron Gun 2. Injection system 3. Booster ring 4. Storage ring 5. Beamline Synchrotron. Image reprinted with permissions from Synchrotron Soleil by EPSIM 3D/JF Santarelli [REF].*

1. **Injection System:** The DLS synchrotron facility operation begins with the generation of electrons by a thermionic emission electron gun (TEG). The TEG consists of a cathode which is heated up (to above 1000 °C) by applying a high voltage under vacuum, providing the electrons in the material

with sufficient energy to overcome the work function of the material (minimum energy required to release the electrons) which is equivalent to:

$$E = \frac{1}{2}mv^2 = eV \tag{2.3}$$

where m is the electron mass, v is the electron velocity as it leaves the FEG, e is the charge of the electron, and V is the Voltage on the anode. The free electrons create a plasma on the surface of the TEG and a strong electric field (positive earthed anode) accelerates the electrons away from the FEG producing a focused stream of electrons at 90 keV. The 90 keV electrons are then accelerated in the 30 m linac to near relativistic energies (100 MeV) using RF cavities. The RF cavities contain oscillating EM fields at radio frequencies and accelerate the electrons, and forces them to bunch into pulses. The pulses are used to fill a single 'bunch' in the storage ring.

2. **Booster Ring:** The electron bunches are fed into the booster synchrotron (3 GeV, 151.4 m) are further accelerated using RF cavities, when sufficient energy is accumulated the electrons are fed into the storage ring.

3. **Storage Ring:** The high energy electron bunches enter the storage ring (3 GeV, 561.6 m) which is contained under high vacuum. The relativistic electrons are accelerated around the orbit of the storage ring consisting of 48 alternating curved and straight sections. In the curved sections powerful bending magnets are used to direct the electron bunches trajectory around the curves to maintain a fixed orbit and for acceleration, emitting X-rays.

   In the straight sections insertion devices (ID) are placed. The ID produces an alternating magnetic field in the longitudinal direction and forces the trajectory of the electrons to follow an oscillating path. The ID can exist in two different modes of operation; wiggler IDs—as used in the DLS—which generates a small oscillation amplitude or undulator IDs—as used at the APS—which generates a large oscillation amplitude as shown in Fig.2.7. At each oscillation ('wiggle') the electrons emit X-rays and in the case of the wiggler IDs these X-rays have a high energy and intense beam, whereas in the case of undulator IDs the X-rays emitted interfere resulting in an interference pattern (in the space and energy planes) producing light that is spatially concentrated and in a narrow cone (of higher brilliance). Given the fixed energy of a synchrotron the energy of the X-rays is dependent on

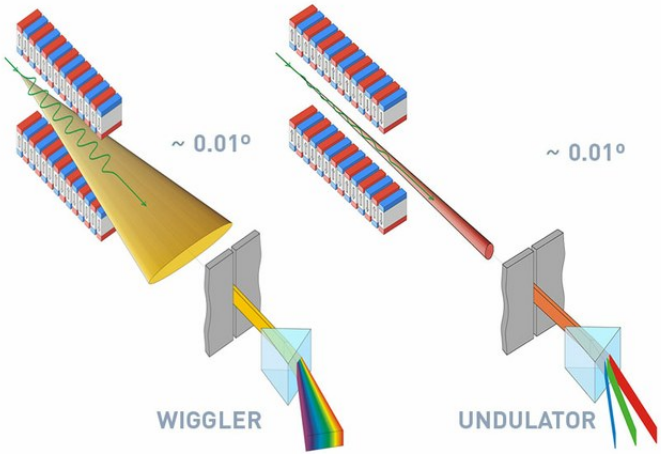

Figure 2.7: *Insertion devices (ID) consisting of alternating periodic arrays of superconducting magnets. Wiggler ID generates a small oscillation amplitude emitting X-rays with a broad radiation fan. Undulator ID generates a large oscillation amplitude emitting X-rays that is spatially concentrated and of higher spectral brightness.*

the magnetic field. The energy can be finely tuned by varying the circulating current in the magnetic array (if the ID magnets consist of coils) or by mechanically separating the array of magnets (if the ID magnets consist of permanent magnets). Strong magnetic fields generate high energy X-rays (hard X-rays) and weaker magnetic fields generate low energy X-rays (soft X-rays).

4. **Beamline:** consists of three sections; the front end, the optics hutch and the experimental hutch. The raw x-rays pass through the front end under a high vacuum. Beam conditioners are used to optimise the condition of the beam. In the optics hutch the desired wavelength (or energy) is selected from the continuous synchrotron spectrum using a crystal monochromater and the beam is focussed to alter the convergence or divergence (focus) of the beam using mirrors. The beam is directed into the experimental hutch where the sample and experimental equipment is housed (notably, if the beam is to enter out of vacuum and into the external environment in the case of X-rays they are passed through a thin beryllium sheet). Detectors are positioned to capture and record X-rays after interacting with the sample. The detectors translate the X-ray photon into either a visible-light photon or an electrical signal (scintillation detectors and semiconductor or charge-coupled device detectors, respectively). The final hutch is where

the investigators can remotely control the experiment and enables control during real time data collection.

The investigations described within this thesis were conducted utilising X-ray radiation at the DLS synchrotron which uses a wiggler ID (accelerator energy = 3 GeV ring circumference = 562 m) to conduct powder x-ray diffraction investigations (for Pair Distribution Fucntion analysis) at the I-15 beamline. The APS synchrotron (accelerator energy = 7 GeV, ring circumference = 1104 m) is optimized to produce radiation of a higher brilliance than that of the DLS and was utlisied to conduct Bragg coherent diffraction imaging (BCDI) investigations at the 34-ID-C beamline.

2.2.3 Coherent X-ray Diffraction

Coherent X-ray diffraction imaging (CDI) utilises highly coherent 'hard' X-rays generated from undulators at third generation synchrotrons, to achieve the high spatial resolution diffraction data. Unlike in an electron microscope, where lenses are used to collect the scattered intensity from the sample revealing an image of the nanoparticle. The use of diffractive X-ray optics in X-ray imaging can limit the resolution of the image due to artefacts in the lenses, such as, aberration. Therefore, CDI avoids these limitations by utilising highly coherent X-rays—generated by undulator sources from third generation synchrotrons—removing the requirement for lenses. The resolution of the CDI technique is therefore only limited by diffraction and dose. Notable the best achievable spatial resolution for a particular experiment also depends on various sample, instrumentation and detector properties.

This measurement records the intensity (measured in terms of absolute counts of photons) but loses phase information. Inversion of the diffraction pattern using phase retrieval algorithms yields a complex 3D image, whose amplitude is related to the 3D electron density (structure) and phase is related to the displacement and strain field of the crystal lattice. CDI can therefore provide powerful insights into the nanoparticle structure and the displacement and strain field within the nanoparticle [Robinson and Harder, 2009]. There are several different types of CDI techniques available for example, plane-wave CDI (PCDI), Bragg CDI (BCDI),

ptychographic CDI (ptychography), Fresnel CDI, reflection CDI, and sparsity CDI. In this investigation CDI is used in the Bragg set up and described further within.

2.2.3.1 Bragg CDI

In Bragg CDI individual grains of different (hkl) Miller indice planes are isolated in reciprocal space, and diffraction data sets are recorded. This process of selecting and analysing different grains correlates with the strain mapping technique used in Chapter 5. However, BCDI is much more complex technique as it is applied in three-dimensions enabling both the 3D strain and structure buried within a nanoparticle to be probed [Xiong et al., 2014b] (down to dimensions of a few nanometres if the coherent X-ray beam is bigger than the size of the object).

This technique has fast become a powerful analytical tool for investigations into, nanoparticles [Robinson and Harder, 2009], nanotubes [Zuo et al., 2003], nanospheres [Newton et al., 2009] and even biological systems [Nishino et al., 2009]. Additionally, BCDI enables the strain evolution of nanoparticles on exposure to an external environment in-situ [Cha et al., 2010] such as, heating/cooling or pressure changes [Yang et al., 2013] enabling properties such as phase transformation, and optimal battery operating conditions to be identified [Ulvestad et al., 2015]. Strain evolution can also reveal alloy diffusion of Copper on gold has been identified by in-situ evaporation of metals onto nanoparticles[Xiong et al., 2014a]. Also, recent BCDI investigations into the alloying behaviour of Pt onto Au nanoparticles have been conducted at the I-07 beamline at the DLS (in which I was contributing investigator). Furthermore, BCDI has been utilised follow the effect that in-situ surface modifications such as, the surface adsorption of molecules, has on the strain of nanoparticles for biomedical applications [Watari et al., 2011].

2.2.3.2 Coherence

In order to measure phase—a retardation or advancement in a wavefront—a coherent source of illumination is required as it acts as the reference wave [Shemilt, 2014]. The contrast between the diffracted wave as a maxima (I_{max}) and minima (I_{min}), is measured in the diffraction pattern collected by the detector. This coherence is

defined by the visibility, V, expressed as:

$$V = \frac{I_{max} - I_{min}}{I_{max} + I_{min}} \tag{2.4}$$

In Eq.2.4 V is equal to one when the minima of the diffraction pattern are zero and so the source is coherent, and V is equal to zero when the maxima and minima cannot be well distinguished, and so the source is incoherent. However, most sources are not a definitive coherent or incoherent illumination—they are partially coherent. Coherence is defined by multi-dimensional entities; longitudinal (temporal) and transverse (temporal) coherence which are a result of a wavefront deviating slightly from the perfect ideal plane wave. This deviation can be caused either by the waves being of slightly different wavelengths or by the waves deviating slightly in direction from the same source [Shemilt, 2014].

Longitudinal coherence length is the length at which two waves with slightly different wavelengths travelling in phase, go out of phase after travelling a distance d_L from the start point. Longitudinal coherence is depicted in the schematic in Fig.2.8 adapted from [Als-Nielsen and McMorrow, 2011], with the two waves one with a wavelength, λ and the other with a wavelength $\lambda - \Delta\lambda$ travelling a distance d_L.

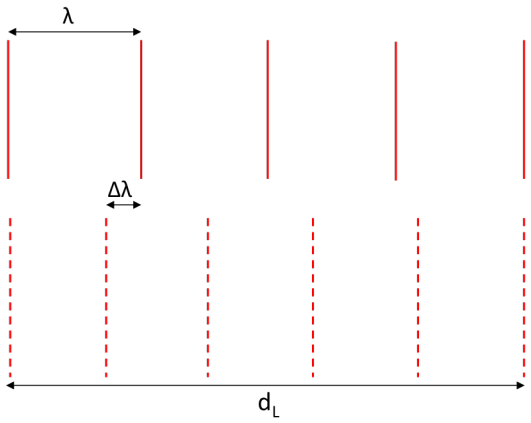

Figure 2.8: *Longitudinal coherence where two waves of slightly different wavelengths begin in phase and then meet again out of phase at travelling a distance d_L. Schematic adapted from J. Als-Nielsen and D. McMorrow [Als-Nielsen and McMorrow, 2011].*

The longitudinal coherence length can be expressed as:

$$d_L = \frac{\lambda^2}{2\Delta\lambda} \tag{2.5}$$

Thus, the longitudinal coherence length is dependant on the bandwidth of the double crystal monochromator where a typical fractional bandwidth is $\Delta\lambda\ 1.4x10{-}4$. Transverse (spatial) coherence is defined when the path of two waves of the same wavelength (from an extended source of vertical size D), propagate in slightly different directions. In Fig.2.9 the waves emanate from either side of the extended source (of size D), and meet in phase, at a distance R from the source, at point P. The transverse coherence length $(2d_T)$ defines the distance from point P along the wavefront of A to where the waves are completely out of phase again. The trans-

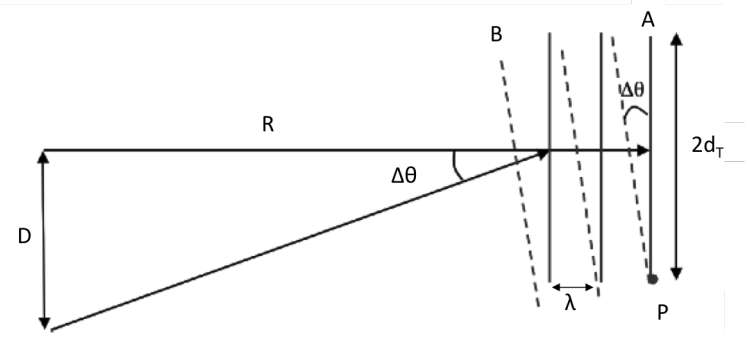

Figure 2.9: *Transverse coherence of two waves (from an extended source of size D), meet in phase at a point P, at a distance R, from the source are completely out of phase at twice the transverse coherence length $(2d_L)$ from point P along the wavefront of A. Schematic adaption of J. Als-Nielsen and D. McMorrow [Als-Nielsen and McMorrow, 2011].*

verse coherence length is described in terms of R when the angle is small, and where the coherence length is defined by the source in this case for synchrotron radiation source (which is a Gaussian distribution which falls into a space of σ).

$$d_T = \frac{\lambda R}{2D} = \frac{\lambda R}{\sigma} \tag{2.6}$$

In most synchrotron X-ray applications, shortly after the monochromator the coherence is set by slits which define the source size. Thus, a higher transverse coherence length can be achieved by using sources with a smaller size (by defining

the slit size) and by increasing the distance between the source and the sample.

Both the transverse and temporal coherence lengths are the space in the field where the source is coherent and in order for CDI to operate the coherence length is required to be the same size or greater than the size of the nanocrsytal. If the transverse coherence length is smaller than the size of the nanoparticle then interference would occur from only part of the nanoparticle and CDI approach would fail. The same applies for temporal coherence in the time frame.

2.2.3.3 Coherent Diffraction Imaging Set-Up

The standard CDI setup consists of a set of coherence-defining slits, a sample mounted onto on a piezo controlled multi-axis positioning stage, and a long multi-axis detector arm with a small pixel area detector as illustrated in the simplified schematic of the setup in Fig.2.10. The coherence defining slits are used mainly

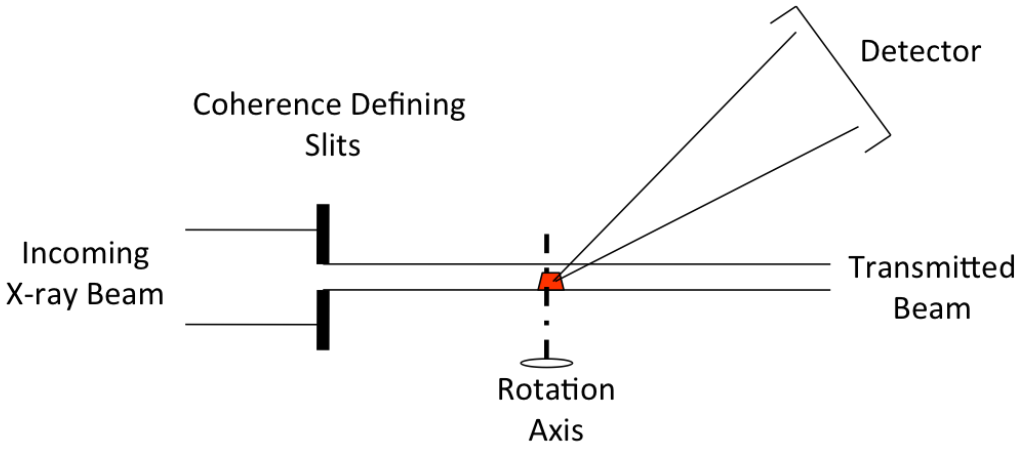

Figure 2.10: *Standard CDI setup with coherence-defining slits, a sample on a piezo controlled multi-axis positioning and tilt stage and a long multi-axis detector arm with an area detector.*

to control the coherence properties of the incoming X-ray beam and are also used for adjustment of beam spot sizes on the sample. Both horizontal and vertical slits are defined so that the slit size is smaller than the transverse coherence length to create a coherent incoming X-ray beam hitting on samples. There is a trade-off between slit size and beam flux, as the bigger the slit size the greater the X-ray flux but if the slit size extends beyond a limit the coherence of the X-ray beam is lost. The coherent beam is illuminated on the sample and detector,

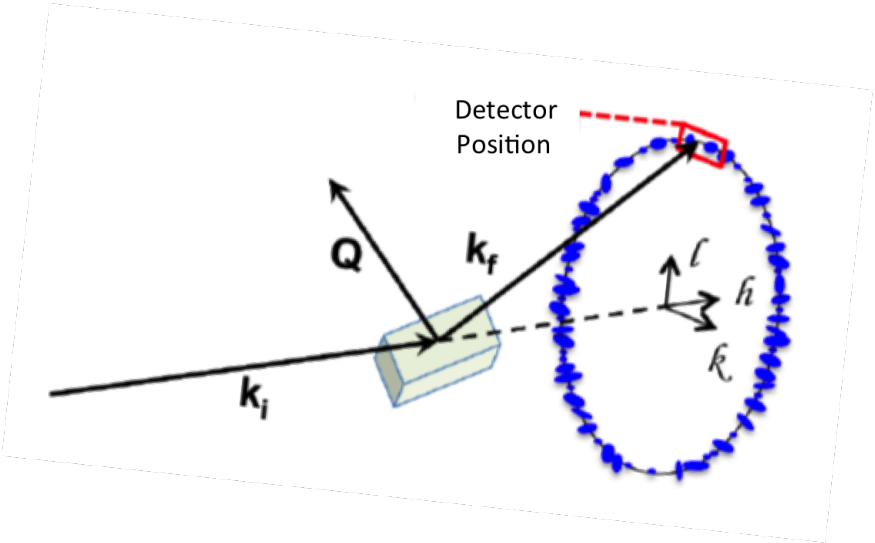

Figure 2.11: *Simplified CDI set up with an incoming coherent beam, k_i, diffracting the beam beam k_f at the Bragg angle 2θ. Reprinted with permissions from I. K. Robinson, CMS conference Liverpool 2013.*

which are orientated such that the Bragg condition is satisfied. The X-ray photons are scattered by the electrons in the sample, and interfere with each other and the diffracted signal is collected on a two-dimensional detector downstream from the sample (positioned at a distance, D, from the sample). Each area detector pixel integrates the diffracted X-ray beam intensity within a specific solid angle. Typically, a range of detectors can be used in CDI measurements, but most commonly used of these are the CCD detectors (with a pixel size 20 x 20 μm) and Pilatus detectors (with a pixel size of $\sim$172 x 172 μm), both developed by the Swiss Light Source, Switzerland. The latter was used in this investigation—a Pilatus 100K detector from Dectris. Fig.2.11 the conical diffraction pattern ring from a given crystal plane (hkl). The Bragg peaks on the powder ring satisfy the Bragg condition at (hkl). Typically, a Bragg peak from crystal that is stable with strong well-defined interference fringes, is selected and isolated. Then a complete diffraction data set can be accumulated by taking rocking curve of the Bragg peak. The rocking curve is collected by varying the crystals angle (ω) with a step size of fraction of a degree.

2.2.3.4 Over-Sampling

It has been mathematically proven that for recorded diffraction data sets to contain enough information to solve the phase problem, they have to satisfy 'over-sampling' conditions [Miao et al., 2005]. For nanoparticles, Sayre states that it would be possible to solve the phase problem if the diffraction data was sampled at a Nyquist rate which is half the unit cell. This criterion is a necessary condition required for the successful reconstruction of both amplitude and phase from measured reciprocal-space diffraction data sets of structures of which both need to be extracted in the reconstructions. Therefore, at least double the amount of unknowns have to be resolved in comparison to the number of reciprocal-space points. 'Over-sampling' of diffraction data sets can be achieved by adhering to the following condition [Williams et al., 2003]:

$$\sigma = \frac{\lambda . D}{\text{Detector pixel size.S}} \tag{2.7}$$

where the detector is positioned at a given distance away from the sample, D, the wavelength of the source is fixed at λ and the size of the crystal, S, is defined by the spacing between two opposing facets. In order to meet this oversampling requirement, D is required to be large enough so that there are at least two detector pixels per fringe [Watari et al., 2011]. First the phase needs to be retrieved using phasing algorithms.

2.2.3.5 Strain Sensitivity

In a typical X-ray diffraction experiment a sample is illuminated with an X-ray beam and the diffracted X-ray beam is recorded in the form of a diffraction pattern in the far field or Fraunhofer region. The X-rays scatter from the whole volume of the nanoparticle and interfere at the detector, forming a diffraction pattern recorded as intensity. The intensity, $I(\mathbf{Q})$, surrounding each Bragg peak, represents the shape of the electron density and is expressed as:

$$I(\mathbf{Q}) = |F^{crystal}(\mathbf{Q})|^2 = \int \rho(r) e^{i\alpha} dr \tag{2.8}$$

where $\rho(r)$is a complex function describing the electron density of the sample at the point r, $F^{crystal}()$ is the reciprocal space scattering amplitude, and phase is $\alpha = \mathbf{Q}.r$. Since only reciprocal space amplitude is recorded in intensity, and the phase is not recorded (despite being mathematically present). This equation shows that the intensity is the FT of the electron density but due to the loss of phase in the measurement the electron intensity cannot be simply retrieved by applying a direct FFT to the diffraction data.

In a finite perfect crystal lattice, the dependence of the intensity on the FT of the shape function would produce a locally symmetric diffraction pattern surrounding the Bragg peak. However, in reality a crystal lattice is never truly perfect. Atomic displacements away from the equilibrium lattice positions can occur in a crystal as the result of forces such as, chemical, physical, magnetic, electrical, or optical. The schematic in Fig.2.12 shows a coherent X-ray interacting with a homogeneously strained crystal lattice. The red lines indicated correspond to the total phase shift of incoming coherent X-ray relative to that of the crystal, which can be calculated by $\Delta\phi = \mathbf{k_i}.\mathbf{u} - \mathbf{k_f}.\mathbf{u}$. This phase shift, $\phi(r)$, is equivalent to $\phi(\mathbf{r}) = \mathbf{Q}.\mathbf{u}(r)$ where $\mathbf{u}(r)$, is the local displacement vector of the lattice fringes, whose values are the projections of the local lattice displacement onto the momentum Q-vector. This strain can be seen in the surrounding Bragg peak,

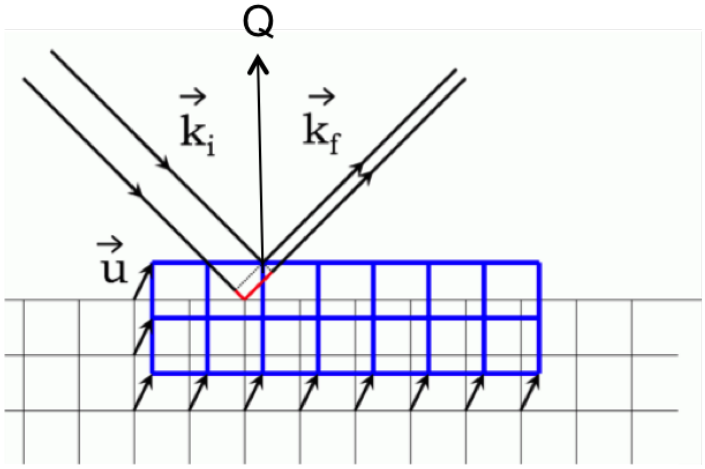

Figure 2.12: *Schematic of strained reciprocal lattice demonstrating the effect of the deviation of lattice (blue) from the perfect reciprocal lattice (black) resulting in displacement strain field* $\mathbf{u}$*, and a phase shift (red)-image. Reprinted with permissions [Robinson and Harder, 2009].*

resulting in an asymmetric data set. The strained region in the crystal will be man-

ifested in the final reconstruction as a region of complex density with the same magnitude from the rest of the crystal but with a phase shift of $\phi(r)$. A 3D phasing algorithm can then be applied to this data set to invert the data from reciprocal space into real space to obtain a 3D image of the object and the corresponding internal strain distributions [Cha et al., 2010] [Newton et al., 2009].

2.2.3.6 Phase Retrieval Algorithms

A phase retrieval algorithm solves the phase problem allowing an image of an object, in real space, to reconstructed from diffraction data in reciprocal space. The diffraction data set, in reciprocal space, is iteratively phased using estab-

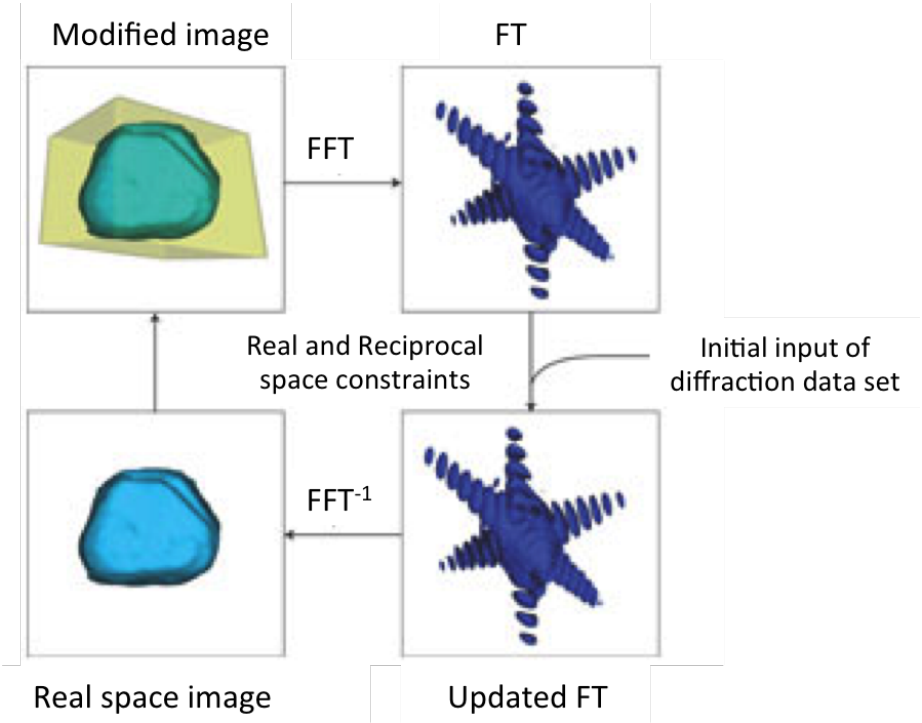

Figure 2.13: *Fundamental principle of CDI iterativde algorithms that permits he reconstruction of a sample distribution from its diffraction pattern by the iterating back and forth between real space and reciprocal whilst applying constraints. Reprinted with permissions from [Robinson and Harder, 2009]*

lished phase retrieval algorithms based on the hybrid input output (HIO) and error reduction (ER) method [Fienup, 1982]. The algorithms work by iterating between real and reciprocal space applying constraints on the finite extent of the object in

real space and the complex diffraction pattern in reciprocal space. This phase retrieval process is depicted in detail in Fig.. [Robinson and Harder, 2009]. Phase information is recovered when the algorithms converge and is typically after hundreds to thousands of iterations. A physical support is created in real space based on a priori knowledge of the sample size and is used to confine the recovered object to a finite size in space. A Fourier Transform (FFT) is applied to the guess at the object size to convert it into reciprocal space (keeping the phase value but replacing the amplitudes with square root of measured intensity of diffraction data) providing a 'guess' of the complex diffraction pattern.

This diffraction pattern is then constrained by replacing the estimated diffraction amplitude with the measured diffraction amplitude and keeping the guessed phase. This new diffraction pattern is then inverse Fourier Transformed (FFT^{-1}) to convert the data back into real space providing a new guess of the object. The support constraints are then imposed by keeping the amplitude inside the support the same but the points outside the support are treated with an error reduction (ER) method.

Once phased, the diffraction data—collected from a series of diffraction patterns over the rocking curve— is inverted using a Fourier transform (FFT) into a real space to give a 3D reconstruction of the nanoparticle structure and strain in complex density maps. The 3D phasing algorithm is used to reveal both the amplitude and phase where the magnitude corresponds to the average 3D electron density and the local displacements in the crystal lattice respectively. The local displacements on the nanoparticles can be quantitatively mapped on iso-strain phase maps resolvable on the picometre scale.

2.2.4 Powder X-ray Diffraction

2.2.4.1 Total Scattering

Total scattering diffraction patterns contain both the Bragg component which provides information on the average crystalline structure; and the diffuse component which reveals the the local deviations from the average periodic structure [Soper and Barney, 2011]. Diffraction patterns collected by conventional XRD

monochromatic Cu K_alpha analysis does not yield a high enough Q to obtain high resolution total scattering diffraction data, thus the diffuse component is usually treated as background and subtracted[Young and Goodwin, 2011]. Only by collecting diffraction data up to high values of Q ($Q\,10A^{-}10$), can high resolution total scattering diffraction data be obtained. Total scattering diffraction data is typically achieved by using neutron or X-ray powder diffraction (or sometimes through the use of monochromater with an Ag source). Atomic pair distribution function (PDF) transforms the reciprocal space data into real space [Proffen and Kim, 2009] yielding the local atomic arrangements of complex materials.

2.2.4.2 Atomic Pair Distribution Function

The atomic pair distribution function (PDF) is a principally well understood analysis method that is defined as the probability of finding an atom in a unit volume, at a distance, $\vec{r}$ from a reference atom. The concept of the PDF was initially described in the classical 1969 textbook, of Warren on X-ray diffraction [Addison Wesley; New-York, Dover]. Traditionally the PDF was used to overcome the difficulties associated in characterising the atomic scale structure of disordered liquids and amorphous systems. Only recently, over the past decade have the tools and software capabilities emerged for the application of the PDF analysis to study disordered nanocrystalline systems [Billinge, 2008] [Newton et al., 2012].

The PDF, G(r), is an inverse sine Fourier transform of the total-scattering structure function S(Q) (experimentally determined high resolution diffraction data) and is defined as:

$$\begin{aligned} G(r) = \frac{2}{\pi}\int_{Q_{min}}^{Q_{max}} (Q[S(Q)-1]sinQr.dQ) \\ = 4\pi r[\rho(r)-\rho_0)] \end{aligned} \tag{2.9}$$

where r is the distance between pairs of atoms, Q is the momentum transfer vector, $\rho(r)$ is the instantaneous pair density at $\vec{r}$ and ρ_0 is the average number density. The lower limit of the integration range, Q_{min}, is restricted by the effects of direct beam, and set at 0, whereas; the upper limit Q_{max} is restricted by the wavelength (λ) of the radiation and corresponds to $Q_{max} = \frac{4\pi}{\lambda}$. The different definitions

of PDF and terminologies has also been clarified by David Keen for application to the field of total scattering [Keen, 2001].

The information that can be extracted from a PDF is demonstrated in Fig.2.14 where the peak positions correspond to quantitative atomic distances within the nanosystem. The first peak corresponds to the distance, r, of the reference atom

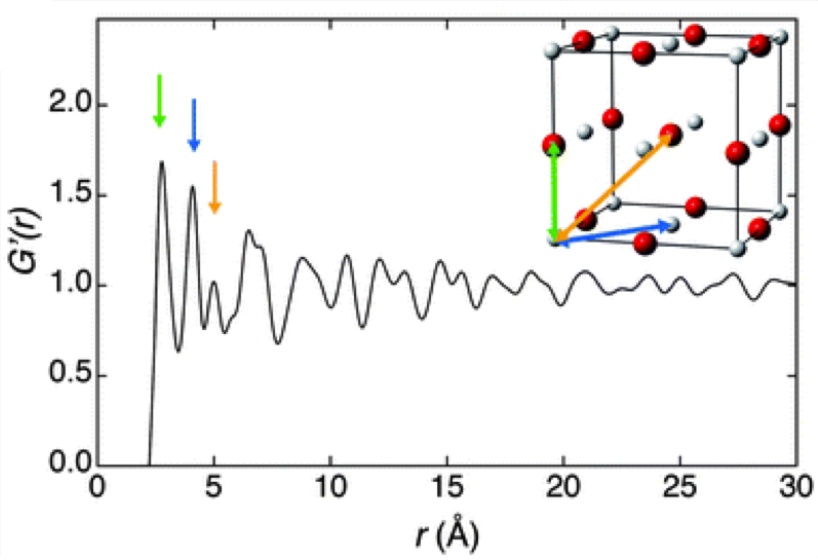

Figure 2.14: *PDF with 1st, 2nd and 3rd NN peaks annotated by the green, blue, and orange arrow respectively, with the corresponding bonds distances indicated in the bcc unit cell (inset). Reprinted with permissions from [Young and Goodwin, 2011] [REF]*

to the first NN shell, and the second peak corresponds to the distance, r, of the reference atom to the second NN shell and so forth to the 3rd, 4th and 5th and so forth. The peaks attenuate with r and the point where the peaks diminish (the 'termination ripples') corresponds to the largest possible bond distance within the atomic system consistent with the diameter of the nanoparticles. The first r value corresponds with the cut-off value (lowest possible resolution). Further information can be extracted from the PDF such as; the presence of thermal vibrations between the atoms (extracted from the peak width) and the co-ordination number of the atoms (extracted from the integrated peak intensity) enabling the average number of NNs to be extracted e.g. a value of 5 could be an average of atoms with 4-fold and 6-fold co-ordination. The PDF equation differs slightly in terms of the radiation type used, as X-rays and neutrons have different structure factors $I(Q)$ and $S(Q)$, respectively.

2.3 Introduction to Neutron Diffraction

2.3.1 Subatomic Particle Waves

In 1856 Joseph John Thomson made the first experimental discovery of the subatomic particle electron in a series of cathode ray experiments showing that the atom can be split releasing negative elementary particles. Thus, proving that the electron is a fundamental constituent of all atomic elements. De-Broglie went on to propose a quantum mechanical behaviour of elementary particles (e.g. electrons, neutrons) where they can exhibit particle-like characteristics aswell as wave-like characteristics. This wave-particle duality of particles, states that all moving matter has wave properties and the wavelength is related to the momentum by:

$$\lambda = \frac{h}{p} \tag{2.10}$$

where $p = mv$, where m is the mass of the subatomic particle. As neutrons and electrons have a finite mass (mass of an electron is 9.109×10^{-31} and neutron is $1.68 \times^{-27}$kg) the kinetic energy and momentum of the neutrons are included in the energy calculation leading to the De Broglie relationship:

$$E = \frac{h^2}{2m\lambda^2} \tag{2.11}$$

Applying de-Broglie's equation a neutron with a wavelength of 1.5 Å has an energy of 36.4 meV whilst an X-ray photon of the same wavelength has an energy of $\sim$ 8.2 keV, which is more than 200,000 times greater than the neutron energy.

2.3.2 Neutron Facilities

In the 1940's neutrons were already in use as fissionable materials for atomic weapons, and it was only in May 1944, when physicist Ernest O. Wollan realised the capabilities of neutrons applied to neutron diffraction. Clifford G. Shull in collaboration with Wollan obtained the first successful neutron diffraction pattern from a crystal during experiments at Clinten Laboratories (now known as the Oak Ridge National Laboratory) and established its corresponding structure. Since

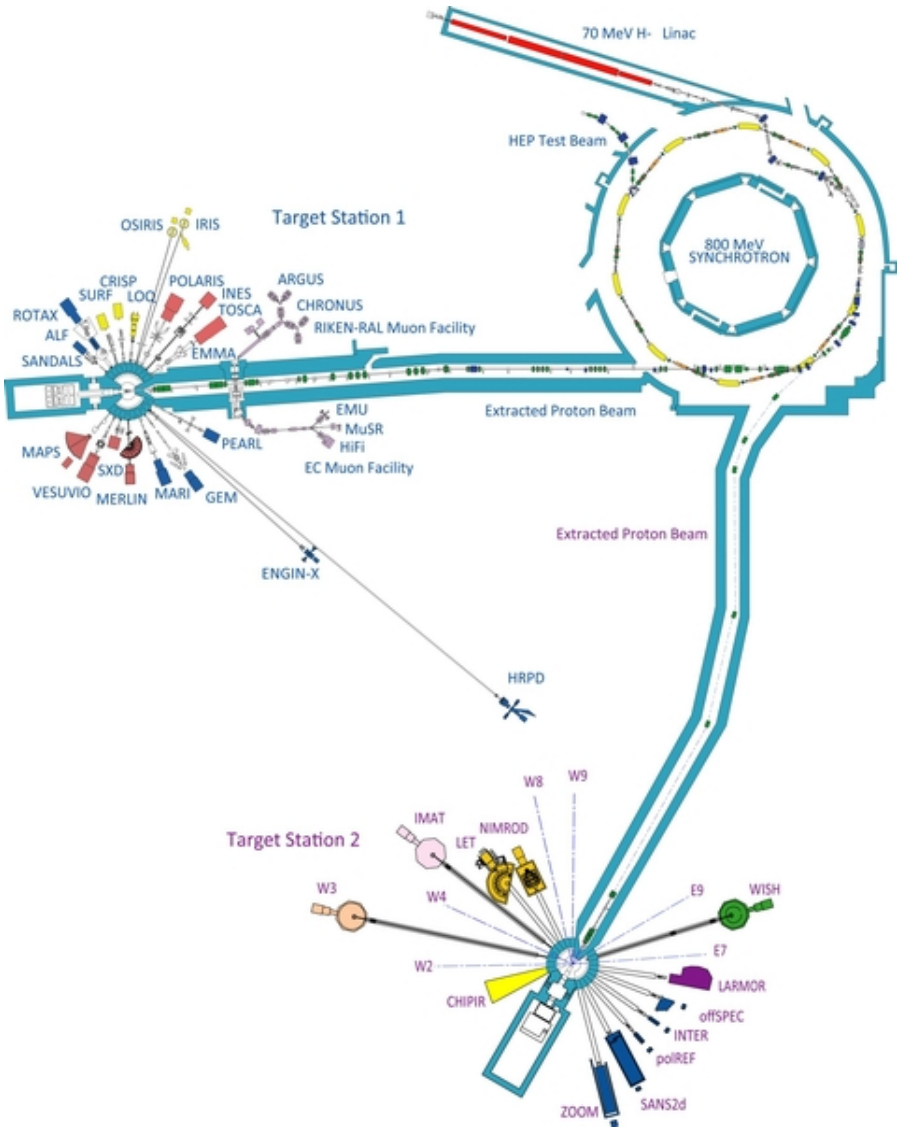

Figure 2.15: *ISIS neutron facility housed at the Rutherford Appleton Laboratory. Reprinted with permission from stfc.*

this discovery neutron facilities became operational enabling reserachers from both academic and industrial institutions to probe the atomic structure of a range of systems including crystallographic, liquid, biological and amorphous materials. The ISIS neutron facility at the Rutherford Appleton Laboratory, Didcot, houses the UK's only neutron facility, which is a spallation neutron source. This spallation neutron source is the second most powerful in the world and is utilised for the neutron powder diffraction experiments conducted within this thesis in Chapter 7. The generation of neutron radiation is detailed below and corresponds to the

schematic in Fig.2.15.

1. **Proton Generator:** The ionisation of hydrogen gas in the ion sources generates a supply of heavy H^- ions that are accelerated in the 50 m linac to 70 MeV. The H^- beam is injected into the synchrotron and is passed through a 'stripper' consisting of thick aluminium oxide foil. The stripper effectively strips the H^- beam of electrons resulting in a beam protons, H^+. The proton beam H^+ is then injected into the proton storage ring.

2. **Proton Storage Ring:** (163 m, 200 μA, 800 MeV,) where there are 10 sections of bending magnets. The protons are accelerated in the proton storage ring to 800 MeV and into 2 bunches via an increasing harmonic RF, and are accelerated around the synchrotron in two bunches (10,000 times) reaching 800 MeV.

3. **Target Station Extraction:** The photons are extracted from the synchrotron, into one of the two target stations (TS) where the neutrons are produced via spallation. TS-1 is optimised for high energy neutron experiments and TS-2 is optimised for low energy neutron experiments. In both TS's the proton beam is directed at a heavy metal tantalum, Ta target coated with tungsten, W. The collision of the proton beam with the nucleus of the Ta atoms results in spallation, which is the disintegration of the nucleus, causing the emission of a neutron. In this case for every incident proton $\sim$ 12 neutrons are generated. In TS-1 the neutrons are moderated or collimated accordingly and directed into one of 20 different beamlines. Notably, at this stage a small percentage of muons are produced by passing the initial neutrons through a graphite target. These muons are utilised for muon, spin spectroscopy. In TS-2 the neutrons are moderated or collimated accordingly to produce short pulses of neutrons with a range of energies (collimated for 13 different beamlines).

In the investigation conducted within the Near and InterMediate Range Order Diffractometer (Nimrod) beamline, situated in TS-2, was selected as the most suitable beamline for this neutron investigation owing to its broad spectral range of energies 0.04 Å$< \lambda >$ 12 Å.

2.3.2.1 Near Intermediate Range Order (Nimrod) beamline

The wide range of detectors of Nimrod with continuous Q range from 0.01 $Å^{-1}$ to 50 $Å^{-1}$ capable of bridging the gap between small angle and wide-angle neutron scattering (SANs and WANs, respectively) [Bowron et al., 2010]. The Nimrod instrument is specifically designed to reduce the degree of complex corrections required to treat inelastic scattering from protonated samples (e.g. solvents and surfactants) which ideal for the performance of hydrogen-deuterium isotopic substitution experiments. Mostly, the use of a forward-scattering geometry (in Nimrod's case only considering scattering angles up to 40°) and relatively high-energy neutrons also help to reduce the degree of inelastic events measured [Soper, 2009]. The Nimrod beamline is indicated in the schematic of the TS-2 beam lines in Fig.2.16a. The external beamline is illustrated in the schematic in the upper image in Fig.2.16b indicating the direction of the incoming beam (red arrow), the location of the shutter, the sample holder (which is in a large sealed vacuum) and the end detector bank. The internal beamline is illustrated in the lower image in Fig.2.16b (capture during beamtime). The neutron scattering from the sample is collected by an array of ZnS scintillator elements located in a detector bank at the end station as imaged in Fig.2.16c. The detector elements detect the neutrons which are converted into a corresponding electrical signal by the connecting photomultiplier tubes positioned over a full range of azimuthal angles $\pm 90°$. The wide-angle detectors enable scattering from the whole nanoparticle system to be detected from the surrounding surfactant (in the small angle region) to the FePt nanoparticle (in the wide angle region). The photograph in Fig.2.16d is of the upper detector hemisphere outwith the detector bank (captured in 2014 during an upgrade for the addition of new detector elements).

2.3.3 Wide Angle Neutron Scattering

2.3.3.1 Contrast Variation

The efficacy of the neutron scattering from the nucleus of an atom is unique to the atom in which the neutron interacts with and is expressed by the coherent, b_{coh} and incoherent scattering lengths, b_{inc} and are experimentally determined parameters. The incoherent scattering length, b_{inc}, of a sample is due to the

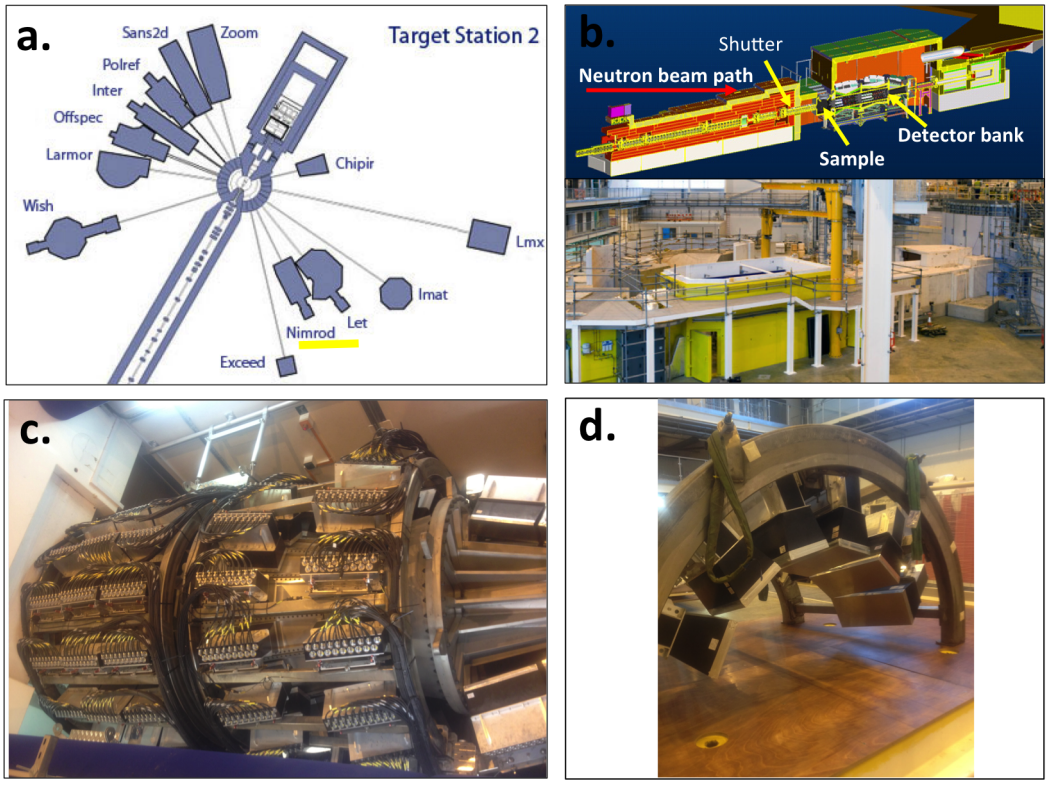

Figure 2.16: *Nimrod beamline (a) TS-2 with the Nimrod beamline indicated (underlined in yellow) (b) Upper schematic of the internal Nimrod beamline and lower photo of the external Nimrod beamline set up with the incoming beam direction indicated by red arrow, the location of the shutter, the sample holder (which is in a large sealed vacuum) and the end detector bank (c) Nimrod detector bank at the end station with 1800 ZnS scintillator element detectors and corresponding photomultiplier tubes positioned over a full range of azimuthal angles* $\pm$ *90° (photographed captured during an instrument upgrade) (d) Photograph of upper detector hemisphere outwith the experimental hutch during decommission.*

correlations between the same nucleus of an atom but at different times, such as phonons, where the scattering is measured from an atom at time = 0, has moved relative to the initial scattering measured. This provides information on the diffusive motion of the atoms as it is isotropic (scatters randomly in all directions) it only really adds a background to the coherent signal. However, hydrogen has a comparably large incoherent neutron scattering length of 25.27 fm which can result in a large inelastic scattering background that needs to be considered in the treatment of the measured diffraction data. The coherent neutron scattering length, b_{coh}, describes the effective area of the nucleus viewed by the neutron and varies in value from different atoms of different elements where $\sum f_j = 1$ the

average b for the system is:

$$\bar{b} = b = \sum_j f_j b_j \tag{2.12}$$

The magnitude and phase of the coherently scattered neutron is uncorrelated with atomic number as illustrated by the variation of b, with atomic number for the elements in Fig.2.17 and is different for isotopes (atoms with the same number of protons but different numbers of neutrons). For example, it can be observed

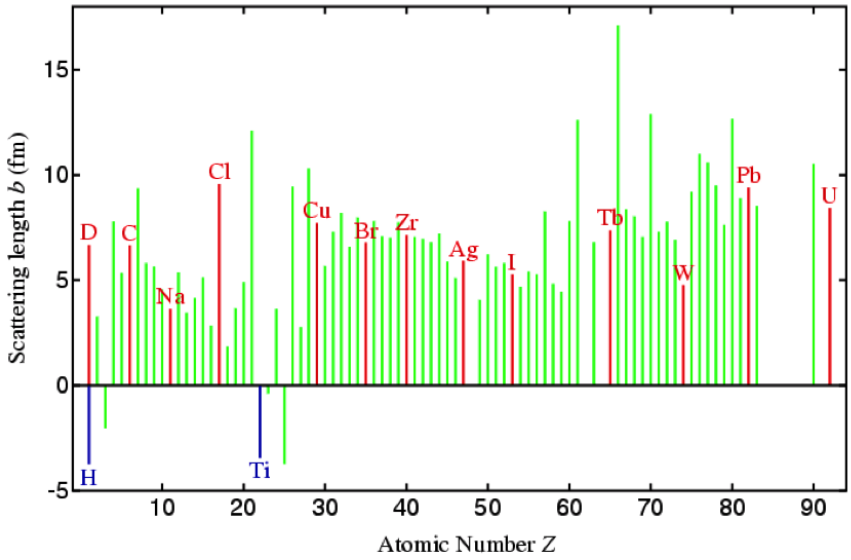

Figure 2.17: *Atomic number of elements, Z, against scattering length density, b (fm). Reprinted with permissions from Jeremy Carl Cockcroft [REF].)*

in Fig.2.17 that for H^1 (no neutrons) b =−3.74 fm, the negative magnitude is due to the scattering length being 180°out of phase. This is in sharp contrast to the corresponding isotope of hydrogen, which is deuterium, H^2 (one proton and one neutron) it has a larger b value and a positive scattering length of b = + 6.671 fm. The contrasting phase and difference in magnitude between the isotopes of hydrogen are greatly exploited in the technique of selectively probing elements and in contrast matching, which currently plays an important role in structural biology and polymer science research.

The scattering from a constituent can be varied by substituting one isotope for another, for example, FePt nanoparticles with deuterated surfactants in a hydrogenated solvent would highlight the presence of the surfactants relative to the solvent as explained in further detail in Section 7.5.0.4. The summation of the different scattering lengths, b, from different elements can be calculated by calcu-

lating the scattering length density, SLD equation:

$$\rho = \frac{\bar{b}}{V_m} \tag{2.13}$$

Where ρ is calculated from the summation of the b_c contribution from each element in the molecule and divided by the molecular volume V_m. The different SLD's of materials are exploited in the design and manufacture of sample holders for neutron diffraction experiments and a sample holder with a low negative scattering or null scattering contrast is desired. For example, in these investigations Titanium Zirconium (TiZr) sample cans (holder) are used. TiZr has b_c values of Ti($-$3.44 fm) and Zr(+7.16 fm) and is alloyed with a specific ratio of Ti:Zr (52.5:47.5 %) giving a total coherent scattering length close to zero resulting in 'null scattering'. This form of zero contrast matching is used to effectively make the holder 'invisible' in the diffraction data.

2.4 Comparison of X-rays and Neutrons as Analytical Probes

X-ray and neutron techniques are typically used as complementary probes to provide a comprehensive study in the characterisation of a system. In X-ray diffraction, because X-rays interact with the electron cloud of an atom its scattering cross-section increases linearly with atomic number, Z, as illustrated in the upper schematic in Fig.2.18. Therefore the scattering contribution from heavy elements dominates the scattering contribution from light elements. Also, the scattering power of an atom falls off with scattering angle resulting in the peak intensities of an X-ray diffraction pattern diminishing at high angles. In the case of neutron diffraction, neutrons interact with the nucleus of an atom and so the scattering cross-section has no coherent relationship with atomic number, Z, as illustrated in the lower schematic in Fig.2.18. Also, because the nucleus of the atoms effectively act as point scatterers the neutron scattering power remains constant with scattering angle resulting in the peak intensities in a neutron diffraction pattern being of high resolution at high angles. Therefore neutron diffraction is very precise and capable of probing the relative positions and motions of atoms in a bulk sample of solid or liquid and they are also sensitive to the presence of organic

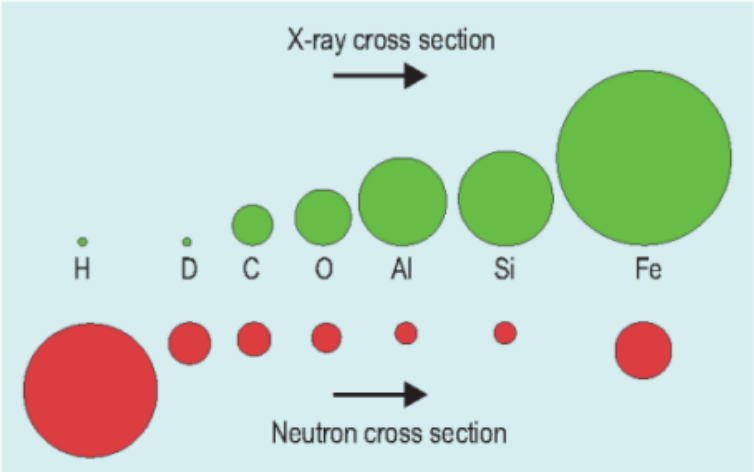

Figure 2.18: *Schematic of relative scattering cross-sections for X-rays and neutrons. Reprinted with permissions from NIST [REF]*

compounds such as proteins and surfactants. There exists a pronounced benefit behind using both complementary diffraction techniques of neutrons and X-rays as analytical probes in the analysis of the FePt metal alloy nanoparticle-surfactant system;

- **X-rays** are sensitive to the FePt nanoparticle core which consists of 'heavy' inorganic metal atoms with a high atomic number, i.e. Fe (Z = 26) and Pt (Z = 78). Also, the high incident flux, ϕ, of X-rays (10^{18} photons $s^{-1}cm^{-2}$) in comparison to the low ϕ of neutrons (10^{4} neutrons$s^{-1}cm^{-2}$) enables data of high statistical value to be collected in X-ray diffraction experiments over much shorter run times.

- **Neutrons** are sensitive to the surrounding hydrocarbon surfactant layer which consists of 'light' atoms of a low atomic number i.e. H (Z = 1), D (Z = 2), C (Z = 12), O (Z = 16). Neutrons are also capable of distinguishing between isotopes of hydrogen [Marco et al., 2009] which can be utilised in isotopic substitution investigations. The magnetic properties of neutrons can also be utilised to determine the magnetic properties of a system in specific spin-polarised investigations but in this is no experiments.

2.5 Introduction to Electron Generation

In TEM investigations electrons are utilised as an analytical probe from use of a range of advanced TEM instrumentation. Each method is explained in further depth in Chapter 4 and the results are presented in Chapter 5. Electrons are generated using a similar concept to light generation used in light bulbs, except it requires higher operating voltages and a thermionic wire to overcome the work function of the wire to create a plasma of free electrons. The free electrons are then accelerated by a potential difference and focused using a set of optics onto the sample under vacuum (to avoid energy loss through collisions of the electrons with the external environment). There are two common types of electron generation sources used in TEM; schottky filaments coated with materials that have a low work function such as, tungsten, W, or lanthanum hexaboride, LaB_6, and FEGs. The original W coated filaments are the least efficient of electron sources, generating electrons with an electron energy distribution of 2.5 eV (given by their own Fermi distribution). Comparatively, LaB_6 coated filaments have a lower work function and generate electrons with a smaller electron energy distribution of 1.5 eV. However, these heated thermionic filaments are restricted due to the effect of the Boltzmann energy distribution which increases the energy distribution wavelength spread. FEGs are the most efficient of the electron sources as they utilise an EM current to tunnel the electrons from the filament, allowing for high coherence of the electron beam and a low electron energy distributions within the range of 1 eV (hot) - 0.5 eV (cold).

The resolution of the TEM is dictated primarily by the operating voltage which impacts the resultant wavelength of the electron probe and can be calculated by substituting in $p = mv$ into Eq.2.3.1 and on considering relativistic effects:

$$\lambda = \frac{h}{\sqrt{2m_e eV}} \times \frac{1}{\sqrt{1 + \frac{eV}{2mc^2}}} \tag{2.14}$$

where $m_e$is the mass of an electron (9.11×10^{-31} kg), eV is the energy where $eV = 1.60 \times 10^{19} C$ and c is the speed of light $2.998 \times 10^8 ms^{-1}$.

Therefore, on applying Eq.2.5 the corresponding wavelength for the TEM instruments can be determined. For example, for a TEM operating at 100 keV, $\lambda \sim 3.71 \times 10^{-12} m$, for a TEM operating at 200 keV, $\lambda \sim 2.51 \times 10^{-12} m$ and for a

TEM operating at 300 keV, $\lambda \sim 1.96 \times 10^{-12} m$. However, there are limitations in achieving these wavelength resolutions in TEM instrumentation due to other factors such as lens aberration and wavelength spread of the electrons. Currently the highest achievable resolution from a TEM is 2×10^{-12}m.

2.6 Probing Matter with Scattering Radiation

When EM radiation or subatomic particle rays, such as X-rays or neutrons respectively, interact with an object the radiation will either be transmitted, absorbed or diffracted. In a typical scattering experiment the incident beam of neutron or X-ray

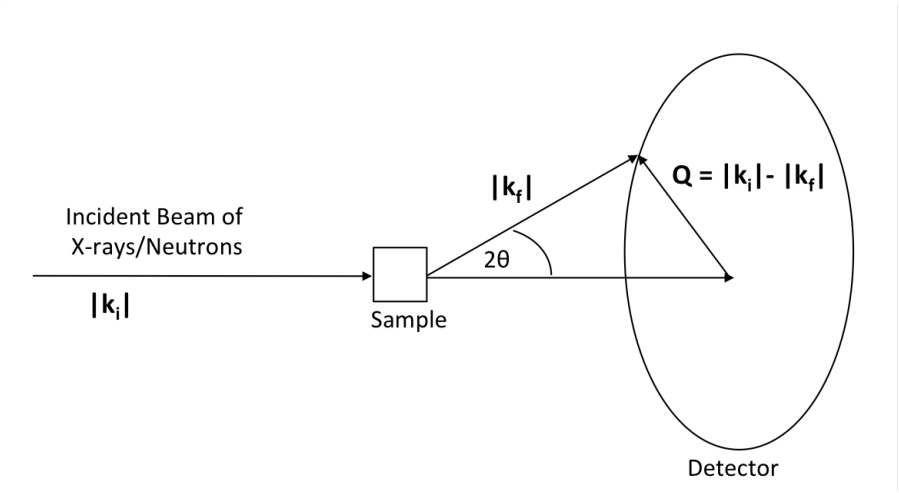

Figure 2.19: *Schematic of a scattering event where **Q** is the momentum transfer vector, k_i is the incoming wavevector and k_f is the diffracted wavevector.*

radiation of wave vector $k_i = 2\frac{\pi}{\lambda}$ interacts with the sample and is scattered with wave vector k_f. The scattered radiation is known as the momentum transfer, Q. The difference between incident and scattered beam is Q and is known as the scattering vector and is related to the wave vectors by:

$$Q = \mathbf{k_i} - \mathbf{k_f}. \tag{2.15}$$

In a diffraction experiment the scattering energy is conserved (elastic scattering) and $|k_i| = |k_f|$ therefore Q is defined as:

$$Q = \frac{4\pi sin\theta}{\lambda} \tag{2.16}$$

where θ is the scattering angle and λ is the wavelength of the incoming radiation. This scattering vector an important quantity in X-ray and neutron investigations as it is related to the energy change that occurs during scattering and the scattering angle.

2.7 Scattering Events

The physical basis behind X-ray scattering is the same as that of neutron and electron scattering although the scattering mechanisms differ due to the different interactions of the radiation with matter. The interactions of radiation with matter is depicted in the schematic in Fig.2.20 and described below.

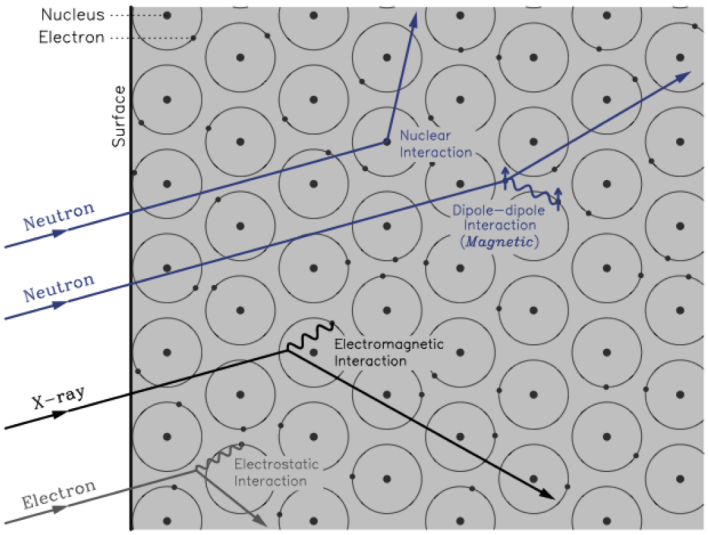

Figure 2.20: *Interaction of neutrons, X-rays and electrons scattering events with matter. Image reprinted with permissions from [Sivia, 2011] [REF].*

- **Neutrons:** Neutrons are neutrally charged and interact with matter primarily with the nucleus of an atom and so are able to probe the precise location

of the nucleus. The short range nuclear forces of the bound nucleus are of the order of $10^{-14} - 10^{-15}$ m, which is small in comparison to the incident neutron wavelength ($\sim 10^{-10}$ m). Thus, the bound nucleus of atoms in the material can be considered as a point-like scatterer to the incident neutron beam. Their interaction with matter is inherently weak [Sivia, 2011] resulting in a short range interaction and a deep penetration depth, within the centimetre range.

- **X-rays:** X-rays have no charge and interact with matter primarily via an EM interaction through Thomson scattering with the charge of the orbital electrons of the atom and so are capable of probing the electron density of the material through either absorption or scattering to determine atomic structure. X-rays are attenuated by matter with a penetration depth in the range of μm - mm.

- **Electrons:** Electrons are negatively charged particles and interact in a similar way to X-rays via an EM interaction through Coulomb forces where the negative electrons interact with the force of the positive nuclear charges. Electrons are highly attenuated by matter with a penetration depth in the 100 nm range and therefore requires very thin samples. Electrons interact with the sample by either inelastic or elastic scattering events as discussed in more detail in Chapter 5.

2.7.0.2 Neutrons Scattering from a Single Nucleus

Scattering geometry of neutron scattering from a single nucleus is depicted in the schematic in Fig.2.21, where k_i is the wavevector of the incident wave and k_f the wavevector of the scatterd wave. The incident beam of neutrons, travelling in the x-direction, is represented as a plane wave with a wavefunction:

$$\Phi_i = e^{-i\mathbf{k}x} \tag{2.17}$$

When the incident plane wave interacts with the bound nucleus, the nucleus acts as a point scatter and re-emits the neutron as a circular wave (or in the case of

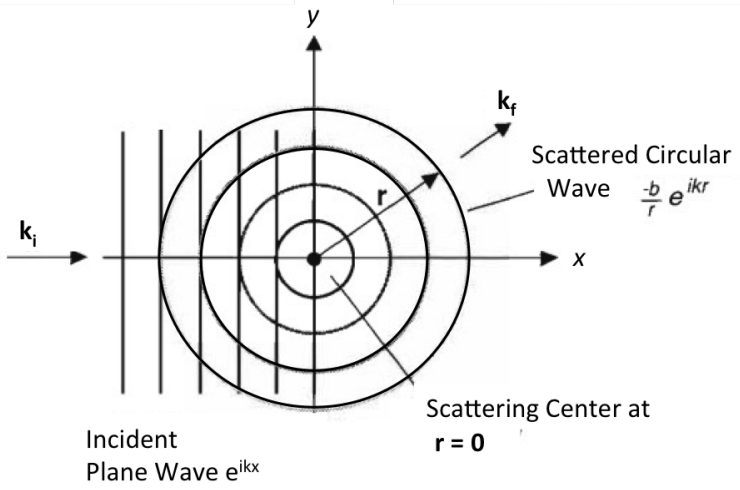

Figure 2.21: *A neutron scattering event from a single nucleus point scatterer with an incident plane wave of wavevector k_i, and scattered circular wave with wavevector, k_f.*

3D scattering an isotropic spherical wave) with a wavefunction:

$$\Phi_f = b\frac{e^{-i\mathbf{k}r}}{r} \tag{2.18}$$

where b is the neutron scattering length (measures the strength of the neutron-nucleus interaction and is an experimentally defined value and specific for different atom species), r is the distance of the scattered wave at position $\mathbf{r}$ from the fixed scattering nucleus at the center origin. This scattering geometry relates to the total cross section by:

$$\sigma_{tot} = 4\pi b^2 \tag{2.19}$$

thus b quantifies the effective area of the nucleus viewed by the incoming neutron.

2.7.0.3 X-rays Scattering from an Atom

The classical description of X-rays scattering from an electron is depicted in Fig.2.22. The flux, ϕ, of the incident beam can be expressed as the modulus of the incident electric field squared, $|E_i|^2$. The incident X-ray photons, on interaction with an electron, causes the electron to vibrate. The electron then is acting as a source radiating an electric field, $|E_rad|^2$, as a spherical wave. The scattered intensity is proportional to ratio of the magnitude of the radiated electric field to

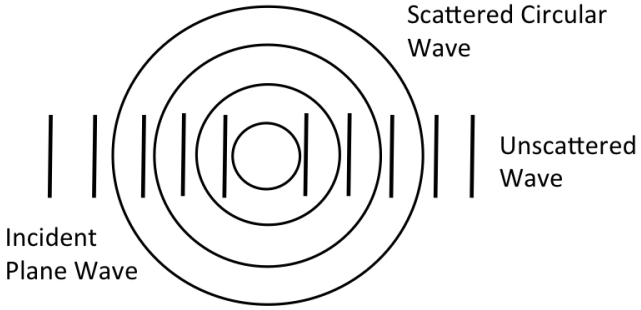

Figure 2.22: *An X-ray scattering event from a free electron in an atom.*

the magnitude of the incident electric field as defined by:

$$\frac{E_r ad(R,t)}{E_i} = -\frac{e^2}{4\pi\varepsilon_0 mc^2}\frac{e^{ikR}}{R}cos\phi \tag{2.20}$$

where ε is the polarisation of the electric field vector, energy $E = mc^2$, the first term refers to the Thomson scattering length of the atom which defines the 'ability' of an electron to scatter X-ray photons and is the fundamental length scale for the interaction between an electron and an X-ray photon. From this classical description the scattering cross-section can be derived and is defined as:

$$\sigma_s = 8\pi r^2 \tag{2.21}$$

2.8 Diffraction

2.8.1 Bragg's Law

Max Von Laue, alongside his co-workers Friedrich and Knipping, won the Nobel Prize in 1912 for the discovery of the scattering phenomenon of X-rays from objects. In their X-ray scattering experiment of Copper Sulphate Hydrate crystal they discovered sharp diffraction spots on the detector (photographic film) as a result of intense scattered beams [Ewald, 1962]. Following on from Laue's conception, William L. Bragg, in the same year analsyed Laue's diffraction pattern of zinc blende crystal to determine its crystal lattice structure. Bragg devised that a certain family of lattice planes—in a periodic crystalline lattice—will diffract inci-

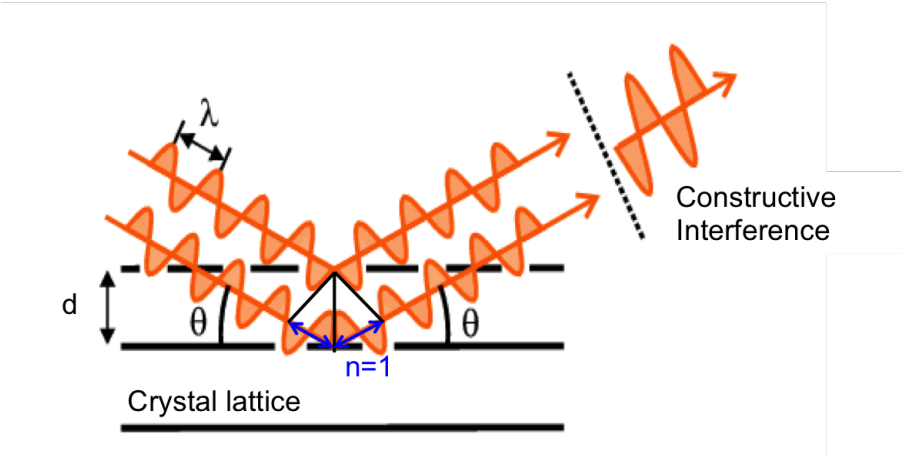

Figure 2.23: *Schematic representation of Bragg's Law. Diffraction of incoming planar wavefront of wavevector, k_i with wavelength, λ, with crystal of interplanar spacing, d, and scattered planar wavefront of wavevector,k_f. For constructive interference to occur, the path difference 2dsinθ must be equal to an integer number of wavelengths nλ. Adapted image reprinted with permissions from Jeremy Karl Cockcroft.*

dent X-rays constructively in phase when oriented in a specific direction. Bragg's law defines these conditions in which diffraction takes place where diffraction from a crystalline lattice will only occur when the path difference of the incident beam is equal to an integer number of wavelengths as expressed in the following equation:

$$2dsin\theta = n\lambda \tag{2.22}$$

where d is the inter planar lattice spacing (the perpendicular distance between successive lattice planes (h,k,l)), λ is the wavelength of the incident radiation, n is a positive integer, and θ is the scattering angle in degrees. This construction doesn't however describe the intensity of the scattering from a crystal in which constructive interference occurs.

2.8.1.1 Miller Indices

The reciprocal space lattice planes h,k,l are noted in crystallography as the Miller indices of the crystal. The sets of parallel planes in a crystal lattice can be notated by three indices hkl (Miller indices) which define the characteristic planes of the Bravais lattice. The Miller indice of planes are calculated by converting the fractional co-ordinates where the plane intercepts the unit cell into reciprocal

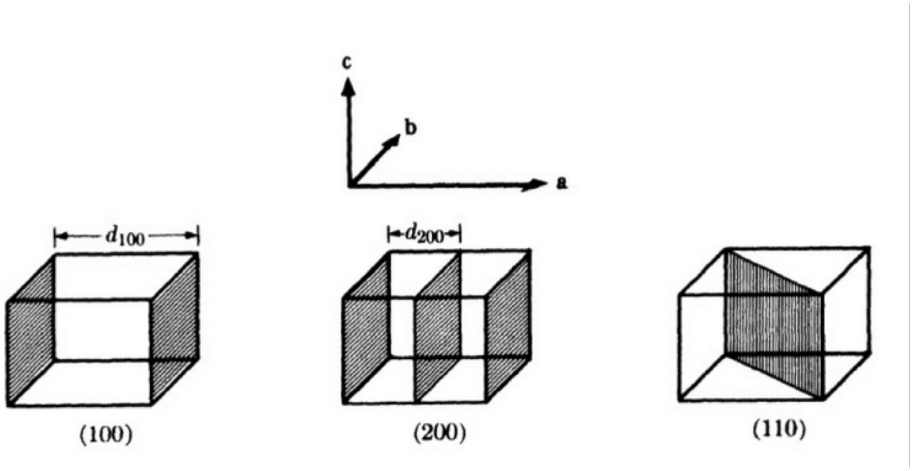

Figure 2.24: *Miller Indices of a cubic system with Miller indices* $(100), (110)$ *and* (111)*. Reprinted with permissions from [Agarwala, 2014].[REF]*

space co-ordinates. A cubic crystal system with low index surfaces with Miller indices $(100), (110)$ and (111) is depicted in Fig.2.24. Each Miller indice is part of a family of planes for example there are a total of six facets to the 100 surface with the planes $(100), (010), (001)$ and $(\bar{1}00), (0\bar{1}0), (00\bar{1})$. In different Bravais lattice systems, there are certain 'allowed' reflections that satisfy the Bragg condition. The allowed reflections for a fcc system are defined by the selection rule in accordance with the crystal system. The selection rule for a cubic system is expressed as:

$$d_{hkl} = \frac{n.a}{\sqrt{h^2 + k^2 + l^2}} \tag{2.23}$$

where d_{hkl} is the inter-planar lattice spacing, a is the unit cell lattice parameter of the crystal. Therefore, for a fcc system in order to be satisfied only reflections from all even or all odd are allowed, and therefore forbidden reflections are mixed odd and even. For example, for fcc FePt nanoparticles the Bragg peak intensities on the diffraction pattern can be assigned to the following planes; $(111), (200), (220), (311)$.

2.8.2 Laue's Condition

A crystalline material has a 3D periodic structure which is comprised of regularly repeating structural unit cells. The scattering amplitude for the crystal is com-

prised of atoms in a unit cell, expressed as:

$$F^{crystal}(\mathbf{Q}) = \sum_{\mathbf{R_n}+\mathbf{r_j}}^{All\,atoms} f_j(\mathbf{Q}) e^{i\mathbf{Q}(\mathbf{R_n}+\mathbf{r_j})} \tag{2.24}$$

where $f_j(\mathbf{Q})$ is the atomic form factor of the atom (which for X-ray scattering is the Fourier Transform (FT) of the electron density of an atom and for neutron scattering is the FT of the nuclear scattering length b_j), r_j is the position of the atom at $\mathbf{r_l} = \mathbf{R_n} + \mathbf{r_j}$, $\mathbf{R_n}$ is the lattice translation vector and $\mathbf{r_j}$ is the position of the atoms inside a unit cell. This scattering amplitude for the crystal can be deconstructed into the product of two terms:

$$\begin{aligned} F^{crystal}(\mathbf{Q}) &= \sum_{\mathbf{R_n}+\mathbf{r_j}}^{All\,atoms} f_j(\mathbf{Q}) e^{i\mathbf{Q}(\mathbf{R_n}+\mathbf{r_j})} \\ &= \sum_n e^{iQ\mathbf{R_n}} \sum_j f_j(\mathbf{Q}) e^{i\mathbf{Q}(\mathbf{r_j})} \end{aligned} \tag{2.25}$$

The first term is associated with scattering from the sum over the lattice sites, and the second term is associated with scattering from the unit cell. This can also be described mathematically by the convolution ('folding') operation where the lattice of points reflects the symmetry of the crystal structure and the unit cell is the lattice structure convolved with a 'basis' repeat unit cell describing the atom positions.

When the sum over the lattice sites is large, the sum of the phase terms is small, and all of the terms will equal unity unless the scattering vector fulfils the following condition:

$$\mathbf{Q}.\mathbf{R_n} = 2\pi m \tag{2.26}$$

The real space lattice points in a Bravais lattice (3D array of discrete points) can be generated by the translation vector:

$$\mathbf{R_n} = x\mathbf{a} + y\mathbf{b} + z\mathbf{c} \tag{2.27}$$

where x, y, z are the 3-dimensional unit , and integers (with a range from 0 to 1), and $\mathbf{a}, \mathbf{b}, \mathbf{c}$, are the 3-dimensional unit vectors.

The reciprocal lattice offers a unique solution to Eq.2.26 where the reciprocal lattice basis vectors are:

$$\mathbf{a}^* = 2\pi\frac{\mathbf{b}\times\mathbf{c}}{V}; \mathbf{b}^* = 2\pi\frac{\mathbf{c}\times\mathbf{a}}{V}; \mathbf{a}^* = 2\pi\frac{\mathbf{a}\times\mathbf{b}}{V} \tag{2.28}$$

where V is volume for a primitive cell, $V = a(b\times c)$. Therefore the sites of the reciprocal lattice points are given by the discrete translation vector:

$$\mathbf{G_{hkl}} = h\mathbf{a}^* + k\mathbf{b}^* + l\mathbf{c}^* \tag{2.29}$$

where (h,k,l) are the reflection points and $\mathbf{a}^*, \mathbf{b}^*, \mathbf{c}^*$ are the reciprocal lattice basis vectors where $*$ indicates perpendicularity with direct lattice vectors. The product of a lattice vector in the reciprocal ($\mathbf{G_{hkl}}$) and direct (R_n) spaces is:

$$\begin{aligned}\mathbf{G_{hkl}}.\mathbf{R_n} &= 2\pi(hx + ky + lz) \\ &= 2\pi m\end{aligned} \tag{2.30}$$

Hence, the Bragg condition is satisfied when, where m is an integer:

$$\mathbf{G_{hkl}} = \mathbf{Q_{hkl}} \tag{2.31}$$

Thus, the scattering amplitude of the crystal is non-zero if and only if $\mathbf{Q_{hkl}}$ coincides with the reciprocal lattice vector, $\mathbf{G_{hkl}}$ the equations in Eq.2.26 are satisfied where at every reciprocal lattice point a Bragg condition is met, $\mathbf{G_{hkl}} = \mathbf{Q_{hkl}}$. This is known as the Laue condition and is the reciprocal space equivalent to Bragg's Law in real space. The Laue condition results in regularly distributed points of intensity in reciprocal space referred to as Bragg peaks or reflection points determined by indice integers h,k,l.

2.8.3 Ewald Sphere

The previous section reveals that diffraction maxima (reflections, diffraction spots) only occur when the Laue condition, or equivalent, the Bragg equation in vector form, is satisfied. This can be visualised in a geometrical construction, known as the Ewald sphere (of reflection), as shown in Fig.2.25 that enables the diffraction maxima accessible in a particular measurement, to be predicted. These predictions can be made using a given orientation of the incident beam of radiation with respect to the crystal and a given wavelength of the beam. There are two

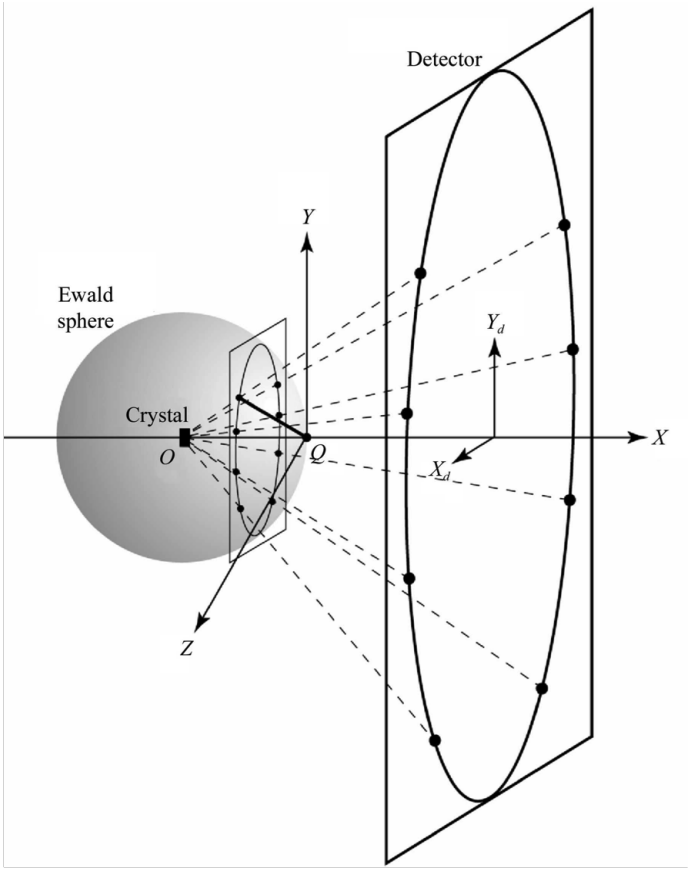

Figure 2.25: *The Ewald sphere construction. The crystal sits at the centre of the sphere, O, and the incoming beam exits the Ewald sphere, Q, creating a diffraction spot on the detector. Each diffraction spot on the detector can be mapped back to its corresponding scattering vector, G, as shown by the bold connecting line. Reprinted with permissions from [Leslie, 2006].*

origins in the sphere; the origin of the crystal at the center of the Ewald sphere; and the origin of reciprocal space at the point where the transmitted beam exits

the Ewald sphere (termed as the reciprocal lattice point). In an elastic scattering event, an incoming beam of wavevector, $\mathbf{k_i}$, interacts with the crystal. The scattered wavevector, sweeps out with a radius, $\mathbf{k_f}$, and each reciprocal lattice point that intersect on the surface of the Ewald sphere will create a diffraction spot on the detector (as shown in Fig.2.25) when the Bragg condition is satisfied (where $\mathbf{Q_{hkl}}$ is equal to a reciprocal lattice vector $\mathbf{G_{hkl}}$). Each diffraction spot on the detector can be mapped back to its corresponding scattering vector as shown by the bold line in Fig.2.25. Rotation of the crystal (in the beam) along the vertical axis can enable points in the whole reciprocal lattice to be collected.

The Ewald sphere (of reflection) can be applied in electron, neutron, and X-ray diffraction. Also, when the Ewald sphere is applied to electron diffraction in TEM microscopy the thin sample results in elongated rods in reciprocal space [Ewald, 1969]. These reciprocal rods are the result of the higher energy of the incoming radiation in TEM microscopy resulting in a larger Ewald sphere of reflection.

Chapter 3

Synthesis of Alloy Nanoparticles

3.1 Motivation

Fabrication of bimetallic magnetic alloy nanoparticles with a uniform size and shape is essential in order to ensure that nanoparticles exhibit the desired properties for their applications. Changing the chemical and physical properties of FePt nanoparticles can dramatically alter their magnetic, optical, and electronic, behaviour for their desired applications. For example, small nanospheres and nanocubes are preferred for data storage [Soichiro Saita, 2005], core-shell nanoparticles are preferred for magnetic applications [Kalambur et al., 2005] (because their magnetic properties can be controlled by their size and shape of the shell) and octapods are preferred for catalytic applications [Wu et al., 2012]. Any slight change in the nanoparticle properties, such as size distribution can alter/hinder their applicability. For example, a uniform shape for biomedical applications is required to ensure there is very little drag for targetted drug delivery. Quantum dots—for biological tracers/light emitting diodes applications—are required to have a narrow size distribution in order to exhibit colour purity. Nanocubes—for data storage applications—are required to have a narrow size distribution in order to form 2D square lattice arrays for high magnetic manipulation.

Conventional laboratory synthesis methods are typically adopted in the fabrication of nanoparticles despite the requirement for technically challenging precise processes. This is because following a synthesis scheme enables control

over the resultant chemical and physical properties of nanoparticles, such as, the composition, size distribution and shape regularity. The first reported liquid phase chemical synthesis method in the fabrication of FePt nanoparticles with a tuneable shape and narrow size distribution was conducted by Sun et al (who remains a leading researcher in field of magnetic alloy nanoparticles [Sun et al., 2000]). Since the first reported synthesis, there has been many ever-expanding set of methodologies developed in the synthesis of alloy nanoparticles with a wide accessible size range of diameters between 1.5 - 22 nm and a wide variety of morphologies from nanospheres [Nandwana et al., 2007], nanocubes [Zhang et al., 2014], [Chen et al., 2006], nanorods [Chen et al., 2007], to: octapods [Wu et al., 2012], [Chou et al., 2009]. However, controlling the shapes and sizes can still be an intricate process due to the wide variety of synthesis parameters that can directly impact the resultant nanoparticle properties [Soichiro Saita, 2005]. The motivation within this chapter was to develop and adapt synthetic schemes to synthesise a range of FePt nanoparticles with controlled shape and size, which is of high importance in order to exploit them for their corresponding applications.

3.2 Introduction

Preliminary investigations were conducted to gain the required expertise to reproducibly fabricate the FePt nanoparticles with different chemical and physical properties. The optimised synthetic schemes are detailed within this thesis. Typically a thermal decomposition method was used in the fabrication of the FePt nanoparticles of the following different shapes and sizes including ultrafine FePt nanospheres of diameter 2$\pm$0.5 nm, FePt nanocubes of maximum width 8.41$\pm$0.56 nm, $FePt@Fe_3O_4$ core-shell nanoparticles of diameter 8.71$\pm$0.44 nm, and FePt octapods of diameter $ 17.0$\pm$2.01 nm. The uniform shape and narrow size distribution. The materials used and methodology of the airless Schlenk line apparatus are described in detail in Appendix 9.1. Furthermore, a specialised pyrolysis method was adopted for the fabrication of ultrafine FePt nanoparticles with isotopic substitutions (protonated and deuterated surfactants).

The nanoparticles fabricated within this chapter were characterised using electrons as analytical probes in Chapter 5 and the larger octapods were also analysed in CDI analysis investigation in Chapter 6. Furthermore, a specialised pyrol-

ysis method was adopted for the fabrication of ultrafine FePt nanoparticles with deuterated surfactants for neutron investigation into the surfactant layer in Chapter 7.

3.2.1 Liquid Phase Chemical Synthesis

Typically, liquid phase chemical synthesis methods involve a facile 'one pot' synthesis under an inert, moisture-free reflux environment (using a Schlenk line set-up which has a vacuum and nitrogen or argon flow system). The liquid phase methods for the synthesis of alloy nanoparticles are classified into two categories; sequential reduction methods and co-reduction. The sequential reduction method, usually termed as 'seeded-growth' involves the synthesis of a metal 'seed' first followed by the reduction of the corresponding metal on the surface to form the alloy [Duan and Wang, 2013]. The metal salts are typically dissolved in a high temperature solvent which allows for a fixed reaction reflux temperature (equal to the boiling point of the solvent) and can promote reduction or oxidation of the metal salts. Also, stabilising surfactants, oleic acid, OA and oleylamine, OLA, are typically used to stabilise the Fe and Pt ions in the reaction [Sebt et al., 2009] and to stabilise the final nanoparticle solution (colloidal FePt nanoparticles coated with a layer of both OA and OAm.)

The nature and the importance of the surfactant layer is discussed and investigated further in section 7. The co-reduction scheme is the most commonly followed scheme in the fabrication of fcc FePt nanoparticles of which there are three principal liquid phase co-reduction methods:

- **Thermal Decomposition:** involves the thermal decomposition of iron penta carbonyl, $Fe(CO)_5$, (injected into the reaction mixture) and the reduction of platinum(ii)acetylacetonate, $Pt(acac)_2$, to form FePt nanoparticles [Sun, 2006].
- **Polyol Reaction:** involves a simultaneous thermal decomposition of $Fe(CO)_5$ and the reduction of $Pt(acac)_2$ it is also proposed that the reaction is catalysed by the presence of a reducing agent such as, 1,2-hexadecanediol [Kalogirou et al., 2010].
- **Pyrolysis:** involves a thermal alleo-catalytic decomposition reaction of the

dual source precusors, iron(iii)ethoxide, $Fe(EtO)_3$, and $Pt(acac)_2$, where the initial decomposition of the Fe precursor acts as a catalyst for the decomposition of the Pt precursor [Soichiro Saita, 2005].

An adaptation of the thermal decomposition synthesis method was selected for the fabrication of FePt nanocubes, FePt octapods and $FePt@Fe_3O_4$ nanospheres. This method was selected due to the ease in creating reproducible nanoparticles of a narrow size distribution in comparison to other methods. For example, the reaction parameters in the thermal decomposition method can be more readily adapted to tune the shape of the nanoparticles in comparison to the other methods, which are mainly designed for synthesis of spherical nanoparticles. Also, as the Fe precursor is injected into the system, this avoids any oxygen exposure risks from adding reagents at high temperatures. Therefore, the addition of excess Fe precursor into the reaction after the FePt nanoparticle formation stage, allows for controlled Fe shell growth resulting in the formation of an Fe oxide shell on the nanoparticle surface (on exposure to the environment). The disadvantage of thermal decomposition method is that the composition distribution [Zhang et al., 2014] is broader than the other methods and the use of the Fe precursor, $Fe(CO)_5$, has inherent hazards as it is flammable at room temperature and is highly toxic resulting in environmental concerns with its use. However, the advantages associated with using this method out-weigh the disadvantages as the ease of shape control is the main requirement in the investigations. Additionally, a pyrolysis synthesis method was adopted for the fabrication of ultrafine FePt nanospheres.

3.2.2 Thermal Decomposition Formation Schemes

This method is termed as the hot-injection method which involves heating one precursor ($Pt(acac)_2$) to a temperature (at a high enough temperature to overcome the nucleation barrier when the Fe precursor is added). At this temperature when the cold $Fe(CO)_5$ precursor is rapidly injected into the solution a burst of nucleation will occur, and an instantaneous lowering of the temperature. This nucleation burst prevents multiple nucleation by providing a distinct energy barrier between the nucleation and crystal growth phases. The thermal decomposition reaction scheme is outlined in the schematic Fig.3.1 where the $Pt(acac)_2$ remains

in the solid phase until the temperature is greater than the thermal decomposition temperature (thermal decomposition temperature of ∼160-180°C.) The Pt^{2+}

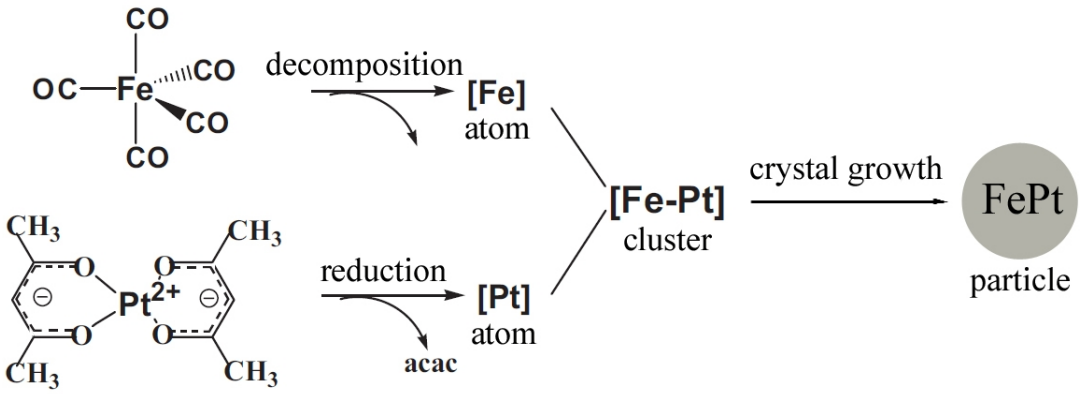

Figure 3.1: *Thermal decomposition of $Fe(CO)_5$ followed by the reduction of $Pt(acac)_2$ to form FePt alloy nanoparticles. Reprinted with permission from [Sun, 2006] Copyright (2006) Wiley.*

complex is then reduced to form Pt^0 seeds. The $Fe(CO)_5$ decomposes by thermal decomposition (decomposition temperature of 105°C) releasing $Fe^0 + 5CO$. Fe^0 is oxidised reacts with the Pt^0 seed forming an FePt nanoparticle.

3.2.3 Nucleation and Growth Theory

There are three different homogeneous nanoparticle formation mechanisms proposed for liquid phase chemical synthesis from analytes in solution. These formation mechanisms are illustrated in Fig.3.2 where nucleation —process by which nuclei (seeds) act as templates for crystal growth—occurs after reaching the minimum critical stage of super-saturation.

- **Formation Mechanism I:** illustrates the LaMer-Dinegar Model of single nucleation and uniform growth [LaMer and Dinegar, 1950].
- **Formation Mechanism II:** illustrates the nucleation and growth of clusters which aggregate to form the nanocrstal.
- **Formation Mechanism IV:** illustrates a diffusion-controlled Ostwald ripening growth due to multiple nucleation events forming pure or alloy metal

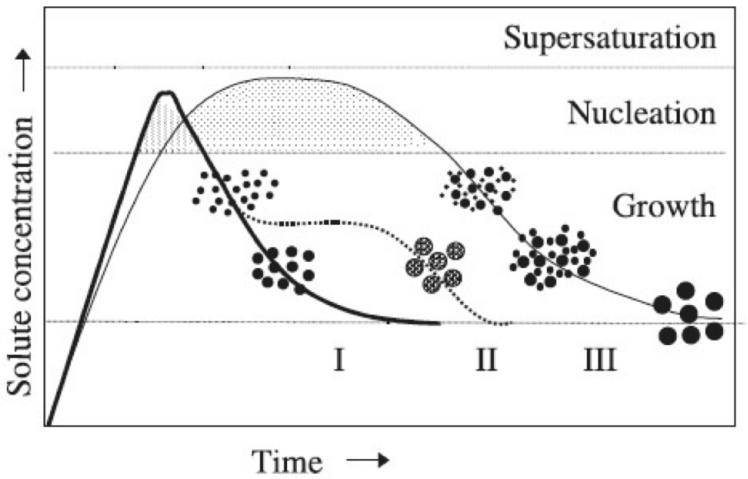

Figure 3.2: *Nanoparticle formation mechanisms of solute concentration with time: formation mechanism I LaMar-Dineger Modelz single nucleation and uniform growth, formation mechanism II nucleation followed by growth by aggregation to form larger nanoparticles, formation mechanism III Ostwald ripening due to multiple nucleation events. Image reprinted with permissions Puerto et al*

clusters of where atom exchange between clusters occurs. The smaller cluster has a lower average coordination of surface atoms in comparison to the larger cluster and resulting in their relative ease of removal being higher and so it 'gives' more atoms to the larger cluster. The larger cluster therefore gets bigger at the expense of the smaller clusters, which shrink and disappear [Bowker, 2002].

The formation mechanism of the FePt nanoparticles through the thermal decomposition can be ascribed to the formation mechanism II represents the LaMer-Dinegar Model where the nucleation rate can be controlled by the injection time of the $Fe(CO)_5$ liquid precursor.

3.2.4 Nucleation and Growth of Alloy Nanoparticles

The proposed nucleation and growth process for FePt nanoparticles is illustrated by the schematic in Fig.3.3. In the formation process it is proposed that the Pt-OAm complex nucleates to form a larger Pt 'seed'. The 'seed' then acts as the surface site for the Fe-OA complex to nucleate resulting in particle growth. The most energetically unstable Fe atoms on the surface will then diffuse into the Pt-rich

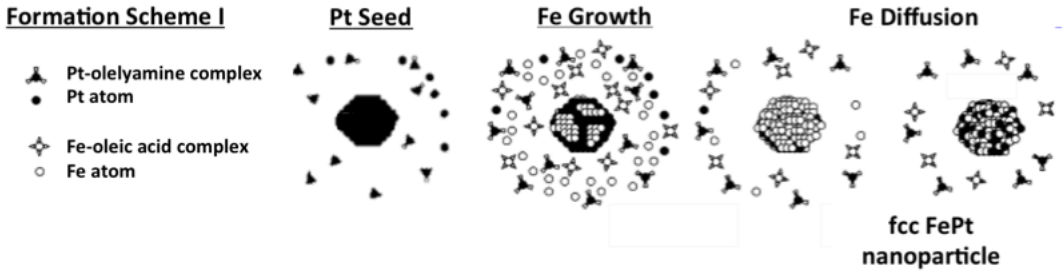

Figure 3.3: *Schematic of proposed nucleation-growth formation scheme in the synthesis of fcc FePt nanoparticles. Reprinted with permissions from [Soichiro Saita, 2005].*

core in order to minimise the high surface energy configuration. This describes the formation of fcc nanoparticles of homogenous distribution [Soichiro Saita, 2005] (The extent of the Fe and Pt distribution in the FePt nanoparticles is investigated further in Chapter 7). Additionally, when the Fe precursor is added in excess an Fe or Fe oxide shell will form on the surface of the FePt nanoparticle. The thickness of the shell corresponds with the volume of excess Fe precursor added. The shape of the nanoparticle is dependent upon the shape of the initial 'seed' and in this demonstration the final spherical nanoparticle formation is due to an isotropic seed growth as described below. However, when there is anisotropic seed growth the initial seed is of a cuboctohedron form and can lead to either the formation of a cube or an octapod 'seed' depending on the reaction pathway. The reaction temperatures plays a role in the nucleation and growth process of FePt nanoparticles during the synthesis process of FePt nanoparticles.

3.2.5 Shape Controlled Facet Growth

The resultant shape of the fcc FePt nanoparticles is expected be controlled by the most energetically favourable growth rate of the (111) and (100) facets of the 'seed' [Zhang et al., 2014] [Chou et al., 2009]. It is proposed that the surfactants play a role in restraining the growth of a facet through selective binding. For example, the OAm surfactant has a stronger facet binding affinity to the Pt(100) facets over the Pt(111) facets, and the OA surfactant has no preferential binding affinity [Chou et al., 2009]). As the OAm will selectively bind to (100) facets there will be more available sites on the (111) facets for the OA to bind therefore it can act to restrain the growth rate of the (111) facets [Zhou et al., 2013]. This binding

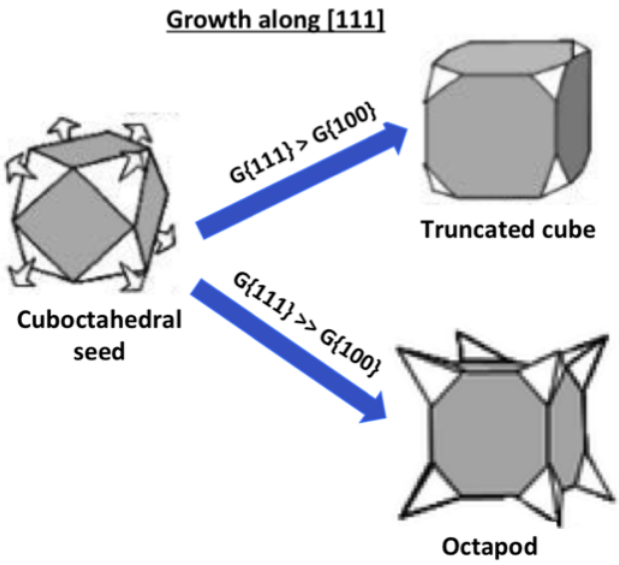

Figure 3.4: *Schematic of cube and octapod formation through energetically favourable [111] plane directions, where (111) facets and (100) facets are represented by the white and grey facets respectively. Reprinted with permission from [Chou et al., 2009] Copyright (2009) American Chemical Society.*

specificity of both OAm and OA can be utilised to control the growth of the (100) and (111) facets and is typically termed as 'surfactant-faceted' growth. When the growth rate of the (111) facet and the (100) facets is equal an isotropic growth will occur resulting in the formation of spherical nanoparticles (equal growth rate of both planes) [Zhang et al., 2014]. In the case of core-shell spherical nanoparticles, where there is an excess of Fe precursor in the system, the Fe growth will continue on the high energy (111) facets and then onto the (100) facets to form the resultant Fe oxide shell.

When the growth rate of the (111) facets is more energetically favourable than the growth rate of the (100) facets (where G(111)>G(100)) then an isotropic growth will occur. In this kinetic growth the (111) facets grow faster and effectively disappear leading to the growth of the (100) facet forming a nanocube, as illustrated in Fig.3.4. The nanocubes consist of (100) facets which are of a high surface energy which can result in the preferential growth of an Fe shell [Wu et al., 2012]. Additionally, when the growth rate of the (111) facets is much more energetically favourable than the growth rate of the (100) facets where G(111)>>G(100), then the growth of the (111) facet continues to form eight corner 'pods' resulting in the formation of an octapod [Chou et al., 2009] as illustrated in Fig.3.4.

3.2.6 Reaction Parameters

There are a range of factors in the synthesis reaction that can affect the resultant properties of the nanoparticles from type of solvent, metal precursor alloy, ratio of surfactant to metal precursor to the heating rate of the reaction. The resultant nanoparticle properties and the corresponding key reaction parameters which alter these properties considerably, are listed below:

- **Composition:** can be affected by the molar ratio of $Pt(acac)_2 : Fe(CO)_5$ e.g. a ratio of 1:1 should effectively give a composition of $Fe_{50}Pt_{50}$, although a slight excess of $Fe(CO)_5$ is usually used to counterbalance the loss of $Fe(CO)_5$ to the vapour phase [Chokprasombat, 2011].
- **Size:** can be affected by many factors for example the the concentration of OA and OAm surfactants, heating rate, injection temperature of the $Fe(CO)_5$ precursor. A high concentration of surfactants results in a slow rate of nucleation [Nandwana et al., 2007] resulting in a larger nanoparticle size (due to a high growth rate). A slow heating rate results in a fast rate of nucleation thus fabricates resulting in a smaller nanoparticle size [Bian et al., 2014]. It has also been observed that with increasing particle size there was a slight increase in Pt content. Additionally the injection temperature of the Fe precursor controls the size and monodispersity of the nanoparticles.
- **Shape:** can be affected by 'surfactant-facet binding' and reflux temperature. There have been many reports that suggest that 'surfactant-facet binding' can be controlled by altering the ratio of OA to OAm. It has been found that on increasing the ratio of OAm to $Pt(acac)_2$ precursor results in an increase in nanoparticle size [Luke Green et al., 2014],[Nandwana et al., 2007] (this applies until reaching a diameter of 10 nm) beyond which bipolar nanoparticles form [Ung et al., 2009]. The reflux temperature also impacts the shape where; nanorods formed at a reflux temperature of 220°C, nanocubes formed at a reflux temperature of 250°C, and nanospheres formed at a reflux temperature of at 298°C [Bian et al., 2014]

The reaction parameters described that impact the resultant properties of nanoparticles are influencing factors but there is a degree of inter-dependency between these parameters which have been extensively reviewed [Ung et al., 2009].

3.3 Experimental Synthesis

All synthesis procedures were conducted and optimised at the UCL Health Biomagnetics and Nanomaterials Laboratory at the Royal Institution throughout the course of my EngD. Many experiments were conducted initially in order to gain the required expertise and synthetic scheme to successfully optimise the synthesis schemes (detalied within the following section). The standard synthesis methods was designed within (based on adaptations of previous synthesis methods [Wu et al., 2012] and [Chou et al., 2009]) and implemented using a standard airless technique in a constant nitrogen atmosphere. The size and shape of the nanoparticles were controlled by varying the synthetic parameters.

The materials and methodology required for the use of the airless Schlenk line apparatus is also described in detail in Appendix 9.1 for the fabrication of FePt nanoparticles. The reaction parameters are outlined in Table 3.5, for the synthesis of the octapods, nanocubes, and core-shell $FePt@Fe_3O_4$ nanoparticles.

Shape	$Fe(CO)_5$	$Pt(acac)_2$	OA	OAm	OA:OAam molar ratio	Pt:Fe molar ratio	Heating Rate 2
Octapod	30 uL (2.24E-4 mmol)	0.088 g (2.24E-4 mmol)	2.6 mL (8.41E-3 mmol)	3.8 mL (1.65E-2 mmol)	0.5:1	1:1	5°C/min
Nanocube	61 uL (4.48E-4 mmol)	0.088 g (2.24E-4 mmol)	0.65 mL (2E-3 mmol)	0.94 mL (2E-3 mmol)	1:1	1:2	12°C/min
Core-Shell	200 uL (4.00E-3 mmoll)	0.1965 g (5.00E-4 mmol)	1.29 mL (4E-3 mmol)	1.88 mL (4E-3 mmol)	1:1	1:2	8 °C/min

Figure 3.5: *Reaction parameters for synthesis of octapods, nanocubes, and core-shell $FePt@Fe_3O_4$ nanoparticle following synthesis method 1.*

3.3.1 Synthesis of Nanocubes and Octapods

In a typical procedure $Pt(acac)_2$, was loaded into the reaction flask containing 10 mL of degassed solvent octa-1-decene (ODE) and the $Pt(acac)_2$ was dissolved in the solvent at room temperature by switching on the magnetic stirrer, at 500 rpm, under a blanket of N_2 for 30 minutes. Then the designated volume of OAm, and OA (if required) were injected into the sealed reaction flask. The mixture of solvent, Pt precursor, and surfactants was then heated to 60°C and degassed under vacuum for 30 min to remove any oxygen and dissolve the Pt precursor to give a uniform solution. The degassing caused the sample mixture to bubble

indicating that oxygen was being ejected from the system and after 30 minutes the bubbling had gone and outgassing was complete.

Subsequently, the reaction vessel was heated at a rate of 4°C per minute up to 120°C under a constant flow of N_2, and left for 2 minutes before injecting in the designated volume of pure $Fe(CO)_5$. After the addition of $Fe(CO)_5$, the colour transitioned from deep yellow to brown to black indicating the formation of nanoparticles in the solution. The temperature was then raised to 250°C at the specified heating rate and maintained at this temperature to reflux for 1 hour. The heat source was then removed and the reaction mixture allowed to cool to room temperature. The FePt pure product was then collected by rinsing the flask with hexane and ethanol and cleaned following the method outlined for large nanoparticles as in Section 3.3.6.

3.3.2 Synthesis of Core-Shell Nanoparticles

The $FePt@Fe_3O_4$ nanoparticles were fabricated via a facile one pot reaction by the chemical reduction of $Pt(acac)_2$ ($5x10^{-4}$ mmol) and thermal decomposition of $Fe(CO)_5$ ($4x10^{-3}$ mmol) in the presence of stabilising surfactants OAm ($4x10^{-3}$ mmol) and OA ($4x10^{-3}$ mmol).

In a typical synthesis procedure 0.1965 g of $Pt(acac)_2$ was added to a 125 mL reaction flask containing a magnetic stirrer bar and 20 mL of degassed octa-1-decene. After purging with nitrogen for 30 minutes, the reaction flask was heated up to 107 °C at a rate of 4°C per minute. Subsequently, the 1.28 mL of OAm and 1.88 mL of OA were injected into the reaction mixture followed by the injection of 100 μL of $Fe(CO)_5$. After the addition of $Fe(CO)_5$, the color transition from yellow to black which suggested formation of nanoparticles in the solution. Then the reaction flask was heated up to 120°C and an additional 100 μL of $Fe(CO)_5$ was added whilst briefly exposing the vessel to atmosphere (by injection of 1 mL of atmosphere). During the controlled exposure to the atmosphere, it is expected that the reduced Fe reacted with the oxygen in the air, resulting in the formation of an Fe oxide shell on the nanoparticle surface. Subsequently the reaction vessel was heated up at a rate of 8°C per minute to 250°C and maintained at this temperature to reflux for 30 minutes. The heat source was then removed and the reaction mixture allowed to cool to room temperature. The $FePt@Fe_3O_4$

nanoparticles product was then cleaned by centrifugation in hexane and ethanol.

3.3.3 Synthesis of Ultrafine FePt Nanoparticles

In order to selectively probe the surfactant layer the nanoparticles were synthesised with isotopic substitutions of OA and hexadecylamine $C_{16}H_{33}NH_2$ (HDA). A high particle loading was required for the neutron investigations in order to account for its inherent low flux. Therefore the standard synthesis method was up-scaled to increase the standard yield from $\sim$0.5 g to $\sim$1.5 g. In order economically fabriacte a large batch of nanoparticles (considering the high cost of deuterated surfactants) the molarity of the acid and amine surfactant used in a standard reaction was kept the same whilst the molarity of the Fe and Pt precursors and solvent was increased. The different isotopic substitutions of OA and

Batch No.	Sample No.	Amine	Acid	Solvent
MM57	1	HDA-H	OA-H	H, D
MM58	2	HDA-H	OA-D	H, D
MM59	3	HDA-D	OA-H	H, D
MM60	4	HDA-D	OA-D	H, D

Table 3.1: *FePt nanoparticles with isotopic substitutions of OA and HDA surfactants dispersed in hexane/eicosane/toluene solvent.*

HDA surfactants and hexane or toluene solvent in which the FePt nanoparticle samples were suspended are outlined in Table 3.1. Notably, the standard surfactant OAm—typically used in partnership with OA—was substituted with hexadecylamine (HDA) as HDA is more readily available in deuterated form. This is likely because direct deuteration of OA, leads to hydrogenation of the C=C bond (forming stearic acid), or isomerisation leading to formation of the trans isomer of OA (elaidic acid). The HDA, $C_{16}H_{35}N$, only varies from OLA, $C_{18}H_{37}N$,by two carbon chain lengths resulting in the decomposition temperature of HDA, b.p = 330°C, being slightly lower than that of OLA, b.p = 348°C. The chemical properties of the two amines are similar, and therefore it was expected that the change of surfactant would not affect the resultant nanoparticles. This theory was shown in prelimiary studies to not affect the synthesis process in Chapter 7.

The 2 nm FePt nanoparticles were synthesised following a specialised up-scaled synthesis was adapted [Nandwana et al., 2005] method with different isotopic substitutions. In a typical synthesis scheme, degassed dioctyl ether (20 mL) was injected into the flask. The system was flushed with N_2 three times and the reaction flask was purged with N_2 for 30 min at room temperature, and the magnetic stirrer was turned on at the rate of 500 rpm. The reaction was heated up to 200°C then left to reflux under a flow of N_2 for 30 minutes. The temperature was kept at a constant 200°C (5°C above the b.p of OA) whilst adding in the powdered amine (0.5 mmol) into the reaction flask arm (which was quickly re-sealed after addition) and the acid surfactant (0.5 mmol) was then injected into the reaction flask. The temperature was then raised to 295°C at a rate of 8°C per minute. The reaction mixture was then refluxed at this constant temperature, under a flow of N_2 for 4 hours. The heat source was then removed and the reaction mixture allowed to cool to room temperature. The FePt pure product was then collected by rinsing the flask with hexane and ethanol and cleaned following the method outlined for small nanoparticles as in Section 3.3.6.

3.3.4 Synthesis of AuPd Nanoparticles

The AuPd nanoparticles were synthesised by Michael Huang et al at the National Tsing Hua University and reprinted as follows: The nanoparticle morphology was finely tuned, by adjusting the amounts of H_2PdCl_4, ascorbic acid. In addition surfactants and gold cores added to grow Pd shells with ultrathin thicknesses. To grow 47, 53 and 77 nm AuPd core@shell nanocubes, 8.81, 8.91 and 8.16 mL of deionized water and 0.048 g of cetyltrimethylammonium bromide (CTAB) were added to glass vials, respectively, followed by the respective introduction of 500, 500 and 600 ÎijL of gold octahedra. Then, 1.1, 0.5 and 0.5 mL of 10 mM H2PdCl4 solution were respectively added to the vials. Then 240 ÎijL of 0.1 M ascorbic acid was added and the solutions were kept in a water bath set at 50 ÂřC for the growth of Pd shells for 1 h. The reactions were stopped by centrifugation at 4500 rpm for 10 min. The synthetic procedures for synthesizing AuâĂŞPd coreâĂŞshell nanocrystals of other shapes and with the use of gold cores of other sizes are similar, and the exact synthetic conditions are provided in Tables S1, S3, and S4, ESI. A reaction time of 1âĂŞ2 h has been used to make other coreâĂŞshell nanocrystals of various shapes. Tuning of H_2PdCl_4 and ascorbic acid amounts,

as well as adjustment of the amounts of CTAB and Au cores used in some cases, is necessary to achieve precise control of the final particle size [Chiu et al., 2014].

3.3.5 Handling of Deuterated Chemicals

Some of the synthesis procedures involved the use of deuterated chemicals and thuse required specialist techniques to ensure the synthesis was conducted in an inert environment. The deuterated chemicals were opened under a flow of inert gas (N_2 and tightly sealed after by purging with N_2 to ensure there was minimal exposure to the environment. It is important when handling any deuterated chemicals to open them under the fume hood and to wear double layer protective gloves.

3.3.6 Retrieval of FePt Nanoparticles

The nanoparticles were retrieved by the following centrifugation and re-dispersion method where two different methods for cleaning and re-dispersion, were carried out depending on the size:

- **Large Nanoparticles:** 10 mL of the pure product was dispensed into a centrifuge tube and centrifuged (at a standard step rate of 9 and T = $20°C$) at 3500 rpm for 10 minutes. The supernatant was discarded and 10 mL of the flocculent, ethanol, was added. The sample in the centrifuge tube was then placed on a vortex (which when pressure is applied sends mechanical vibrations through the sample) and then vortexed for 1 minute in the in and the centrifugation and re-dispersion process was repeated twice.
- **Small Nanoparticles:** 8 mL of ethanol, was added to 2 mL of pure product in a centrifuge tube and centrifuged at 8500 rpm (higher rpm to separate small nanoparticles) for 15 minutes. The supernatant was discarded; and 5 mL of hexane was added; and the sample was then vortexed for 1 minute to re-disperse the nanoparticles in solution. 5 mL of ethanol was then added. The centrifugation and re-dispersion of nanoparticles was repeated twice at the reduced rate of 3500 rpm for 30 minutes each time. The final clean

nanoparticle products were redisposed in 10 mL of a nonpolar organic solvent, hexane/toluene.

3.4 Conclusion

The three main liquid phase chemical synthesis reactions are outlined in this Chapter; thermal decomposition, polyol synthesis and pyrolysis. The thermal decomposition reaction procedure was implemented for the fabrication of FePt nanocubes, $FePt@Fe_3O_4$ core-shell nanospheres, and FePt octapods. Also, the pyrolysis reaction procedure was implemented for the fabrication of ultrafine FePt nanospheres with isotopic substitutions of OA and HDA involved a specialised synthesis in the use of deuterated surfactants (as required for neutron diffraction analysis in Chapter 7).

The nanoparticle formation mechanism for the nanoparticles of different shapes is also proposed where; the resultant shape of the fcc FePt nanoparticles is expected to correspond with the most energetically favoured growth rate of the (111) and (100) facets [Zhang et al., 2014] [Chou et al., 2009]. Additionally, the main reaction parameters, which control the resultant composition, size and shape of the nanoparticles are discussed (applicable to thermal decomposition reactions only).

Chapter 4

Sample Quantification Methods

4.1 Motivation

The motivation behind this Chapter is to provide a knowledge platform of the fundamental concepts behind the comprehensive characterisation of the FePt nanoparticles of different shapes and sizes synthesised in Chapter 3.

4.2 Introduction

Both conventional and advanced analytical techniques were implemented in the comprehensive study of the chemical and physical properties of the FePt nanoparticles. The conventional techniques were implemented at the Health Biomagnetics and Nanomaterials Laboratory (Royal Institution) and included powder X-ray diffraction and TEM analysis. The advanced nano-characterisation was implemented using the state-of-the-art TEM nano-characterisation instrumentation at the Centre for Materials Science, Japan Advanced Institute for Science and Technology (JAIST) in Asahati, Japan. The Centre for Materials Science contains a broad range of nano-characterisation instrumentation all situated under one facility (which is typically very rare) and included; high resolution TEM (HRTEM), scanning TEM-HAADF, aberration corrected scanning TEM-energy dispersive spectroscopy, and TEM tomography.

4.3 Fourier Transfrom Infra Red Spectroscopy

Fourier Transform infra red (FTIR) spectroscopy is an optical laboratory based analytical technique that can probe the speciation of organic molecules by creating a 'molecular fingerprint'. In this investigation FTIR was used to confirm the bonding of the OA and HDA surfactants on the FePt nanoparticle surface and to understand the adsorption mechanism. A typical FTIR experiment requires placing a small mass of dry nanoparticle on a diamond head and IR light is directed through the sample. The IR light interacts with the organic sample and emits

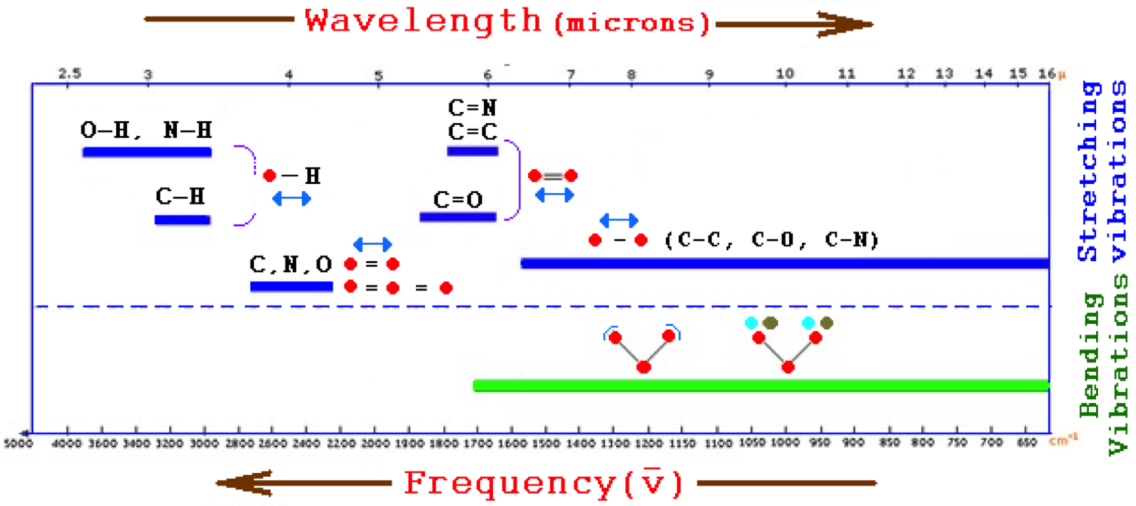

Figure 4.1: *FTIR spectrum with the regions of the various vibrational bands from different bonds indicated.*

a resultant absorbance or transmittance spectrum (user-defined), subsequently an in-system FT is applied by the internal software to give the FTIR absorbance or transmittance spectrum which represents the molecular transmittance of the sample. The vibrational peaks correspond to the specific vibrational modes of the bonds of the molecules present on the sample, an example of this is depicted in Fig.4.1 with the different frequencies indicated.

4.4 Powder X-ray Diffraction

Quantification of the nanoparticles in real space to confirm the phase was implemented using conventional X-ray powder diffraction, on a Panalytical X'Pert XRD diffractometer operating at 40 kV and 40 mA with a Co-K_α radiation source of characteristic λ, 1.791 Å. The sample was prepared by slowly drop-casting the nanoparticle solution onto a silicon wafer with a Kapton film protective coating. Effort was made to ensure the layer of sample dried onto the protective coating with an equal thickness. The prepared sample was dried under ambient conditions in a Petri dish to protected the sample from any contamination for example, from any air-borne particles. The software program, X'pert high score data viewer was used to collect the XRD data and X'Pert high score plus, was used for the data interpretation. The diffraction pattern data was treated to remove the background the diffraction peaks were profile fitted as detailed in Appendix 9.2.1.

4.4.1 X-Ray Generation

The X-rays are generated by bombarding high-energy electrons at a metal anode target ejecting an electron from the inner shells of the atoms creating an electron shell vacancies. The vacancy is quickly filled by orbital decay of outer-shell electrons emitting energy in the form of characteristic X-rays with sharply defined frequencies. The orbital decay being a transition from the n = 2 to n = 1 levels resulting in K_α X-rays, or a transition from the n = 3 to n = 1 levels resulting in K_β X-rays and so forth. Additionally, a continuous X-ray distribution is emitted in the form of "Bremsstrahlung" radiation, the intensity of which increases with the operating voltage. However, only the K_α radiation is considered when considering a metal anode target as it releases the highest frequency X-rays. The λ of the characteristic X-rays are a function of the atomic number of the target element (in accordance with Moseley's $1/\lambda$ = c(Z-σ). Cobalt, Co-K_α = 1.78901 Å) and copper, Cu-K_α = 1.5406 Å) are commonly used as X-ray sources. Cobalt is selected specifically when analysing systems with Fe in order to avoid the effect of Fe fluorescence (due to the X-rays from a Cu source fall within the absorption band of Fe).

4.4.2 X-Ray Diffractometer

The X-rays are then filtered (using a monochromater) and collimated, the monochromatic beam is directed onto the crystalline material. The incident radiation is scattered at different scattering angles (in accordance with Braggs law), depending on the lattice spacing, d, in the material as depicted in the example in Fig.4.2. A spanning diffractometer collects the scattering from the sample over a range of 2θ angles. The sample stage is also rotated in order to collect diffraction data from all crystallographic orientations. The X-ray diffraction (XRD) data is collected by a

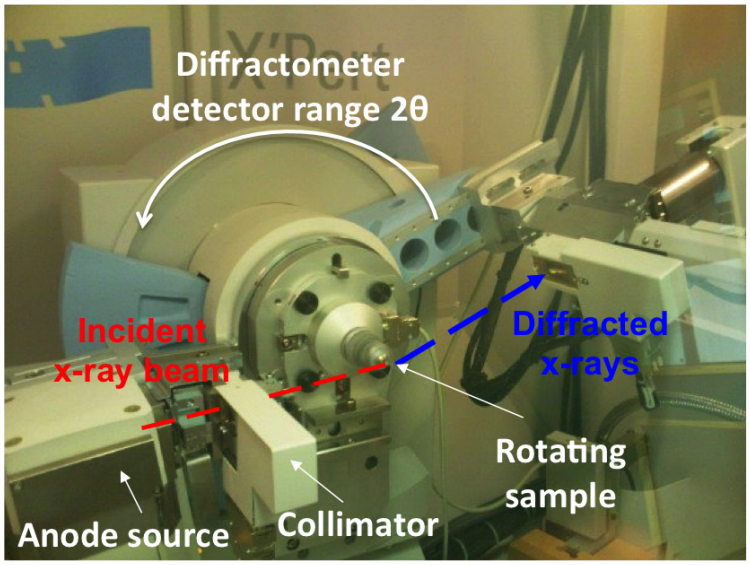

Figure 4.2: *XRD image of the X'Pert diffractometer set up for Ag-K_α source diffraction θ_i-$2\theta_i$, where diffractometer detector range is indicated and is twice as fast ($2\theta_i$) as the incident beam for angle of incidence = angle of reflection.*

detector and plotted in a two-dimensional pattern of intensity vs. angular position. The diffraction pattern acts as a unique 'finger-print' enabling sample identification by comparison of the planes to a known powder diffraction database most commonly used is the Joint Committee on Powder Diffraction Standards (JPCDS) from the International Crystal Structure Database.

Powder XRD is commonly used to characterise the nanoparticles from the diffraction intensities (Bragg peaks) which correspond to specific planes in the crystal unique to each phase. The intensities of the peaks correspond to the quantitative plane fractions, enabling phase information to be derived. Also, because an angu-

lar relationship exists with the sample composition the peak positions of an FePt sample with a high Pt content will be at a slightly lower angle in comparison to a sample with a low Pt content owing to the different lattice parameters of the pure materials (Pt a_{Pt} = 3.939 Å, and Fe, a_{Fe} = 2.912 Å). Thus the peak positions can provide an indication of the ratio of Fe to Pt present in the sample [Green, 2014]. Additionally, broadening of the Bragg peak corresponds to the effect of strain.

A similar concept to powder XRD data acquisition is applied at the I-15 beamline, but the sample is typically loaded into a capillary which is rotated to maximise data collection from all crystallographic orientations. The wide-angle position sensitive detectors at the I-15 beamline allow the rapid collection of powder patterns. Synchrotron based powder diffraction analysis utilises X-rays of a much higher intensity than those used in laboratory based techniques thus can probe more deeply into the sample. In general, diffraction data acquired from synchrotron sources results in XRD patterns of higher resolution than data from laboratory based sources. Thus, broadening the possibility of advanced data interpretation such as pair distribution function analysis (PDF) which is conducted in Chapter 7.

4.4.2.1 Crystallite Size Calculation

The mean crystallite size, τ of a crystallite—such as, a dried nanoparticle powder—can be determined through application of the Scherrer equation in Eq. 4.1 from analysis of the powder diffraction data.

$$\tau = \frac{K\lambda}{\beta cos\theta} \tag{4.1}$$

where θ is the Bragg angle attained from the peak position on the XRD pattern; β = B_{obs}-$B_{standard}$, B_{obs} is the full width at half maximum of the peak otherwise known as the integral breadth of a reflection (in radians 2θ), $B_{standard}$ is the instrumental broadening term due to the diffractometer (typically ranging from $\sim$ 0.04-0.08), K is the correction shape factor or 'Scherrer constant' defined by the shape of the nanoparticles for example, K = 0.89 for spherical nanoparticles and K = 0.94 for cubic nanoparticles, λ = characteristic K_α wavelength of the radiation. According to the Scherrer Eq the size of the peak width varies inversely with crystallite size and the average crystallite size decreases in accuracy with decreasing particle

size. Therefore, alongside Scherrer analysis conventional TEM size distribution analysis is most commonly used, to provide a complementary quantitative determination of the average size of individual nanoparticles and the size distribution of hundreds of nanoparticles.

4.5 Transmission Electron Microscopy Background

The concept of an electron microscope was developed due to the limitations in the resolution of light microscopy imposed by the wavelength of light. TEMs are capable of probing samples with a much greater resolution owing to the small de Broglie wavelength of high energy electrons. Since the first commercial TEMs—produced in the 1930s, by Max Knoll and Ernst Ruska—the electron microscope has seen continued improvement, with HRTEM and scanning transmission TEM imaging being realised in the mid-1970s. TEM is a very powerful analytical technique which allows the sample to be imaged directly to effectively 'see' the sample on the nanoscale. The electrons act as a high resolution analytical probe capable of investigating materials on the nanoscale. In a typical TEM observation a uniform electron beam is focussed on the sample (in vacuum) using a set of illuminating condenser lenses and apertures the emerging scattered electrons are detected on a phosphorescent screen or a charge coupled device (CCD) camera. Compositional information is also attainable using TEM instruments coupled with secondary detection techniques such as energy dispersive X-ray spectroscopy (EDX).

4.6 Interaction of Electrons with Matter

When high energy electrons are bombarded at a nanomaterial a range of electron interactions can occur resulting either elastic or inelastic scattering of the electrons. These interaction are detailed in the schematic in Fig.4.3 with the corresponding TEM techniques detailed in brackets:

- **Elastic Interactions:** arise when there is no energy transfer from the incoming electron beam to the sample. These interactions result in the elec-

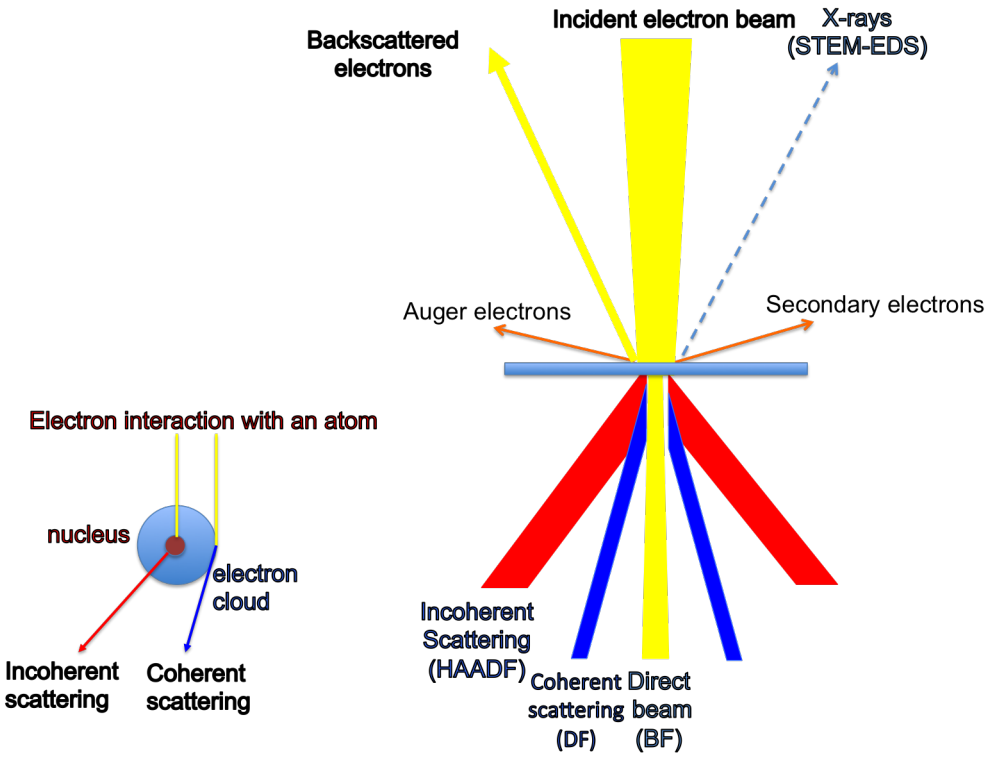

Figure 4.3: *Interaction principle of electrons with matter with simplified scattering interaction of electrons with an atom.[REF]*

trons either passing straight through the sample—as a direct beam—or being scattered by the sample—as coherent or incoherent scattering. The coherent and incoherent interaction of high energy electrons with an atom is illustrated in the simplified schematic of an atom in Fig.4.3. Coherent scattering—typically scatters at angle within the range of $<$10 mrad—is the result of the localised interaction of the electrons with the positive potential of an atoms electron cloud. Bright field (BF) TEM imaging collects this coherent scattering in phase contrast images which reflect the atomic structure. Incoherent scattering—scatters at angle within the range of $\sim$50-70 mrad—is the result of the interaction of the incoming electrons with the nucleus of the atom, or the tightly bound s states. Incoherent scattering is detected by dark field (DF) STEM imaging and reflects the chemical information.

- **Inelastic Interactions:** arise when there is an energy transfer from the incoming electron beam to the sample, resulting in backscattered electrons or secondary or Auger electrons. The backscattered (secondary) electrons

are the primary imaging electrons for scanning electron microscopy, whilst TEM relies on forward scattering electrons. Emission of characteristic X-rays can also occur reflecting the elemental information of the atom ionised and detected using STEM-EDS imaging

4.7 TEM Instrumentation

The following TEM instrumentation was utilised for the FePt nanoparticle characterisation:

- **Bright field (BF) imaging:** was performed to collect 2D electron micrographs either for imaging or for TEM tomography was performed on a conventional JEOL JEM-1200 EX electron microscope, with an operating voltage of 120 kV, to confirm the size and distribution of nanoparticles.
- **High resolution BF imaging:** was performed on an advanced Hitachi H-7650 TEM, with an operating voltage of 200 kV, equipped with a eccentric single axis tilt goniometer, with a $\pm 60^{\circ}$range and 0.5° increment limit, to collect images for TEM tomography. TEM tomography reconstructions were performed using Hitachi Reconstruction software.
- **High contrast HRTEM imaging:** was performed on a H-9000NAR HRTEM, with an operating voltage of 300 kV, providing crystallographic information of the nanoparticles.
- **Scanning transmission electron imaging and compositional mapping** were performed using an aberration corrected JEOL JEM-ARM200F STEM, with an operating voltage of 200 kV, equipped with an HAADF detector and energy dispersive X-ray (EDS) spectrometer, providing both crystallographic and elemental information of the nanoparticles.

4.8 Transmission Electron Microscopy

4.8.1 TEM Imaging Modes

There are two main modes in TEM; reciprocal space (selected area diffraction mode) and real space (bright or dark field imaging modes) and these can be set up according to the insertion position of an aperture in the optics system of the TEM as depicted in the schematic in Fig.4.4. Although the real space imaging mode was only used within this thesis. Nevertheless, the experimental concept of reciprocal space imaging in TEM, displays similarities with the calculated concept of reciprocal space imaging conducted by image processing, where a Fourier Transform is applied to the real space (as detailed in the Gradient Phase Approximation strain analysis section). In reciprocal space imaging, a diffraction pattern

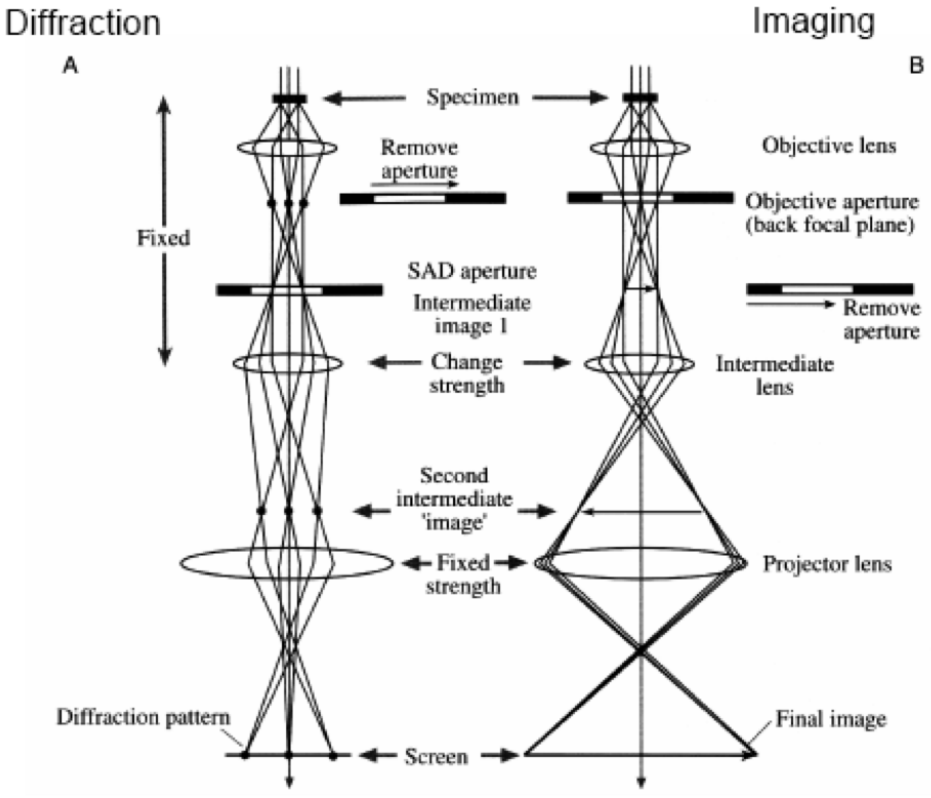

Figure 4.4: *Imaging principle of TEM optics (a) reciprocal space - diffraction mode (b) real-space imaging mode. [REF]*

is created by inserting a selected area diffraction aperture below the objective

lens in the image plane as illustrated in Fig.4.4a. The emerging electrons represent the angular distribution in the form of electron diffraction patterns. The aperture enables individual diffraction spots to be isolated.

In real space imaging—which is the most commonly used technique by TEM microscopists—an image is created by inserting an objective aperture into the back focal plane of the objective lens as illustrated in Fig.4.4b, allowing the direct beam through and excluding emerging electrons from the scattered beam. The resultant spatial distribution of the emerging electrons is represented in the form of intensity and can be distinguished by phase contrast images. In TEM imaging mode, phase contrast can be produced by positioning an objective aperture to either exclude emerging electrons from the coherently scattered diffracted beam (BF imaging) or from the direct beam on axis (high resolution dark field imaging). The BF imaging mode was used in the TEM imaging and TEM tomography studies of the nanoparticles to acquire 2D phase contrast images (typically termed as electron micrographs). In the HRTEM and STEM-HAADF investigations of the nanoparticles high resolution dark field imaging mode was used.

4.8.2 TEM Radiation damage

In all electron microscopy methods the possibility of radiation damage due to the highly energetic electron beam focussing on the sample has to be considered. The high energy of the beam can be transferred to the sample resulting in inelastic scattering. For example, for a metal sample the possible effect of the high energy beam could result in energy transfer from the electron to the sample potentially causing; phonon generation in the sample (where the atoms in the lattice absorb energy resulting in collective oscillations of the crystal lattice vibrations); or knock on damage (where an atom can absorb the energy and move) resulting in point defects e.g. Frenkel defects. The possibility of radiation damage can be controlled/lowered by reducing the exposure time and by focussing on a nearby artefact when taking repeated images of the same sample, e.g. in TEM tomography.

4.9 Electron Tomography

Electron tomography is an extension of the conventional TEM method and is used to reconstruct a 3D image of an object (sample) by collating TEM images acquired at different tilt series. The TEM tomography technique has been well developed and can offer an insight into the 3D morphology of macro systems [Günter Möbus, 2007], such as biological specimens [Sousa et al., 2011], but it is still a considerably new technique in the application to nanomaterial's in particular nanoparticles. Electron tomography involves the collation of 2D electron micrographs over an incremented tilt range with a fixed axis of rotation. The images are then aligned and can be electronically reconstructed using a reconstruction algorithm [Paul Midgley, 2009]. Tomography can be utilised in the majority of TEM imaging modes e.g. BF and DF, HAADF-STEM, and energy filtered, the benefits and drawbacks of which are discussed in Midgley's report on the 'Fundamentals of Electron Tomography'[Paul Midgley, 2008], where recent developments in electron tomography are also discussed in detail [Ersen et al., 2015].

The TEM tomography technique has been well developed and can offer an insight into the 3D morphology of macro systems [Günter Möbus, 2007], such as biological specimens [Sousa et al., 2011]. However, it is still a considerably new technique in the application to nanomaterials', and in particular nanoparticles. The extent of the data attainable using 3D electron tomography to analyse nanoparticles has been demonstrated for example, a individual dislocations at a resolution of 0.24 nm were identified in a 10 nm Au [Scott et al., 2012]. Also, Florea et al (2012) made a complete structural analysis of 5 nm diameter Pt nanoparticles, confirming the usefulness of the tomography approach [Florea et al., 2012]. The TEM tomography technique was applied to analyse FePt nanoparticles to gain a reliable visualisation of the 3D morphology and segmentation of the nanoparticles that could not be obtained from the 2D TEM images alone. The results of which are presented in Chapter 5.

4.9.1 Fourier Projection Theorem

The Fourier projection theorem (FPT) states that this Fourier Transform (FT) of the 2D parallel projection of an object, $\mu(u,v)$, taken at an angle ϕ, gives a slice

that is equivalent to a 2D slice through 3D Fourier space of the object subtending an angle ϕ with the u-axis. In the FPT a collection a 2D electron micrograph of the object, creating a 2D projection of the object, as illustrated in the top and bottom left side of Fig.4.5. A 2D Fourier Transform is then applied to the 2D projections of the object to give a 2D Fourier Slice of the object (as illustrated in the right hand side in Fig. 4.5). A 3D inverse Fourier transform then creates the slice of the final

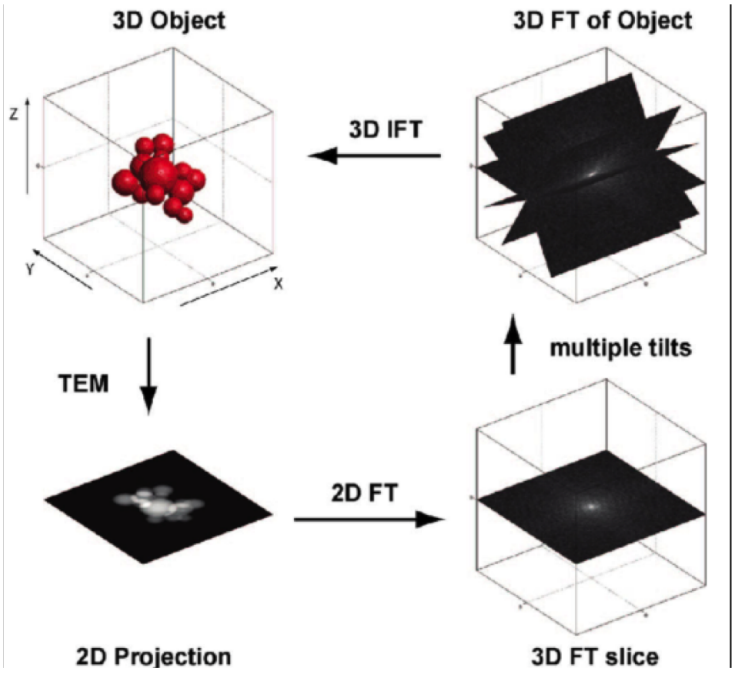

Figure 4.5: *Schematic representation of a tomographic reconstruction in reciprocal space: Starting from bottom left anti-clockwise: acquisition of 2D projection of the object, FT, combination of FT at different tilt-angles, and an inverse FT to reconstruct original shape. Image reproduced from [Friedrich et al., 2009]*

reconstruction. This process is repeated by collecting 2D projections at different tilt angles so that these 3D Fourier slices represent the object in 3D Fourier space which can be transformed by Inverse FT into a real space representation of the object.

4.9.2 Reconstruction Resolution in Fourier Space

The acheivable resolution of the 3D reconstruction of an object is sometimes estimate by the Crowther resolution. In an ideal situation the 3D resolution of a

reconstruction, of a spherical object can be estimated to be in accordance with he Crowther resolution criterian defined as:

$$d = \frac{\pi.D}{N} \tag{4.2}$$

where N is the number of projections, and D is the object size [Crowther et al., 1970]. However, the Crowther resolution assumes a tilt series collected over a whole $\pm 90^{\circ}$ tilt. The Crowther resolution is useful for identifying a tradeoff between the object size and resolution for achievable 3D reconstructions. However, this tilt

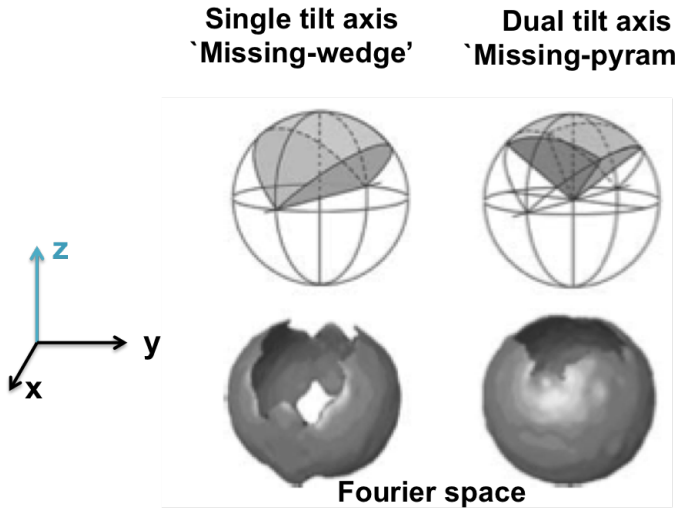

Tilt Range	Single	Dual
±70°	78%	93%
±60°	67%	84%
±45°	50%	67%

Figure 4.6: *Correlation of missing wedge of information for both single and double tilt stages with corresponding Fourier Space sampled. Image reprinted with permissions from [Nudelman et al., 2011][REF].*

range is not accessible using the TEM due to the limited physical tilt range of the goniometer and the degree of eccentric tilt axis rotation of the goniometer.

The tilt range in a TEM goniometer usually varies from $\pm 45^{\circ}$ to a tilt range of $\pm 70^{\circ}$ and the tilt axis can be either a single tilt axis of rotation or dual tilt axis of rotation. The tilt series can therefore only be acquired over a limited tilt-range and axis resulting in a 'missing-wedge' or 'missing-pyramid' of information as depending on the tilt range and axis and illustrated in Fig.4.6 which correlates with the percentage of Fourier space sampled as detailed in the Table in Fig. 4.6.

In the TEM tomography investigations in Chapter 5, a single tilt goniometer with a tilt range of $\pm 60^{\circ}$ is used, this results in a 'missing wedge' of information corresponding to 33% of Fourier space being left un-sampled. This loss of information

can be partially recovered through the application of a reconstruction algorithm to the tomographic data. Improvements to the resolution could also be carried out by altering the degree and consistency of the increment step through the use of equal sloped tomography or by using different reconstruction algorithms.

4.10 High Resolution TEM

The HRTEM operates at a much greater operating voltage (120-300 kV) in comparison to conventional TEM (100-120 kV) and is used for high magnification studies for high contrast imaging. The set up is similar to conventional TEM but the direct beam is collected as well as the diffracted beam. The interference of these beams at the back focal plane results in atomic lattice images as illustrated by a single diffracted wave in the schematic of the optical set up in Fig.4.7. The

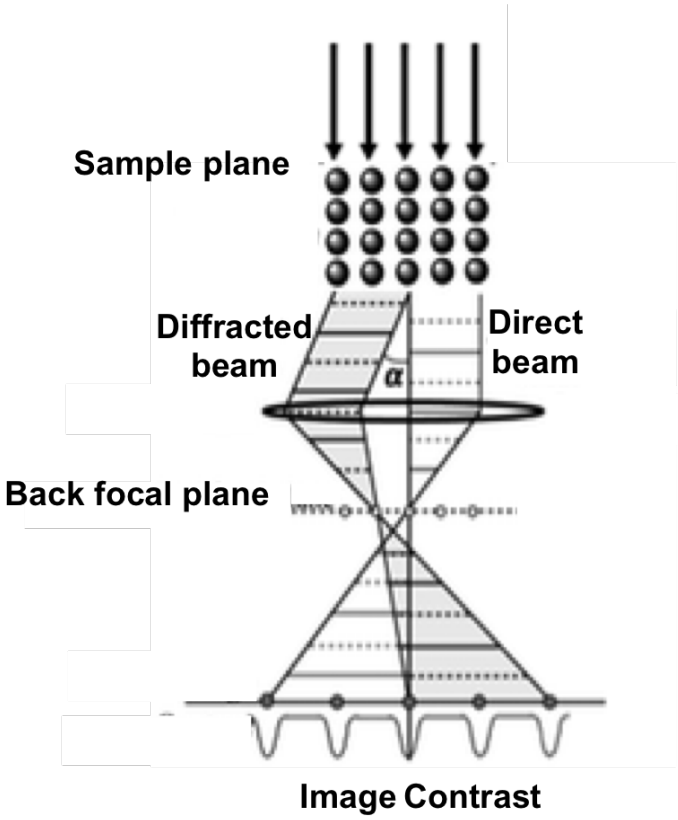

Figure 4.7: *Schematic of optics set-up in a High Resolution TEM [Abe, 2012].*

HRTEM lattice images of the nanoparticles are of near atomic resolution and the atoms appear as dark contrast. The HRTEM is an effective technique for determining crystallographic information and any lattice defects in the nanoparticles.

4.11 Scanning Transmission Electron Microscopy

An STEM is equipped with an HAADF detector and energy dispersive X-ray (EDS) spectrometer. The high thermal stability of the STEM its aberration corrected condenser lenses, C_s, results in a high atomic spatial resolution of 0.08 Å which is the highest in the world amongst commercial microscopes. The set up is similar to conventional TEM but in reverse, whereby the focussed beam of electrons is used as the analytical probe.

4.11.0.1 STEM-High Angle Annular Diffraction

In STEM-HAADF imaging mode the fine electron probe of atomic size is raster scanned across the atomic columns of the nanoparticle. Only the scattered electrons transmitted from the sample are collected at high angle using a high angle annular diffraction detector (HAADF) as demonstrated in Fig.4.8. The purpose of the high angle annular detector (with an inner radius of 50-70 mrad) is to collect only the incoherently scattered electrons that scatter strongly on interaction with the nucleus of the sample, omitting collection of the coherently scattered Bragg electrons. The high angle scattered electrons have been scattered by the nucleus of the atoms in the column, and the scattering angle is approximately proportional to the atomic number squared ($\sim (Z)^2$), creating mass thickness contrast. Therefore, lighter atoms will give lower contrast e.g. the Fe (Z = 26) atoms in an FePt sample will be of lower contrast in comparison to Pt (Z = 78). The STEM-HAADF technique is otherwise termed as Z-contrast STEM and is monotonically proportional to thickness. STEM-HAADF is a useful technique for acquiring high atomic resolution lattice spacing images.

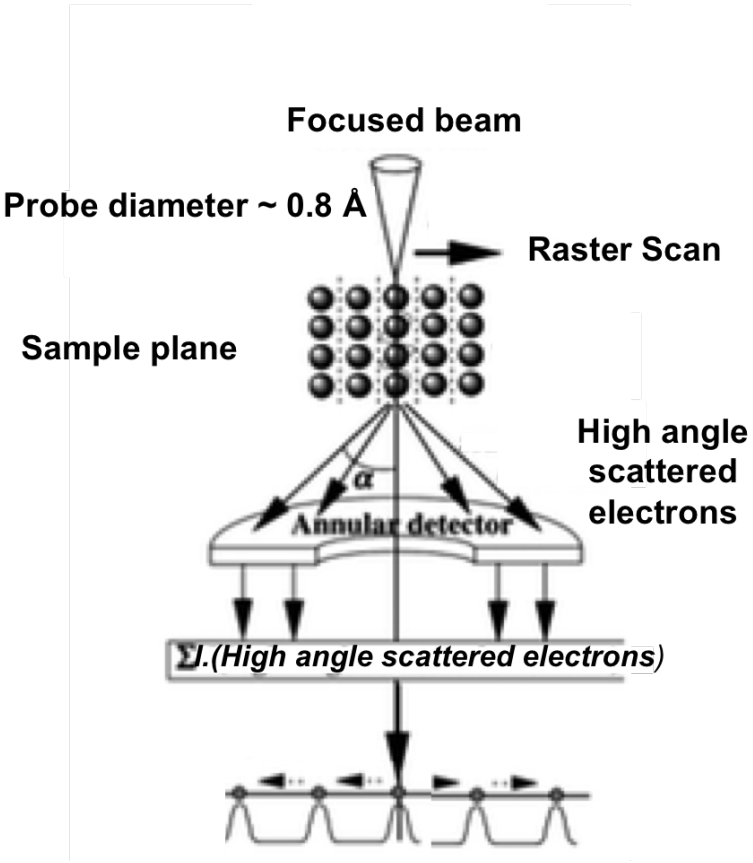

Figure 4.8: *Schematic of optics set up in STEM-HAADF. Image reprinted with perimssions from [Abe, 2012][REF].*

4.11.0.2 STEM-Elemental Dispersive Spectroscopy

In STEM-EDS imaging mode the fine electron probe of atomic size is raster scanned across the sample columns. An EDS detector is positioned above the sample plane and detects the X-rays emitted at a characteristic energy as the probe scans the atomic columns. The X-ray emission follows the same concept as the characteristic X-ray emission of metal anode targets in X-ray diffraction in Chapter 4 (Section4.4.1) and each element has a different core strength depending on the electronic configuration of the atom. Elements present in the sample can therefore be identified by their characteristic energy loss edge in the spectrum, as shown in the example spectrum in Fig.4.9. 2D spatial imaging of the spectrum enables elemental maps of the emitted X-rays from a sample area to be generated. In order to visualise the distribution from different elements, the resultant X-ray spectrum can be filtered so that only specific energies are

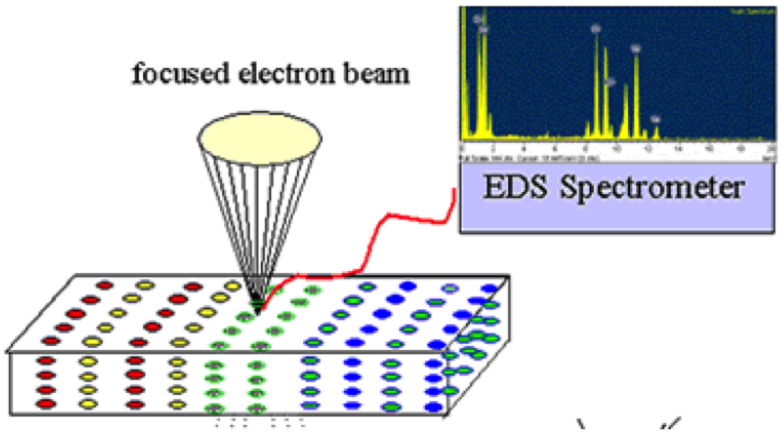

Figure 4.9: *Schematic of Scanning TEM-EDS imaging principle where X-ray spectra are generated by raster scanning the 0.8 Å electron probe across a region of interest. Image reprinted with permissions from [Nudelman et al., 2011].*

mapped e.g. Fe K-edge, O K-edge, Pt M-edge. allowing for 2D spatial imaging from a desired elemental energy range. Red Green Blue (RGB) maps can enable a superposition of 3 different elements of an assigned colour (in this case the Fe columns are assigned red, Pt columns are assigned blue, and O columns are assigned green) so they be visualised on the same map. The elemental maps were further analysed using Image J—an open source software program [Schneider et al., 2012]—to extract line scans of the elemental distribution.

4.12 Summary

In this Chapter the interaction of X-rays and electrons with matter was outlined and correlated with the use of the radiation sources as analytical probes for the characterisation of nanoparticle systems. The fundamentals of both powder XRD techniques and range of TEM techniques are detailed. Overall, this chapter provides a knowledge platform describing the range of nano-characterisation techniques that can be adopted to fully characterise alloy nanoparticles. These TEM techniques are applied in Chapter 5 and the XRD investigations are used in both conventional lab based sample quantification in Chapter 5, and in advanced powder X-ray and neutron diffraction sample quantification in Chapter 7.

Chapter 5

Nanoscale Analysis and 2D Strain Mapping using Transmission Electron Microscopy Techniques

5.1 Motivation

Elucidation of the crystallographic, compositional distribution, 3D morphology and distribution, and strain properties of magnetic alloy nanoparticles is of high importance to researchers in order to engineer the nanoparticles characteristics. Although the synthesis and magnetic properties of the FePt nanoparticles have been extensively investigated [Zeng et al., 2003], [Sahu and Bahadur, 2013], there have been very few comprehensive studies of small alloy nanoparticles. Therefore one of the key motivations behind this Chapter was to conduct a comprehensive study of the FePt nanoparticles of different shapes and sizes and correlate their properties with their potential applications.

Also, the fine nanoparticles (of diameter < 10 nm) synthesised in Chapter 3 are of a size well below the resolution limit of CDI $\sim$ 20 nm as a result of instrumental limitations (with the larger FePt octapods being the only exception and these are analysed by BCDI in Chapter 6). As a consequence alternative analysis approaches were required to be devised to analyse the 3D morphology and strain distribution of the fine nanoparticles, which was one of the key motivation behind

this Chapter

5.2 Introduction

In this study both qualitative and quantitative TEM image analysis was conducted, for elucidation of the crystallographic, compositional distribution, 3D morphology and distribution, and strain properties of magnetic alloy nanoparticles. The fine FePt nanoparticles (synthesised in Chapter 3) of different shapes and sizes were analysed within this Chapter using an array of state-of-the-art TEM nanocharacterisation methods (and conventional XRD and spectroscopy methods). Understanding the properties of the following model FePt nanoparticles fabricated within—nanocubes of diameter 8.41$\pm$0.56 nm to, $FeP@Fe_3O_4$ core-shell nanoparticles of diameter 8.71$\pm$0.44 nm, and octapods of diameter 17.0$\pm$2.01 nm—will enable these nanoparticles to be further tuned for application.

Characterisation of the FePt nanoparticles included the use of the following instrumentation at JAIST (Japan); TEM, TEM tomography, aberration-corrected HRTEM scanning TEM-high angle annular dark field (STEM-HAADF) and, STEM-energy dispersive spectroscopy (STEM-EDS) analysis (as introduced in Chapter 4). Additional analysis techniques adopted in the quantification of the nanoparticles include; ICP-OES to determine the nanoparticle compositions, conventional XRD to determine the crystallographic phase, and X-ray photoelectron spectroscopy (XPS) to distinguish the phase of the oxide shell in the core-shell $FeP@Fe_3O_4$ nanoparticles.

Conventional TEM bright field imaging of the nanoparticles enabled the morphology, 2D distribution, and mono-dispersity of the nanoparticles to be determined. TEM tomography investigations were conducted on a TEM equipped with a double tilt axis sample holder, which enabled 3D reconstructions of an isolated nanoparticle (or array of nanoparticles) to be built. The 3D morphology of the core-shell nanoparticles was further visualised using an Avizo software package—enabling phase segregation effects of the core-shell nanoparticles to be better understood. High resolution TEM (HRTEM) and STEM-HAADF enabled crystallographic information to be extracted from isolated nanoparticles. The interplanar lattice spacings (d-spacings) extracted from the HRTEM images

enabled the crystallographic phase and, the preferred orientation of the nanoparticles on the substrate to be determined. Additionally, STEM-elemental distribution spectroscopic (STEM-EDS) imaging enabled the compositional distribution of Fe, Pt, and O within individual nanoparticles to be identified. Also, average compositional scan analysis from a rectangular region of interest (ROI) was used to gauge the elemental distribution within the nanoparticles.

Alternative synchrotron-based strain analysis methods to BCDI have been adopted for analysis of nanoparticles below the resolution limit of CDI. For example, extended x-ray absorption fine structure (EXAFS) [Strasser et al., 2010] and high energy powder X-ray diffraction (XRD) [Kuo et al., 2013]. However, these alternative strain analysis methods require access to large-scale synchrotron facilities and are based on average ensembles of nanoparticles. More conventional strain analysis methods have been applied to nanostructured material such as scanning electron microscopy (SEM) cross sectioning [Usuda et al., 2005] which is intrusive as the lamellar cross sectioning in SEM can induce or even remove any internal strain with-in the nanoparticle. Strain can, in principle, be seen in lattice images of materials such as aberration corrected scanning TEM (STEM), and has been adopted to quantify lattice deviations associated with the strain release mechanisms in core-shell nanoparticles [Bhattarai et al., 2013]. Although this form of direct analysis is a less-intrusive strain analysis it only gives an indication of the extent of the strain and has not yet provided a clear picture of strain gradients throughout the nanoparticle structure. A powerful extension to this direct STEM method is the Geometric Phase Analysis (GPA) technique, developed by Hytch et al [Hytch et al., 2003] which enables the quantitative mapping of 2D strain fields from a crystal system [Hytch et al., 2003] [Hytch et al., 2008]. The Fourier dark-field filtering capability of the GPA method allows the slow-varying distortions of the lattice to be extracted for quantitative evaluation. This strain analysis tool was devised within using an

5.3 Data Acquisition and Processing Methods

5.3.1 Instrumentation

The fundamentals behind the following instrumentation utilised within this Chapter are outlined in the Chapter 4. X-ray diffraction patterns of the dry nanoparticle samples were collected using a conventional laboratory Co-K_{alpha} source diffractometer (based at the Royal Institution, UK). The instrumentation used in TEM and TEM tomography observations is detailed in Section 4.7. XPS analysis of the core-shell nanoparticles was implemented using a Shimadzu Kratos AXIS-ULTRA delay-line detector high-performance XPS system, operating at a vacuum level of 10^{-7} Torr.

5.3.2 Sample Preparation

The nanoparticle samples were prepared for TEM, HRTEM, STEM, and TEM tomography analysis by drop casting three $\sim$0.5 μL drops of a dilute nanoparticle suspension onto a carbon-coated/holey carbon copper grid substrates and the hexane was left to evaporate. Another sample preparation method used was also used which followed dip-coating and drying after each suspension in solution the sample. This method has been proposed to remove the formation of a ring of nanoparticles at the edge of the grid, which occurs as a result of drop formation. Additionally, when preparing TEM grids the first important factor is to ensure that the solution is cleaned properly because any excess surfactant can contaminate the sensitive vacuum system of a TEM (especially if the TEM is not very modern). It is also important to ensure the samples are dried properly as any excess solvent on the grid can also be a contaminant.

The samples were prepared for XPS analysis by drop casting a 15 μL drop of sample solution, one drop at a time, onto an Si substrate allowing the hexane to evaporate after each drop. The sample was loaded by placing the substrate onto a conductive double-sided carbon tape and attaching it to the XPS sample stage for insertion into vacuum. Photoelectrons were excited by monochromatic aluminium K_{α} radiation (emitted from an X-ray tube operating at 150 W) and focused

on the centre of the specimen surface irradiating an area of 300 x 700 μm^2.

5.3.3 Nanoparticle Size Distribution

The mean particle size, d, and size distribution, σ, were calculated from the TEM images using the Java enabled digital software package, ImageJ 64. The maximum Feret diameter (the maximum perpendicular distance between two parallel planes) was used as the indicator of the size of the nanoparticles, which were not completely spherical. Firstly, a bright field TEM image of the nanoparticles at a low magnification was selected so that there were many nanoparticles that could be sampled and the image was calibrated.

A region of the image was selected with even illumination, as any uneven illumination can affect the thresholding this region was duplicated as a new image. A 'Band pass filter' was applied to the duplicated image to flatten the image with the following settings altered; filter large structures down to 20 pixels, filter small structures up to 3 pixels. The band pass filter allows signals of a low spatial frequency to pass, but attenuates other high spatial frequencies (that cause image blurring) outside the 'allowed' range. It can also minimise the effec of horizontal or vertical stripes that may be created by scanning an image line by line.

Subsequently the threshold was adjusted with a dark background and over/under filter selected so that the outline of the nanoparticles could be clearly defined and filled. The position of thresholding just before the peak (nanoparticles) is usually a good level to threshold at. The nanoparticles were analysed first by selecting 'outlines' in the pull-down menu and selecting 'exclude on edges' to avoid counting nanoparticles that are fully in the image. In the resulting image of nanoparticle outlines any artefacts that are observed can be removed from the threshold image by cleaning which entails using a paintbrush and also by increasing the minimum size limit (e.g. 5-infinity nm^2) and the lower limit of the circularity outlines (e.g. 0.6-1). Once the image is clean the results can be displayed by selecting 'display results'. The Ferret diameter was selected and a histogram plotted displaying the average size distribution and the standard deviation. Notably, the maximum Ferret diameter (the maximum perpendicular distance between two parallel planes) was used as the indicator in the analysis of nanoparticles, which were not completely spherical.

5.3.4 Crystallographic Data Extraction

The STEM-HAADF images were calibrated and the d-spacing was extracted from the lattice images using ImageJ following a direct analysis method of a line scan drawn perpendicular to the crystallographic planes (as indicated by the yellow line scan on Fig.5.5a). The corresponding line profile was plotted and the distance of line scan was divided by the number of peaks. A Fast Fourier Transform (FFT) was applied to the selected masked image intensity to transform the image into reciprocal space as shown in Fig.5.5a which showing the Bragg spots that correspond to the various sets of lattice planes of the nanoparticle as shown in Fig.5.5b. Notably, this technique can be compared to (but not the same as) acquiring reciprocal space electron diffraction image of a sample using TEM diffraction imaging mode set up (diffraction imaging mode is explained in more detail in Chapter 4. The intensity of the spot corresponds with the most preferred orientation of the nanoparticle on the substrate; where the highest intensity spots correspond with the most prominent nanoparticle plane orientation on the substrate. The d-spacing value of these spots can be extracted by highlighting a peak of interest and it is then displayed in 'nm/cycle' (d-spacing of the plane) status bar.

The d-spacing values and the distance of the diffraction spots from the central peak extracted from the FFT images, were used to index the image. Indexing the FFT 'electron diffraction patterns' enabled the diffraction spots to be ascribed to their corresponding planes (hkl), which is required for identifying the most prominent planes present in the lattice image and also for identifying planes of interest in the strain mapping analysis of the nanoparticles.

5.3.5 TEM Tomography Data Acquisition

In the TEM tomography investigations, a 3D reconstruction of a nanoparticle is built from a series of 61 electron micrographs, collected over a tilt series of $\pm 60^{\circ}$ (in 2° increments) from TEM images. After each subsequent tilt the software automatically corrected for shifts in the imaging position by the use of feedback control. The image was then auto-focussed followed by manual focus. Manual focussing was conducted on a nearby feature to reduce the possibility of radiation

damage from over exposure of the beam on the sample of interest. The electron micrographs were reconstructed using a Hitachi reconstruction software.

5.3.6 Tomographic Reconstructions

To reconstruct the TEM tomography data a topography based reconstruction (TBR) algorithm [Norio Baba, 2008] was applied. The TBR uses a density constraint within a defined volume, leading to a cleaner reconstruction in comparison with the conventional weighted Fourier Back Projection reconstruction methods of Weyland et al (2001). Firstly, the collation of electron micrographs acquired from the tilt series were inverted and axially aligned. Topographic profiles of the specimen were estimated by the application of stereo-photogrammetry. The principle of stereo-photogrammetry involves the recovery of the exact position of surface points from the specimen by relating each corresponding point along the cross section to another in 3D space to map the geometry. An area was then cropped around the nanoparticle region of interest and the 3D reconstruction was calculated using the TBR method. In the TBR, a density distribution of the image along that section was converted to a thickness value and used as the initial approximation of the subsequent calculations. The calculated thickness distribution was then updated iteratively until all the density distribution in each image agreed with the 3D projection simultaneously. The reconstructed image is displayed with volume rendering or multilateral slice in this system. In some cases, the converged full 3D density distribution, as a tiff stack, was recompiled using Avizo visualisation allowing for ortho-slicing through the software and movies were created. The initial aim of the TEM tomography investigations was to analyse an isolated nanoparticle. However, difficulties were faced in obtaining a clean reconstruction of nanoparticles of diameter < 10 nm. These difficulties could be ascribed to the increased contribution from background artefacts as the sample size decreased which interfered with the reconstruction process. Therefore, in order to obtain cleaner reconstructions for nanoparticles of diameter < 10 nm, isolated collections of nanoparticles were analysed rather than isolated nanoparticles.

5.3.7 Gradient Phase Analysis

The GPA method used in this Chapter was implemented with a MatLab script used to evaluate the high resolution TEM images in three steps: i) the nanoparticle image is isolated by manual masking from its neighbours ii) the masked image density is Fourier transformed with an FFT iii) a Bragg peak from the crystal lattice is isolated and cut out from the bright field diffraction pattern iv) this local region of the diffraction pattern is re-centred and inverse Fourier transformed back to a real space complex image v) the amplitude of the real space complex image closely resembles the original crystal and vi) the phase of the real space complex image is a projection of the lattice distortions in the direction of the selected Bragg peak. This method has a close similarity to the Bragg Coherent Diffraction Imaging method of imaging strains with X-rays (Robinson and Harder, 2007).

The resultant phase image is a real-space map of the local displacement of the lattice fringes whose values are projections of the local lattice displacement onto the Q-vector, where $\phi(\mathbf{r}) = \mathbf{Q}.\mathbf{u}(r)$. By choosing different Bragg peaks at the intermediate stage, images of different projections of the local lattice displacement field were obtained in the form of phase images. This is termed as the 2D strain mapping technique which is sensitive to displacements a small fraction of a unit cell in magnitude. These strained regions can be qualitatively mapped in the resultant 2D strain maps, acquired using the Matlab GPA code (detailed in the Appendix 9.2.3). The strain decay behaviour was analysed by extracting the phase from a line profile (x,y) across the strain map (phase image) of the nanoparticle. The extracted phase was treated by dividing the phase output value by 1000 (to correct for the multiple by 1000 in the GPA code). In the case of core-shell nanoparticle (which resulted in $-$ve and +ve phase ramps at the core shell interface) $\pm 2\pi$ was added to either side of the line profile to correct for phase wraps at the interface. Also, in the strain analysis of the core-shell nanoparticles the theoretical % strain, ε, was calculated using the following equation:

$$\varepsilon = \frac{a_{core} - a_{shell}}{a_{core}} \tag{5.1}$$

The strain values were then compared to the experimental strain which was extracted from the strain gradients of the line displacement plots.

5.4 Nanocharacterisation of FePt@Fe Nanocubes

The synthesis of FePt nanocubes using chemical methods has been well reported (as outlined in Chapter 3). In a recent study FePt nanocubes with a monoatomic (one atomic layer thickness) Fe shell were reported which was proposed to form when a small volume of Fe precursor was used in excess during the synthesis [Zhang et al., 2014]. The authors identified that on increasing the volume of excess Fe precursor above a certain level the thickness of the Fe shell increased and resulted in the formation of an Fe oxide. Despite confirming the presence of the Fe shell using solvothermal methods, the authors found that the layer was too thin to be observed using conventional TEM techniques. Therefore, in this section the advanced TEM analysis techniques were utilised to probe the FePt nanocubes and surrounding , to provide an insight into both the chemical and physical properties of this newly reported structure of an Fe shell on FePt nanocube.

5.4.1 Nanocube Array Formation and Size Distribution

From the TEM observations of the FePt nanocubes, the formed 2D self-assembled arrays with a square- or brick- like mosaic on the substrate as seen in Fig.5.1a and Fig.5.1b. The primary factors that result in this array formation are the high monodispersity of the nanoparticles and the presence of the surfactant layer physically preventing aggregation. Also, it can be seen that there is a clear minimum particle separation distance of 1.6 nm, which corresponds to a compacted surfactant layer with the surfactant tails interpenetrating. The fully-extended lengths of the OA and OLA surfactants are 2.08 and 2.06 nm, respectively. In the regions of the nanocube arrays where the monodispersity was high, the nanocubes formed this preferred square (3 by 3) nanocube motif array on the substrate, as observable in the HRTEM image (high magnification) of the nanocubes in Fig.5.1c. However, in the regions where the monodispersity was low, the nanocubes formed a less defined brick- like or hexagonal formation. A region of low contrast can be observed surrounding the nanocubes indicating the presence of a shell on the surface. The average size distribution of the FePt nanocubes (from the TEM image analysis of the Feret diameter of 322 FePt nanocubes), was calculated to be

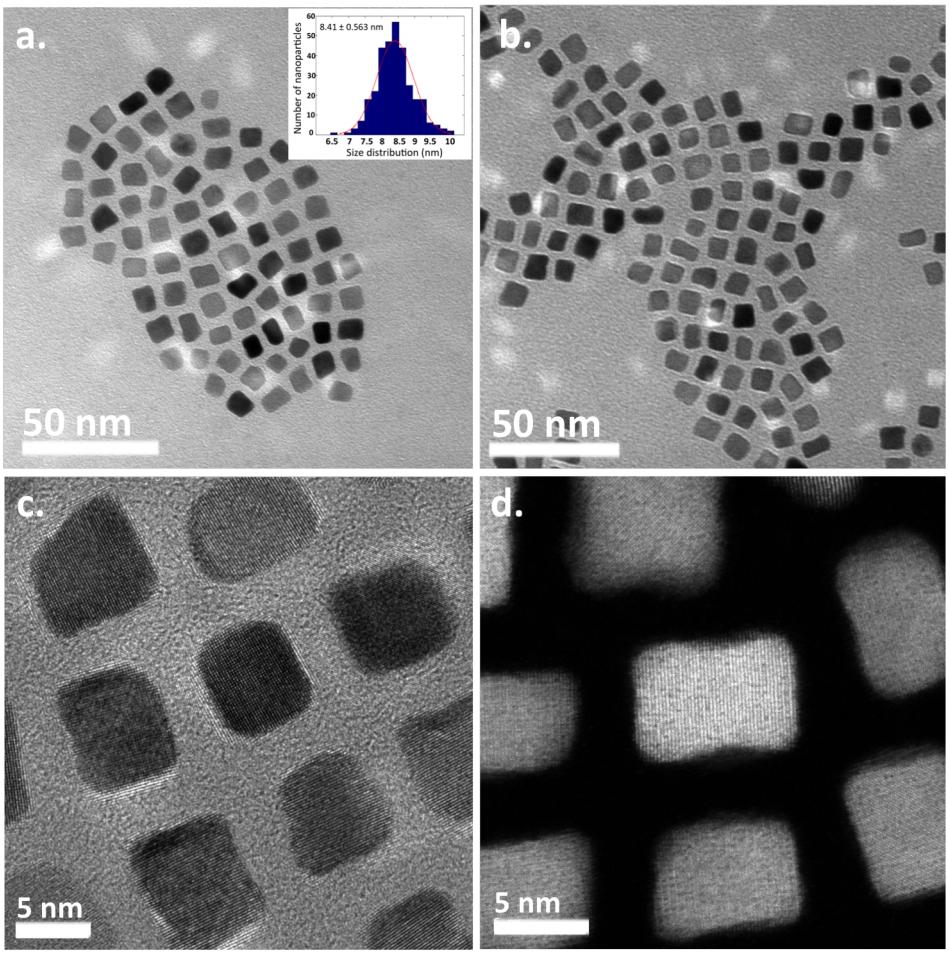

Figure 5.1: *FePt nanocube TEM analysis (a) Low magnification and, (b) high magnification TEM image of FePt nanocube showing a 2D square array with a size distribution histogram inset, (c) HRTEM image of FePt nanocubes at high magnification, (d) STEM-HAADF image (analysed further by STEM-EDS in Fig.5.8 a-d).*

8.41$\pm$0.56 nm as shown in the size distribution histogram inset in Fig.5.11. The d-spacing of the nanocube crystal lattice is resolvable in both the HRTEM and STEM-HAADF images in Fig.5.1c and Fig.5.1d. This crystallographic information contained within the lattice images can be extracted and analysed to determine the phase and processed to determine the strain in the nanoparticles (as shown later).

5.4.2 Powder X-ray Diffraction of Nanocubes

The observed XRD lines of the FePt nanocubes match closely to the reference pattern Platinum Ferroan, $Fe_{25}Pt_{75}$, (JPCDS-00-029-0717), a = 3.871 Å) as indicated by the black reference pattern in Fig.5.2. From XRD analysis the lattice parameter,a, was calculated to as 3.874 Å, slightly smaller than the reference pattern. Powder XRD pattern analysis of the peaks revealed the characteristic fcc planes with d-spacings; d_{111} = 2.371 Å, d_{200} = 1.936 Å, and d_{220} = 1.368 Å, representative of a chemically-disordered fcc phase of FePt nanoparticles. For

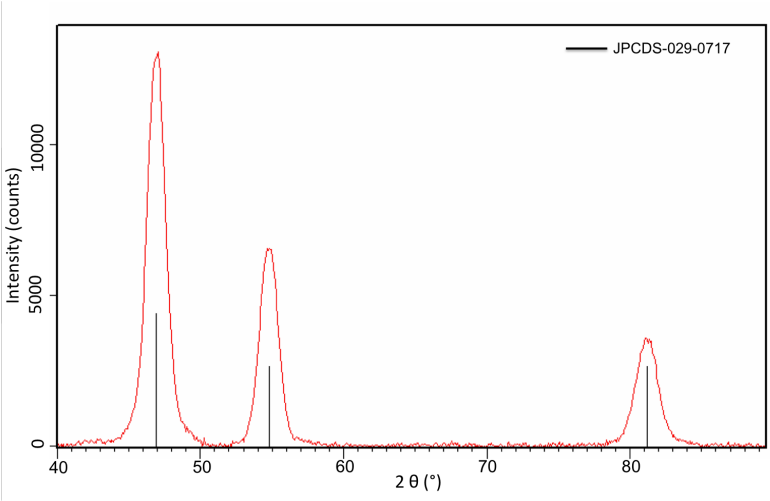

Figure 5.2: *Powder XRD of FePt nanocubes with corresponding reference pattern, Pt Ferroan (JCPDS-029-0717).*

example, a higher Pt content results in the alloy having a larger lattice spacing, because the lattice parameter of Pt, a_{Pt} = 3.939 Å, is larger than the lattice parameter of Fe, a_{Fe} = 2.912 Å. Therefore, when there is a higher Pt content the peaks from the whole pattern will be at a lower angle in comparison to pattern from a sample with a lower Fe content. Green et al (2014), demonstrate this angular relationship with Fe and Pt content in their recent paper. The average crystallite size was calculated, from XRD pattern analysis, using the Scherrer equation, for each peak and was determined as 8.9 nm which corresponds well with the nanocube diameter determined by TEM analysis.

5.4.3 3D Morphology of Nanocubes

The morphology and allignment of a cluster of eleven nanocubes was investigated by TEM tomography following the procedure outlined in Chapter 4. The

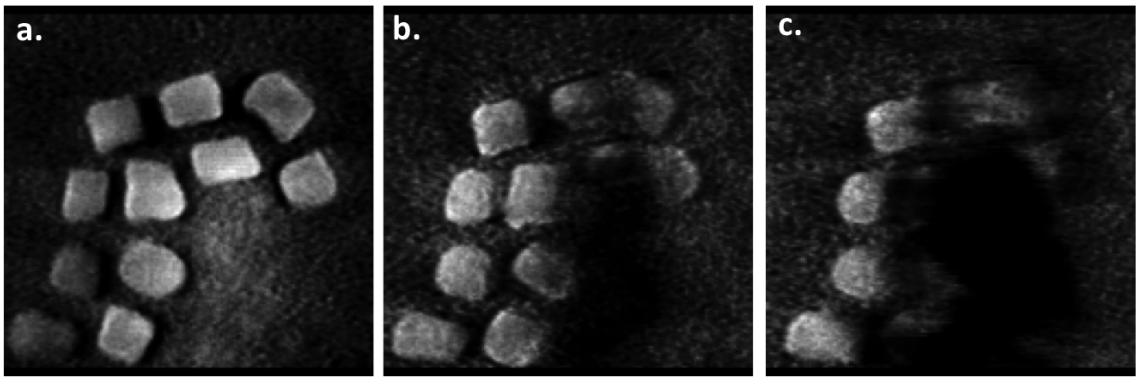

Figure 5.3: *3D Hitachi reconstruction of eleven nanocubes with orthoslices taken at the different y positions; (a) y = -12, (b) y = -23, (c) y = -33.*

resultant 3D Hitachi reconstruction of the eleven nanocubes in Fig.5.3a-c shows ortho-slices at different positions through the y-axis of the reconstruction. The reconstructions illustrate the cubic morphologies of the nanocubes and the distinct separation distance between the nanocubes due to surfactant layer. Determining the distribution of the nanocubes using TEM tomography in this way is particularly important for engineering nanoparticles for high density data storage applications. In this case the majority of nanocubes are aligned 'side-on' with their c-axis parallel to the substrate, it is also evident that there are some nanocubes aligned 'edge-on' on the substrate.

5.4.4 Crystallographic Study of Nanocube 1 and Nanocube 2

In this section crystallographic information from lattice images (acquired by either from STEM-HAADF or HRTEM observations) were analysed to determine the phase of the nanocubes. Two nanocubes orientated differently on the substrate were analysed; Nanocube 1 orientated 'side-on' on the substrate (Fig.5.4a) and Nanocube 2 orientated 'edge-on' on the substrate (Fig.5.4b) to provide an example of how the d-spacing can be extracted. The average d-spacing extracted from the line scan of Nanocube 1, in Fig.5.5 (as shown inset) is 2.20 Å, which

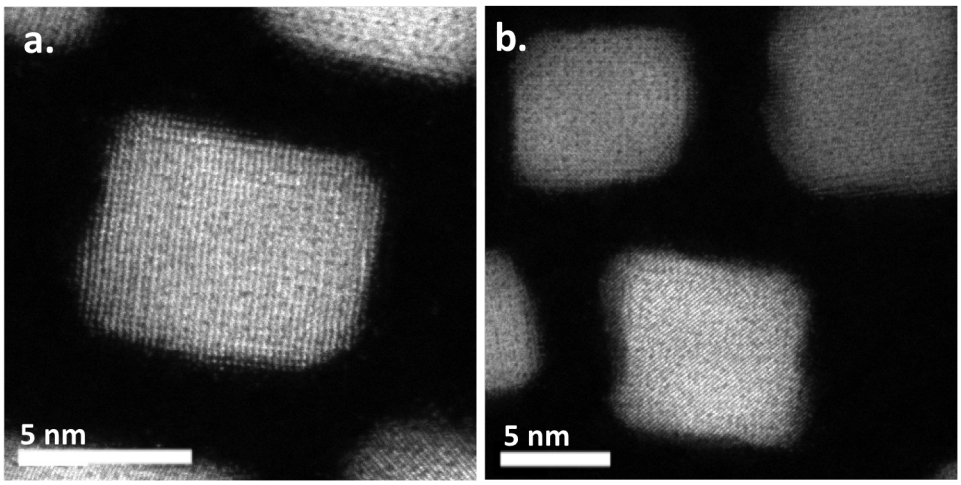

Figure 5.4: *STEM-HAADF lattice images of nanocubes (a) Nanocube 1, 8.60 nm length x 7.00 nm width and, (b) Nanocube 2, 8.17 nm length x 7.73 nm width.*

corresponds closely to d_{200} = 1.936 Å, thus the diffraction spot was ascribed to the (200) plane as indicated in the corresponding FFT in Fig.5.5b. The average

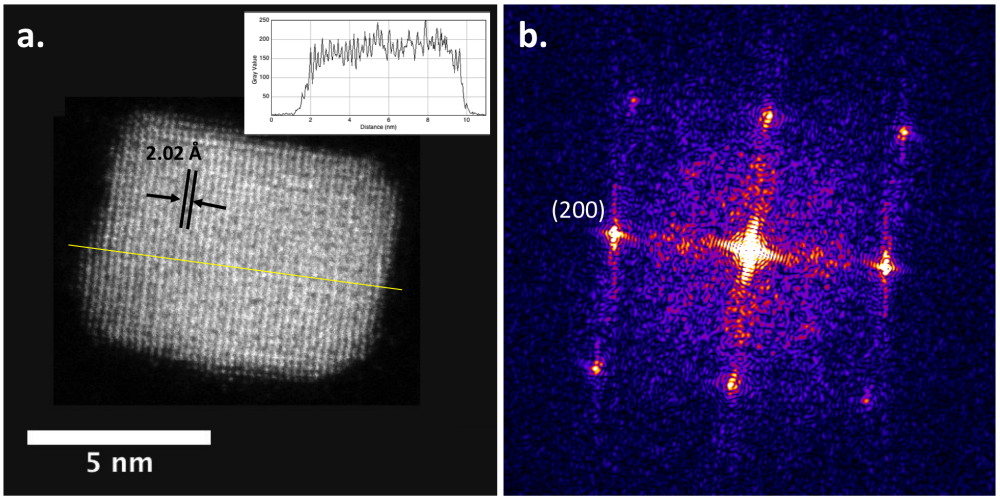

Figure 5.5: *Cyrstallographic analysis of Nanocube 1 (a) STEM-HAADF image (with background subtracted) with the average d-spacing value of 2.20 Å extracted from a line scan (yellow) perpendicular to the lattice with corresponding line profile inset, (b) Corresponding Fast Fourier Transform (FFT) image with corresponding (220) diffraction spot labelled.*

d-spacing extracted from the line scan of Nanocube 2, in Fig.5.6 (as shown inset) is 1.40 Åwhich corresponds closely to d_{220} = 1.368 Å, thus the diffraction spot was ascribed to the (220) plane as indicated in the corresponding FFT in Fig.5.5b. The results of the crystallographic study of FePt nanocubes of different orientations on the substrate suggest that the nanocubes are enclosed by (100)

and (110) facets and the corresponding planes were labelled in Fig.5.6b.

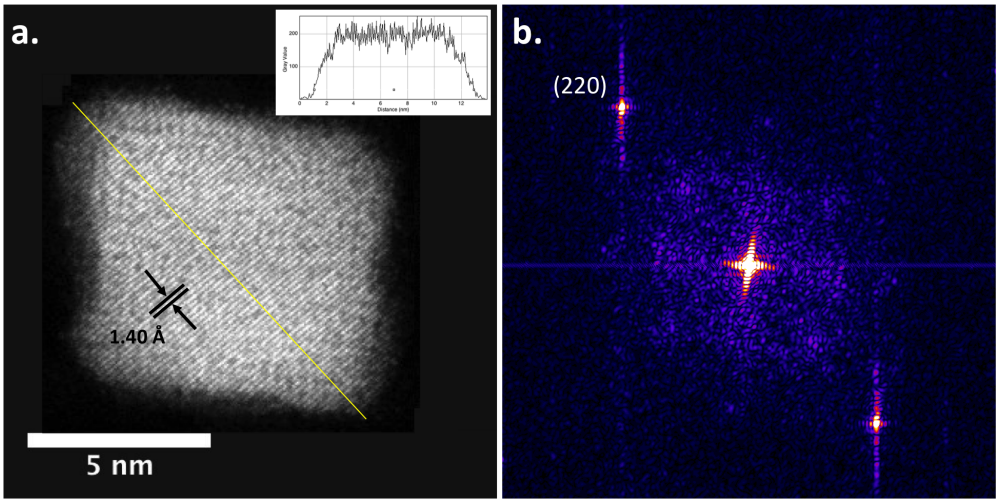

Figure 5.6: *Cyrstallographic analysis of Nanocube 2 (a) STEM-HAADF image (with background subtracted) with the average d-spacing value of 1.40 Å extracted from a line scan (yellow) perpendicular to the lattice with corresponding line profile inset, (b) Corresponding Fast Fourier Transform (FFT) image with corresponding (200) diffraction spot labelled.*

5.4.5 Comprehensive Analysis of Nanocubes

Complementary crystallographic, elemental, and strain mapping analysis was conducted on a single nanocube.

Firstly, a threshold was applied to the STEM-HAADF image of the nanocubes as shown in Fig.5.7a to identify what cannot be observed in the HRTEM or STEM-HAADF images alone. The thresholded image shows regions of background intensity in blue. The surrounding region around the surface of the nanocube indicates the presence of a shell with an average thickness of $\sim$ 0.65 Å(calculated from direct measurements of the image). The average d-spacing extracted from the line scan of the nanocube, in 5.7b (as shown inset) is 2.01 Å, which corresponds closely to d_{200} = 1.936 Å, thus represents a (200) plane.

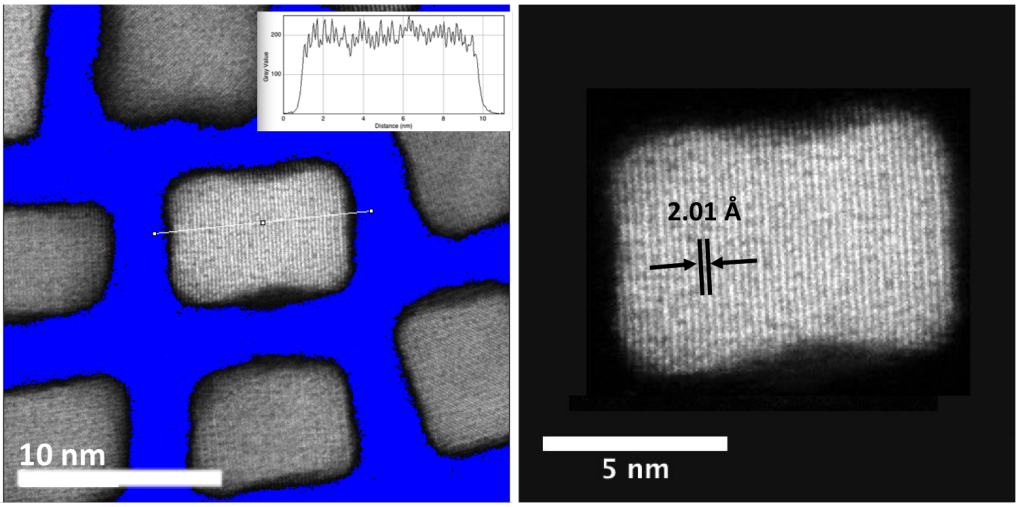

Figure 5.7: *STEM-HAADF lattice images of nanocubes (a) nanocube square array with threshold applied for clarity (where blue is equivalent to the lowest intensity) (b) STEM-HAADF image (with background subtracted) of isolated nanocube with d-spacing value of 2.01 Årepresentative of the (100) facet parallel to the substrate.*

5.4.6 Elemental Distribution of Nanocubes

Elemental maps were acquired for the core-shell nanobubes, as imaged in the STEM-HAADF in Fig.5.7a, using STEM-EDS elemental mapping. The O K-edge, Fe K-edge and Pt M-edge were mapped in Fig.5.8a-b and the elemental overlay mapped in Fig.5.8d. The O K-edge elemental contribution (represented in green) in Fig.5.8a is homogenously distributed on the nanocube and with such a low signal it can be attributed to the typical surface contamination. The Fe K-edge elemental contribution (represented in red) in Fig.5.8b is homogenously distributed throughout the nanocube core extending to the surface of the nanocube core and shell. The Pt M-edge elemental contribution (represented in blue) in Fig.5.8c is distributed only in the core. An overlay of the three elemental maps is shown in 5.8d confirms the presence of the Fe shell. The line profiles across of the O K-edge, Fe K-edge and, Pt M-edge are shown in Fig.5.9e. The integration regions are shown in Fig.5.8a-c. The intensity profiles quantitatively demonstrate that the higher Pt signal is localised in the core while the Fe contribution extend slightly beyond the core into the shell in Fig.5.9.

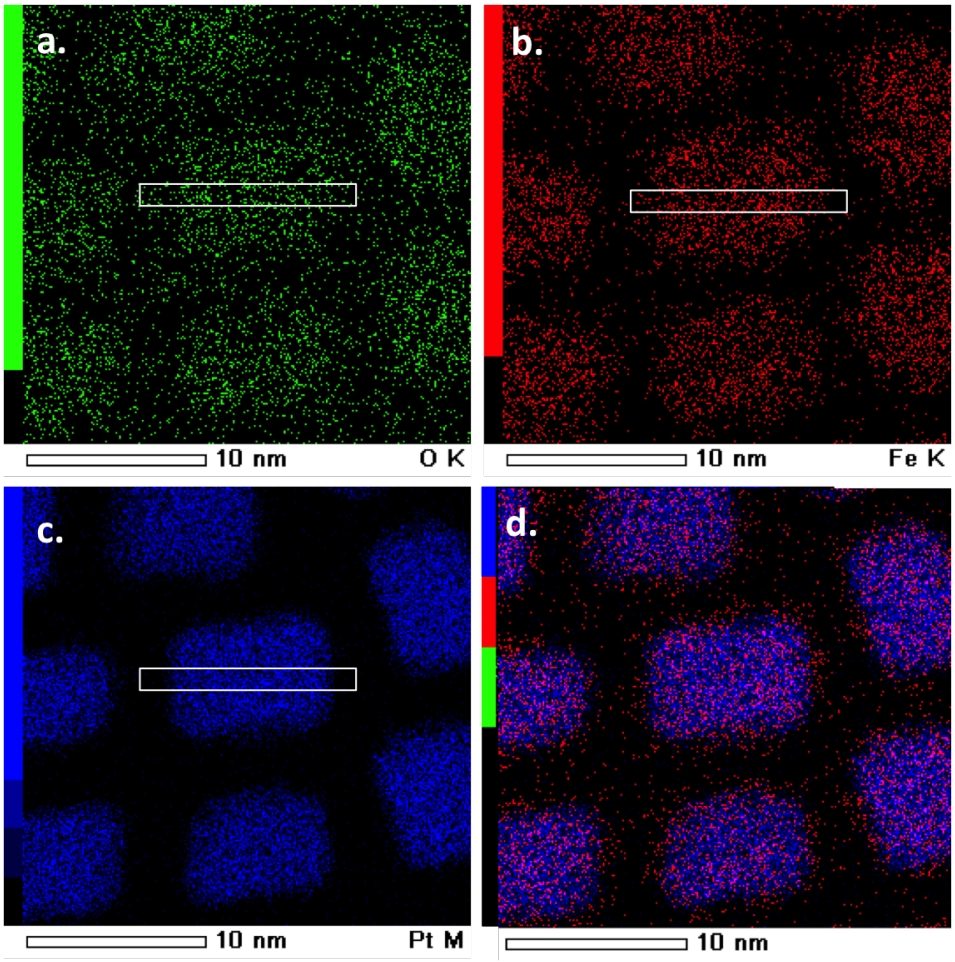

Figure 5.8: *STEM-EDS elemental maps of Nanocube 2 (corresponding STEM-HAADF in Fig.5.4b) (a) O K-edge, (b) Fe K-edge, (c) Pt K-edge and, (d) Elemental overlay, with rectangular ROI's (plotted in Fig.5.9).*

5.4.7 2D Strain Analysis of Nanocubes

5.10a. A single Bragg spot was selected, as circled in Fig.5.10a (with a radius cut off of 50 pixels), and re-centered in Fig.5.10b. The selected peak is a (200) peak of the FePt lattice, so it is the distortions from the 100 planes that are imaged by GPA. The region of reciprocal space surrounding this selected Bragg spot, sufficiently large to include the interference from the overlapping Bragg peaks of the Fe oxide shell, was Fourier transformed into a real space complex image; the geometric phase is shown in Fig.5.10e and the image amplitude in Fig.5.10f. The STEM-EDS elemental map of the same crystal is reproduced in Fig.5.10d showing the approximate location of the core shell interface. The geometric phase

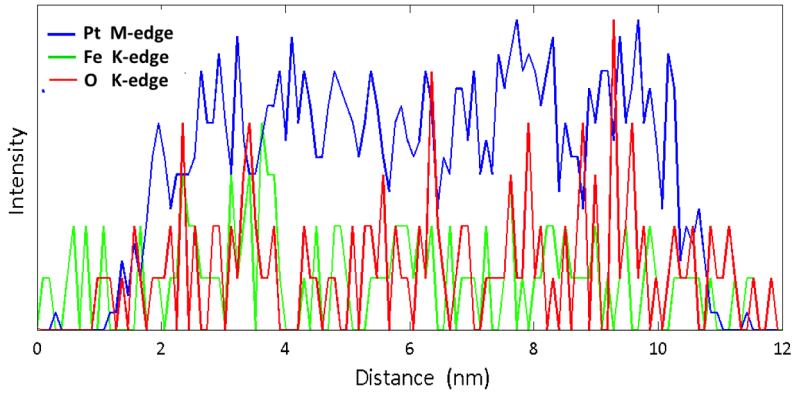

Figure 5.9: *Corresponding intensity profiles of rectangular ROI's from Fig.5.8a-b, through the centre of an individual FePt nanocube.*

image in Fig.5.10e, a map of the 2D strain projection, represents the displacement of atoms from the perfect crystal lattice, ranging from -π (white) to + π (black), shows the strain along the (200) direction. The full phase range of 2 π corresponds to a displacement of a single lattice spacing. Note that the phase becomes meaningless in the regions outside the nanoparticle, where the amplitude of the complex density drops to zero. Also, the amplitude variation is a known 'feature' of the GPA, resulting from it being a dark-field image.

The core and shell can be clearly distinguished in Fig.5.10e by the phase shift enclosing the shell (dark region). There are slight deviations from the median value within the core which might be due to defects, possibly dislocations, in the FePt crystal structure. Regions of high strain gradients and phase wraps surrounding the core of the nanoparticle are due to the strains present in the shell, which is seen to be less homogeneous than the core. Some of these apparent strain inhomogenities could also be due to local compositional variations of the oxide. The local amplitude image in Fig.5.17f shows this intensity variation in the selected (200) plane direction, with an intensity scale ranging from yellow (high intensity) to dark blue (low intensity).

In order to examine the strain decay behaviour at the core-shell interface the cross section line in Fig.5.10e, is plotted in Fig.5.10g. The linear phase ramps seen on the two sides of Fig.5.10g represent the difference in lattice constant between the FePt, and the Fe shell. The displacement vs. position appears slightly modulated flat throughout the core of the nanoparticle which indicates the presence of strain,

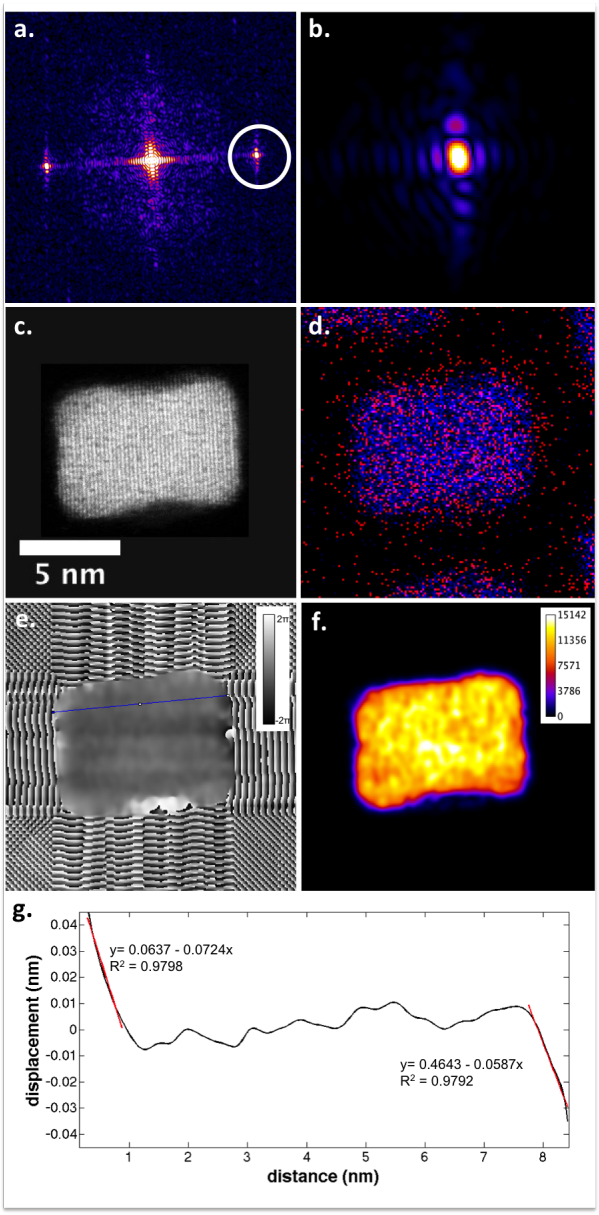

Figure 5.10: *2D strain analysis of an isolated $FePt@Fe_3O_4$ nanoparticle (a) calculated reciprocal space pattern of the masked STEM-HAADF image (b) re-centered Fourier filtered Bragg spot (c) masked STEM-HAADF image with a high threshold (blue) to distinguish shell (d) STEM-EDS map of an overlay of the Fe K-edge (red), O K-edge (green) and Pt K-edge (blue) elemental distributions (e) Real space geometric phase map of the local displacement of the lattice fringes with a cross section line indicating the core (blue) and the shell (red). Phase values run from $-\pi$(black) to π (white) (f) Real space local amplitude image (with intensity scale inset) (g) Cross section plot of the phase variation with phase slope change at the core indicated by the dashed lines.*

there are localised phase features might correspond to point defects. A clear phase ramp can be seen on both sides of the particle, whose direction across the scan from positive to negative indicates an outward expansive strain (Aranda et al 2010). Strains (displacement gradients) of -7.24% ($\pm$ 0.1%) and -5.87 % were extracted from the least squares regression fits of the negative and positive phase ramps, indicated in Fig.5.10e. Based on the known 2.00 AÅlattice spacing of the FePt core, this gives spacings for the Fe shell of 1.87 Åand 1.88 Å.

5.4.8 Nanocubes Characterisation Conclusion

In conclusion, an adapted synthetic method was used to fabricate core-shell $FePt@Fe_3O_4$ nanoparticles by thermal decomposition creating the shell by controlled addition of excess $Fe(CO)_5$ precursor. The investigations conducted within this section elucidated the crystallographic, compositional distribution, 3D morphology and distribution, and strain properties of FePt nanocubes (with a diameter of 8.41 $\pm$ 0.56 nm).

The resultant magnetic nanocube suspension was of narrow size distribution and highly monodisperse forming 2D self-assembled hexagonal arrays on the substrate, which is desirable for magnetic data storage applications. The XRD analysis of the FePt nanocubes showed the chemically-disordered fcc phase of FePt nanocubes. The 3D morphology and alignment of the nanocubes was successfully achieved using TEM tomography. The resultant 3D reconstructions were visualised and controlled ortho-slicing through the nanocube revealed that the nanocubes exhibited a typical 'edge-on' distribution which is favourable for applications in, for example, ultrahigh density data storage media.

The high-resolution lattice spacing information acquired from HRTEM images of the NPs enabled phase identification of two FePt nanocubes enclosed by (100) facets with (110) edge. The kinetic growth theory states that the formation of nanocubes involves the faster growth of the (111) facet in comparison to the (100) facet leading to the fast formation of (111) facets which effectively disappear. The most preferred crystallographic orientation of the nanocubes on the substrate when the nanocubes (111) facets are aligned parallel to the substrate and the (001) facets normal to the substrate. When these domains are aligned in cubic arrays they become more stable against external perturbations in comparison

to hexagonal arrays [Weddemann et al., 2010]. Therefore, this preferred [100] orientation of the nanocubes and inter-particle orientation (with a high degree of crystallographic alignment between the nanocubes) can be utilised as a 'building block' for 3D layering. These nanocubes are therefore an ideal candidate for data storage applications; where the alignment of the nanocubes enables a greater ease of magnetic manipulation in comparison to the nanosphere counterparts.

The STEM elemental distribution maps showed the localised distribution of Pt within the core region only and a more homogenous distribution of Fe, with a slightly higher contribution in the shell. The presence of a thin Fe shell on the FePt nanocube surface provides experimental evidence that the nanocubes are enclosed with high energy (100) facets which promote the segregation of the Fe to the surface of the nanocubes [Zhang et al., 2014]. Also, this core-shell alloy formation exhibits a non-stoichiometric composition, $Fe_{25}Pt_{75}$, which has been shown to systematically lead to nanoparticles with an Fe-depleted core and an Fe-rich shell [Soichiro Saita, 2005]. The monoatomic Fe layer could act as a site for catalysis and could also help to promote the full phase transformation of the nanocubes into the desired fct phase.

Strain maps of the strain displacement fields in individual FePt nanocubes were acquired using GPA mapping of the STEM lattice images. This showed a clear interface between the core and the shell, with a highly strained shell. The strain seen in the oxide shell appeared to be the result of the interfacial lattice mismatch which was quantified to be 24.25%. The lattice strain induced in the shell from the core makes these core-shell nanobubes an interesting candidate for further analysis and development for catalytic and data storage applications. Mapping the presence/absence of this strain is therefore useful in the development of these functional nanoparticle materials.

5.5 Nanocharacterisation of Nanospheres

Coating FePt nanoparticles with a biocompatible layer such as iron oxide is of practical interest because it can lower the cytotoxicity grade, and allows for direct bio-functionalization of the nanoparticle surface [Thanh and Green, 2010], [Lai et al., 2008], [Kalambur et al., 2005]. As described in Chapter 3, by use of excess Fe precursor in the fabrication of the FePt nanospheres an accumulation of unstable Fe occurred on the surface, resulting in iron oxide shell formation upon subsequent exposure of the particles to air. The thickness of the shell can be tuned by controlling the volume of iron precursor added in excess. Iron oxide can form three different oxides; FeO (wustite), Fe_3O_4 (magnetite), and Fe_2O_3 (maghemite or hematite) depending on the extent of oxidation, and requires analysis methods such as X-ray photoelectron spectroscopy to distinguish [Sahu and Bahadur, 2013]. Fe_3O_4 has a cubic inverse spinel structure and exhibits unique electric and magnetic properties based on the transfer of electrons between Fe^{2+} and Fe^{3+} in the octahedral sites [Rochelle Cornell, 2006]. $FePt@Fe_3O_4$ nanoparticles are of specific interest as potential candidates for biomedical applications such as, magnetic resonant imaging contrast agents, magnetic hyperthermia treatment of cancer and targeted drug delivery for therapeutic treatments [Kalambur et al., 2005]. These Fe_3O_4 shells are also of great use for protecting the nanoparticles during high temperature phase transformation which can typically result in the shell reducing to Fe to form a highly magnetic fct phase.

Despite the chemical synthetic procedures and resultant magnetic properties of these $FePt@Fe_3O_4$ nanoparticles being well documented [Zeng et al., 2003] [Sahu and Bahadur, 2013] [Wang et al., 2009] [Lai et al., 2008] there have been very few investigations into the core-shell interface which can be directly impacted by morphology and strain. In particular, understanding the strain present in core-shell nanoparticles is beneficial for application to mass transport devices [Pratt et al., 2014] and also plays an important role in catalytic reduction reactions [Gan et al., 2012]. Typically research into these core-shell nanoparticles has focussed on magnetic studies of the nanoparticle identifying exchange coupling effects between a magnetically ‘hard’ fct FePt core and magnetically ’soft’ Fe_3O_4 shell : [Zhang et al., 2014] causing a smooth co-operative magnetic switching transition at the core-shell interface. Therefore the research focus in this sec-

tion is to conduct a comprehensive analysis of the nanoparticles.

Nevertheless interfacial strain in core-shell nanoparticles has also been mapped and correlated with defects and also an anomalous magnetic behaviour [Wetterskog, 2013]. A recent study involved the investigation of strain fields within the shell of $Fe@Fe_3O_4$ nanoparticles using GPA analysis [Pratt et al., 2014]. These authors found that strain gradients arose from confined oxide domain formation within the shell, which enhanced ionic movement. Understanding the strain present in the oxide shell is therefore beneficial for application of core shell nanoparticles to mass transport devices [Pratt et al., 2014] and also plays an important role in catalytic reduction reactions [Gan et al., 2012]. The GPA approach opens an opportunity to investigate the strain fields within a whole nanoparticle and correlate them with their compositional morphology.

5.5.1 Nanosphere Array Formation and Size Distribution

From the TEM observations, the $FePt@Fe_3O_4$ nanoparticles formed 2D self-assembled hexagonal arrays on the substrate, as seen in Fig.5.11a and Fig.5.11b. This array formation is specifically ascribed to the high monodisperity of the sample and the surfactant separation between the nanoparticles. The shape of the nanoparticles was defined as not completely speherial therefore Ferret size analysis was conducted. The average size distribution of the $FePt@Fe_3O_4$ nanoparticles (from the TEM image analysis of the Feret diameter of 309 $FePt@Fe_3O_4$ nanoparticles), is 8.71$\pm$0.44 nm as shown in the size distribution histogram inset in Fig.5.11. It can be seen that there is a clear minimum particle separation distance of 1.7 nm, which corresponds to a compacted surfactant layer with the surfactant tails interpenetrating. The fully-extended lengths of the OA and OLA surfactants are 2.08 and 2.06 nm, respectively. The contrast between the core and shell in the HRTEM image in Fig.5.11c, is due to the different electron penetration efficiencies between the 'heavy' FePt core (high Z) and the 'lighter' Fe_3O_4 shell (low Z). The single crystal core has a lattice spacing of 1.94 Å which is characteristic of the (100) lattice planes in the chemically disordered fcc FePt phase. The phase of the Fe_3O_4 shell was however difficult to uniquely distinguish.

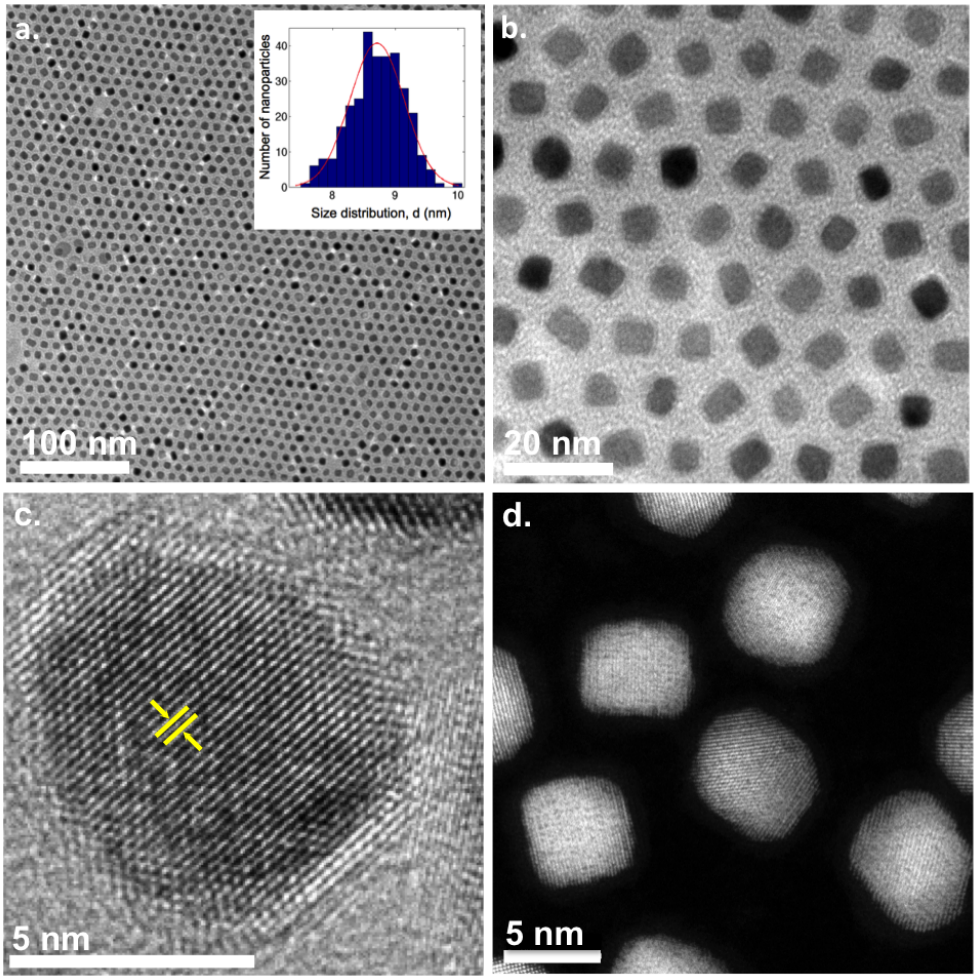

Figure 5.11: *$FePt@Fe_3O_4$ nanoparticle TEM analysis (a) Low magnification and (b) high magnification TEM image of $FePt@Fe_3O_4$ nanoparticles showing a 2D hexagonal array with a size distribution histogram inset (average diameter 8.7 $\pm$ 0.4 nm) (c) HRTEM image of an individual $FePt@Fe_3O_4$ nanoparticle with the inter-planar lattice spacings of the FePt core and the Fe oxide shell denoted in yellow and red respectively (d) STEM-HAADF image (analysed further by STEM-EDS in Fig.5.16 a-d).*

5.5.2 Powder X-ray Diffraction of Nanospheres

The observed XRD lines of the$FePt@Fe_3O_4$ core-shell nanoparticles match closely to the reference pattern Platinum Ferroan, $Fe_{25}Pt_{75}$, (JPCDS-00-029-0717), a = 3.871 Åas indicated by the black reference pattern in Fig.5.12. Powder XRD pattern analysis of the peaks revealed the characteristic fcc planes with d-spacings;d_{111} = 2.2239 Å, d_{200} = 1.937 Å, and d_{220} = 1.369 Å, representative of a chemically-disordered fcc phase of FePt nanoparticles. Additional XRD peaks are ascribed

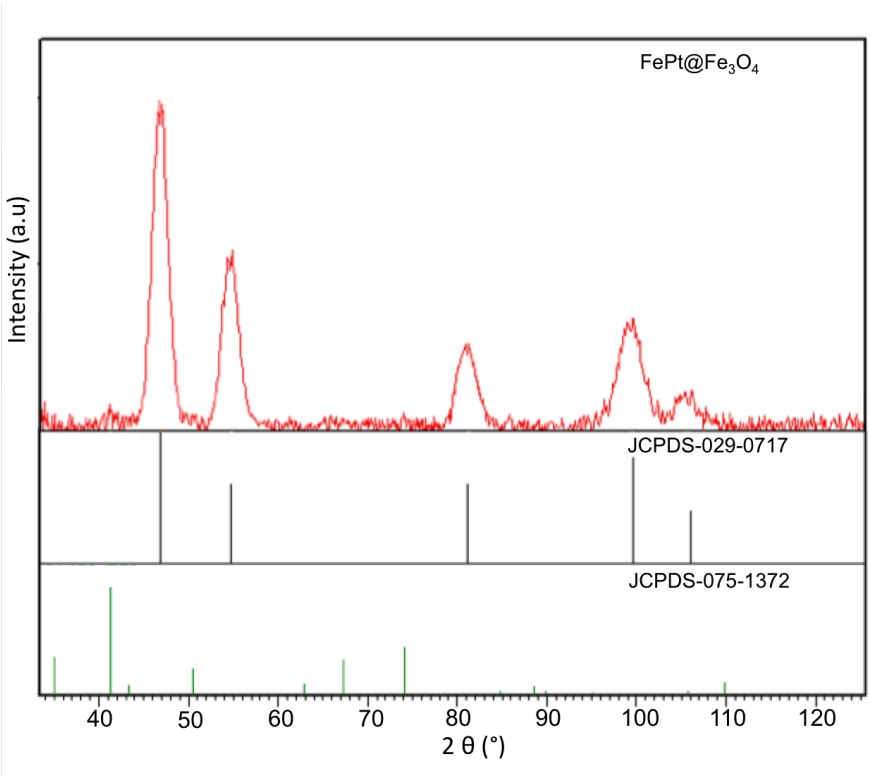

Figure 5.12: *Powder XRD of $FePt@Fe_3O_4$ core-shell nanoparticles with corresponding reference pattern Pt Ferroan (JPCDS 029-0717) as indicated by the green reference pattern Fe_3O_4 (JPCDS-00-075-1732).*

to the contribution from the Fe_3O_4, shell, as indicated by the reference pattern magnetite, (JCPDS-00-075-1372). The lack of prominent peaks from the Fe oxide is expected to be due to the epitaxial growth of the shell with the core, and the comparatively lower volume of Fe oxide. The average crystallite size was calculated, using the Scherrer equation, for each peaks and was determined as 8.9 nm which corresponds well with the nanocube diameter determined by TEM analysis. The composition of the FePt reference match corresponds reasonably to the ICP-OES results; where atomic percent of Fe is 31% and atomic percent of Pt is 69%.XRD analysis of the $FePt@Fe_3O_4$core-shell nanoparticles.

5.5.3 X-ray Photoelectron Spectroscopy

The deconvoluted XPS spectra of Fe 2p, Pt 4f, and O 1s core level spectra are shown in Fig.5.13 a,b and c respectively. The Fe 2p spectrum in Fig.5.13a is

composed of two peaks at Fe $2p_{3/2}$ and Fe $2p_{1/2}$ at a binding energy (BE) of 713.5 eV and 731.6 eV, respectively.

The Fe 2p spectrum in Fig.5.13a was deconvoluted into five different Fe species, including Fe^0, Fe^{2+}, Fe^{3+} high-binding energy surface structures and satellite peaks using a Gaussian-Lorentzian mixed function by XPSPEAK41 software. The $2p_{3/2}$ peak was deconvoluted into three peaks; Fe^0 at a BE of 708.0 eV, Fe^{2+} at a BE of 709.6 eV, and Fe^{3+} at a BE of 711.3 eV with a satellite peak at 718.0 eV. The $2p_{1/2}$ peak is deconvoluted into Fe0 at a BE of 721.6 eV, Fe^{2+} at BE 723.2 eV, and Fe^{3+} at a BE of 725.2 eV with a satellite peak at 731.6 eV. The stoichiometric proportion values of Fe^0, Fe^{2+}, Fe^{3+} were calculated, based on the XPS analysis, as Fe^{3+} = 7%, Fe^{2+} =52%, and Fe^{3+} = 41%. Theoretically, the stoichiometric bulk proportion of Fe^{2+} in Fe_2O_3 is 0%, Fe_3O_4 is 33 % and FeO is 100%, while the proportion of Fe^{3+} in Fe_2O_3 is 100%, Fe_3O_4 is 67 % and FeO is 0%. While there is insufficient information to assign the oxide fractions categorically, the simultaneous presence of both extremes is considered less likely than the mixed oxide because they would interconvert. If all the Fe^{3+} were in Fe_3O_4. there would be a balance of 34% of the oxide as FeO (wustite).

The Pt 4f spectrum in Fig.5.13b is composed of two peaks indicating spin-orbit split doublet of Pt into $4f_{5/2}$ and $4f_{7/2}$ at a BE of 70.72 eV and 74.08 eV respectively, with a separation in BE of 3.5 eV, which is typical for metallic FePt. The O 1s signal in Fig.5.13c is composed of two peaks at lower and intermediate BE's at 529.5 eV and 531.7eV, as a result of the iron oxide shell. The XPS results substantiate the TEM and XRD data, and confirm the phase of the shell as Fe_3O_4.

5.5.4 3D Morphology of Core-Shell Nanoparticles

The morphology and allignment of a cluster of nine $FePt@Fe_3O_4$ nanospheres was investigated by TEM tomography. The resultant 3D Hitachi reconstruction of the nine nanoparticles is shown in Fig.5.14a-c at different y ortho-slice positions (slicing through the y-axis of the reconstruction). The lower three nanoparticles (indicated by the box in Fig.5.14a) were examined more closesly in Fig.5.14d-f demonstrating the core-shell morphology; where the Fe_3O_4 shell is distinguished from the FePt core by its lower contrast due to core being more electron-dense. An Avizo reconstruction was built in order to visualise and segment the cluster

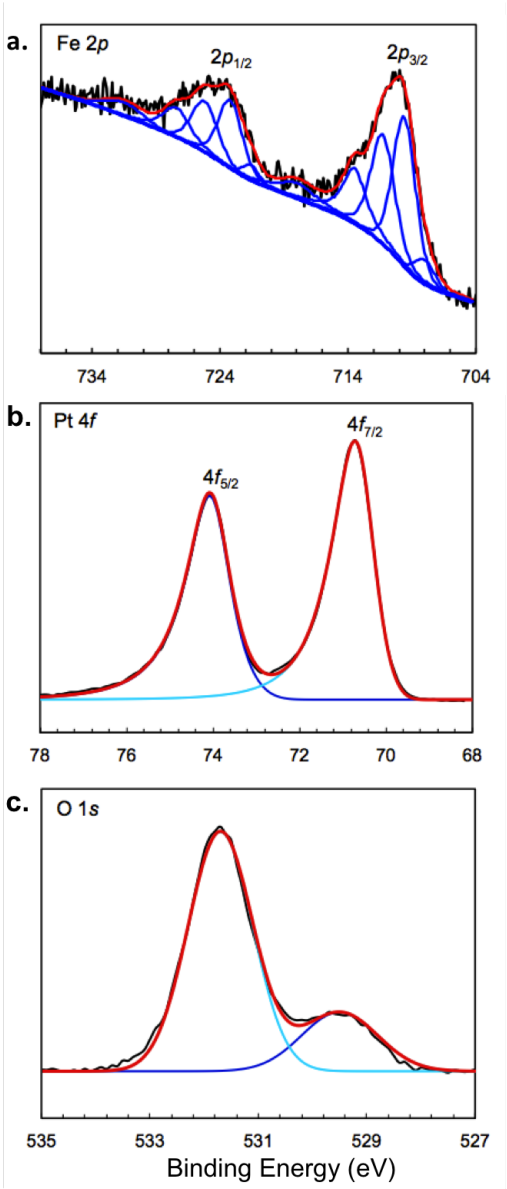

Figure 5.13: *Deconvoluted X-ray photoelectron spectroscopy spectra (a) Fe 2p spectrum, (b) Pt 4f spectrum and, (c) O 1s spectrum. Light and dark blue curves are the individual peaks, whose sum gives the red curve fitting the data (black).*

into the nine nanoparticls from the raw TEM reconstructed data. The core can be differentially segmented from the shell as illustrated in Fig. 5.14a, where the FePt core is shown in yellow and the Fe_3O_4 shell in grey. An ortho-slice through the centre of the cluster in is shown in Figure 5b where the FePt core is represented in light blue and the Fe_3O_4 shell in dark blue for clarity. The core can be differentially segmented from the shell as illustrated in Fig.5.14b, where the external FePt core

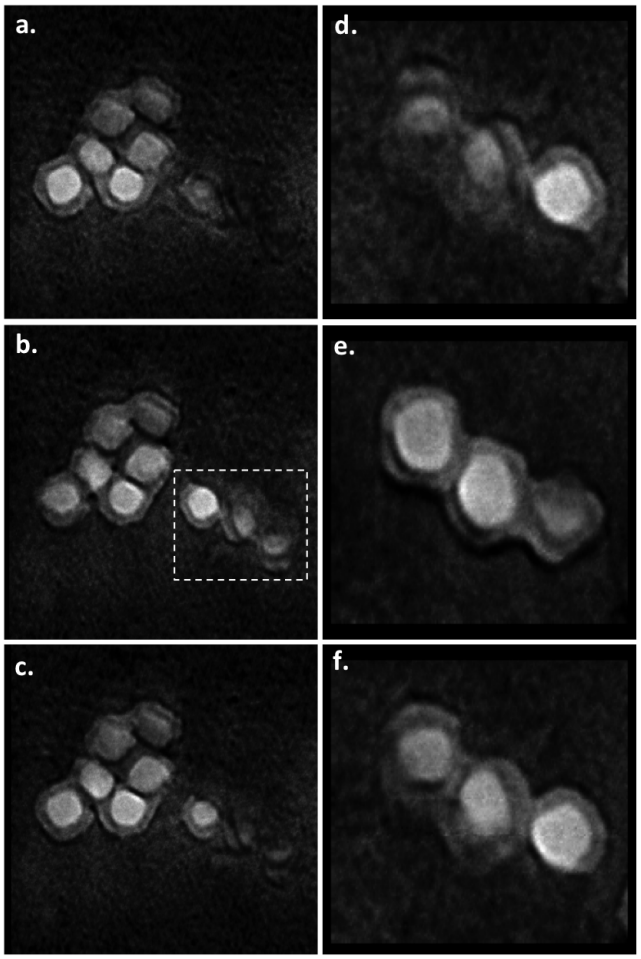

Figure 5.14: *3D Hitachi reconstruction of nine $FePt@Fe_3O_4$ nanoparticles at ortho-slice positions; (a) y = 15, (b) y = 5, (c) y = 10, and corresponding selected zoom of three $FePt@Fe_3O_4$ NPs (indicated by the box at ortho-slice positions; (d) y = 0, (e) y = -15, and (f) y = -5.*

is represented in yellow and the external Fe_3O_4 shell in grey.

5.5.5 Elemental Distribution of Core-Shell Nanoparticles

Elemental distribution maps were acquired of the $FePt@Fe_3O_4$ nanoparticles using STEM-EDS mapping. The corresponding STEM-HAADF image is shown in Fig.5.11d.) The O K-edge elemental contribution (represented in green) in Fig.5.16a is homogenously distributed throughout both the core and the shell of the nanoparticle and is and is clearly higher than the typical background (present

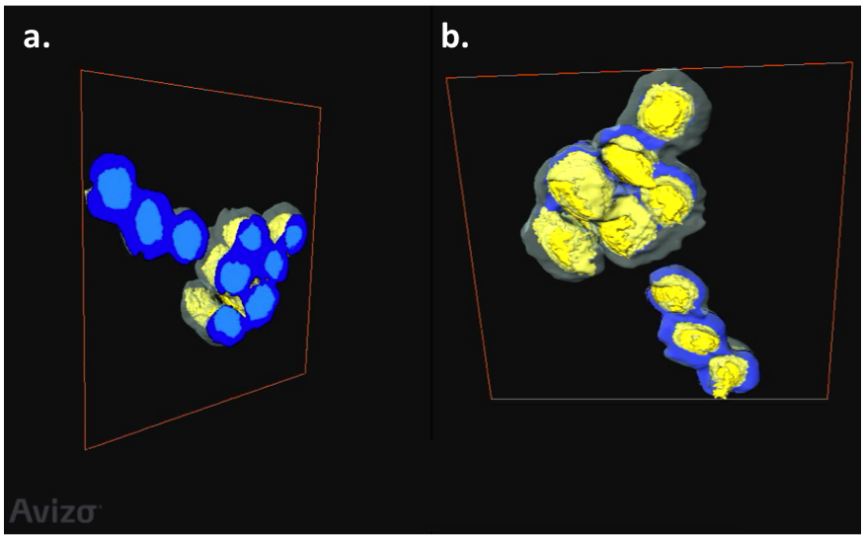

Figure 5.15: *Avizo 3D reconstruction (a) snap shot of the 3D reconstruction where the FePt core (yellow) is enclosed by a Fe_3O_4 shell (grey) (b) ortho-slice through the centre of the cluster showing a clear segregation of the FePt core (light blue) and the Fe_3O_4 shell (dark blue).*

from surface contamination). The Fe elemental contribution (represented in red) in Fig.5.16b is homogeneously distributed throughout the core and shell, with a more prominent contribution from the shell. The Pt M-edge elemental contribution (represented in blue) in Fig.5.16c is distributed only in the core. An overlay of the three elemental maps is shown in Fig.5.11d and confirms the presence of the Fe oxide shell. The line profiles across of the O K-edge, Fe K-edge and, Pt M-edge are shown in Fig.5.11e. The integration regions are shown in Fig.5.11a-d. The intensity profiles quantitatively demonstrate that the higher Pt signal is localised in the core while the Fe and O contributions extend beyond the core into the shell.

5.5.6 2D Strain Analysis Core-Shell Nanoparticles

5.17a. A single Bragg spot was selected, as circled in Fig.5.17a (with a radius cut off of 35 pixels), and re-centered in Fig.5.17b. The selected peak is a (200) peak of the FePt lattice, so it is the distortions from the 100 planes that are imaged by GPA. The region of reciprocal space surrounding this selected Bragg spot, sufficiently large to include the interference from the overlapping Bragg peaks of the Fe oxide shell, was Fourier transformed into a real space complex image; the

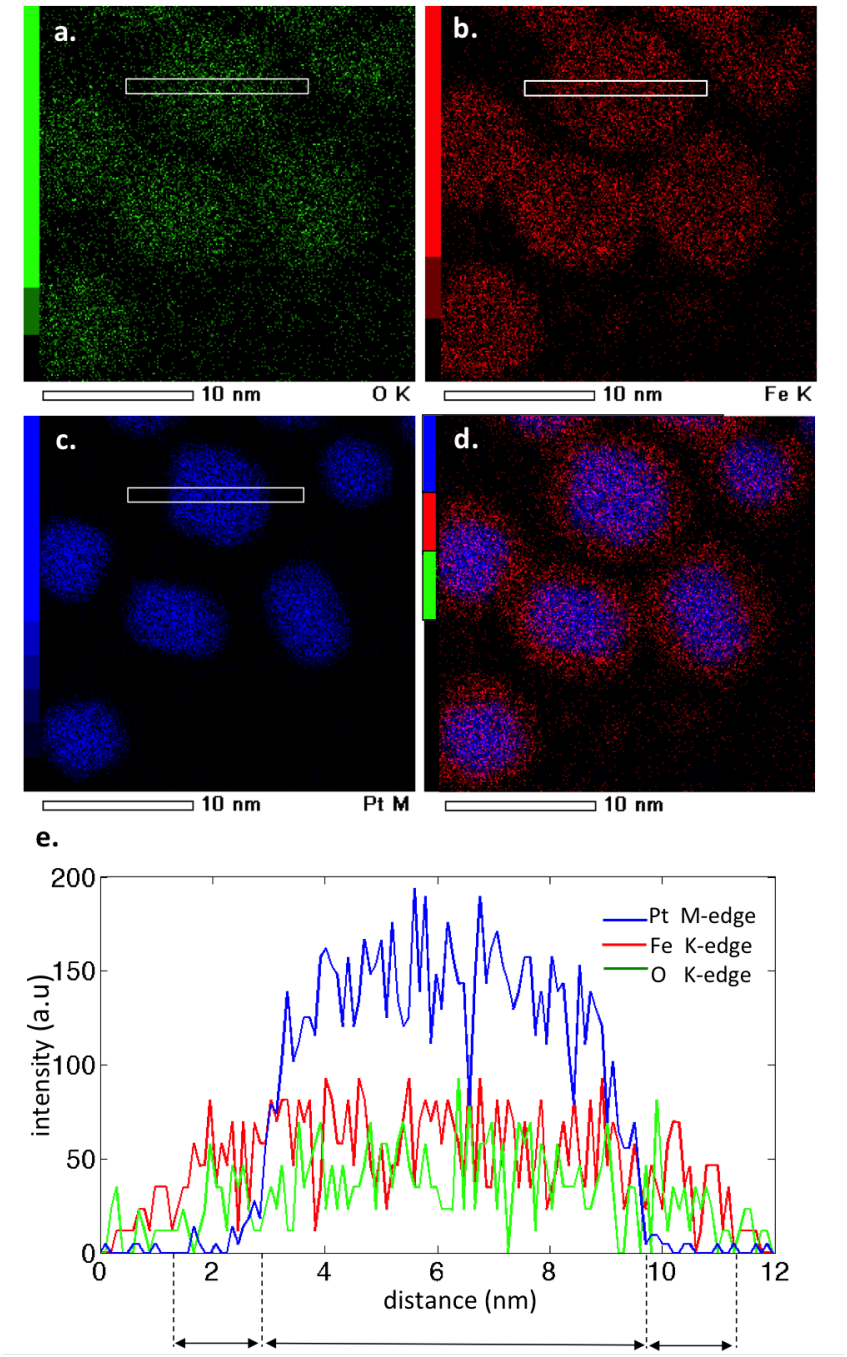

Figure 5.16: *STEM-EDS elemental maps of $FePt@Fe_3O_4$ core-shell nanoparticles with rectangular line scan indicated (corresponding STEM-HAADF image in Fig.5.11d.) (a) O K-edge (b) Fe K-edge (c) Pt K-edge and, (d) elemental overlay.*

geometric phase is shown in Fig.5.17e and the image amplitude in Fig.5.17f. The STEM-EDS elemental map of the same crystal is reproduced in Fig.5.17d show-

ing the approximate location of the core shell interface. The geometric phase image in Fig.5.17e, a map of the 2D strain projection, represents the displacement of atoms from the perfect crystal lattice, ranging from -π (white) to + π (black), shows the strain along the (200) direction. The full phase range of 2 π corresponds to a displacement of a single lattice spacing. Note that the phase becomes meaningless in the regions outside the nanoparticle, where the amplitude of the complex density drops to zero.

The core and shell can be clearly distinguished in Fig.5.17e by the phase shift enclosing the shell (dark region). There are slight deviations from the median value within the core which might be due to defects, possibly dislocations, in the FePt crystal structure. Regions of high strain gradients and phase wraps surrounding the core of the nanoparticle are due to the strains present in the Fe_3O_4 shell, which is seen to be less homogeneous than the core. The local amplitude image in Fig.5.17f shows this intensity variation in the selected (200) plane direction, with an intensity scale ranging from yellow (high intensity) to dark blue (low intensity).

In order to examine the strain decay behaviour at the core-shell interface the cross section line in Fig.5.17e, covering the core (blue) and the shell (red) regions, is plotted in Fig.5.17g. The linear phase ramps seen on the two sides of Fig.5.17g represent the difference in lattice constant between the FePt, and the Fe_3O_4. The location of the core-shell interface is indicated by the dashed lines with the shell thickness being 1.39 nm on the left and 1.54 nm on the right, corresponding to an average shell thickness of 1.5 nm. A clear phase ramp can be seen on both sides of the particle, whose direction across the scan from negative to positive indicates an inward compressive strain (Aranda et al 2010). Strains (displacement gradients) of 27% and 19% ($\pm$ 4%) were extracted from the least squares regression fits of the positive and negative phase ramps, indicated in Fig.5.17e. Based on the known 1.94 Å lattice spacing of the FePt core, this gives spacings for the Fe_3O_4 shell of 2.46 Åand 2.31 Å.

5.5.7 Core-Shell Nanoparitcle Characterisation Conclusion

In conclusion, an adapted synthetic method was used to fabricate core-shell $FePt@Fe_3O_4$ nanoparticles by thermal decomposition creating the shell by con-

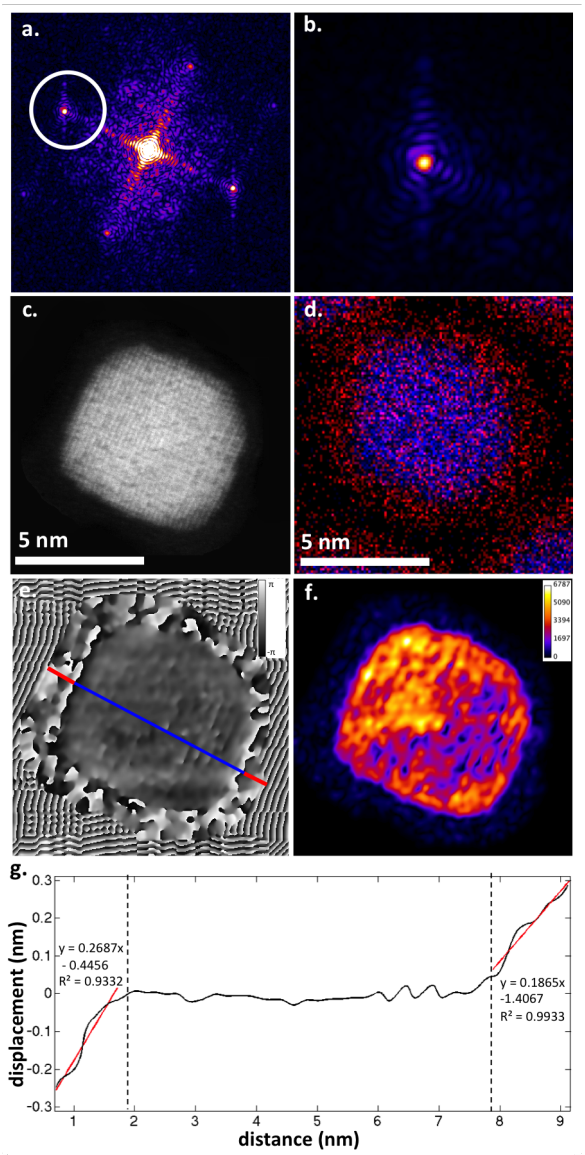

Figure 5.17: *2D strain analysis of an isolated $FePt@Fe_3O_4$ nanoparticle (a) calculated reciprocal space pattern of the masked STEM-HAADF image (b) re-centered Fourier filtered Bragg spot (c) masked STEM-HAADF image with a high threshold (blue) to distinguish shell (d) STEM-EDS map of an overlay of the Fe K-edge (red), O K-edge (green) and Pt K-edge (blue) elemental distributions (e) Real space geometric phase map of the local displacement of the lattice fringes with a cross section line indicating the core (blue) and the shell (red) Phase values run from $-\pi$(black) to π (white) (f) Real space local amplitude image (with intensity scale inset) (g) Cross section plot of the phase variation with phase slope change at the core indicated by the dashed lines.*

trolled addition of excess $Fe(CO)_5$ precursor. The investigations conducted within this section elucidated the crystallographic, compositional distribution, 3D mor-

phology and distribution, and strain properties of $FePt@Fe_3O_4$ nanospheres (with a diameter of 8.71 $\pm$ 0.44 nm).

The resultant magnetic nanosphere suspension was of narrow size distribution and highly monodisperse forming 2D self-assembled hexagonal arrays on the substrate, which is desirable for magnetic data storage applications. The high-resolution lattice spacing information acquired from HRTEM images of the NPs enabled phase identification of both the core (chemically disordered fcc FePt phase) and the shell (Fe3O4 phase) and the XRD showed a corresponding mixed phase pattern. Additionally, XPS surface analysis of the NPs distinguished the phase of the oxide as Fe_3O_4 (magnetite) rather than Fe_2O_3 (maghaemite). The STEM elemental distribution maps showed the localised distribution of Pt within the core region only and a more homogenous distribution of Fe, with a slightly higher contribution in the shell. The 3D reconstructions and visualisations from the TEM tomography data show a distinct segmentation of the FePt core from the Fe_3O_4 shell.

Strain maps of the strain displacement fields in individual $FePt@Fe_3O_4$ nanoparticles were acquired using GPA mapping of the STEM lattice images. This showed a clear interface between the core and the shell, with a highly strained shell. The strain seen in the oxide shell appeared to be the result of the interfacial lattice mismatch which was quantified to be 23%. The lattice strain induced in the shell by the core is attractive for many potential applications for example in, mass transport devices [Pratt et al., 2014] in catalytic[Gan et al., 2012] and nanoscale multiferroic applications. Mapping the presence/absence of this strain is therefore useful in the development of these functional nanoparticles materials.

5.6 Nanocharacterisation of FePt Octapods

Bimetallic alloy nanoparticles can act as catalytically active nano-magnets used for the oxygen reduction reaction (ORR) for the application in fuel cell technologies. An FePt nanoparticle is a CO tolerant alloy and is more economical than the pure Pt counterpart. Also, the FePt nanoparticles have a higher electrocatalytic activity toward ORR in comparison to Pt nanoparticles. Additionally, the surface energy of the high index facets enclosing the ‘pods’s can results in an enhanced

electrochemical activity of the FePt octapods in comparison to nanospheres and nanocubes. Catalysis is sensitive to shape and the eight corner 'pods' on the octapods creates a high surface to volume ratio increasing the number of active sites on the catalyst surface and resulting in a better tolerance to CO than nanocubes. Also as the octopod is rich in the stepped edges, this is preferred for active sites for oxygen reduction reactions. The shape and morphology of octapods therefore enhances electrocatalytic activity making them ideal candidates for catalytic applications such as methanol oxidation [Wu et al., 2012]. Determining the distribution of the octapods on a substrate can provide an idea of the octapod distribution when prepared for catalysis which typically involves coating a surface with octapods.

5.6.1 Octapod Array Formation and Size Distribution

From the TEM observations, the FePt octapods formed a similar array formation to the nanocubes (but less ordered), as seen in Fig.5.18a and Fig.5.18b. In the HRTEM image, Fig.5.18c stepped atomic edges were observed at the corners and sides of the 'pod's. The variation in contrast at the edges of the octapod—observed in the HRTEM and STEM-HAADF lattice images of the octapods in Fig.5.18c and Fig.5.18d respectively—are ascribed to a slight assymmetry in the 'pod' formation. Also, the presence of un-formed octapods in the form of irregular shaped nanocubes in Fig.5.18a, Fig.5.18b, and Fig.5.18d, can be ascribed to the initial nanocube 'seed' in the formation of the octapods. This could be ascribed to a variation in the nucleation rate for some octapods. The average size distribution of the octapods was too irregular to plot using the typical histogram size distribution analysis. Therefore the size distribution was calculated through manual selection and data collecting from analysis of 160 octapods. These octapods were identified to exhibit an average diameter of 17.0 nm in length. Notably, although the shape of the FePt nanoparticles are referred to as octapods from this point onwards some of the shapes formed could also be referred to as distorted nanocubes post octopod formation (as describred above).

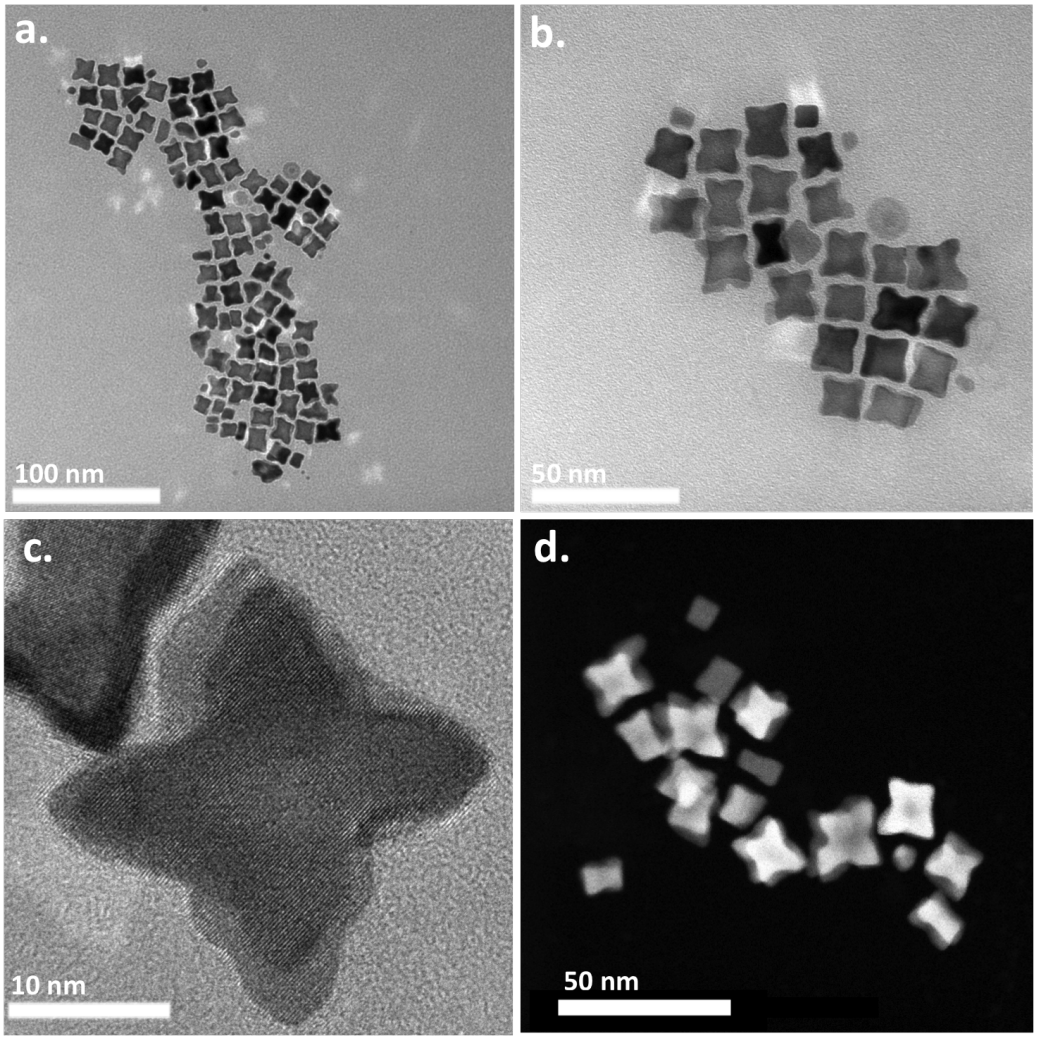

Figure 5.18: *Octapod TEM analysis (a) Low magnification and (b) high magnification TEM image of FePt octapods (c) HRTEM image of an individual FePt octapod (d) STEM-HAADF image (analysed further by STEM-EDS in Fig.5.22a-d).*

5.6.2 Powder X-ray Diffraction of Octapods

The observed XRD lines of the FePt octapods match closely to the reference pattern Platinum Ferroan, $Fe_{25}Pt_{75}$, (JPCDS-00-001-1194, a = 3.871 Å) as indicated by the black reference pattern in Fig.5.12. The slight offset between the reference pattern and the experimental pattern can be ascribed to the comparatively higher Fe content in the alloy sample resulting in the peak angle position being slightly lower than that of the given reference pattern. Powder XRD pattern analysis of the peaks revealed the characteristic fcc planes with d-spacings; d_{111} = 2.239

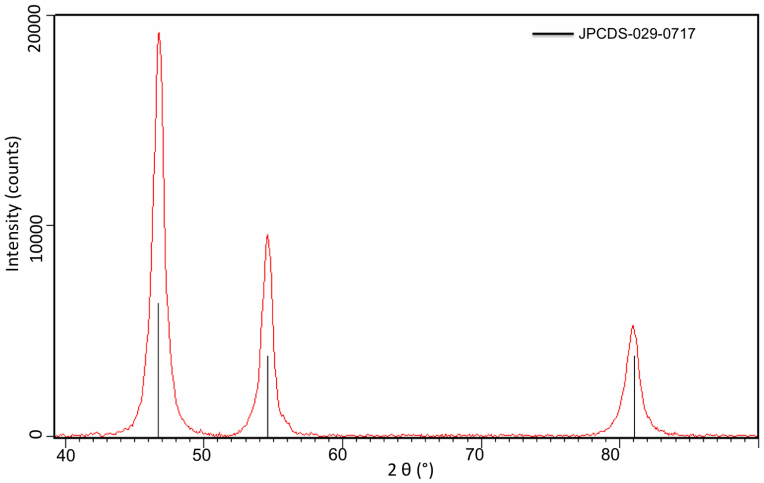

Figure 5.19: *Powder XRD of FePt octapods with corresponding reference pattern Pt syn, (JCDS-001-1194).*

Å, d_{200} = 1.937 Å, and d_{220} = 1.369 Å, representative of a chemically-disordered fcc phase of FePt nanoparticles. The average crystallite size was calculated, using the Scherrer equation, and was determined as 13 nm which is comparatively lower than the crystallite size measured using Scherrer analysis, and is expected to be due to the irregularity of the dimensions of the octapods.

5.6.3 3D Morphology of Octapods

The morphology and alignment of both an isolated octapod and a cluster of four octapods were investigated by TEM tomography. The resultant 3D Hitachi reconstruction of the isolated octapod is shown in Fig.5.20a-c at different y ortho-slice positions (slicing through the y-axis of the reconstruction). The ortho-slicing revealed the presence of the 8 corner 'pod's of the octapod. Cleaner reconstructions of the octapods were achieved from the analysis of a cluster of octapods and the ortho-slices through the y-axis are shown in Fig.5.20d-f.

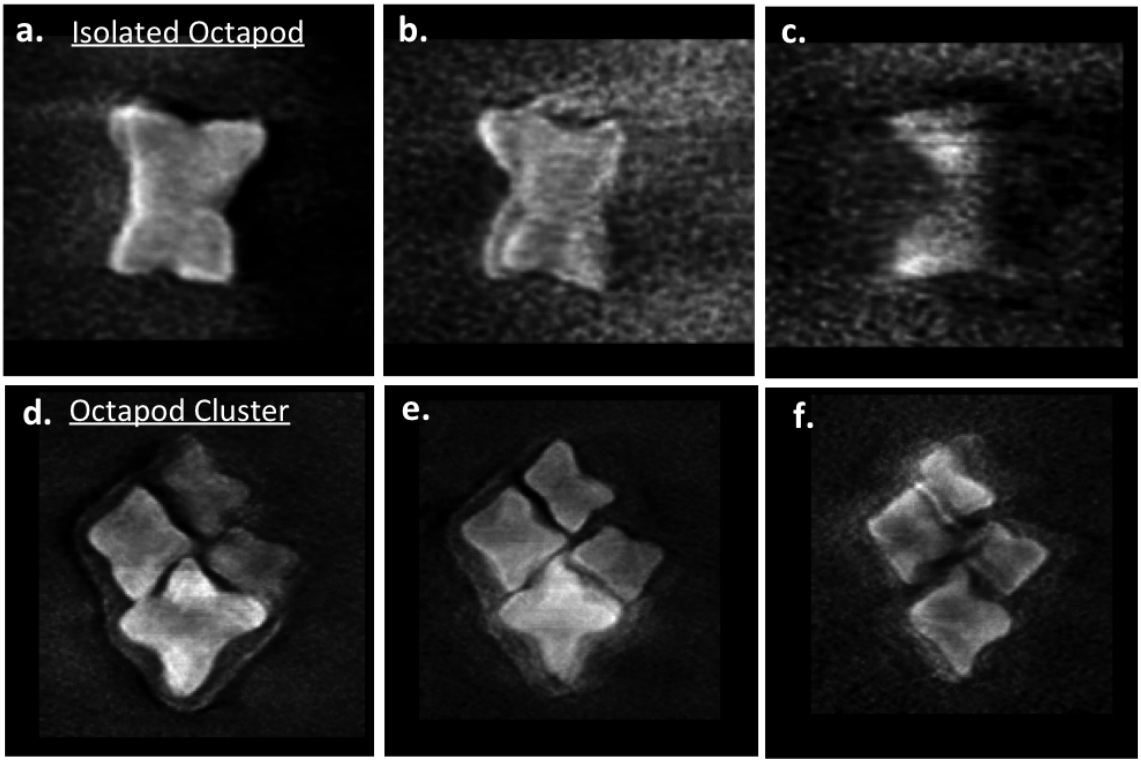

Figure 5.20: *Ortho-slices through a 3D Hitachi reconstruction of an isolated FePt octapod at different y positions (a) y = -24 (b) y = 10 (c) y = 51 and cluster of four FePt octapods at different y positions y = -30 (d) y = -20 (e) y = +25.*

5.6.4 Individual Octapod Analysis: Octapod 1 and Octapod 2

From analysis of the TEM images of the octapods it was observed that the orientation of the octapods on the substrate was most commonly orientated with the tetragonal block 'side-on' on the substrate. Least commonly the octapods were orientated with the tetragonal block 'edge-on'. In this section two octapods that represent these different orientations on the substrate (labelled as Octapod 1 and Octapod 2 for clarity) were characterised for complementary crystallographic, elemental and strain mapping analysis. Octapod 1 as seen 'side-on' in the top right of the STEM-HAADF lattice image in Fig.5.21a is of dimension 17.57 length x 11.2 nm width. Octapod 2 as seen 'edge-on' in the middle of the STEM-HAADF lattice image in Fig.5.21b is of dimension 14.7 nm length x 12.16 nm width.

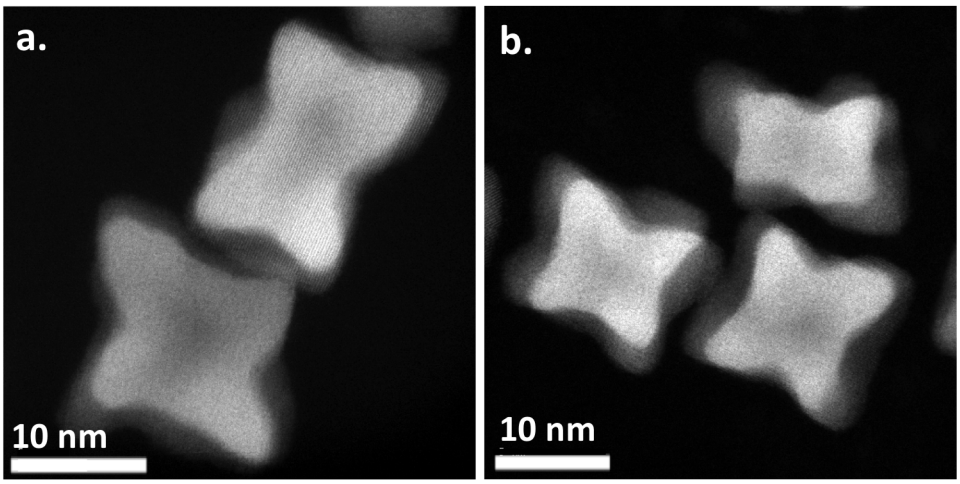

Figure 5.21: *STEM-high angle annular diffraction images of different Octapod clusters (a) Octapod 1; top right octapod (17.57 nm length x 11.2 nm width) and (b) Octapod 2; middle octapod (14.7 nm length x 12.16 nm width).*

5.6.5 Octapod Phase Determination

The crystallographic d-spacings were extracted from the 'pods' and the 'nanocube' region of the individual FePt Octapod 1 (Fig.5.21a) giving values of 0.201 nm. A similar result was found for the d-spacing of Octapod 2 (0.200 nm) in Fig.5.21b. This d-spacing did not appear to change on analysing the 'pods' and the 'nanocube' of the octapods indicating that the whole octapod was of the same crystallographic orientation with the (100) facet being the most favoured orientation to the substrate. This finding is in contrast to the findings of Chou et al who identified that the 'pod's of the octapods consisted of (111) facets d_{111} = 0.2246 nm [Chou et al., 2009]. However, notably this was identified at a different crystallographic orientations using an HRTEM equipped with a single tilt axis stage enabling analysis at 25°(by using an HRTEM equipped with a single tilt stage enabling analysis). Therefore, further HRTEM analysis, at a different tilt angles, would be required in order to accurately determine the crystallographic lattice spacing's of the octapods. (Notably the HRTEM used in this analysis is not equipped with a tilt stage).

5.6.6 Elemental Distribution of Octapods 1 and Octapod 2

Elemental maps were acquired of Octapod 1 and Octapod 2 with the corresponding STEM-HAADF in Fig.5.21a and Fig.5.21b, respectively. The O K-edge, Fe-K edge, and Pt M-edge of both octapods were mapped in Fig.5.22a-b and Fig.5.23a-b, respectively. The elemental overlay of these maps is shown in Fig.5.22d and Fig.5.23d. In both Fig.5.22a and Fig.5.23a the O K-edge elemental contribution (represented in green) is low and is mainly due to a slight unavoidable surface contamination of the nanoparticle and substrate during analysis. The Fe K-edge elemental contribution (represented in red) is homogenously distributed throughout the octapods, and a comparatively lower Fe contribution on the 'edge-on' Octapod 1 in Fig.5.22a in comparison to the 'side-on' octapods in Fig.5.23b. The Pt M-edge elemental contribution (represented in blue) in Fig.5.22c and Fig.5.23c is homogenously distributed throughout the octapod and is of the highest intensity contribution in both overlay maps in comparison to the Fe and O intensity contributions.

5.6.7 2D Strain Analysis of Octapod 1

5.24a. A single Bragg spot was selected, as circled in Fig.5.24a (with a radius cut off of 20 pixels), and re-centered in Fig.5.24b. The selected peak is a (200) peak of the FePt lattice, so it is the distortions from the 100 planes that are imaged by GPA. The region of reciprocal space surrounding this selected Bragg spot, sufficiently large to include the interference from the overlapping Bragg peaks of the Fe oxide shell, was Fourier transformed into a real space complex image; the geometric phase is shown in Fig.5.24e and the image amplitude in Fig.5.24f. The STEM-EDS elemental map of the same crystal is reproduced in Fig.5.24d showing the approximate location of the core shell interface. The geometric phase image in Fig.5.24e, a map of the 2D strain projection, represents the displacement of atoms from the perfect crystal lattice, ranging from -π (white) to +π (black), shows the strain along the (200) direction. The full phase range of 2 π corresponds to a displacement of a single lattice spacing. Note that the phase becomes meaningless in the regions outside the nanoparticle, where the amplitude of the complex density drops to zero.

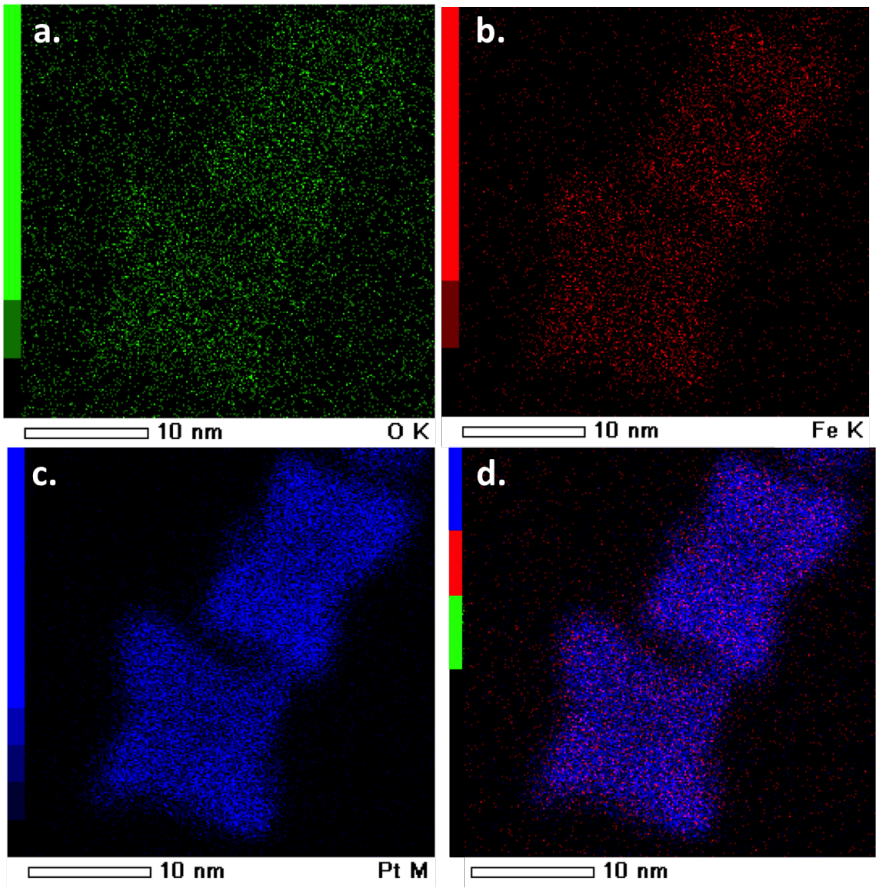

Figure 5.22: *STEM-energy dispersive spectroscopy compositional mapping of two octapods (with Ocatpod 1) showing the periodical arrangements of (a) O K-edge (b) Fe K-edge (c) Pt M-edge and (d) elemental overlay.*

Qualitative analysis, of the geometric phase image of the (200) plane in Fig.5.24e from Octapod 1, revealed very little phase modulation along the (200) direction whilst at the edges the modulations were high especially at the corners of the 'pod's. In Fig.5.24b the re-centred (200) Bragg peak has very diffuse interference fringes which is the indicative of a strained crystal this is apparent from both qualitative and quantitative analysis of the geometric phase image. Quantitative analysis of the phase in phase Fig.5.24g along the (200) direction there is strong linear phase gradient. To examine the strain decay behaviour of the octapod the phase along the displacement map of the FePt octapod in Fig.5.17e from the cross section line is plotted in Fig.5.17g. The lack of linear phase ramps in Fig.5.17g indicate that the octapod is of the same FePt crystal phase and that there is no presence of any large phase ramps due to a shell on the surface (as

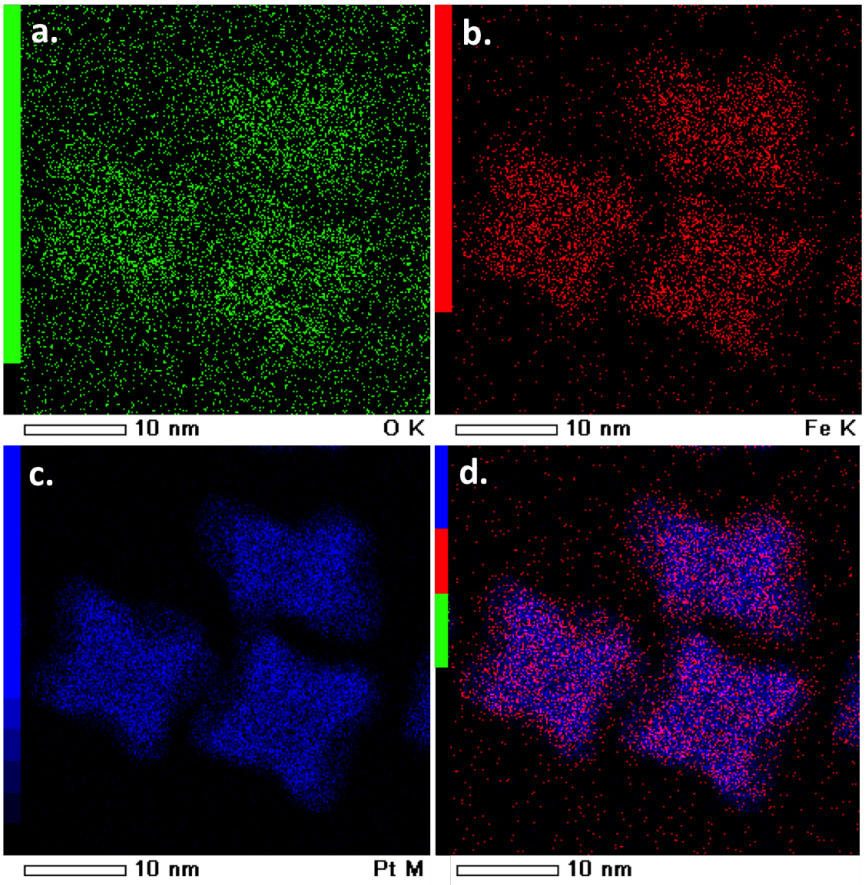

Figure 5.23: *STEM-EDS compositional maps of an octapod cluster (with Octapod 2), showing the periodical arrangements of (a) O K-edge (b) Fe K-edge (c) Pt M-edge and (d) Elemental overlay.*

observed for the nanocubes and the core-shell nanoparticles).

However, there is an indication of slight phase ramp across the scan from − ve to +ve indicating a very weak inward compressive strain which correlates with a strain deviation of 9.7 % (as calculated from the gradient of the phase ramps). This variation indicates highly strained regions which are favourable for applications of the octopods as nanocatalytic devices.

5.6.8 Octapods Characterisation Conclusion

In conclusion, an adapted synthetic method was used to fabricate FePt octapods by thermal decomposition. The investigations conducted within this section elu-

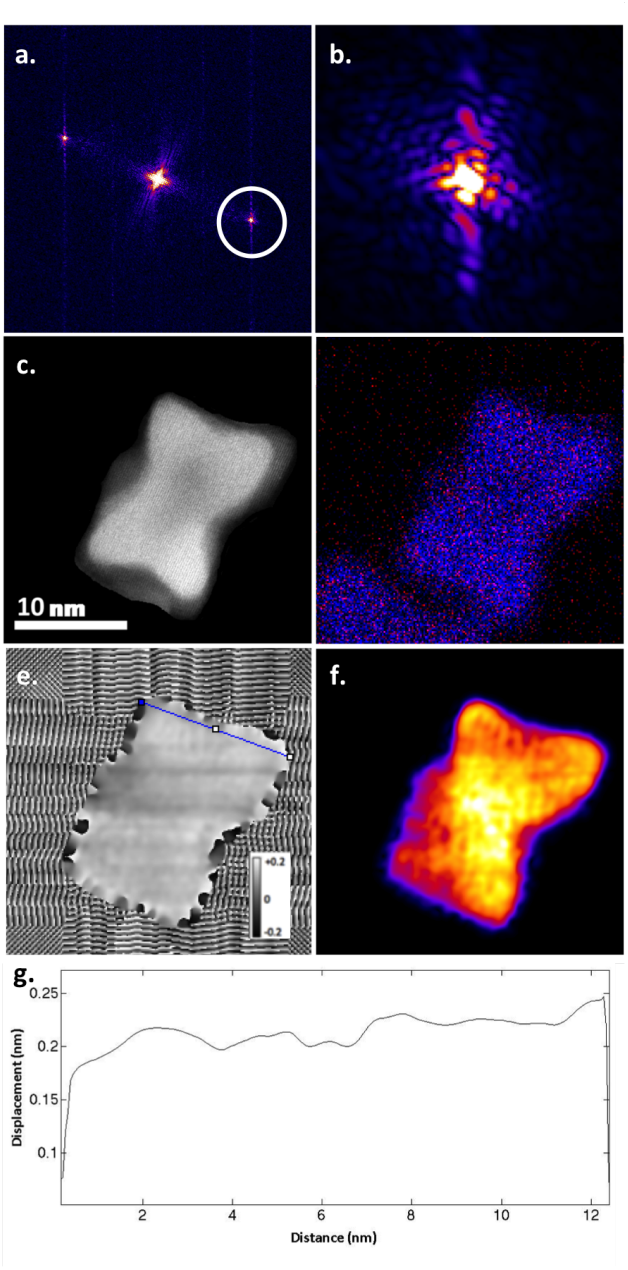

Figure 5.24: *2D strain analysis of an isolated FePt octapod (a) calculated reciprocal space pattern of the masked STEM-HAADF image (b) re-centered Fourier filtered Bragg spot (c) masked STEM-HAADF image with a high threshold (blue) to distinguish shell (d) STEM-EDS map of an overlay of the Fe K-edge (red), O K-edge (green) and Pt K-edge (blue) elemental distributions (e) Real space geometric phase map of the local displacement of the lattice fringes with a cross section line indicating the core (blue) and the shell (red). Phase values run from $-\pi$(black) to π (white) (f) Real space local amplitude image (with intensity scale inset) (g) Cross section plot of the phase variation.*

cidated the crystallographic, compositional distribution, 3D morphology and distribution, and strain properties of FePt octapods with an average diameter of 17 nm.

The resultant magnetic FePt octapod suspension formed a 2D self-assembled hexagonal arrays on the substrate in regions of high monodispersity. The high-resolution lattice spacing information acquired from HRTEM images of the octapods revealed that the FePt octapods consisted of (100) facets and the the 8 'pod's were of the same crystallographic orientation as the 'nanocube' centre. However, it is proposed that in order to probe the crystallographic properties of the individual 'pods'—which are expected to have higher degree facets— use of an HRTEM tomography would be a more precise approach. HRTEM tomography would also enable a stage tilt of 25°(which is required to satisfy the Bragg condition of the (111) planes of FePt) and could reveal the proposed growth formation where the (111) facets grow faster are proposed to grow faster than the (100) thus forming high index 'pod's. The stepped edges identified in HRTEM imaging, have been proven to enhance electro-catalytic activity of the octapods making them ideal for catalytic applications such as methanol oxidation [Wu et al., 2012].

The STEM elemental distribution maps of the Fe K-edge, Pt M-edge and O K-edge of two octapods revealed a homogenous distribution of Fe and Pt. The 3D reconstructions and visualisations of the octapods from the TEM tomography data enabled visualisation of the 8 corner 'pods'. The high surface to volume ratio of the octapods (as evident by the TEM tomography imaging) implies that there is a high number of available active sites for catalytic activity making the octapod morphology desirable for catalytic applications. Strain mapping of an isolated octapod is demonstrated within which is of fundamental importance in order to tune the catalytic activity of the octapods. The orientation of the octapods on the substrate resulted in different degrees of strain in the (100) planes.

5.7 Summary and Future Outlooks

The complementary nano-characterisation methods conducted within this study enabled a comprehensive analysis of the nanocubes, core-shell nanoparticles and octapods, which is of fundamental interest in the fine-tuning of these nanopar-

ticles for application. The success of the novel 2D strain mapping analysis method presented within this Chapter will likely realise great use by future researchers. Strain analysis of nanoparticles is increasingly becoming an area of research focus in nanotechnology enabling nanoparticles properties to be tuned by adapting synthesis schemes and corresponding strain engineering. The prompt and effective strain engineering method developed within can be applied to all forms of crystallographic nanomaterial's acting as an efficient strain engineering tool. This technique could find use by researchers in the field of nanoparticle catalyst analysis as an efficient method to iteratively 'see' and then finely tune surface strain in nanoparticles in order to optimise the electrocatalytic activity. These complementary techniques of TEM tomogpraphy and GPA enabled an alternative analytical approach to CDI enabling the 3D morphology and strain distribution of small isolated nanoparticles to be achieved.

Suggested improvements to the TEM tomography analysis could enable faster data acquisition. For example, difficulty was experienced in locating the nanoparticles after changing tilt angle, specifically on reaching +60°, back to 0 to scan 0 to $-60°$. Also, the brightness and focus altered at each tilt (even with the small 2°steps) resulting in a potential loss of the region of interest. High resolution carbon finder grids could resolve this issue by removing the need to trace the sample during each tilt. In addition the finder grids could enable complementary analysis of the nanoparticles to be conducted, for example using all of the TEM analysis techniques detailed within. Although this would increase the risk of over exposure of the sample to the electron beam.

Factors, that influence the quality of the reconstruction in TEM tomography stem from the data acquisition methods used. For example, in order to optimise the final 3D reconstruction the increment size, tilt range, and exposure could be tuned. The increment size of the 2D electron micrographs could be altered to follow a Equally Sloped Tomography (EST) algorithm as implemented by Scott et al [Scott et al., 2014]. EST is a fairly new analysis approach and involves the calculation of the increment size for each tilt in order to overcome the missing wedge of information in the reconstruction (specifically in the z-axis). Furthermore, without the aspect of instrument limitation, a dual tilt goniometer could be used with the same tilt range of 60°to leave only 16% of Fourier Space un-sampled (in comparison to 33% when using the single tilt goniometer). Ideally an even larger tilt range could be used to decrease the percentage of Fourier Space that is left

un-sampled. However, a careful balance needs to be made between step size and range to ensure the sample is not over exposed to the beam through excessive imaging. With regards to the 3D reconstructions further analysis from prior knowledge of the voxel size of the Avizo reconstructions could allow the volume of the nanoparticles to be calculated enabling an accurate quantification of the surface to volume ratio. This ratio can provide valuable catalytic information about the nanoparticles and enable the fine tuning of the core and shell volume for magnetic application such as, exchange coupling applications.

Chapter 6

Novel Stabilisation Methods for the Analysis of Small Nanoparticles using Coherent X-ray Diffraction Imaging

6.1 Motivation

Strain analysis using coherent x-ray diffraction is a well-developed technique for the quantitative analysis of the 3D structure and strain fields present in nanoparticles [Newton et al., 2009] [Robinson and Harder, 2009]. It is however limited to a current spatial resolution limit of $\sim$20 nm which can limit this technique to larger nanoparticles. Therefore, the motivation behind the BCDI investigations conducted within this chapter was to develop a prompt and efficient approach to resolve the limitations of the BCDI, and extend the accessible size regime. Furthering the knowledge and understanding of the fundamental properties of the nanoparticles will enable key applications in medicine, catalysis and information technologies. In this work, a novel stabilisation method was developed and CDI investigations were conducted at the Argonne Photon Source 34-ID-C beamline on chemically synthesised 17 nm FePt octapods, and 60 nm - 120 nm AuPd nanoparticles stabilised in a silica matrix.

6.2 Introduction

In a typical BCDI experiment, a coherent beam of X-rays illuminates a nanoparticle and the whole diffraction data set surrounding a Bragg peak is collected. These diffraction data sets are reconstructed using phase retrieval algorithms [Fienup, 1982] to achieve quantitative 3D reconstructions of the nanoparticle with strain field displacements. BCDI has fast become a powerful analytical tool for investigations of nanoparticles [Robinson and Harder, 2009], nanotubes [Zuo et al., 2003], nanorods [Newton et al., 2009] and even biological systems [Berenguer et al., 2015]. However BCDI has until recently, failed for the size regime below 80 nm accessible by chemical synthesis despite the physical spatial resolution of the BCDI technique being from 20 - 30 nm. This size window in which the BCDI technique has typically failed can be ascribed to the rotational movement of small un-bound nanoparticles when illuminated by the highly coherent beam.

The rotational movement of the nanoparticle has been utilised to conduct BDCI Brownian motion tracking of the rotational single particle motion of small nanoparticles embedded in a viscoelastic colloidal gel matrix [Liang et al., 2014]. Also radiation induced bending of silicon nanowires has been studied using BCDI where a peak-splitting effect was observed in the diffraction pattern originating from the X-ray beam exposure [Shi et al., 2012]. However, in structural and strain studies using BCDI, this rotational movement is undesirable as it restricts whole diffraction data sets from being acquired. Preliminary BCDI investigations of unbound 17 nm - 20 nm FePt octapods at the 34-ID-C beamline at the APS showed Bragg peaks appearing and disappearing within the 5s exposure time of the detector. Hence, a full rocking curve series of the Bragg spots could not be recorded owing to the rotational movement of the nanoparticles on illumination by the beam. It was proposed that, during these BCDI investigations, the high energy and direct focus of the beam dominated over the force between the nanoparticle and the substrate surface resulting in the rotation and movement of small nanoparticles. The difficulties encountered in analysing small nanoparticles using BCDI motivated a range of stabilisation methods to be tested (with the aim to prevent the rotational movement).

The first stage of the BCDI investigations involved developing an optimum matrix to ‘fixate’ the small 17-20 nm FePt octapods in a thin ‘transparent’ solid matrix.

FePt octapods (capped with OA and OA) were dried onto a silicon substrate and two stabilisation methods were tested. Firstly, the nanoparticles were coated with a thin layer of epoxy glue (which solidified immediately) and secondly, the nanoparticles were coated with a eutectic metal alloy, gallium indium (which solidified on cooling in-situ). However, both stabilisation techniques showed no indication of any stabilisation improvements and the rotational movement of the nanoparticles was still observed on illumination by the beam. Potential reasons could be ascribed to the high energy of the incident beam on the sample causing the eutectic to 'melt', or due to the networks only forming a layer on top of the nanoparticles, or even due to the incompatibility of the surfactant layer with the coating. The difficulties encountered in analysing small nanoparticles using BCDI, prompted a range of stabilisation methods to be tested and were the motivation behind this study. A novel stabilisation technique was developed to stabilise small nanoparticles, extending the lower size limit of BCDI nanoparticle analysis. This led on to the concept of a solid silica-based matrix used in partnership with a silicon substrate, such that the amorphous silica, SiO_2, coating was compatible with the Si substrate effectively forming a strong encapsulating and embedding nanocomposite network.

Surface functionalization of nanoparticles with inert silica, SiO_2, coatings is typically conducted to prevent nanoparticles from sintering on exposure to high annealing temperatures (required for phase transformation from fcc to fct in some nanoparticles). Sintering of nanoparticles is highly undesirable as it can result in coalescence and agglomeration of isolated nanoparticles into larger crystals, resulting in a loss in crystal surface area. For example, uncoated FePt nanoparticles will sinter at annealing temperatures greater than 400°C [Chen et al., 2004]. Therefore, nanoparticles are functionalised with silica shells of tuneable thickness (2-6 nm), which act as a protective thermal barrier to prevent this agglomeration. Based on this concept, that silica is a 'transparent' thermal barrier a silica stabilisation method was devised. There are various available methods commonly used to functionalise nanoparticles with silica, such as direct methods using nanoreactors [Chen et al., 2010] or atomic layer deposition [Liang et al., 2010]. However, these methods require access to advanced coating equipment, which is not readily available at synchrotron facilities. Meanwhile, laboratory based chemical coating methods include modified Stober methods [Chen et al., 2011], sol-gel polymerization method [Lu et al., 2002], and oil in water emulsion [Fan et al., 2004]

methods. However, these chemical coating methods typically require extensive preparation due to long reaction times (up to 24 hours in some cases) to ensure efficient coating of all nanoparticles. These chemical methods are designed to create a silica shell on the surface of isolated nanoparticles, which has already been proven unsuccessful in stabilising the FePt and AuPd nanoparticles during preliminary BCDI investigations. Therefore, in this study it was required to embed the nanoparticles in a thin matrix of silica effectively forming a rigid layer encapsulating the nanoparticles into a 3D network of silica.

Few studies report direct silica layer coating routes and they typically involve chemical procedures. For example, homogeneously coated Fe_2O_3 nanoparticles with silica layers were controlled hydrolysis by varying TEOS concentration and pH in a condensation reaction of TEOS on the Fe_2O_3 surface forming a Fe-O-Si chemical linkage on the surface. Subsequent condensation resulted in lateral polymerization forming a three-dimensional network via siloxane bond formation (Si-O-Si) with increasing TEOS concentration and degree of hydrolysis. However, this approach also required laboratory access and several treatment steps. In this study, we report the development of a novel and prompt one-step silica coating method utilising the sol-gel polymerisation concept to create a silica nanocomposite. The silica matrix could therefore protect the nanoparticles from the beam and stabilize them to enable a full rocking curve series to be acquired from the Bragg peak. In order to conduct an investigation with best achievable spatial resolution the BCDI investigations were conducted at the APS on the 34-ID-C beamline. Chemically synthesised nanoparticles, 17 nm - 20 nm FePt octapods, and 60 - 65 nm AuPd nanoparticles (supplied from Michael Huang) were stabilised in silica and annealed at high temperatures to test the limit of the BCDI technique. These stabilisation methods were identified as a prompt and efficient approach in resolving the limitations of the BCDI, extending the size regime for other synchrotron users.

6.3 Preliminary Investigations

6.3.1 Instrumentation: 34-ID-C Beamline Set Up

The instrumental set-up at the 34-ID-C beamline is described. The undulator beam source was tuned to the wavelength of 0.138 nm (app. 9 KeV) by changing the undulator gap spacing. A partially coherent beam was defined using a pair

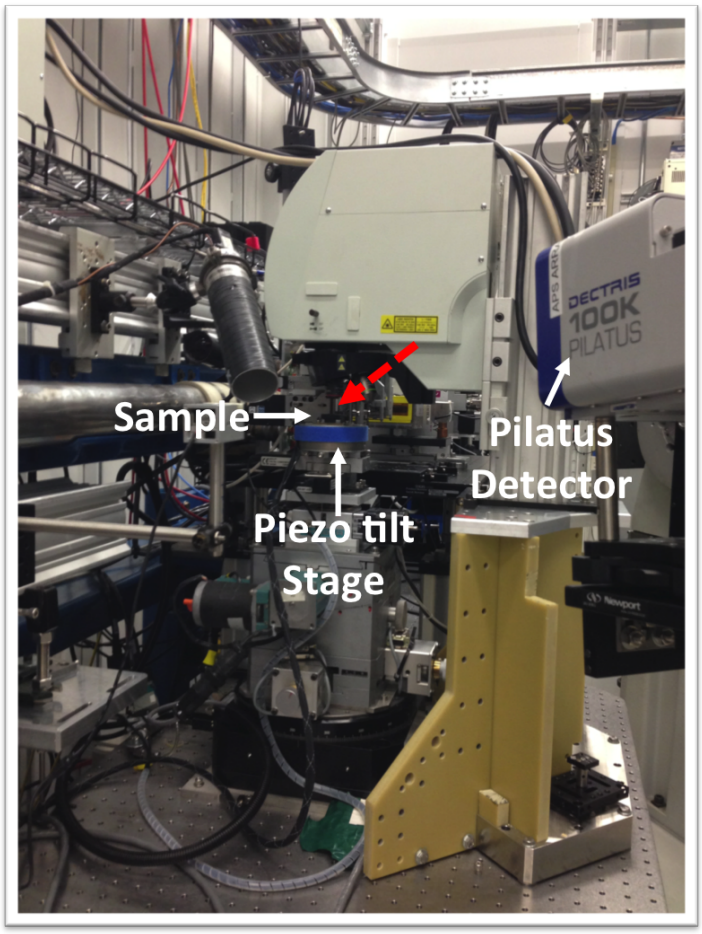

Figure 6.1: *34-ID-C setup indicating the sample on the piezo stage, the incoming X-ray beam (red line) and the Pilatus detector.*

of JJ slits, with a size of 20 μm in both the horizontal and vertical directions, placed before the sample. The very small size of the nanoparticles meant that the part of the beam incident on an individual nanoparticle had sufficient coherence. The X-ray beam was illuminated on the sample and after passing through the

sample, the diffracted beam passed an evacuated flight path of R = 1.2 - 1.6 m, to the Pilatus detector positioned on a robot arm (that can be positioned up to 6m away). In this experiment, to identify known powder rings the Pilatus detector, was positioned at a specific angle, 36.35° to detect the FePt fcc (111) powder ring, 29.31° to detect the FePt fct (110) powder ring and, 34.22° to detect the AuPd fcc (111), powder ring.

6.3.2 Reconstruction of the Nanoparticles

The reconstructions were conducted following Jesse Clark's reconstruction method and implemented by Ana K Estandarte. Firstly, the measured diffraction patterns from a rocking curve series were stacked in one image using ImageJ. The diffraction pattern was cropped to an area of interest with an array size of 100 x 100 array. The phasing algorithms were performed, using Matlab, on a total of 36 frames defining the array size in the z-dimension. No binning was done on the data. A real space constraint was defined and allowed to evolve during the iterations using Shrinkwrap. Shrinkwrap was applied every five iterations and the iterations in-between were fixed. A guided approach was used together with the ER and HIO algorithms. Eight independent runs consisting of 200 iterations each were performed with each run having a different starting phase. The 200 iterations started with ER then at the 5th iteration, the algorithm was switched to HIO and switched back to ER at the 180th iteration. The amplitude and phase of the best reconstruction from the eight runs were merged with those of the remaining seven reconstructions. The resulting merged reconstructions and the best reconstruction were then used as the initial guess for the next generation of reconstructions. A total of five generations were done. The 3D images were generated from the resulting phased 2D slices using Mayavi. BCDI is only sensitive to displacements that are a small fraction of a unit cell in magnitude. Therefore, for crystals that are highly strained resulting in full unit cell displacements, phase wrapping occurs, which has to be unwrapped in order for the displacements to be accurately resolved.

6.3.3 Rotational Effect of the Beam

The effect of the rotational movement of the small nanoparticles was observed during preliminary BCDI investigations of unbound FePt octapods, at the 34-ID-C beamline at the Argonne Photon Source (Illinois, USA). The octapods were selected, as they have the largest FePt nanoparticle size accessible by chemical synthesis and would push the extremities of the BCDI resolution limit. These BCDI investigations were designed to test the extremities of the size limit for BCDI imaging of nanoparticles by probing nanoparticles smaller than previously possible to probe using BCDI.

In the preliminary BCDI investigations the sample was prepared by evaporating the nanoparticle suspension (surfactant stabilised FePt octapods suspended in hexane) onto a Si substrate to form a dried colloid on the substrate. The nanoparticle sample on the substrate was then heated up to temperatures of 250°C.

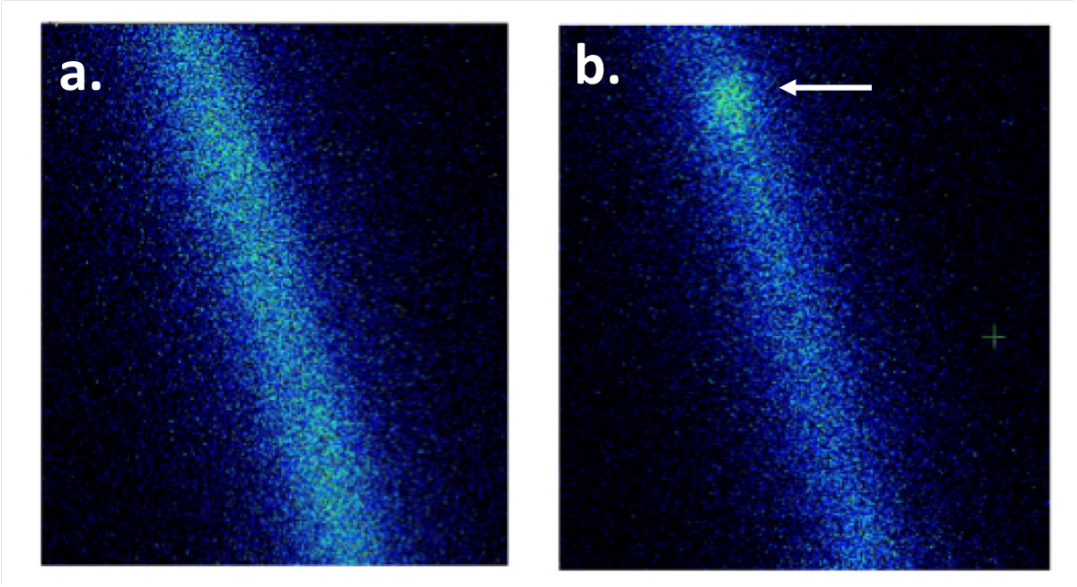

Figure 6.2: *Previous BCDI investigation of un-bound FePt nanoparticles showing the diffuse (111) powder ring with two adjacent 5 sec exposures without moving anything (a) No diffraction peaks observed (b) Diffraction peak from an isolated nanoparticle as indicated by arrow.*

During the BCDI investigation of the un-bound FePt octapods the diffraction spots in the FePt (111) fcc powder ring from individual nanoparticles (as in Fig.6.2a and b) were appearing and disappearing without moving anything within 5s exposure and hence a full rocking curve series of the spots could not be recorded. These

preliminary results, are due to the movement of the un-bound nanoparticles and further prompted the aim of this chapter; to develop an efficient novel method to directly embed the nanoparticles in a silica matrix that could be implemented at the synchrotron without the use of extensive chemical procedures or coating equipment.

6.3.4 Tested Stabilisation Methods

Extensive BCDI investigations were conducted in preliminary investigation to find an optimal stabilising matrix firstly both epoxy and a eutectic metal alloy were tested. In the BCDI, investigations, of FePt nanoparticles samples coated with a thin layer of epoxy glue (which solidified immediately), there were no stabilisation improvements observed. Potential causes for this could be due the epoxy 'solid network' weakening on exposure to the high energy beam, or due to the metal only forming a layer on top of the nanoparticles.

Gallium indium is eutectic and so is a liquid at room temperature, and a solid at it solidification temperature (-15°C). Taking advantage of the eutectic nature of this metal alloy, the liquid metal was used to coat the nanoparticles at room temperature, and the freezing point enabled the sample to be cooled in-situ (using a cooling/heating sample stage) solidifying the metal. On solidification of the eutectic metal it was expected that this would effectively fixate the nanoparticles in a metal matrix. However, there was no indication of any stabilisation improvements and nanoparticles were still moving. Potential causes could be ascribed to the high energy of the incident beam on the sample causing the eutectic to 'melt', or it could have been due to the metal only forming a layer on top of the nanoparticles.

Efforts were made to ensure the limiting factor in these investigation was not the small nanoparticle size, by testing the coating methods above with larger silver nanoparticles (100 nm). The unbound silver nanoparticles also had a tendency to be un-stable and rotate on exposure to the beam, in both the epoxy and the eutectic metal. Therefore, it was concluded that another procedure for a stabilisation of the nanoparticles was required to be developed. A preferred solid matrix would ideally be silica based such as SiO_2 (amorphous SiO_2), as this is compatible with the Si substrate, so could effectively form a strong embedding network.

6.4 Silica Matrix Formation

6.4.1 Tetraethylorthosilicate Reaction Scheme

The nanoparticles were embedded in an SiO_2 matrix via a novel 'drop-cast' method which was devised from the concept of sol-gel polymerisation of tetraorthoxysilanes, such as, tetra-ethyl-ortho-silicate (TEOS), $SiO(EtO)_4$, tetra-methyl-ortho-silicate (TMOS), $SiO(MeO)_4$). The shematic in Fig.6.3 outlines the hydrglysis-

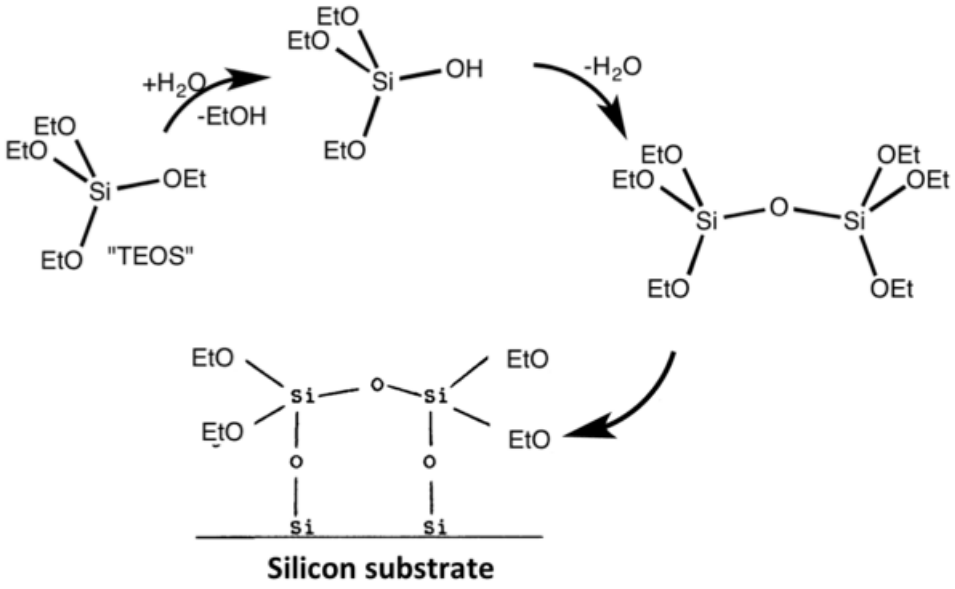

Figure 6.3: *Schematic of silica formation on a substrate from the hydrolysis-condensation reaction scheme of tetra-ethyl-ortho-silicate in the presence of water and ethanol.*

condensation reaction scheme of TEOS in the presence of ethanol ($EtOH$) and water, (H_2O). The reaction begins with the TEOS which is hydrolysed (gain of H_2O) and alkoyzed (loss of an $EtOH$). Subsequent condensation (loss of H_2O) from the TEOS intermediates results in the formation of a silane bridge forming an epoxy network. This reaction continues forming a long chain polymer network of silica.

The resultant rigid silica gel network, consists of polymerised silane bridges, on the substrate. It was expected that, on combining this sol-gel polymerisation with nanoparticles, the silica could also form silane bridges that would stabilise the

nanoparticles by encapsulating them in a silica matrix whilst bonding to the substrate surface providing additional stabilisation. In order to encourage a rigid polymerised silica network thermal annealing of the silica-nanoparticle matrix was required.

6.4.2 FePt Octapod and AuPd Nanoparticle Samples

FePt octapods, of diameter 17-20 nm, as shown in the TEM images in Fig.6.4, were chemically synthesised as described in Chapter 3. The octapods were sta-

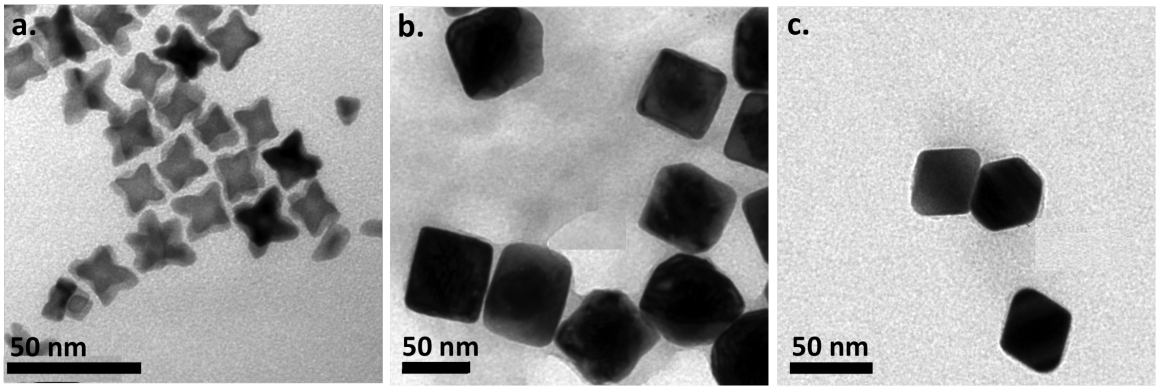

Figure 6.4: *TEM images of (a) FePt octapods, (b) AuPd nanocubes (c) AuPd octahedrons.*

bilised in hydrophobic OA and OAm surfactants which have non-polar tails, and dispersed as a colloid in a non-polar hexane suspension. AuPd nanoparticles, of diameter 65 nm as shown in the TEM images in Fig.6.4a and Fig.6.4b, were chemically synthesised by Michael Huang, National Tsing Hua University. The AuPd nanoparticles, were stabilised in a hydrophilic cetyl trimethylammonium bromide (CTAB) surfactant, and re-suspended from the original polar water suspension into an ethanol suspension for ease of evaporation of the nanoparticle solution onto the substrate.

6.4.3 TEOS Stock Solution Optimisation

Firstly, the BCDI investigations focussed on finding the optimal ratio of TEOS:EtOH solution (stock solution) to create a silica matrix of optimum thickness. If the

silica layer was too thick reflection issues were encountered during the sample alignment and if the silica layer was too thin there were stabilisation issues encountered (owing to the nanoparticles not being fully coated by the silica). The concentration of the TEOS stock solution was optimised to lower the number of drops required to coat the sample. The ratios tested were from the initial stock solution one: 0.02 mL TEOS in 6 mL $EtOH$ (1:350) to stock solution two: 0.04 mL TEOS in 6 mL $EtOH$ (1:150) to the final stock solution three: 0.08 mL TEOS in 6 mL $EtOH$ (1:75). The optimised stock solution three was found to be the most effective in creating a silica matrix of optimum thickness and the TEOS:EtOH ratio of 1:75 was used to coat the nanoparticle samples.

6.4.4 TEOS Solution Drop-Casting Procedure

The nanoparticles were embedded in an SiO_2 matrix using a novel 'drop-cast' method which was devised from the concept of sol-gel polymerisation which applies to tetraorthoxysilanes Tetra-ethyl-ortho-silicate (TEOS), SiO_2EtO_4, tetra-methyl-ortho-silicate (TMOS), $SiO_2(Me_4$. Firstly, the nanoparticle suspension (suspended in a hexane/ethanol solvent) was evaporated onto a Si substrate to form a dried colloid of the nanoparticles. It was realised that a balance in the concentration of the nanoparticle suspension was required. In one respect, if the colloidal solution was too dilute the nanoparticles would be sparsely distributed on the substrate resulting in difficulties finding a nanoparticle. Whilst in the other respect, if the colloidal suspension was too concentrated there was a high possibility that over-crowding of the nanoparticles would occur on the substrate resulting in difficulties isolating individual nanoparticles during the BCDI investigations. Once the hexane was evaporated, the TEOS stock solution was drop-cast onto the dry colloid using a pipette in controlled drops of volume 20 μ L, which were left to evaporate before addition of the next drop. During both the drop casting of the sample solution and the TEOS stock solution the substrate was kept on a warm hot plate at 70°C to encourage ethanol evaporation. The coated samples prepared on Si substrates were then annealed in a thermal oven at various temperatures to encourage a rigid silica network formation. Notably, another approach to prepare the solution could be to mix the dry nanoparticle solution in with the optimised TEOS stock solution. However because the mass of octapod sample was limited the process above enabled minimal loss of sample during sample preparation.

6.4.5 Annealing Procedure

The coated samples prepared on Si substrates, were annealed in a thermal oven, as shown in Fig.6.5a, to encourage a rigid silica network formation. The following annealing temperatures and times were investigated using BCDI for the FePt-silica nanocomposite samples; 250°C for 4hours, 350°C for 4 hours and 800°C for 1.5 hours. The following annealing temperatures were investigated using BCDI

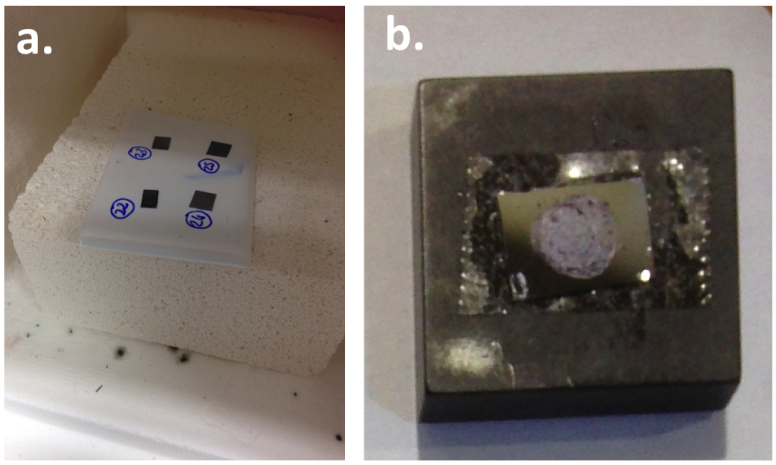

Figure 6.5: *Prepared silica nanocomposite samples on Si substrates (a) samples in thermal oven (b) Mounted samples on sample holder*

for the AuPd-silica nanocomposite samples; 250°C, 350°C and 600°C with a constant annealing time of 4 hours. The resultant annealed samples were of a slight opaque colour due to the formation of the silica nanocomposite matrix as shown in the mounted sample in Fig.6.5b.

6.5 FePt Octapods Stabilised in a Silica Matrix

From BCDI investigations of the FePt-silica nanocomposite samples annealed at 250°C and 350°C, the FePt (111) fcc powder ring was observed to be very diffuse and the Bragg peaks were not stable for long enough to record a full rocking curve series of an individual peak. From the BCDI investigations of the FePt-silica nanocomposite samples annealed by rapid thermal annealing at 800°C (to test the extremities of the annealing temperature range), the FePt (111) fcc powder

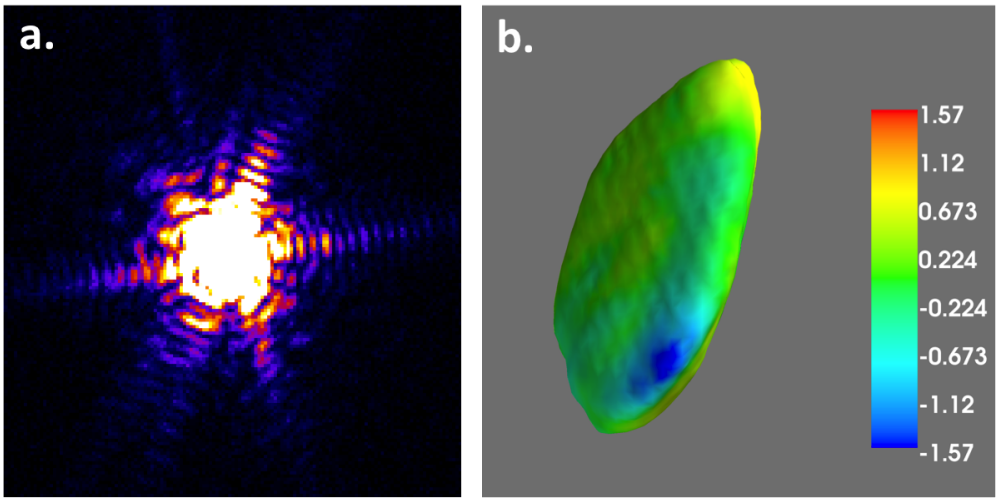

Figure 6.6: *FePt nanoparticles in a silica matrix (annealed at 800°C for 1 hour 30 minutes) (a) Bragg diffraction frame, where the centre is strongly saturated in the display, and (b) corresponding 3D morphology (157 nm x 39 nm x 38 nm) and 3D strain isosurface (colour scale units in radians where the red is displacement along Q while blue is displacement opposite of Q.*

ring and the FePt (110) fct powder ring (due to phase transformation at annealing temperatures above 500°C) were observed. The majority of the Bragg peaks located on the (111) fcc powder ring were stable and occasionally strongly saturated with defined interference fringes. The Bragg peak is shown in a Bragg diffraction frame at the centre of the rocking curve in Fig.6.6 a. The strain isosurface reconstruction (with the colour scale units in radians) of the 3D morphology of the FePt nanoparticle in Fig.6.6b provided an insight into the strain at the facets of the nanoparticle and the size of the nanoparticle (of length, 157 nm, width 39 nm and, breadth 30 nm). The isosurface strain map showed the crystal had regions of strain at the edge facets (blue) that could be due to the re-distribution and homogenous segregation of Fe or Pt during the larger crystal formation. The size of an isolated octapod is on average 17 - 20 nm therefore it was evident that large crystal formed in the reconstruction is a result of sintering of the isolated FePt nanoparticles during the high temperature annealing. It is proposed that this larger crystal formation was due to the silica not forming an encapsulating network around the individual FePt nanoparticles and instead only forming an 'over-layer' on the nanoparticles (enabling sintering of the octapods beneath this layer). This is expected to be the result of the hydrophilic acid and amine surfactant monolayer, where the hydrocarbon end groups do not act as a suitable

compatible primer for silica thus preventing silica matrix encapsulation.

6.6 AuPd Nanoparticles Stabilised in a Silica Matrix

From the BCDI investigations of the AuPd (111) fcc powder ring annealed at 350°C, the Bragg peaks at this temperature were more stable in comparison to the samples annealed at 250°C and 600°C (this also applied to larger nanoparticles, such as Au nanorods, but this is not discussed further within this investigation). Therefore, the optimum annealing temperature for AuPd nanoparticles, in which the movement of the nanoparticles was significantly reduced/prevented was identified as 350°C.

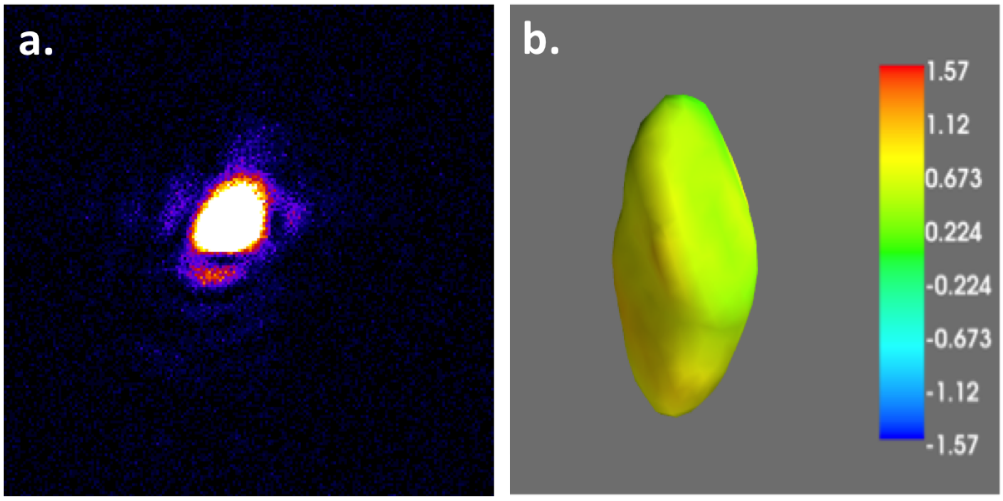

Figure 6.7: *BCDI imaging of an isolated AuPd octahedron in a silica matrix annealed at 350° C for 4 hours: (a) Bragg diffraction frame and (b) corresponding 3D morphology (120 nm x 65 nm x 56 nm) and strain isosurface (colour scale units in radians where the red is displacement along Q while blue is displacement opposite of Q.*

Fig.6.7a shows a central Bragg diffraction frame, from an AuPd nanoparticle silica nanocomposite (with an annealing time of 4 hours at a temperature of 350°C). The corresponding 3D isosurface and morphology reconstruction created from the rocking curve of the Bragg peak is shown in Fig.6.7b. The morphology of the AuPd nanoparticle was slightly elongated with a length of 120 nm, but was of small width, 60 nm, and breadth, 56 nm. The strain isosurface was also visible with only a slightly strained surface on the high index facets.

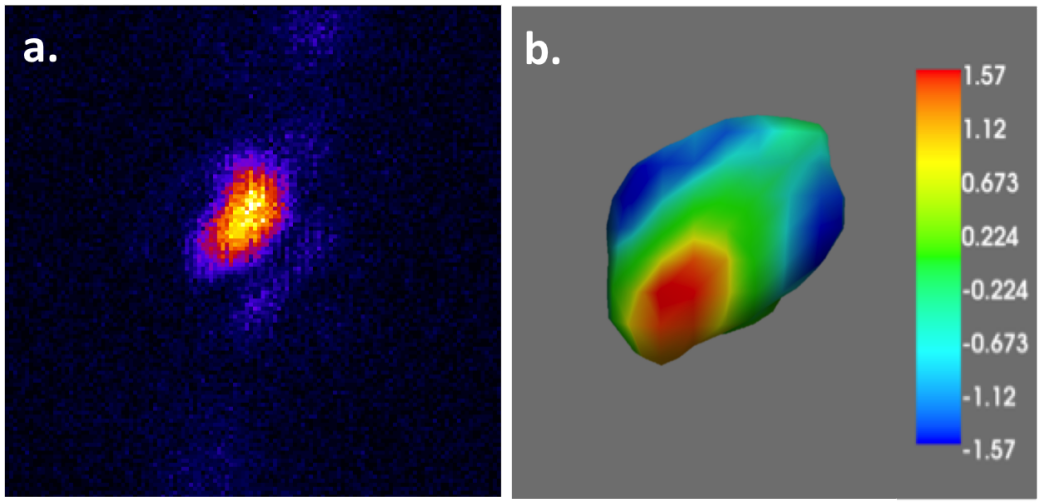

Figure 6.8: *BCDI imaging of isolated AuPd cubic nanoparticle in a silica matrix annealed at 350°C for 4 hours (a) Bragg diffraction frame and (b) corresponding 3D morphology (64 x 65 x 56 nm) and strain isosurface (colour scale units in radians where the red is displacement along Q while blue is displacement opposite of Q.*

Fig.6.8a shows a central Bragg diffraction frame, from another AuPd nanoparticle silica nanocomposite (with an annealing time of 4 hours at a temperature of 350°C) showing some additional fringes. The corresponding 3D isosurface and morphology reconstruction created from the rocking curve of the Bragg peak is shown in Fig.6.8b. The morphology of the nanoparticle was found to be of a cubic form with a length of 64 nm and width of 65 nm and breadth of 56 nm, with rounded facets and highly strained regions at opposite edge facets. These 3D reconstructions acquired from nanoparticles with dimensions of 65 nm indicate the success of the silica stabilisation method. The stabilisation of AuPd nanoparticles is expected due to the hydrophilic CTAB surfactant monolayer, acting as a primer to bond the nanoparticles with the silica matrix. This network between the silica matrix and the nanoparticle is expected to form prior to annealing, where it is expected that the surfactant formed a silane bridge with the silica thus encapsulating the nanoparticles into the silica matrix network forming the AuPd-silica nanocomposite. Furthermore, it is proposed that at the annealing temperature of 350°C, eutectic bonding of the Si(substrate)-Au(nanoparticle) may have occurred as Si-Au has a eutectic temperature as low as 250°C [Hamidinezhad et al., 2011].

6.7 Discussion

From the BCDI investigations of the FePt silica nanocomposites annealed at low temperatures: 250°C and 350°C for 4 hours, the Bragg peaks in the FePt (111) powder ring were not stable indicating the rotational movement of the nanoparticles due to the beam was still existent. Only on rapid thermal annealing of the prepared FePt silica sample at 800°C (for 1 hour 30 minutes) was it possible to record a full rocking curve series from a Bragg peak, at the FePt (111) powder ring, as the Bragg peaks remained stable enough to record a full rocking curve series. Notably, the isolated Bragg peaks on the fcc FePt (111) powder ring were larger than observed previously (before stabilization) and with defined diffraction fringes. Also, the FePt fct (110) powder ring was detected indicative of a phase transformation of the FePt nanoparticles from the fcc to fct phase, as a result of the high annealing temperature. The stabilization method enabled a good 3D reconstruction of the FePt nanoparticle of dimension; length 157 nm, width 39 nm, and breadth 30 nm. It was evident that the high annealing temperature caused the isolated FePt nanoparticles to sinter together to form a larger FePt crystal formation in the fct phase. The scarce hydrophobic nature of OA and OAm could have resulted in only a partial coating of silica on the FePt ocatpods (as also previously observed by Assam et al) that prevented stabilisation at low temperatures and caused this crystallisation at high temperatures.

From the BCDI investigations of the two AuPd silica nanocomposite samples, both annealed at a temperature of 350°C for 4 hours, the Bragg peaks in the AuPd (111) powder rings were stable enabling whole diffraction data sets to be recorded from a rocking curve series of isolated AuPd nanocyrstals. For both AuPd nanoparticles, the movement of the nanoparticles was significantly reduced/prevented, enabling a 3D reconstruction of two AuPd nanoparticles with the smallest nanoparticle of dimension: length 65 nm, width 65 nm, and breadth 56 nm. The stability of the AuPd nanoparticles on exposure to the beam suggests that the silica encapsulated the nanoparticle whilst attaching onto substrate creating a rigid three dimensional silica network. If the surfactant was compatible with silica then it would act as the nucleation site for silica to hydrolyse and condense. In these investigations it is proposed that the hydrophilic CTAB surfactant acts as a nucleation site for TEOS and on subsequent thermal annealing of the nanocomposite (at a temperature above the b.p of CTAB ($\sim$243°C)) the CTAB

was calcined. It is expectd that the surfactant evaporates through the pores of the silica network. It is also expected that the low annealing temperature resulted in a rigid silica network formation encapsulating the nanoparticles in the matrix whilst ensuring the nanoparticles retained their structural integrity. Furthermore, it is proposed that at the annealing temperature of 350°C, eutectic bonding of the Si(substrate)-Au(nanoparticle) may have occurred as Si-Au has a bonding temperature of 350°C.

6.8 Summary and Future Outlooks

This study demonstrates the progressive steps in the development of a novel silica stabilisation method for BCDI of small nanoparticles. BCDI investigations were conducted at the 34-ID-C beamline at the Argonne Photon Source (Illinois, USA) to devise the optimum stabilisation technique. It was revealed that the use of a novel 'drop-cast' stabilisation method, devised in this study, can efficiently encapsulate and isolate nanoparticles in a silica matrix. The stablisation method is based on a solution devised from the concept of the hydrolysis-condensation reaction scheme where TEOS, in the presence of $EtOH$ and H_2O (from moisture in air), hydrolyses and condenses to form silica. The polymerisation of the silica matrix was further encouraged by thermal annealing to form a rigid silica nanocomposite. In this study the stabilisation method was optimised by testing a range of concentrations and annealing temperatures. Small chemically synthesised nanoparticles, 17 nm - 20 nm FePt octapods with a hydrophobic surfactant layer of OA and OLA, were analysed to test the limits of the BCDI and stablisation techniques. In addition 60 nm - 65 nm AuPd nanoparticles with a hydrophilic surfactant layer of CTAB were analysed using BCDI.

Overall, the stabilisation method could be devised according to the sample and readily implemented at the synchrotron without the use of extensive chemical procedures or coating equipment. An indication of the success of the new method is that it is now being adopted by members of the APS beamline as an effective nanoparticle stabilisation method for the reconstruction and analysis of nanoparticles.

In the case of nanoparticles coated with a hydrophilic layer, such as the FePt

nanoparticles, in order to optimise the stabilisation process, appropriate surface functionalisation of the nanoparticles is necessary. For example, functionalisation of the nanoparticles with organo-silane surfactants, such as aminoproxysilane or (3-mercaptopropyl)-trimethoxysilane, will promote interfacial bonding between the nanoparticle and the silica matrix [Palma et al., 2007]. The silane functional groups of the surfactants act as a primer for condensation of TEOS on the nanoparticle surface [Aslam et al., 2005]. The functional group could also bond with the silica substrate increasing the compatibility of the nanoparticles with the silica matrix. Thus, forming a more rigid encapsulation matrix. In other cases, surface functionalisation of the nanoparticles may not be necessary. For example, in oxide nanoparticles such as Fe oxides (Fe_2O_3, Fe_3O_4 or ZnO) the dominant hydroxide terminated surface acts as a nucleation site for TEOS condensation and hyrdrolysation.

Chapter 7

Neutron and X-Ray Pair Distribution Function Analysis

7.1 Motivation

Magnetic nanoparticles can be engineered for an array of potential applications so it is vital to be able to not only understand the nanoparticles chemical and physical properties but also their surface functionality. Elucidation of the structural properties, bonding speciation, and ratio of surfactant on the nanoparticle surface is of great importance. In particular to the biomedical industry where chemical functionalisation of the nanoparticle surface with a biomolecule is common for targeted drug delivery application. Thus, gaining a comprehensive understanding of a nanoparticles structure and bio-conjugation and bio-modification behaviour will enable their properties to be optimised for application. The motivation behind this chapter was to develop a novel characterisation method to probe the whole FePt nanoparticle-surfactant system using a pair distribution function (PDF) analytical technique of data acquired from FePt nanoparticles with isotopic substitutions utilising both neutron diffraction and also high energy X-ray diffraction analysis.

7.2 Introduction

A range of conventional analysis techniques are currently available to probe either the atomic scale structure of a nanoparticle or the surrounding surfactant layer. However, there are very few methods that can be used to quantitatively probe *both* the nanoparticle and the surfactant layer as a whole which was the motivation behind the neutron diffraction investigations detailed in Chapter 7. These surfactant layer investigations could be applicable in the field of biomedical research, for example, to understand nanoparticle drug carrier systems—nanoparticle with surfactant exchanged with a biomolecule drug—and optimise them for targeted drug delivery [Thanh and Green, 2010].

Conventional laboratory techniques are most commonly adopted by researchers to probe the surfactant layer of nanoparticles in colloidal suspensions. For example, dynamic light scattering (DLS) is a conventional approach typically used to gain an indication of the thickness of the surfactant layer and the size distribution profile of nanoparticles in suspension. DLS is a technique based on Brownian motion that utilises light scattering from a nanoparticle suspension to determine the hydrodynamic radius distribution profile from the sample—the radius of the nanoparticle plus the surfactant layer—. The disadvantage of DLS is that it exhibits a low degree of accuracy when used for the analysis of dark nanoparticles (due to high absorption), such as FePt nanoparticles.

Fourier Transform Infra-Red (FTIR) spectroscopy is typically used to probe the adsorption and bonding mechanism of the surfactant layer on the nanoparticle surface [Zhang et al., 2006], [Shukla et al., 2003]. However, FTIR does not quantitatively determine the speciation of the surfactant bonding and so is only really used to confirm the presence and bonding of the surfactant layer.

Quantification techniques such as thermal gravimetric analysis (TGA) can determine the surfactant packing ratio on the nanoparticle surface by measuring the % organic weights loss during a thermal decomposition [Yung et al., 2014]. TGA is a valuable technique as it provides quantitative measurement of mass change in materials associated with thermal degradation. However, it is also a destructive technique, which destroys the organic layer during the measurements which is not suitable for sample preservation particularly when dealing with expensive deuterated surfactants.

Advanced analytical techniques such as small angle neutron scattering (SANs) analysis are usually adopted to obtain more detailed information about the surfactant layer only. SANs is typically used to probe the thickness and packing density of the surfactant and provide valuable structural information as described within [Edit, 2003]. However, the use of SANs alone only does not take into consideration the length scale of the nanoparticle.

Only recently, over the past decade have the tools and software capabilities emerged for the application of a well known PDF analysis to disordered nanoparticle systems [Billinge, 2008] [Newton et al., 2012]. The X-ray PDF technique has been most commonly reported in the analysis of the internal structure of inorganic nanoparticles using high resolution X-ray diffraction data. However, it is common that the organic surfactant shell surrounding the nanoparticle is ignored, and considered as negligible in these investigations. For example, in an XPDF investigation into the structure of OA surfactant capped CdSe nanoparticles only the influence of surfactant on the atomic ordering of the nanoparticles was considered whilst the surfactant layer itself was assumed amorphous. Therefore, the aim of this investigation was to utilise the capabilities of both the neutron and X-ray PDF analysis technique to probe both the nanoparticle and the surrounding surfactant layer of the 2 nm FePt nanoparticles synthesised with isotopic substitutions of OA and OLA surfactants (as outlined in Chapter 3).

Neutron PDF (NPDF) investigations can enable structural information to be ascertained from the surfactant layer such as the bonding speciation and ratio of surfactant on the surface through the analysis of isotopic substitutions. The near intermediate range order diffraction (Nimrod) beamline, housed at the neutron facility at the Rutherford Appleton Laboratories (Oxfordshire), was selected as the most suitable beamline for this investigation as it enables, in the case of the FePt nanoparticle-surfactant systems, the length scale range of FePt nanoaprticle ($\sim$2 nm) down to the length scale of the intermolecular bonding in the surfactant chain ($\sim$ 1 nm) to be probed

In addition, complementary X-ray PDF (XPDF) investigations were conducted at the Dight Light Source I15 beamline enabling structural information from both the FePt nanoparticle to be extracted. Furthermore the XPDF data was used to refine a theoretical model of the FePt core.

7.3 Nanoparticle Modelling and Refinement Programs

7.3.1 'Nanoparticle Builder' DIFFUSE Modelling Program

The combined Diffuse Scattering Und (and) Structure Simulation (DIFFUSE) modelling package [Proffen and Neder, 1999] is designed by Prof Reinhard Neder and Prof Thomas Proffen for the simulation of a wide range of structures from; perfect, disordered and infinite crystals, to glass, liquid and amorphous materials. This modelling platform has only recently been developed to enable the simulation of nanoparticles and required the development of code to account for surfactant contributions. Within the modelling package there are three sub-programs—DISCUS,

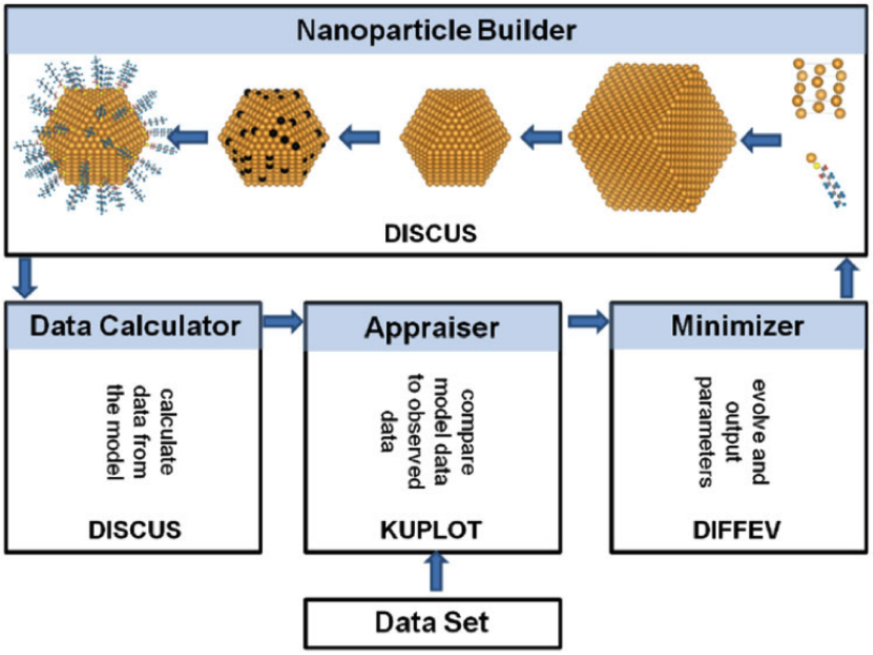

Figure 7.1: *DIFFUSE Package flow chart demonstrating the full capabilities of the software packages DISCUS, KUPLOT and DIFFEV. Image reprinted with permissions from [Page et al., 2011][REF].*

KUPLOT, and DIFFEV— each of which are designed to run the different tasks each of which are detailed in the Appendix 9.3.

This DISCUS and KUPLOT sub-package were mainly used to build a 3D model of the FePt nanoparticle. The nanoparticle was built according to the information already known about the system. In this investigation the following is defined; ra-

dius, composition, cell parameters, and morphology. Also the atomic distribution is defined (e.g. disordered, core-shell, short-range order, long-range order). Surfactant molecules can also be created by using data from the ICSD and inputting this into a cell file and attached onto nanoparticle surface sites with a defined speciation ratio.

7.3.1.1 Reverse Monte Carlo Profile

The Reverse Monte Carlo (RMC) Profile program is a refinement software program built by a collaboration between scientists at Rutherford Appleton laboratory, University of Cambridge, University of Oxford and, National Institute of Standards. This RMC profile program is designed to model neutron or X-ray total scattering data and also energy X-ray absorption fine spectra, and single crystal diffuse scattering [Tucker et al., 2007] [Tucker et al., 2001].

In this investigation a novel RMC profile code was compiled by Philip Charter (beamline scientist at I-15) and used to refine the initial DISCUS input model with experimental XPDF data to gain a closest representative of the nanoparticle model. This approach is not as computationally expensive as using DIFFEV to refine the model, however the RMC Profile modelling program is still its infancy in terms of capabilities to refine nanoparticle-surfactant systems.

7.3.2 Preliminary Pair Distribution Function Investigations

Preliminary XPDF investigations of the FePt nanoparticles were conducted by Valeri Petkov at the 11-ID-C beamline at the Advanced Photon Source. The objective of the study was to demonstrate the quantitative structural information that can be obtained using the PDF approach even from these very small nanoparticles. Petkov has played an important role in developing the field of PDF analysis and modelling for nanoparticle alloys. The results of the PDFs of four test samples of 20 Å FePt OA-H HDA-H nanoparticles are plotted in Fig.7.2. A simplistic reverse Monte Carlo fit was applied to the uniform fcc FePt lattice across the nanoparticle PDFs, to extract quantitative structural information. The red circles and blue solid lines in Fig.7.2 correspond to the experimental data and the fit,

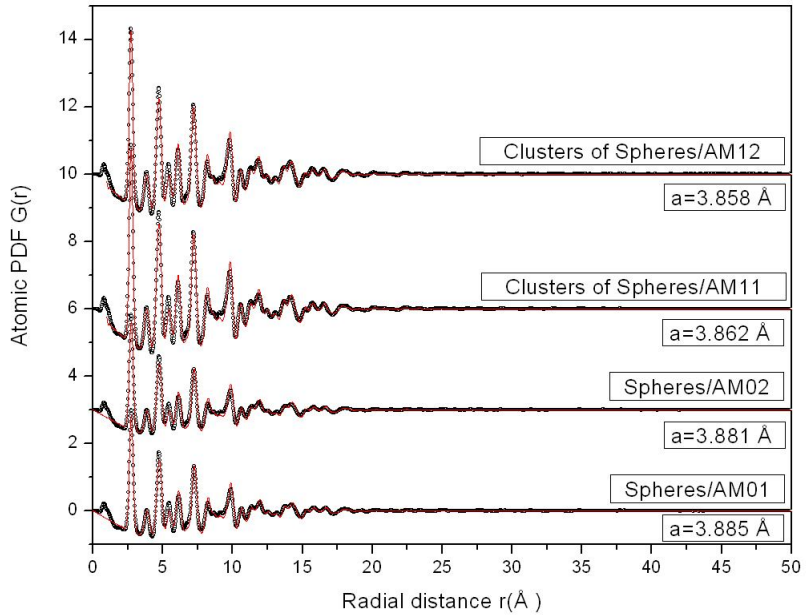

Figure 7.2: *Four samples of FePt nanoparticles with an average diameter of ∼20 Å where the red circles and blue solid lines correspond to the experimental data and the fit. Datasets obtained by Valeri Petkov.*

respectively. From the results of the fits of the FePt OA-H HDA-H nanoparticles (AM12) PDF of diameter 2.1 nm the cell parameter was extracted as 3.858 Å, and as the nanoparticle size decreased the cell parameter increased, as notable from the for nanoparticles (AM01) of 1.7 nm the cell parameter was extracted as 3.885 Å. Higher values of a indicate a higher platinum content in the sample these values are used as input parameters in the FePt models.

This preliminary study confirms that high quality structural information can be attainable from X-ray PDF analysis of ultra-fine nanoparticles. However this study also highlights the limited degree of structural information attainable on the intermolecular level, as shown by the lack of high intensity peaks below the first NN peak of the FePt nanoparticle. Thus, the preliminary results emphasize the requirement for neutron PDF studies to probe the surfactant shell. It also highlights the feasibility of further X-ray PDF analysis that would enable the chemical inhomogeneities of the FePt nanoparticles such as, core-shell or short-range order in the nanoparticles to be modelled.

7.3.3 Preliminary Nanoparticle Modelling

The DISCUS modelling package was used to build spherical models of $Fe_{16}Pt_{84}$ all with a random atomic distribution. The atomic arrangement of the atoms is automatically disordered with randomly correlated Fe and Pt atoms (but short range or long range disorder can also be defined). The effect that the diame-

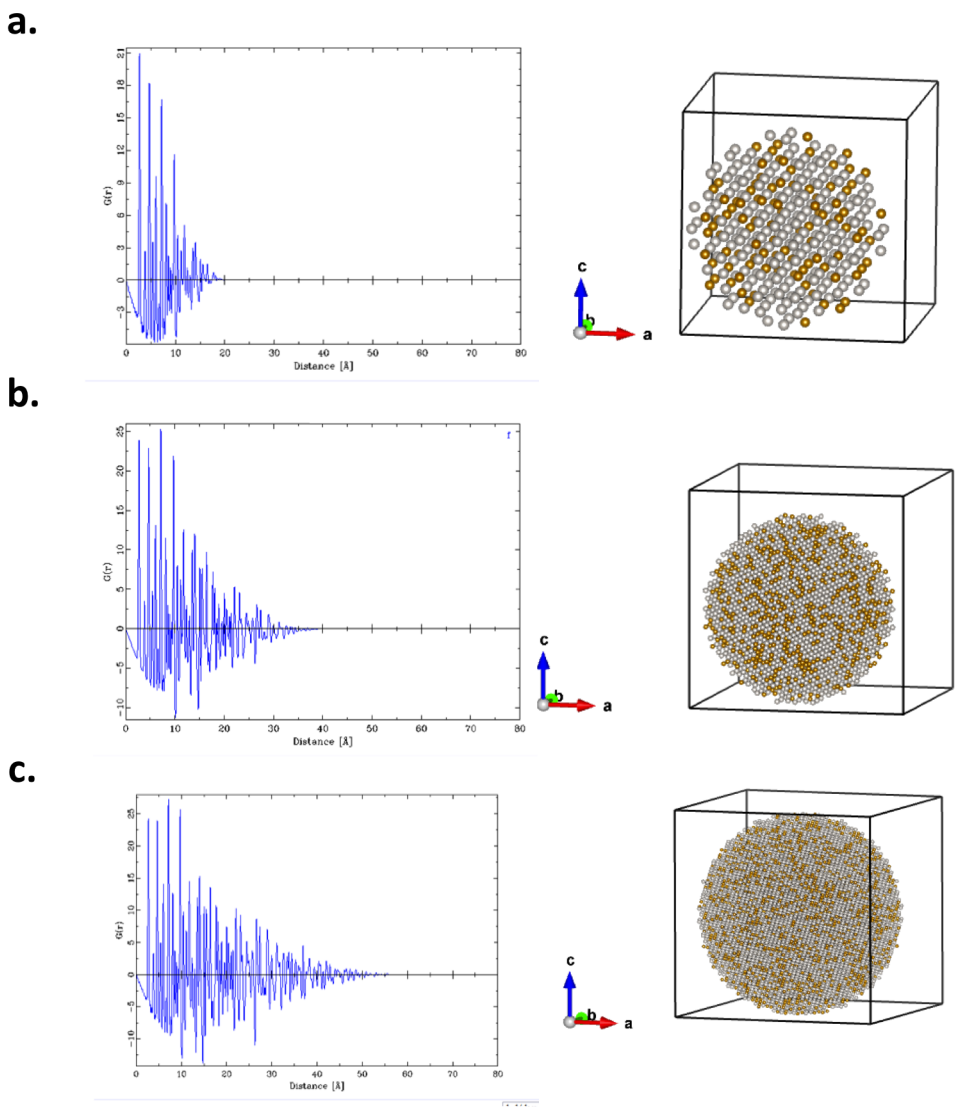

Figure 7.3: *Spherical $Fe_{16}Pt_{84}$ nanoparticle DISCUS models of (a) 2 nm, (b) 4 nm and (c) 6 nm with corresponding calculated PDFs.*

ter of the nanoparticle has on the corresponding calculated PDFs can be seen

from the DISCUS models in Fig.7.3a-c of diameter of 2 nm, 4 nm, and 6 nm, which can be identified by the point where the peaks diminish. The following

$Fe_{16}Pt_{84}$	k x k x k	Total no. of atoms
2 nm	6 x 6 x 6	642
4 nm	12 x 12 x 12	4694
6 nm	16 x 16 x16	16302

Table 7.1: *DISCUS parameters from FePt nanoparticle models in Fig. 7.3*

structural parameters were used; symmetry = Pm-3m, cell parameter = 3.885 Å(obtained from Petkov's preliminary XPDF results). Also, the experimental input parameters; Q_{max}= 27 Å, radiation type = neutrons, and wavelength = 0.15 Å, were defined in the main macros code. The supercell (k x k x k) input values and output parameters of the DISCUS models are detailed in Table 7.1. Page et al demonstrates further nanoparticles models of different morphology, size and atomic arrangement (created in DISCUS) have on the corresponding calculated PDFs [Page et al., 2010].

7.4 Nanoparticle Samples

The ultrafine FePt nanoparticle samples fabricated in Chapter 3.3.3 Section 3.3.3 were required to exhibit consistent physical and chemical properties with a high monodispersity, uniform size, shape, and composition. This was desired to ensure the collective ensemble analysed were a closest representative of an individual nanoparticle-surfactant. Also, FePt nanoparticles of a small diameter were fabricated in order to increase the signal of the neutron diffraction statistics to the surfactant layer (as small nanoparticles have a larger surface:volume ratio and so have a higher surfactant to FePt ratio in comparison to larger nanoparticles).

In each stage of the Nimrod investigations diffraction data was acquired from all or selected samples of the ultrafine FePt nanoparticles with isotopic surfactant substitutions. The isotopic substitutions were used to create contrast variation between the nanoparticle (core) and the surfactant layer (shell) effectively enabling the surfactant contribution to be probed.

7.5 Sample Quantification

In order to fully quantify the samples and to determine the nanoparticle input parameters (for nanoparticle modelling) the four FePt nanoparticle samples with different surfactant isotopic substitutions were analysed using the following techniques at the RI laboratories; FTIR to identify the presence of the surfactant layer on the nanoparticle surface, TEM analysis to determine the shape and size distribution of the nanoparticles, and conventional XRD analysis to determine the average crystallite size and phase of the nanoparticles. Additionally, the composition of all four samples was confirmed by external ICP-OES which was conducted at JAIST.

7.5.0.1 FTIR Confirmation of Surfactant Layer

FTIR spectra were acquired from the four samples in Fig.7.2 of FePt nanoparticles, with different surfactant isotopic substitutions. In the FTIR spectra vibration mode windows indicated by dashed lines in Fig.7.2 correspond to the unique vibrations of the surfactant backbone ($v(CH)$) and the functional groups of the acid ($v(COO)$), and amine surfactants ($v(NH)$). The vibration mode of the two peaks within the range of $\sim$1290cm^{-1} and $\sim$1670cm^{-1} (indicated by the turquoise dashed lines in Fig.7.2) correspond to the unique stretching frequencies of $v(COO)_{asymmetric}$ and $v(COO)_{symmetric}$ associated with the carboxylic acid group of OA bonded symmetrically and at angle to the nanoparticle surface, respectively [Tao, 1993].

The wavenumber separation, Δ, between the $v(COO)_{asymmetric}$ and the $v(COO)_{symmetric}$ stretch, correlates with the bonding formation. The Δ extracted from the FTIR spectra in Fig.**??** was extracted for each sample; sample 1: Δ = 128.67 cm^{-1}, sample 2 Δ = 146.76 cm^{-1}, sample 3 Δ = 148.29 cm^{-1} and sample 4 Δ = 133 cm^{-1}. The Δ identified for all four samples are just below or within the medium Δ range indicating that the chemical adsorption of the OA on the nanoparticle surface was via a bridging bidentate interaction between the COO^{-} moiety and the Fe on the nanoparticle surface. (Notably a small Δ <110 cm^{-1} corresponds to a chelating bidentate interaction and a large Δ = $200-300cm^{-1}$ corresponds to a chelating bidentate interaction.)

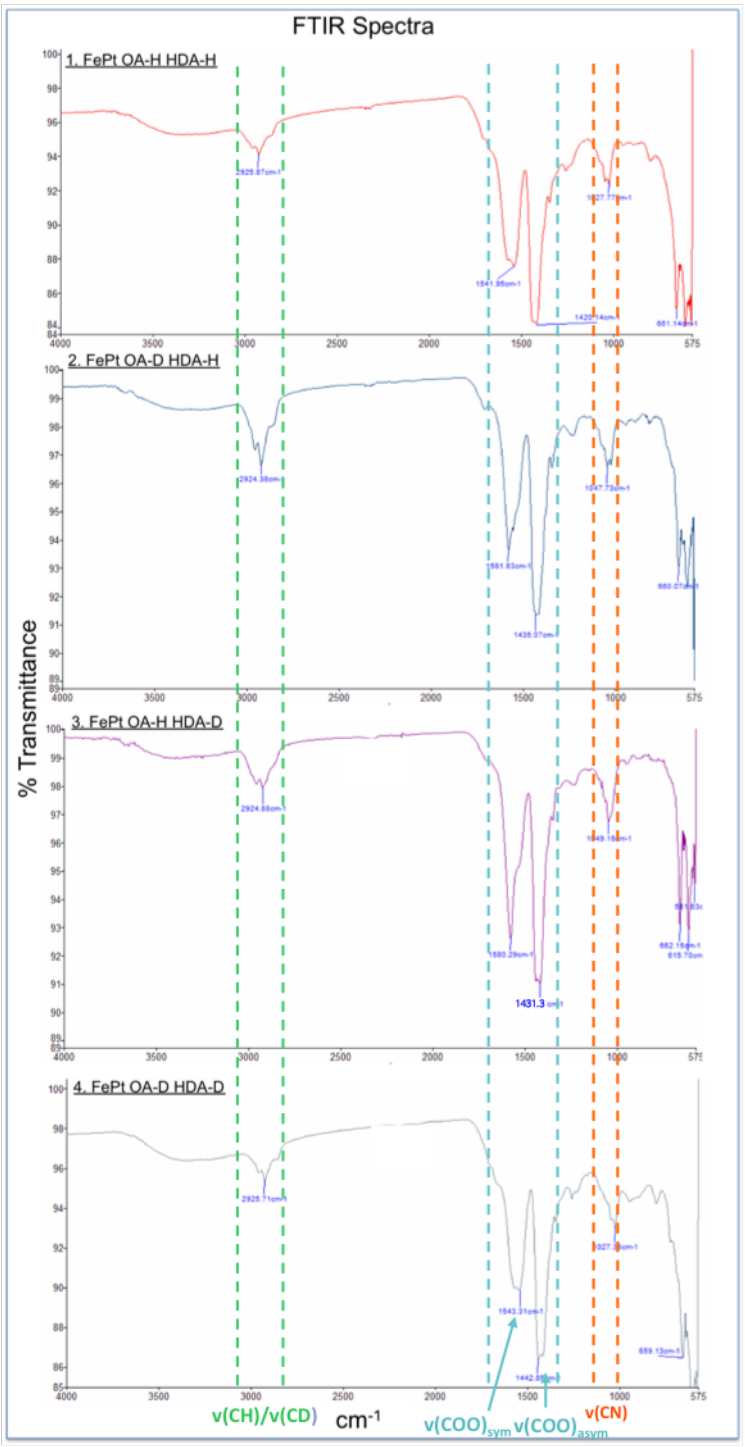

Table 7.2: *FTIR spectra of FePt nanoparticles with different surfactant isotopic substitutions. The stretching mode windows unique to specific bonds are also indicated.*

The vibration mode of the two peaks in the range of ∼2820 cm^{-1} - ∼3000acm^{-1} (indicated by the lilac dashed lines in Fig.7.2) correspond to the unique stretching frequencies of $v(CH_2/CD_2)_{asymmetric}$ and $v(CH_2/CD_2)_{symmetric}$ associated with the deuterated and protested hydrocarbon backbone of the OA and HDA surfactants, respectively. The vibration mode of the peak in the range of ∼1020 cm^{-1} and ∼ 1050 cm^{-1} (indicated by the grey line dashed lines in Fig.7.2) corresponds to the unique stretching frequencies of $v(CN)$ associated with the amine group of the HDA surfactant. These FTIR spectra observations confirm the adsorption of the OA surfactant onto the nanoparticle surface through the formation of a Fe-O monodentate bond and HDA surfactant onto the nanoparticle surface through the formation of a Pt-NH_2 bond.

7.5.0.2 Conventional TEM Analysis

The average size distribution of the nanoparticles (from TEM image analysis of the Feret diameter of 560 FePt nanoparticles) was calculated to be 2.10 ± 0.56 nm. The FePt OA-H HDA-H nanoparticle sample is observed to be well distributed on the substrate in Fig.7.4a. The FePt nanoparticle with OA-D HDA-H surfactant in Fig.7.4a, with OA-H HDA-D sample in Fig.7.4c and also with fully deuterated OA-D HDA-D surfactant in Fig.7.4d are agglomerated in some regions. The slight agglomeration is not expected to be due to the deuterated surfactant as it was evident that the deuterated samples dispersed well in polar solvents indicating the presence of the surrounding hydrophobic surfactant layer. Thus, it is proposed that the high concentration of the solvent suspension causd the nanoparticles to sinter together when the solvent evaporated.

7.5.0.3 Powder X-ray Diffraction of Ultrafine Nanoparticles

Powder XRD pattern analysis of the FePt nanoparticle samples using a conventional laboratory source Co-K_{alpha} diffractometer revealed the typical (111), (200), and (220) peaks representative of the chemically-disordered fcc phase of FePt. The closest reference match was identified as Pt ferroan $FePt_3$, a = 3.877 Å, as indicated by the black reference lines (JPCDS 001-1194) in Fig.7.5. The d_{hkl}-spacings were calculated from the diffraction data and assigned to the peaks

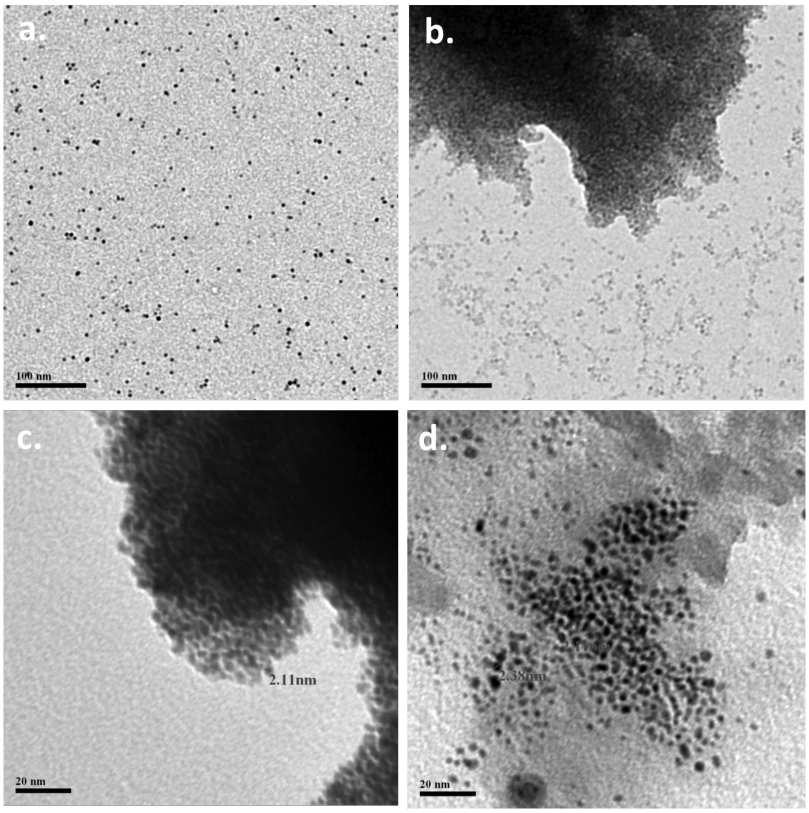

Figure 7.4: *TEM images of FePt nanoparticles with different surfactant isotopic substitutions (a) FePt OA-H HDA-H, (b) FePt OA-D HDA-H, (c) FePt OA-H HDA-D and, (d) FePt OA-D HDA-D.*

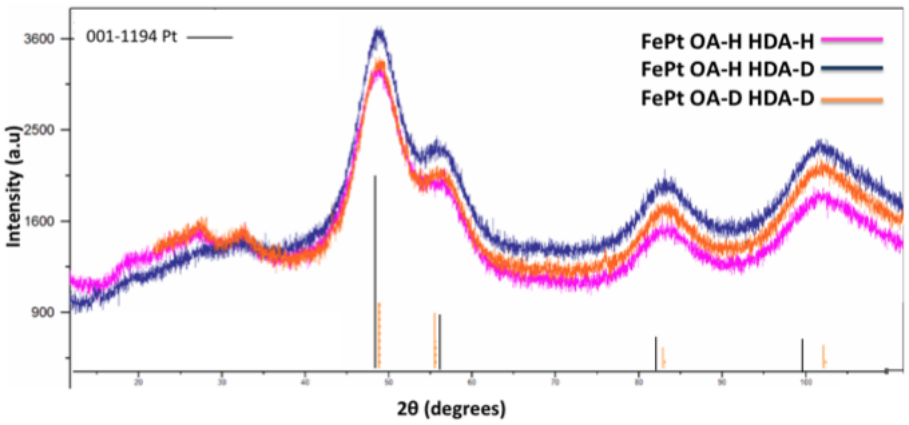

Figure 7.5: *X-ray diffraction pattern comparison of FePt nanoparticles with different surfactant isotopic substitutions with corresponding reference pattern, Pt ferroan (JPCDS-00-001-1194).*

of the fcc FePt nanoparticle planes. The sample composition of the nanocubes was confirmed for each sample by ICP-OES as: $Fe_{16}Pt_{84}$ for sample 1, $Fe_{14}Pt_{86}$ for sample 2, $Fe_{15}Pt_{85}$ for sample 3, $Fe_{14}Pt_{86}$ for sample 4. The following values of the average crystallite size of the nanoparticles was determined by Scherrer analyses; 2.2 nm for FePt OA-H HDA-H, 2.0 nm for FePt OA-H HDA-D, 1.9 nm for FePt OA-D HDA-H, and 2.0 nm for FePt OA-D HDA-D samples. These crystallite size values are in accordance with the average diameter of the nanoparticles acquired from TEM analysis.

7.5.0.4 Isotopic Substitutions

Isotopic substitutions can be used to perform contrast variation measurements (as introduced earlier in this chapter—see Section 2.3.3.1) by altering the ratio of protonated to deuterated solvent the contrast of the particle can be changed. Isotopic substitutions are particularly interesting when applied to core-shell particles, where the core (e.g. FePt nanoparticles) and shell (e.g. surfactant layer) have different SLDs and so high contrast. SLD calculations of the surfactants ($0.0776 \times 10^{10} cm^{-2}$), are two orders of magnitude smaller than that of the FePt nanoparticles ($5.528 \times 10^{10} cm^{-2}$) and the toluene solvent ($5.4 \times 10^{10} cm^{-2}$).

The isotopic substitutions in the Nimrod investigations were designed to specifically probe different elements in the system with the aim to extract structural information qualitatively and by difference measurements. Difference measurements simplify the data interpretation and can reveal correlations from specifically labelled elements. The neutron sample preparation and investigations within were designed with these order difference measurements in mind, with the aim to acquire the following information:

1. The difference between solutions FePt OA-H HDA-H in solvent-D and FePt OA-D HDA-D in solvent-D to give the structure of the system from the origin of the hydrogen sites on OA and HDA.
2. The difference between solutions FePt OA-H HDA-H in solvent and solvent to give the structure of the system from the origin of the FePt sample and OA and HDA surfactants.

7.6 Results Nimrod Investigations

The neutron powder diffraction investigations were conducted at the Nimrod beamline, where the success of the beamtime proposals enabled access to the large-scale neutron research facility over the course of this thesis. The objective of these investigations was to extract structural information from the whole FePt nanoparticle-surfactant system.

7.6.1 Data Acquisition

The samples in the Nimrod investigations were exposed to a monochromatic beam of neutrons of, λ = 1.5 Å, and a corresponding $E = 56meV$, enabling a Q_{max} up to 20 Å to be reached with a resolution of $\sim$0.32 Å. The raw diffraction data, was collected over the whole small and wide angle Q-range with a defined count time according to the sample set up, with the aim to obtain a high enough scattering intensity data and counting statistics suitable for PDF analysis. The data collection and processing stages are detailed in Fig.7.6.

7.6.2 Preliminary Nimrod Investigations

7.6.2.1 Standard Sample Cell Investigation

The first round of beamtime in the Nimrod investigation involved the suspension of the nanoparticles in the hexane solvent, in which FePt nanoparticles are most commonly suspended. The nanoparticle solvent suspensions were loaded into a cut out of the TiZr sample can shown in the side of the can in Fig.7.7a and the top of the open can in Fig.7.7b. The FePt nanoparticle sample dispersed in hexane was suspended in colloidal solution and sealed into the can using the flat plate lid and exposed to the collimated monochromatic beam of neutrons for a count time of 5 hours. Despite the nanoparticles being suspended in the hexane solvent before dispensing into the can (observable by the dark black coloured nanoparticle solution) a loss of statistics was observed with data collection over time. This was expected to be due to the gradual precipitation of the nanoparticles

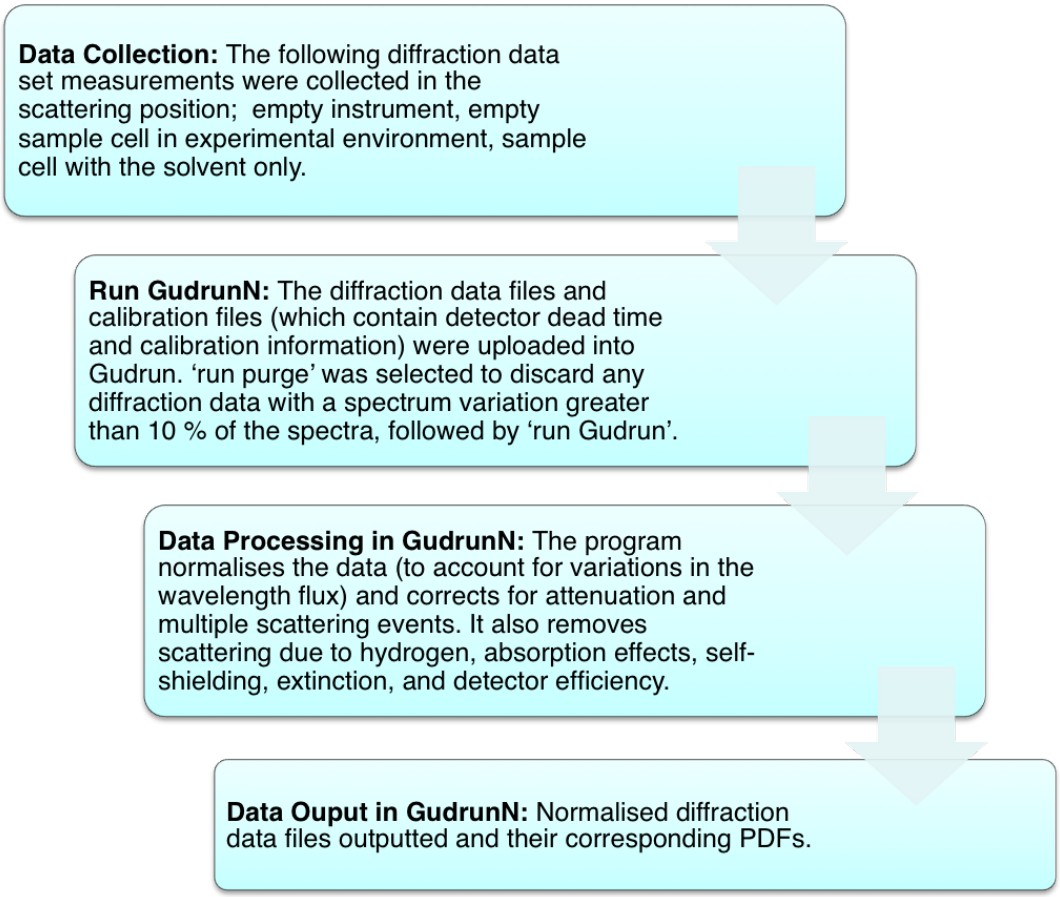

Figure 7.6: *Flow chart summarising the diffraction data collection and processing.*

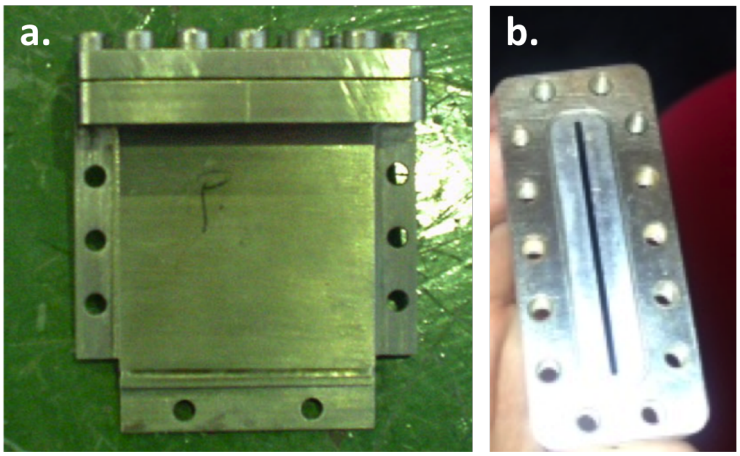

Figure 7.7: *TiZr sample can (a) side-on view (b) edge-on view.*

out of the solvent suspension, with the long count time.

7.6.2.2 Novel 'Open Window' Investigation

The next stage in the investigation was to resolve the suspension issue of the nanoparticles that resulted in low statistics in the first round. In this investigation a new solvent suspension and experimental design was implemented using a hydrocarbon wax (eicosane, $C_{20}H_{44}$) solvent and a novel 'open window' sample holder. The eicosane wax was selected as the 'solvent' with the aim to disperse the nanoparticles fully in the melted wax in the new 'open window' sample holders preventing the nanoparticles from precipitating out of solution (on drying). The novel 'open window' aluminium sample holder was designed manufactured

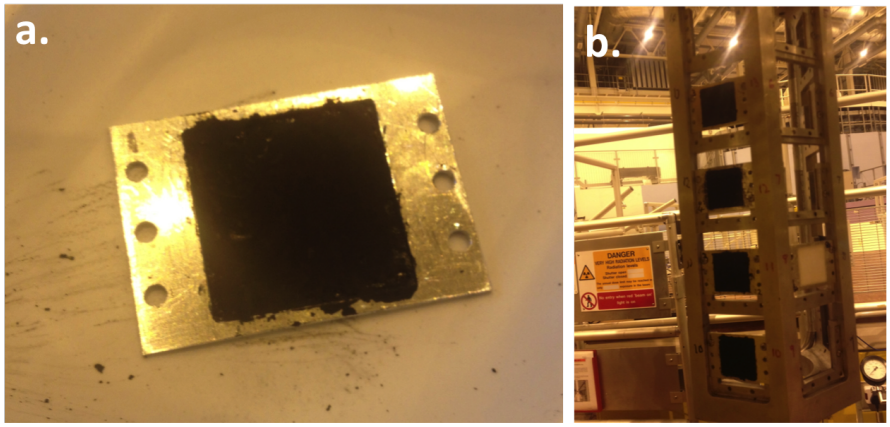

Figure 7.8: *Novel'open window' aluminium sample holder with a central square mould cut out with (a) nanoparticle eicosane wax solution dispensed in the 'open window' (b) samples mounted in sample changer.*

for this investigation. The 'open window' region of the sample holder enabled the sample to be exposed directly to the beam, which was beneficial for the neutron diffraction measurements as there was no requirement to subtract any background interference due to the sample holder. The dried nanoparticle sample solutions were suspended in the melted wax and sealed, on drying, into the newly designed aluminium sample holders as shown in Fig.7.8a (the sample holder is of dimension 2 x 20 x 20 mm which allowed for 1.6 cc (1.245 g) of eicosane-sample suspension.) The 'open window' sample holder could be readily attached to the standard Nimrod sample changer, as shown in Fig.7.8b. This set up enabled

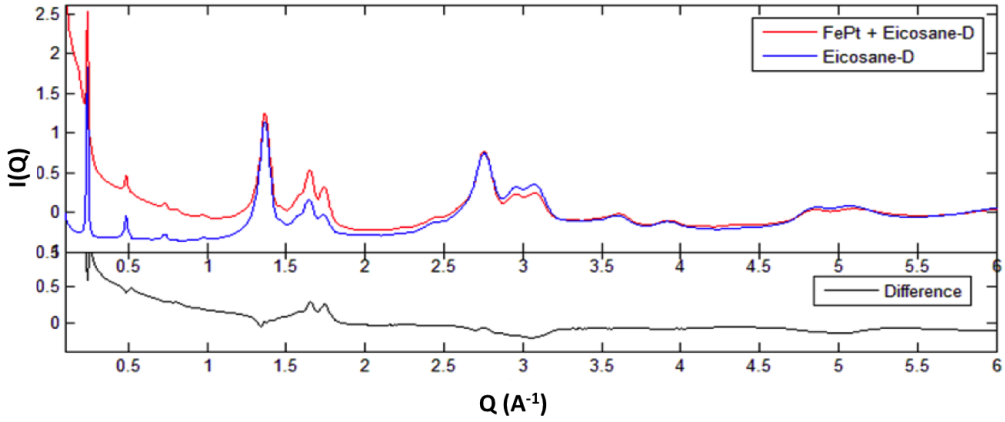

Figure 7.9: *Difference diffraction data (black line) between FePt OA-H HDA-H nanoparticles in eicosane-D44 (red line) and pure eicosane-D (blue line).*

four samples to be loaded and exposed to the collimated monochromatic beam of neutrons with each sample having a count time of 8 hours making optimum use of experimental time. The nanoparticle-solvent solution could also be readily retrieved from the protonated wax for re-suspension in the deuterated wax, and data could be collected from all of the samples. However, despite a high nanoparticle loading, which accounted for approximately one third of the total scattering signal, the semi-crystalline eicosane wax had a preferred orientation, which resulted in strong Bragg peaks. The FePt nanoparticles were buried amongst the strong peaks from the eicosane-d44 diffraction data, as shown in Fig.7.9 owing to the low proportion of FePt nanoparticles in the overall sample. The system did however display a significant small angle signal associated with the nanoparticle surfactant contribution, as observed in the low-Q region of the difference curve (black line) in Fig.7.9. The signal from the surfactant was promising, however it was required to develop a new method in order to avoid the crystalline diffraction peaks of the solid wax suspension. The newly designed sample holders did however allow for efficient use of the beam time by use of the sample changer and the open window prevented any need for background extraction. Therefore the sample holders would be beneficial for future users to analyse pure solid solvent wax suspensions.

7.7 Novel Flow Cell Nimrod Investigations

The previous two Nimrod investigations led to the design of a completely new optimised instrumental novel flow cell instrumental set-up to analyse the nanoparticles in their most abundant state—dispensed in a colloidal solvent suspension. Additionally, the solvent was changed from an eicosane suspension to an amorphous liquid suspension to ensure that there would be no sharp Bragg contributions from the solvent (as encountered in the previous round). The suspension of the nanoparticles in different long chain polar solvents (hexane, toluene, ethanol) was tested and toluene was identified to keep the nanoparticles well dispersed without falling out of the sample suspension in comparison to hexane. The sample loading was increased in comparison to the previous rounds to ensure a high nanoparticle concentration in attempt to increase the contribution of the scattering from both the nanoparticle and the surfactant. The novel flow cell set up illustrated in Fig.7.10 consists of an external and internal looped steel hollow tubing connecting the upper and lower nozzle of the TiZr can, and a gore connector tubing for the inflow and outflow of the sample. The external region of the flow cell set-up in Fig.7.10, consists of a nanoparticle solution injector input, a connector valve designed to control the 'insertion/re-collection' flow of the nanoparticle solution (current set up has valve open for nanoparticle solution recollection after experiment) and a peristaltic pump that is latched onto the flexible gore tubing (with a Teflon coated inner diameter, to protect against solvent dissolution) to circulate the flow cell solution in the tubing network. The internal region of the flow cell is contained within the sealed vacuum chamber where the sample, in the TiZr can, is positioned central to the incoming neutron beam. The nanoparticle solution was circulated through the flow cell at a suitable flow rate in the direction shown in Fig.7.10 such that the nanoparticles would remain dispersed and suspended in solution at all times.

7.7.1 Flow Cell Data Acquisition

In this flow cell investigation diffraction data was acquired from the following FePt nanoparticles with surfactant isotopic substitutions (the average concentration of $1.76 \times 10^{-2} mol.L^{-1}$, was desired however there were slight discrepen-

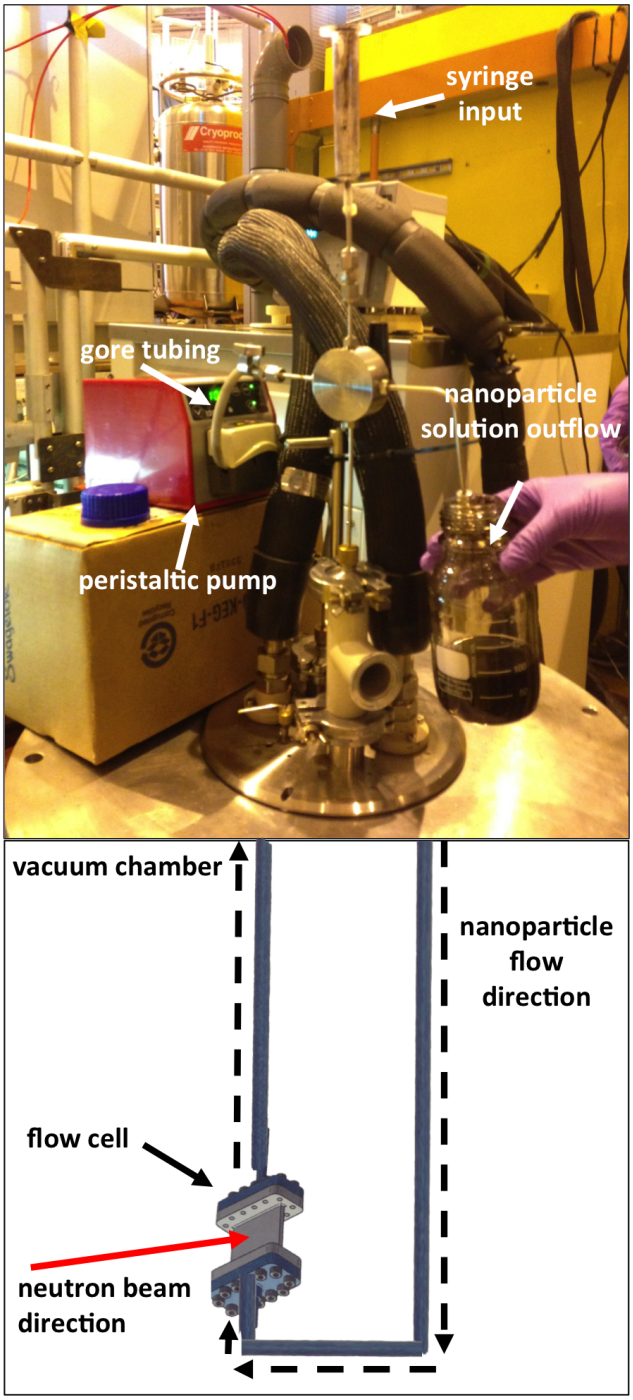

Figure 7.10: *Newly designed experimental flow cell set-up. Upper image: External region for nanoparticle solution input and pump flow source (image captured during sample recollection stage). Lower image: Internal region with the flow cell set up in a vacuum chamber and the sample cell positioned central to the incoming neutron beam.*

cies between the concentrations). Ideally the full set of samples with isotopic substitutions—including the FePt OA-H HDA-D and FePt OA-H HDA-D nanoparticles in toluene-H and redispersed in toluene-D—would have also been analysed enabling a full set of measurements to be collected, as detailed in Section 7.5.0.4. However, it was not economically feasible to fabricate the full set of isotopic substitutions for these flow cell investigations thus the following most important samples were probed:

- FePt OA-D HDA-D sample suspended in toluene-H and re-suspended in toluene-D ($\sim$0.2 g/mL)
- FePt OA-H HDA-H sample suspended in toluene-H and re-suspended in toluene-D ($\sim$0.4 g/mL)
- Background standard solutions of pure toluene-D
- Background standard solutions of pure toluene-H

Each sample was circulated in the flow cell set up and exposed to the collimated monochromatic beam of neutrons for an average count time of 4.5 hours per sample. Notably, in an attempt to increase the statistics the mass of the FePt OA-H HDA-H sample was increased to 0.4 g/mL toluene. This increase was not economically feasible for the FePt deuterated samples due to the limitation of isotopicallly-substituted samples. Thus only the solvent contributions from only the FePt nanoparticles with protonated surfactants were analysed.

7.7.2 Flow Cell Diffraction Patterns

The diffraction patterns acquired from the isotopic substitutions—spanning both the high-Q and low-Q range—are plotted in Fig.7.11 (offset from the zero baseline for clarity). Distinct differences can be observed between the samples suspended in deuterated toluene in comparison to the sample suspended in the protonated solvents. The diffraction peaks of the sample in the deuterated samples are broader and have a less distinct background. Also a higher baseline was evident for the samples with protonated solvents in comparison to the samples in deuterated solvents, ascribed to the incoherent scattering contributions from

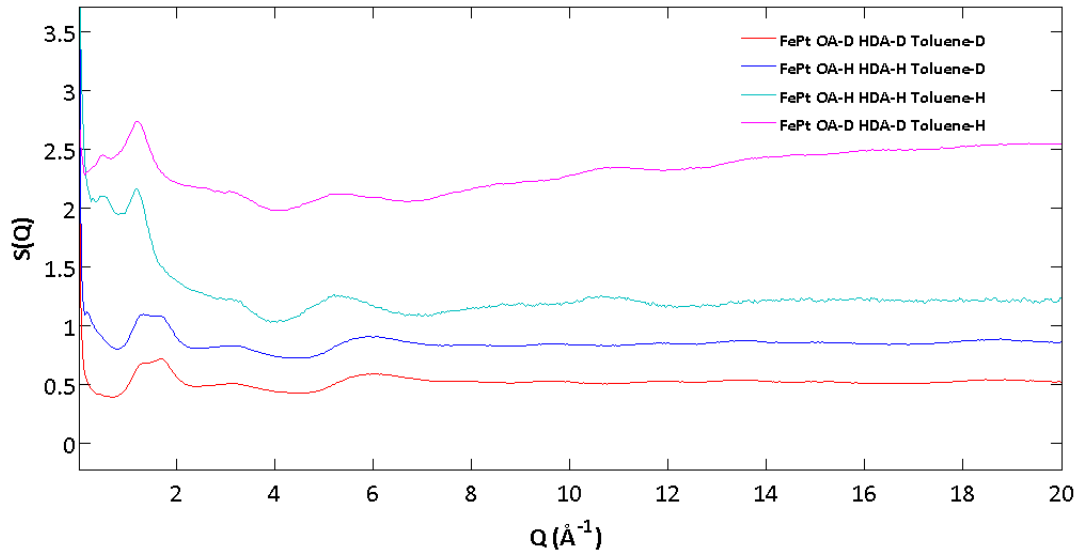

Figure 7.11: *Flow cell neutron diffraction patterns of FePt nanoparticle isotopic substitutions in deuterated and protonated toluene solvent.*

the hydrogen. The solvent contributions were removed by subtracting the FePt OA-H HDA-H sample in toluene-D (blue curve) from the toluene-D (green curve) to give the neutron diffraction pattern difference curve (black curve) as plotted in Fig.7.12. The whole difference curve in the diffraction pattern (in Fig.7.12)

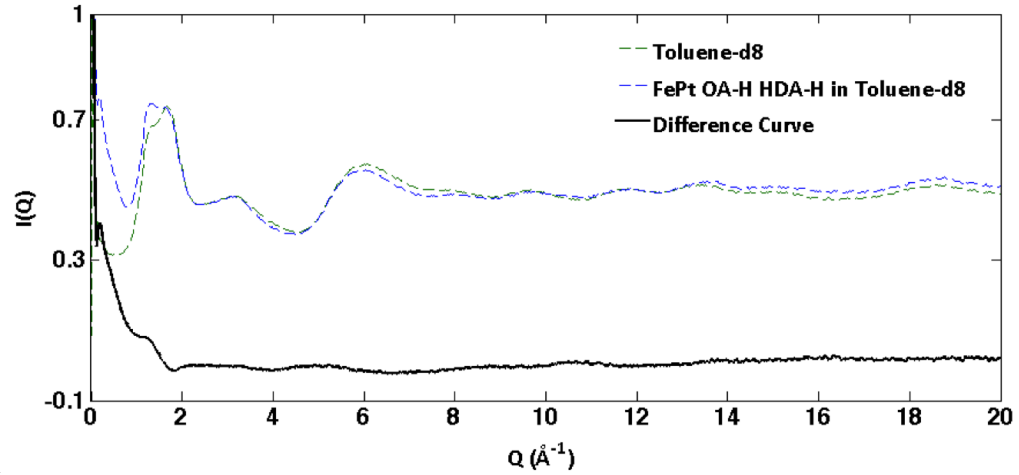

Figure 7.12: *Diffraction data of difference curve (black line) showing the FePt OA-H HDA-H nanoparticle contribution calculated from subtraction of FePt OA-H HDA-H nanoparticles in toluene-D (blue line) and FePt OA-D HDA-D nanoparticles in toluene-D (red line).*

is diplayed in Fig.7.13 to inspect the FePt nanoparticle Bragg peak contribution.

The Bragg peaks from the FePt nanoparticles are manifested in the background contributions resulting in their peak intensities being difficult to distinguish. The peak positions that correspond with the planes from the fcc FePt nanoparticle phase are denoted in Fig.7.13. The low-Q region of the difference curve in the

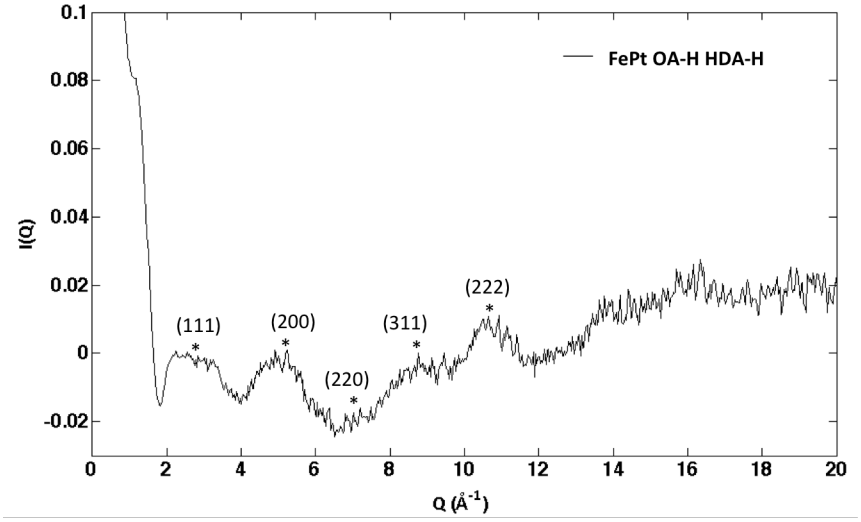

Figure 7.13: *High Q-region of difference curve contribution from the FePt OA-H HDA-H nanoparticles.*

diffraction pattern in Fig.7.12 was re-plotted in Fig.7.14, to inspect the surfactant contribution. A significant signal in the small angle region can be observed with a steep rise in intensity at low-Q, associated with the incoherent scattering from the presence of the surfactants. The sharp peak identified at Q = 0.1967 Åcorresponds to a real space value of 31.94 Å(3.19 nm) which could be ascribed to the distance of the nanoparticle (2 nm) plus compacted surfactant layer (1.19 nm).

7.7.3 Flow Cell Neutron PDFs

The corresponding NPDFs of the diffraction patterns of the isotopic substitutions (in Fig.7.11) are displayed in Fig.7.15, with the NPDFs from the pure solvents without sample contribution in the lower plot (offset from the baseline). Differences between the PDFs of the FePt nanoparticles in the protonated and deuterated solvents are evident in the PDFs and typically correspond to the characteristic peaks of the pure toluene PDFs although additional peaks are evident in the PDFs of the samples, indicating contributions from the sample. The sam-

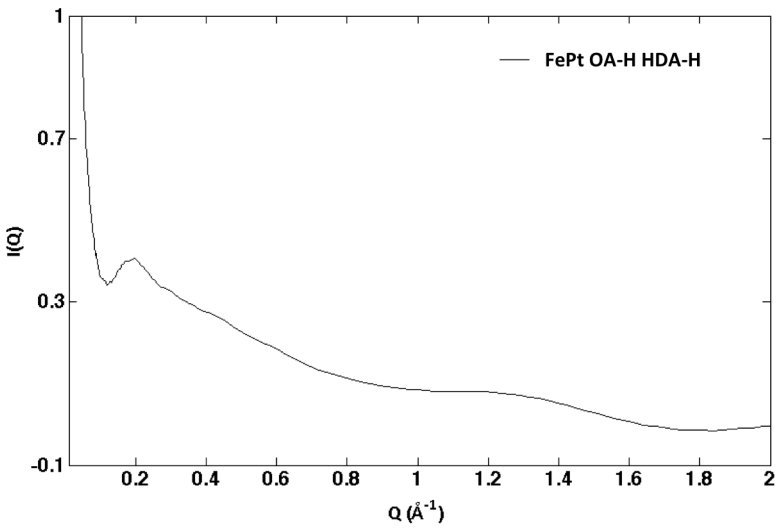

Figure 7.14: *Low Q SANs region of difference curve contribution from the FePt OA-H HDA-H nanoparticles.*

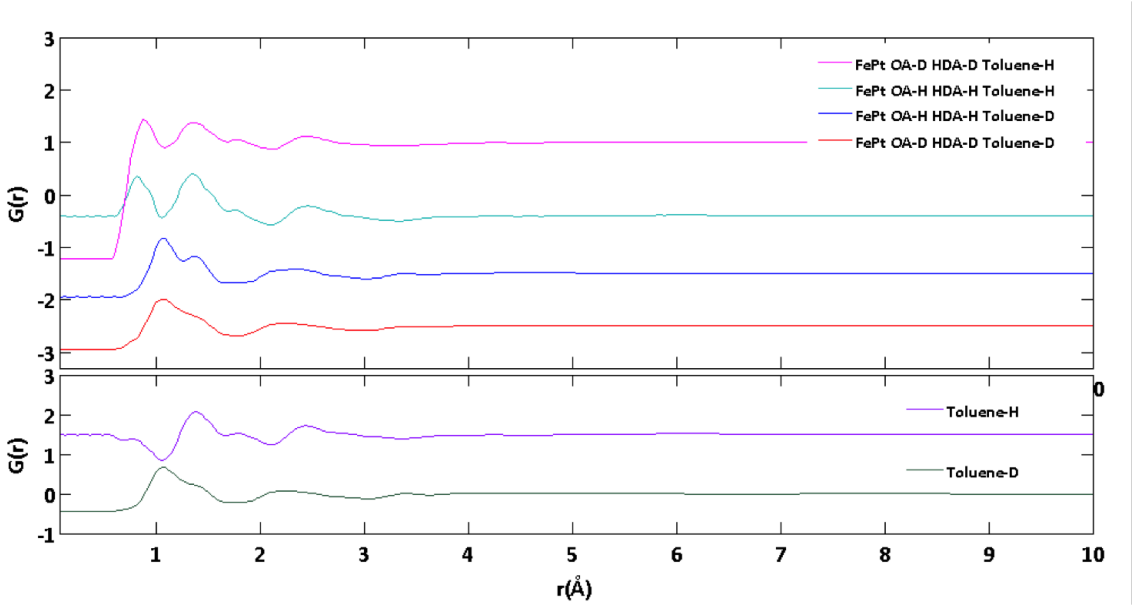

Figure 7.15: ***Upper plot:*** *Flow cell NPDFs of FePt nanoparticle isotopic substitutions in deuterated and protonated toluene solvent (offset from the baseline).* ***Lower plot:*** *Flow cell NPDFs of pure deuterated and protonated toluene.*

ples with protonated surfactants showed the most pronounced differences to the pure toluene PDFs. The features in the pure toluene-H PDFs and toluene-D PDFs show a well defined first co-ordination shell representative of toluene methyl carbon-methyl carbon and a second diffuse co-ordination shell representative of

a toluene ring center to ring center.

The PDF difference curve of the FePt OA-H HDA-H in toluene-D (blue curve) and FePt OA-D HDA-D in toluene-D (red curve) is displayed in Fig.7.16, to effectively reveal the structure of the system from the origin of the hydrogen sites on the OA and HDA surfactants.

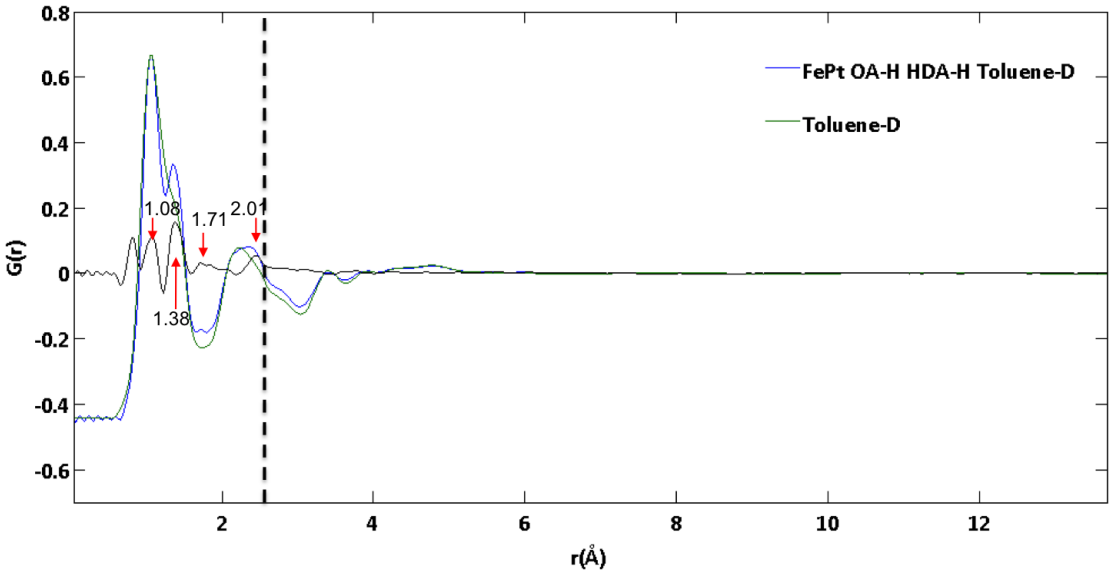

Figure 7.16: *FePt OA-H HDA-H in toluene-D (blue) and pure toluene-D (green) with difference curve (black) with r-values of peaks at low r denoted.*

The co-ordination peaks in the low-r region in Fig.7.16, below the position of the first NN peak of the FePt alloy (indicated by the dashed line) are ascribed to the intramolecular contributions of the organic surfactant (and possibly excess solvent). Solvent perturbation and interaction with the nanoparticle and surfactant layer can also mediate the peaks in the PDFs. The peaks denoted on the PDFs are ascribed to the following intramolecular bonds (under the assumption that the peaks were not the result of the Fourier Transform):

- The peaks at 1.05 and 1.08 Å could be ascribed to the hydrogenated surfactant backbone C-H(1.09 Å) contribution.
- The peaks at 1.35 and 1.38 Å could be ascribed to the alkene contribution in the surfactant backbone, C=C (1.38 Å). They could also be ascribed toluene ring contribution, C-C and C=C of which are all the same length (1.397 Å).

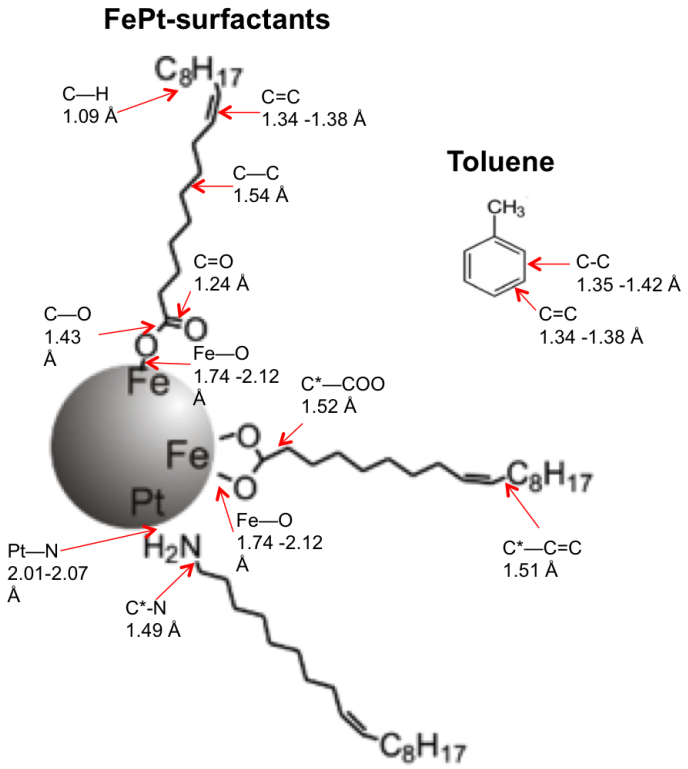

Figure 7.17: *Schematic of an FePt nanoparticle (with oleic acid and oleylamine surfactants attached) and toluene, with the intra-molecular bond lengths denoted.*

- The peaks at 1.71 Å could be ascribed to the Fe-O contributions (1.74 Å)
- The peaks at 2.00 and 2.01 Å could be ascribed to the Pt-N contributions (2.01-2.07 Å)

Peaks beyond these denoted points are indicative of the intermolecular bond distances between the surfactant chains. For clarity, the theoretical bond lengths (acquired from the 'Tables of bond lengths determined by X-ray and neutron diffraction' [Allen et al., 1987]) are denoted on the schematic of the FePt-surfactant and toluene in Fig.7.17 (notably the olelyamine surfactant is imaged but it is directly comparable to HDA surfactants in terms of bond length distances). The results show evidence of the surfactant layer contributions and excess solvent in the PDF. In addition the presence of the Fe-O bond corresponds with the theory that the functional group of OA bonds to the Fe of the FePt nanoparticle and the presence of the Pt-N bond corresponds to the HDA bonds to the Pt of the FePt nanoparti-

cles through electron donation from the nitrogen atom of the NH_2 group.

7.7.4 Flow Cell Discussion and Future Outlooks

In conclusion, the novel flow cell set up was designed and optimised to enable diffraction data to be acquired from the FePt nanoparticles with isotopic surfactant substitutions. Difference subtractions were conducted to subtract the solvent contributions. From analysis of the difference PDF pronounced co-ordination peaks were observed in the low-r region of the PDF (demonstrating the sensitivity of neutrons to the surfactant layer). Structural information from the surfactant contributions were extracted from the peaks at low r (positioned before the first NN peak of the FePt nanoparticles). The peaks were ascribed to theoretical bond length distances of the surfactant and excess solvent. Extracting peak values from complex systems can be challenging due to the multitude of scattering atoms in the system that can cause difficulties in yielding interatomic correlations from individual modes. Also, the contribution from the partial penetration of the toluene solvent into the surfactant shell, were considered negligible in this investigation, but they can also feature in the scattering curves and resultant PDFs. Penetration of the solvent is an important feature to consider that has great potential for future exploration.

Developments to the nanoparticle synthesis and flow cell investigations are required to improve the counting statistics from the FePt nanoparticle signal. The continuation of this flow cell investigation would enable optimisation of this novel technique. For example, the isotopically substituted nanoparticles could be synthesised with a larger diameter (to 10 nm) to increase the signal from the FePt contribution. Additionally, the synthesis yield could be increased to enhance the Bragg peak contribution from the FePt nanoparticle. In addition, the mass of sample for the neutron PDF investigations could be up-scaled by fabricating the deuterated surfactants in house instead of out-sourcing them. This would involve a specialised hydrogen-deuterium exchange reaction of the hydrogenated surfactants (OA [Darwish et al., 2013] and the original OLA [Liu et al., 2014]). On improving the statistics and supply of deuterated surfactants this would enable future NPDF investigations to be conducted on the following isotopic substitutions:

1. The difference between solutions FePt OA-H HDA-D in solvent-D and FePt OA-D HDA-D in solvent-D would give the structure of the system from the origin of the hydrogen sites on OA.
2. The difference between solutions FePt OA-D HDA-H in solvent-D and FePt OA-D HDA-D in solvent-D would give the structure of the system from the origin of the hydrogen sites on HDA.
3. The difference between solutions FePt OA-D HDA-D in solvent-H and FePt OA-D HDA-D in solvent-D would give the structure of the system from the origin of the hydrogen sites on solvent.
4. Additionally the fully protonated OA-H and HDA-H against a solvent-D background would provide the best contrast in the SANs region providing surfactant-surfactant information.

Developments of the flow set up are also required to prevent the necessary delays between sample runs owing to the requirement to wait until the sample was no longer 'hot' (radioactive) after each run (which resulted in experimentally and economically expensive neutron beamtime being lost). The flow cell set up could be optimised by devising a more efficient way to input and retrieval of the sample from the flow cell set up (rather than the temporary plastic syringe attached to a nozzle, as used in this investigation). For example, a permanent closed loop input/output stop cock flow system would enable controlled input and retrieval of the sample into a sealed container preventing the need to open the set up. Thus, preventing the need for down time between data collection runs.

The neutron diffraction flow cell investigation could also be extended to determine the effect different suspension solvents have on the nanoparticle surfactant layer and on the nanoparticle aggregation properties. Use of the empirical potential structure refinement (EPSR) package could enable the solvent structural information to be obtained. EPSR—developed by Alan Soper and Daniel Bowron of Rutherford Appleton Laboratory—is a well established modelling package typically used to interpret solvent structure and behaviour. To achieve full data analysis of the whole nanoparticle-surfactant-solvent system the nanoparticle-surfactant model could be incorporated into the solvent model and refined. This complex model would enable the effect of penetration of the solvent with the surfactant layer to be modelled.

7.8 Dry Powder Nimrod Investigations

Complementary neutron and high-energy XPDF investigations were conducted in the analysis of the FePt OA-H HDA-H sample in the dry state. The samples were analysed in the dry state in order to increase the mass of sample analysed. This high nanoparticle loading enabled the extreme of the neutron diffraction technique to be investigated, it also removed the need for solvent subtraction and enabled a more direct comparison of the complementary analysis techniques.

7.8.1 Data Acquisition

The NPDF investigation was conducted at the Nimrod beamline following the same procedure as described for the initial Nimrod investigations of the sample in hexane (except with a dried sample). Sample preparation for the Nimrod investigation involved filling the TiZr sample can with two dried batches of nanoparticles (the dry sample 1 $Fe_{16}Pt_{84}$ OA-H HDA-H nanoparticles plus an additional batch of $Fe_{14}Pt_{86}$ OA-H HDA-H nanoparticles) enabling a high sample loading of ($\sim$3.86 g). The sample was exposed to a monochromatic beam of neutrons of λ = 0.15 Åwith a corresponding, E = 56 meV, enabling a Q_{max} up to 20 $^{-1}$ and a PDF resolution of $\sim$0.31 Å.

The preliminary XPDF investigation was conducted at the I-15 beamline at the DLS synchrotron. The diffraction data was collected from the dry sample over a 2-hour count time. Sample preparation for the XPDF investigation involved insertion of the dry $Fe_{16}Pt_{84}$ OA-H HDA-H nanoparticles ($\sim$1.6 mg) into the narrow opening of the 2 mm glass capillary up to a length of 1 mm. The sample region of the sample capillary containing the dry FePt OA-H HDA-H sample. The sample was exposed to a monochromatic beam of X-rays of λ = 0.1722 Å with a corresponding E = 72 keV, enabling a Q_{max} of 27 Å^{-1} and a PDF resolution of $\sim$0.232 Å. The beam was focussed down to approximately 70 μm without sacrificing much flux, allowing for the required beam size to achieve a reasonable resolution on the 2D detector. The X-ray diffraction data was collected from the rotating dry sample over a 10-minute count time. The raw neutron and X-ray diffraction data was treated for background and normalised. Corresponding PDFs were acquired using both the GudrunN program (for neutron diffraction data interpretation) and

GudrunX (for X-ray diffraction data interpretation).

7.8.2 Neutron Diffraction Pattern of Dry FePt OA-H HDA-H Nanoparticles

The neutron diffraction data, acquired from the dry FePt OA-H HDA-H sample, plotted in Fig.7.18, displayed a similar signal to the neutron diffraction data acquired from the colloidal FePt OA-H HDA-H sample in (Fig.7.12 investigated in Section 7.7). In comparison to the colloidal sample, the diffraction data in Fig.7.18

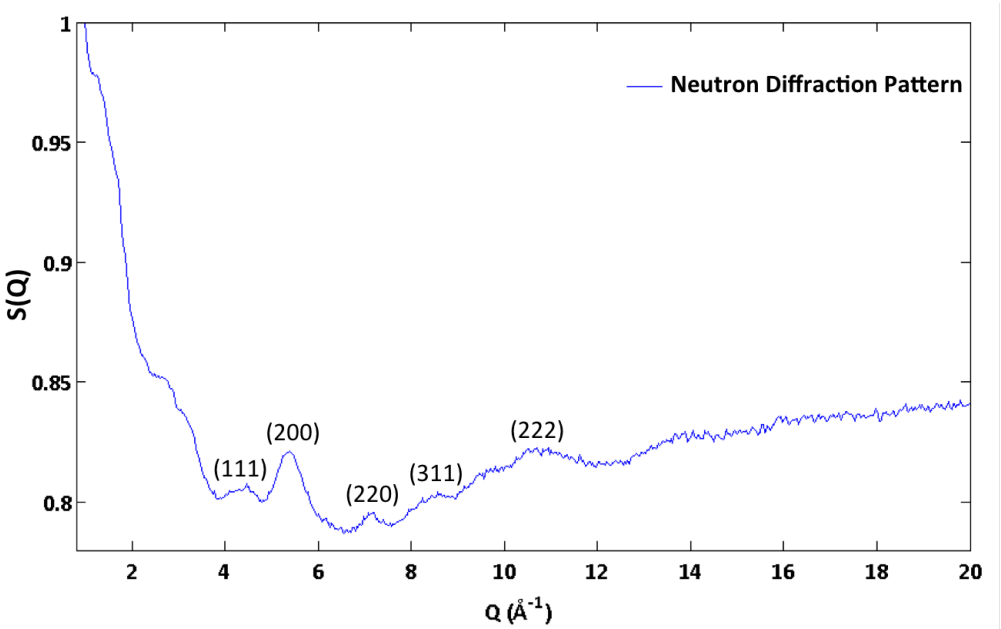

Figure 7.18: *Neutron diffraction data of dry FePt OA-H HDA-H nanoparticles.*

showed a similar significant rise at low-Q which was ascribed to the surfactant contribution. Also, weak (but yet slightly more pronounced) Bragg peaks ascribed to the FePt nanoparticle contribution manifested in the background. The peaks are ascribed to the fcc FePt nanoparticle phase as denoted in Fig.7.18. Compartively, the NPDF of FePt nanoparticles in the dry sample showed slightly stronger Bragg peak contributions from the FePt nanoparticles which ws expected to be due to the lack of solvent contributions.

7.8.3 High Energy X-Ray Diffraction Pattern of Dry FePt OA-H HDA-H Nanoparticles

The X-ray diffraction data acquired from the dry FePt OA-H HDA-H sample displayed sharp Bragg peaks of much higher intensity than the neutron diffraction data. The Bragg peaks were ascribed to the fcc FePt nanoparticle phase, as denoted in Fig.7.19. The high flux achievable from using X-rays as the analytical

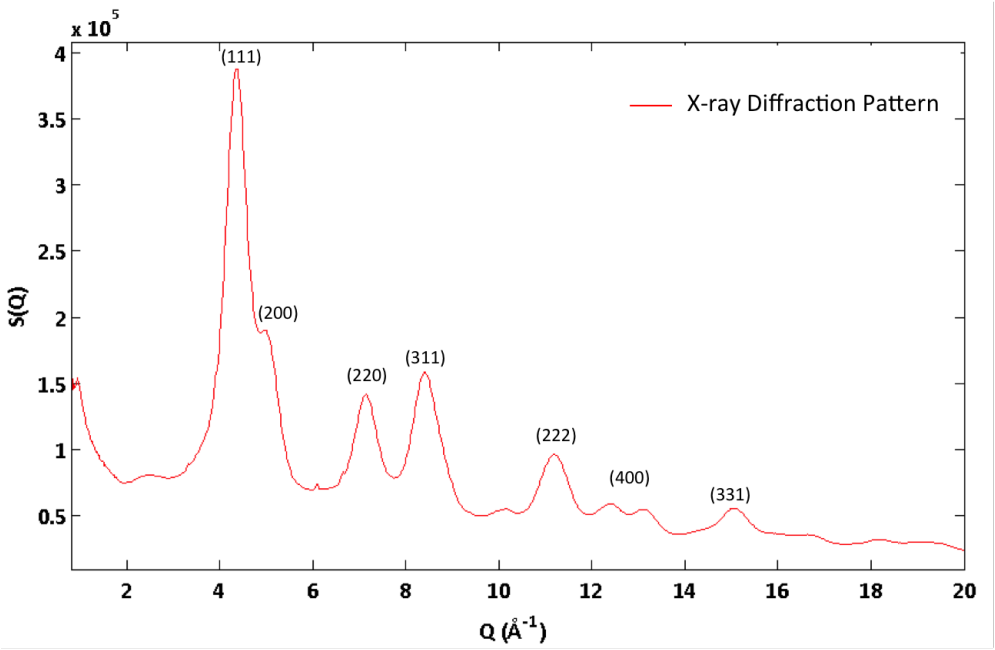

Figure 7.19: *X-ray diffraction data of dry FePt OA-H HDA-H nanoparticles.*

probe—in comparison to neutrons—is evident by the high intensity of the Bragg peaks and the comparatively lower count time (the X-ray count time was a factor of ten lower than neutron count time).

7.8.4 X-ray and Neutron PDF Comparison

The corresponding NPDF and XPDF data sets were acquired from the diffraction data (in Fig.7.18 and Fig.7.19 respectively) and are displayed in Fig.7.20. The NPDF (blue curve) displayed pronounced coordination peaks in the low-r region (before the first dashed line), which corresponding to the surfactant contribution.

The peaks are correlated with the proposed bond distances of the intermolecular surfactant bonding and indicated on the PDF. The first three NN peaks in the high-r region of the NPDF correspond to the expected NN peak distances of the fcc FePt nanoparticles and are denoted on the PDF (as detailed in the Table 7.3). The XPDF (red curve), divided by 100 for clarity, displayed two very weak

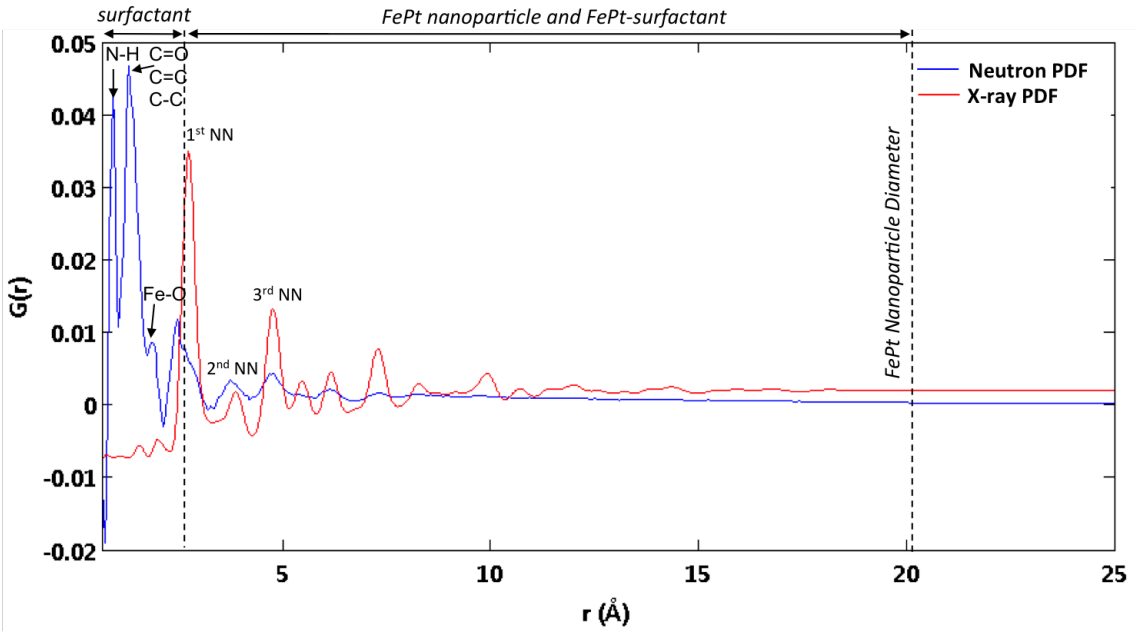

Figure 7.20: *NPDF and XPDF of dry FePt OA-H HDA-H nanoparticles with corresponding bond lengths and NN positions denoted (XPDF divided by 100 for clarity).*

coordination peaks in the low-r region which could correspond to a weak signal from the surfactant layer. The first three NN peaks (denoted) also correspond well to the expected NN peak distances of fcc FePt nanoparticles (as detailed in the Table 7.3). The second dashed line indicates the point where the peaks in the XPDF diminish at r = 20 Å(2.0 nm) which corresponds closely with the FePt nanoparticle diameter.

Radiation Source	FePt OA-H HDA-H	1st NN (Å)	2nd NN (Å)	3rd NN (Å)
Neutron PDF	Dry FePt	2.64	3.75	4.77
X-ray PDF	Dry FePt	2.79	3.87	4.80

Table 7.3: *Nearest neighbour distances extracted from the neutron and XPDF in Fig.7.20 of dry FePt OA-H HDA-H nanoparticles.*

The distance, from the central atom to the first NN shell in the NPDF is of a distance, 2.64 Å, which is slightly larger than the first NN distance extracted from

the XPDF which is of a distance, 2.79 Å. The same applied to the distance from the central atom to the second NN shell in the NPDF, which is of a distance, 3.75 Å, and is slightly larger for the XPDF at 3.88 Å. Similarly the 3rd NN shell which is at 4.62 Å in the XPDF and 4.30 Å in the NPDF. The larger NN distances extracted from the XPDF—in comparison to the XPDF— could be ascribed to a slightly lower Pt content in the sample analysed in the X-ray measurements. This lower Pt content likely impacted the short range order distances e.g. a lower Pt content results in a larger lattice parameter value [Jochym et al., 2015], and so larger NN distances. Alternatively these differing NN values in the XPDF and NPDF could just be a result of the larger errors associated with identifying the peak position in the NPDF oweing to the low signal.

7.8.5 Complementary Neutron and X-ray PDF Analysis Conclusion

The NPDF of the dry FePt OA-H HDA-H sample displayed broad coordination peaks in the low-r regions which could be ascribed to the close packed nature of the dry sample resulting in the compression of the surfactant layer. Thus, highlighting the benefit of the flow cell investigations to probe the surfactant layer in its most abundant state. However, the NN coordination peaks from the FePt nanoparticle were much more pronounced in comparison to the NN peaks from the NPDF of the colloidal sample (analysed in the flow-cell experiments) owing to the higher nanoparticle loading. The high intensity peaks from the surfactant layer in the NPDF and the high intensity peaks from the FePt nanoparicle in the XPDF demonstrates the benefit of using complementary techniques to analyse the whole surfacant-nanoparticle layer.

In addition, the XPDF of the dry FePt OA-H HDA-H sample displayed sharp NN co-ordination peaks associated with the FePt nanoparticle contribution highlighting the sensitivity of X-rays to ‘heavy’ elements e.g. the FePt alloy. The pronounced NN peaks were visible at high r and only diminished on reaching the nanoparticle diameter, thus provided sufficient structural information for nanoparticle modelling as conducted in the following section.

7.9 Nanoparticle Modelling and Refinement

The chemical in-homogeneities of the FePt nanoparticles such as, core-shell or short-range order were analysed using nanoparticle modelling and RMC refinemnet. An initial input model of a 2 nm $Fe_{16}Pt_{84}$ nanoparticle, in the fcc phase, was built using DISCUS for the refinement process as detailed in Section 7.3.3. The following structural parameters were used; symmetry = Pm-3m, cell parameter = 3.86 Å(obtained from preliminary XPDF results) and supercell = 4 x 4 x 4. Also, the experimental input parameters; Q_{max}= 27 Å, radiation type = X-ray, and wavelength = 0.1772 Å, were defined in the main macros code. An example of this code is detailed in the Appendix . The resultant calculated XPDF of this model of the 2 nm $Fe_{16}Pt_{84}$ nanoparticle, created in DISCUS, was compared to the observed (experimental) XPDF in Fig.7.21, with the model inset. The experimental XPDF data was then refined with the calculated XPDF using

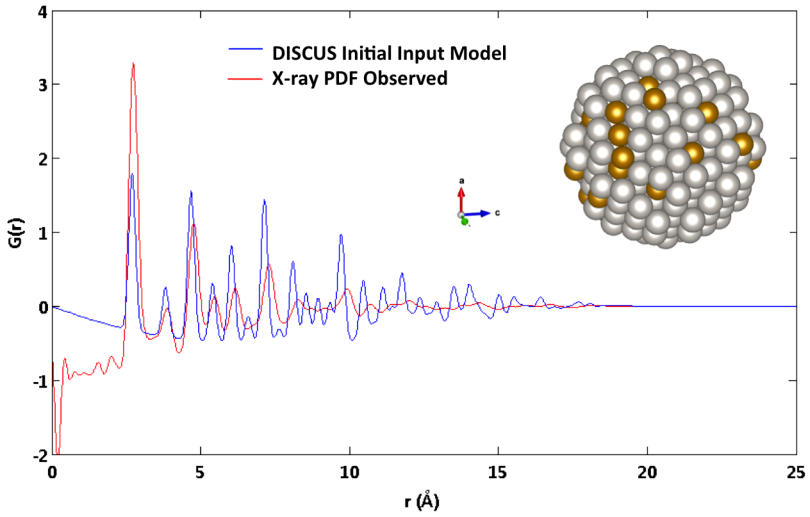

Figure 7.21: *Comparison of experimental XPDF with the calculated PDF from the initial input model of the 2 nm $Fe_{16}Pt_{84}$ nanoparticle, created in DISCUS, with the model inset.*

RMC Profiling. Firstly the experimental XPDF was manually corrected to remove contributions from neighbouring nanoparticles. These corrections were implemented so that the data was representative of a single nanoparticle under the assumption that the sample consisted of spheres of a constant radius and density [Kodama et al., 2006]. The initial model of the DISCUS nanoparticle of the metal core was used as the starting point of the RMC Profile refinements. Dur-

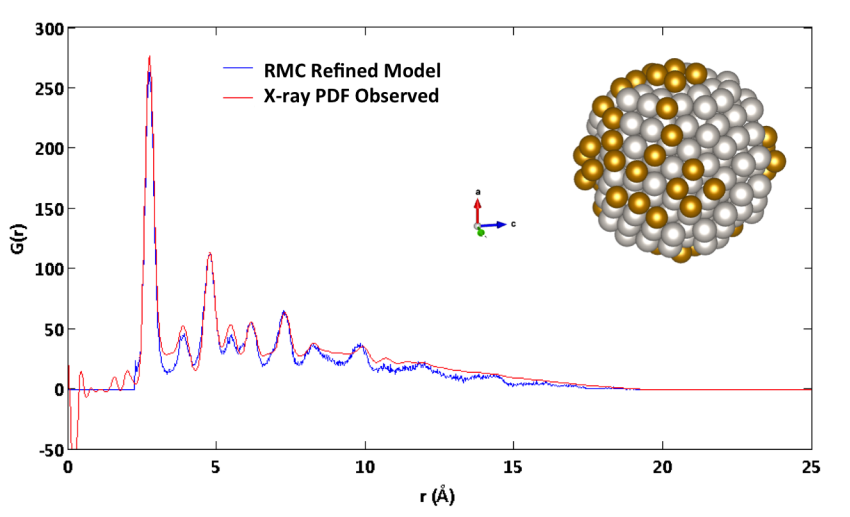

Figure 7.22: *Comparision of observed XPDF with the refined output PDF (after RMC profile refinement) of the 2 nm $Fe_{16}Pt_{84}$ nanoparticle model, created in RMC, with the model inset.*

ing refinement, all of the atoms were allowed to move up to 0.01 nm per move and atoms of different types (Fe and Pt) were allowed to swap positions (only the atoms were interchanged—the lattice constant, vibration factors and size of the particle were kept the same). The refinement was allowed to continue until no further improvement was observed in the fit statistics (for 150 iterations). The refined calculated model of the 2 nm FePt nanoparticle was compared to the observed XPDF in Fig.7.21 with the new refined 3D model inset. The external views of the initial DISCUS model and the final refined model are compared in the upper and lower images, respectively, in Fig.7.23 at different axis orientations. From observation of the refined model at different axis orientations it is evident that the Fe atoms have migrated to the surface of the nanoparticle forming slight clustering of the Fe. This correlates with the growth mechanism where Fe growth occurs on the surface of the nanoparticle and form energetically favourable clusters.

Another explanation for the Fe clustering is that the refined model was impacted by the scaling of the data; where if the first peak is larger than it should be, the RMC refinement will move the more strongly scattering Pt atoms towards the centre of the particle where it has a full coordination shell and so the Fe atoms were moved to the surface.

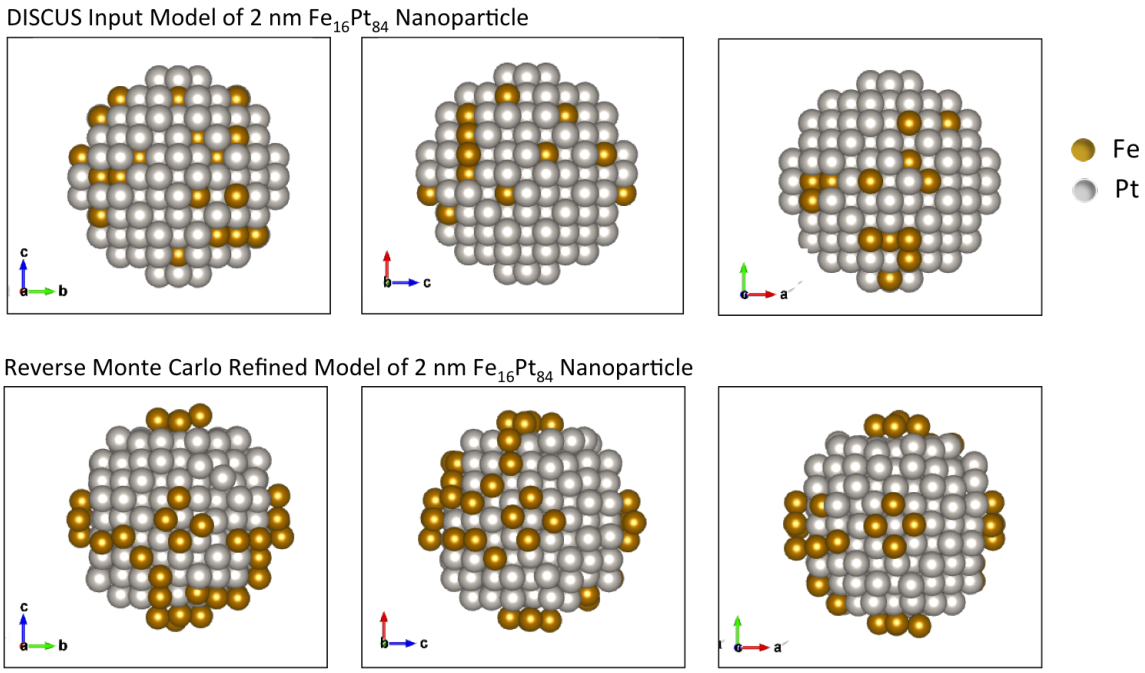

Figure 7.23: *Comparison of 3D models of 2 nm $Fe_{16}Pt_{84}$ nanoparticles with 529 atoms (external view) at different axis orientations with* ***top panel*** *initial input model of the 2 nm $Fe_{16}Pt_{84}$ nanoparticle and* ***bottom panel. Refined output model after RMC profile refinement, achieved in collaboration with Philip Chater.***

7.9.1 Preliminary Nanoparticle-Surfactant Modelling

The preliminary steps of surfactant attachment in DISCUS are outlined to demonstrate the process required to model an FePt nanoparticle with a surfactant layer attached. The same steps can be repeated for the attachment of the HDA surfactant, however the surfactant attachment process is complex and further development of the DISCUS code is required to enable dual surfactant attachment. Therefore, in this case, only the OA surfactant was attached to the DISCUS model of the $Fe_{16}Pt_{84}$ nanoparticle (which was modelled in the previous section). The DISCUS code for the attachment process is detailed in the macros file 'ligand.macros' in the Appendix 9.3.1. First, the OA surfactant model was created in DISCUS, using structural data obtained from the ICSD. The corresponding NPDF was calculated showing pronounced coordination peaks at low-r, and termination ripples at high-r $\sim$ 2 nm corresponding to the extended length 2.8 nm of the surfactant. Furthermore a model of the deuterated OA was created in DISCUS and the PDF compared to that of the protonated OA, in Fig.7.24. This comparison

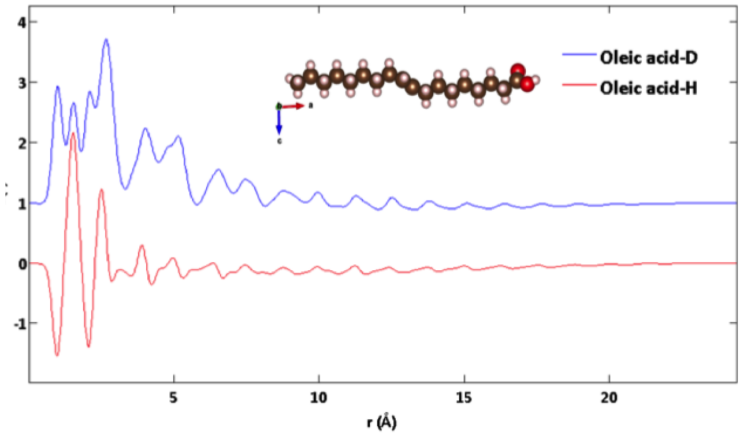

Figure 7.24: *Calculated NPDFs and corresponding models of OA-H and OA-D surfactant molecule with OA-H surfactant inset where hydrogen is represented by the white atoms, carbon represented by the brown atoms and oxygen represented by the red atoms.*

demonstrates the contrast achievalbe by using two istopic substitutions of surfactants where again there are contrasting first co-ordination peaks which can be ascribed to oppostite phase of hydrogen and deuterium. The first step in the process of modelling the FePt nanoparticle with the OA surfactant layer was to define a ratio of surface sites for surfactant attachment by using 'dummy' atoms. The Fe surface atoms were replaced with 'dummy' Pd atoms by inserting a reference Pd atom at the origin, which was used to locate Fe atoms at a distance greater than a defined radius and a user defined separation distance. For example, 50 surfactant sites defined with a separation distance of 3.72 Å enabled a spread of surf actant sites, as shown in Fig.7.25a. On increasing the number of surfactant sites to 102, a lower separation distance of 2.68 Åthis enabled a spread of surfactant sites, as shown in Fig.7.25a. These distances and ratios be more accurately determined by using experimental input parameters. For example surfactant site information can be extracted experimentally from SANs analysis and data extraction. Also, TGA investigations into the mass of the surfactant layer would also enable an estimate of the number of surfactant sites to be defined, allowing for fewer iterations in the refinement process. The OA surfactant was then attached to the defined surfactant sites, and orientated parallel to each other. The code was modified by Prof Reinhard Neder to enable the carbon backbone of the surfactant was orientated normal to the surface (in the case of FePt in the [100] direction) to resolve the issue of the program automatically aligning the surfactants in one direction. The OA surfactant was attached to the 3D 2 nm $Fe_{16}Pt_{84}$ nanoparticle model with

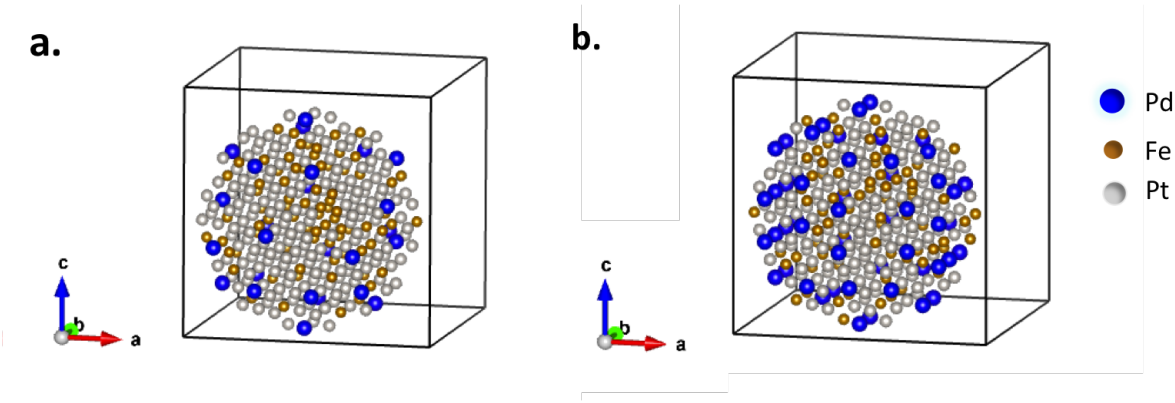

Figure 7.25: *3D DISCUS models of 2 nm $Fe_{16}Pt_{84}$ nanoparticles with a total of 592 atoms with surfactant sites defined by the blue Pd 'dummy' atoms: (a) 50 surfactant sites (b) 102 surfactant sites.*

102 surfactant sites specified and the Pd dummy atoms were replaced with the original Fe atoms.

The NPDF of the FePt OA-H surfactant system is plotted in Fig.7.26 with the model inset (replotted in Fig.7.27 for clarity). In the PDF in Fig.7.26 a surfactant contribution in the low-r region can be observed however this is not fully representative of the sample as the HDA surfactant is not attached.

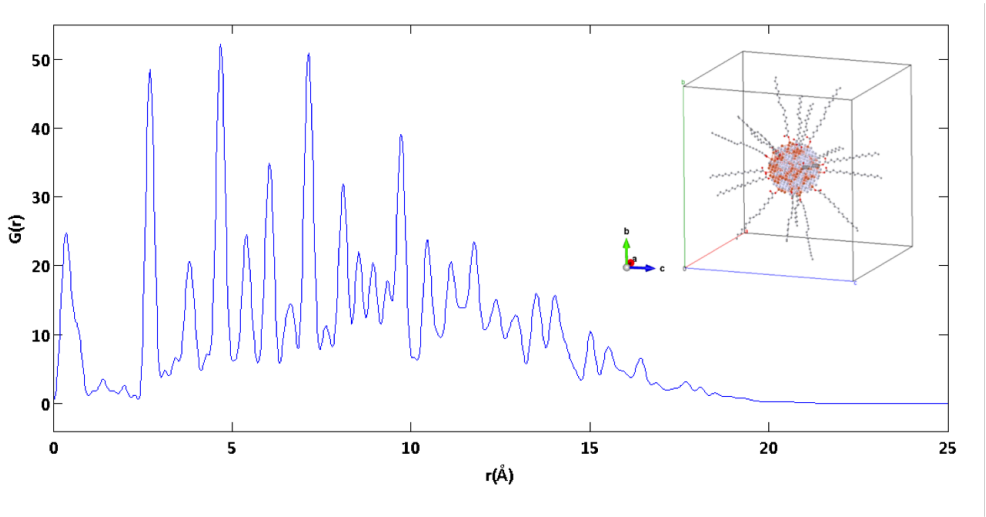

Figure 7.26: *Calculated NPDF of 2 nm $Fe_{16}Pt_{84}$ nanoparticle model with 102 OA-H surfactants attached to the surface. Model created in DISCUS.*

Also, in Fig.7.29 the calculated NPDF of the DISCUS model of 2 nm $Fe_{16}Pt_{84}$

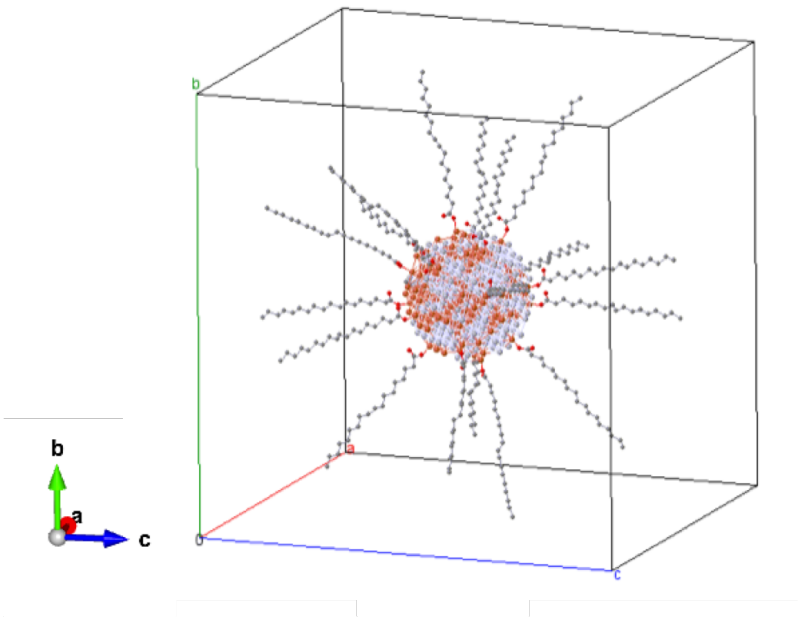

Figure 7.27: *3D model of 2 nm $Fe_{16}Pt_{84}$ nanoparticle with 102 OA-H surfactants attached to the surface. Model created in DISCUS in collaboration with Reinhard Neder.*

with OA-H surfactant attached, was compared to the same model but with no surfactant attached. It is evident from this comparison that the surfactant layer contributes towards the PDF not only in the low r region but it is also evident in additional peaks in the high r region, and shows added intensity absent in the core-only model. In Fig.7.29 the calculated NPDF of the DISCUS model of 2 nm $Fe_{16}Pt_{84}$ with OA-H surfactant attached was compared to the experimental PDF of the dry neutron data with the FePt OA-H HDA-H surfactant attached. It is evident from this comparison that the FePt NN peak contribution from the experimental data is notably weaker than that of the calculated model, which could indicate the lower degree of ordering of Fe.

7.9.2 Nanoparticle Modelling Conclusion

The preliminary model of the FePt nanoparticle with the OA surfactant attached was built. Further developments of the DISCUS code is necessary to enable the FePt nanoparticle to be modelled with dual surfactant species attached (OA and HDA). Also, the ratio of surface sites in these FePt models with surfactant attached is selected for modelling purposes only, refinement of this initial model

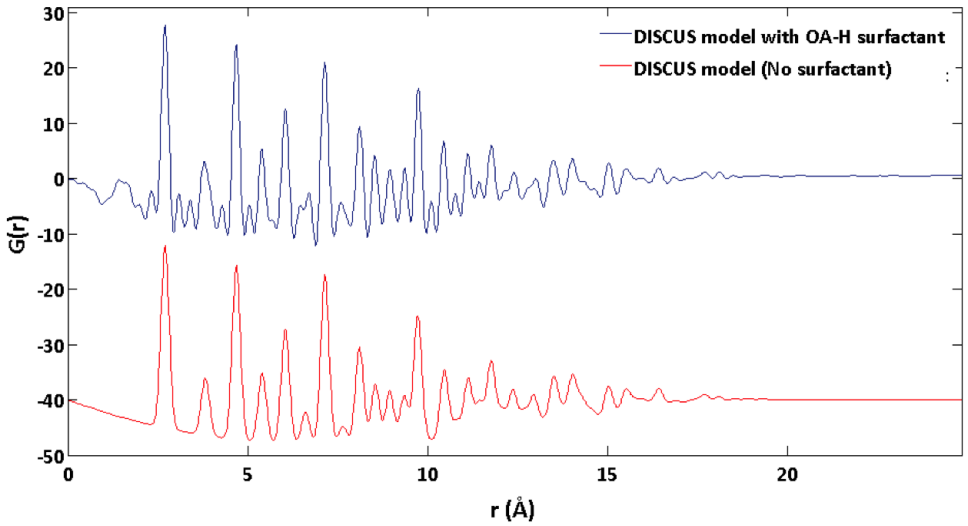

Figure 7.28: *Comparison of DISCUS model of 2 nm $Fe_{16}Pt_{84}$ with OA-H surfactant (blue line) and core only FePt nanoparticle (red line).*

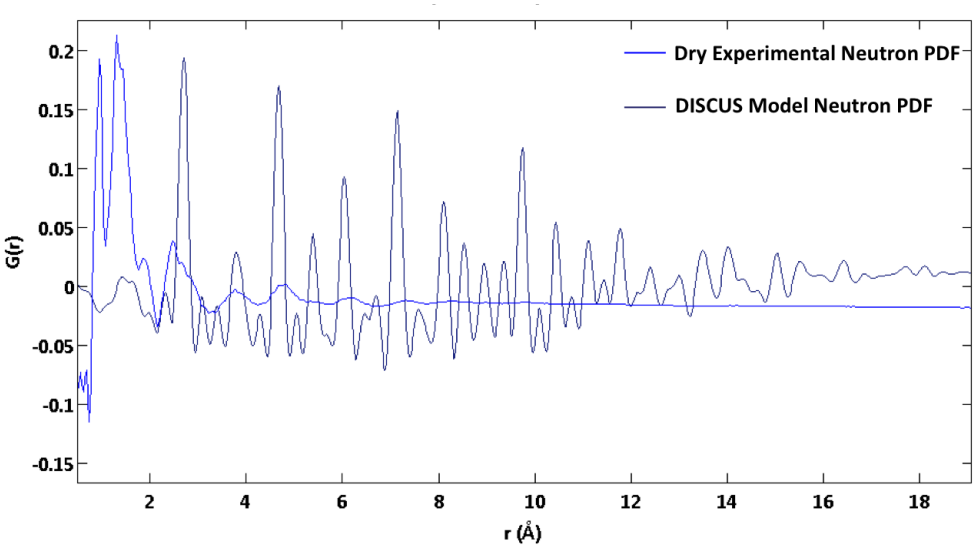

Figure 7.29: *Comparison of the calculated DISCUS NPDF (light blue) with the experimental NPDF (dark blue) of dry FePt OA-H HDA-H sample.*

would enable the number of surfactant sites to be iteratively refined so that they are representative of the nanoparticle-surfactant system. Also in order to reduce the number of iterations the average surface speciation could be calculated (using TGA analysis to quantify the mass of the surfactant per nanoparticle) and inputted before refined. In addition, SANs data analysis would also enable structural information about the surfactant shell to be extracted from Porod analysis.

The PDF data could then be more accurately refined in the RMC refinement and this technique could be adopted as an alternative refinement method to DIFFEV.

A FePt nanoparticle model was created in DISCUS and refined with experimental XPDF data to obtain a refined model which showed in clustering of Fe on the surface. However, in order to gain a higher degree of confidence with the resulting refined model of the FePt nanoparticle core, then the surfactant shell has to be accounted for. The first step would be to use the RMC profile program to (as accurately as possible) define the experimental parameters of the shell such as, the composition, thickness, and density of the shell.

7.10 Summary and Future Outlooks

The FePt nanoparticle samples with isotopic substitutions of organic surfactants, OA and HDA, were successfully synthesised and the samples were quantified at the RI using the following analysis methods; FTIR analysis to identify the presence of the surfactant layer on the nanoparticle surface, TEM analysis to determine the shape and size distribution of the nanoparticles, and conventional XRD analysis to determine the average crystallite size and phase of the nanoparticles. Additionally, the composition of all four samples was confirmed by external ICP-OES which was conducted at JAIST. FTIR analysis of the four isotopically substituted samples revealed vibrational modes from the functional groups and carbon chain of the surfactants— $v(COO)$, $v(CH)$, and $v(NH)$—confirming the chemical adsorption of the OA and HDA surfactants onto the FePt nanoparticle surface. This result confirmed that the deuterated surfactants had attached onto the surface of the nanoparticle and so it is concluded that the deuterated surfactants did not affect the bonding mechanism of the surfactants onto the nanoparticle surface. TEM observations of the samples revealed that the FePt nanoparticles with fully protonated surfactants were of higher monodispersity in comparison to the nanoparticles with partially or fully deuterated which were slightly aggregated on the substrate. All four samples remained dispersed and suspended well in toluene solution indicating that the aggregation was not due to the use of deuterated surfactants but could have been due to the energetically unstable size of the nanoparticles causing the nanoparticles to sinter on drying. Conventional XRD diffraction pattern analysis of the samples showed typical fcc peaks as ascribed

to the fcc FePt nanoparticles phase and Scherrer analysis determined the crystallite size as 2 nm (which corresponded with the size determined from the TEM results). The composition of the samples was confirmed by ICP-OES to be of an average composition range between $Fe_{14}Pt_{86}$ to $Fe_{20}Pt_{80}$. The results from the quantification of the samples alongside the preliminary XPDF results were used as nanoparticle input parameters, in the nanoparticle model.

In the XPDF investigations of the FePt nanoparticles with isotopic substitutions, the progressive steps required to optimise the experimental set-up and nanoparticle solvent suspension are detailed over the course of the investigations conducted at Nimrod. It was important to ensure that the nanoparticles remained in a suspension over the extent of the long measurement count times so that the samples could be probed in their most abundant colloidal state and to collect diffraction data with high count statistics. The first stage of the investigation involved the analysis of the nanoparticles in a hexane solvent suspension (in which FePt nanoparticles are most commonly suspended). However, the diffraction data results revealed a loss of statistics over the course of the experimental runs, which was expected to be due to the gradual precipitation of the nanoparticles out of hexane solvent solution.

The next stage of the investigation focussed on resolving the suspension issue —that occurred in the initial stage of the investigation—resulting in low scattering statistics. A hydrocarbon wax (eicosane, $C_{20}H_{44}$) was selected as the 'solvent' to disperse the nanoparticle sample fully (in the melted wax) and to prevent the nanoparticles from precipitating out of solution (on solidification of the wax). A novel 'open window' aluminium sample holder was designed and manufactured specifically for the neutron diffraction measurements which did not require any sample can subtractions. The diffraction data and corresponding PDFs of the nanoparticle samples suspended in eicosane wax, both showed a signal from the surfactant. However, it was realised that a new method was required to be developed in order to observe the FePt contribution without the interference of the crystalline diffraction peaks of the solid wax suspension.

The previous developments in the Nimrod investigations led on to the implementation of a completely new experimental set up which involved the design and manufacture of a novel flow cell environment. The final experimental 'flow cell' set-up was designed and manufactured specifically for this investigation to analyse the

nanoparticles in their most abundant colloidal state using neutron diffraction PDF analysis. The experimental NPDFs, acquired from the isotopic substitutions, were analysed qualitatively to extract structural information about the surfactant layer but there was very little structural information that could be extracted from the FePt nanoparticles. Also, the NPDF results from the dry sample showed the sensitivity of neutrons to the surfactant layer (as previously demonstrated in the flow cell experiments) enabling structural information to be extracted from the PDF and be ascribed to inter-atomic surfactant bonds.

Complementary XPDF investigations were conducted to probe the structure of the FePt nanoparticles. The results from the XPDF investigation demonstrates the sensitivity of the X-rays to the inorganic FePt nanoparticles, enabling structural information of high statistical value. A n FePt nanoparticle model was created using the nanoparticle builder program, DISCUS within the DIFFUSE package [Proffen and Neder, 1999] and the corresponding XPDF was refined with the experimental XPDF. Additionally, the first steps in building a model of the nanoparticle-surfactant system were demonstrated with the OA surfactants attached to the FePt nanoparticle model and corresponding PDFs created. Structural information could be readily extracted from the FePt contributions in the PDF. However, further code development and modelling is detailed in order to model the full FePt nanoparticle system with both OA and HAD surfactant. Overall, these investigations highlight the benefit of conducting complementary X-ray and neutron PDF analysis of nanoparticle surfactant systems.

Chapter 8

Final Thoughts

The investigations conducted in this thesis present an array of focused yet complementary multi-disciplinary characterisation techniques demonstrated on alloy FePt nanoparticle systems of different shapes and sizes. The methods used to characterise the unique properties of the nanoparticles are fundamental tools required to engineer and exploit nanoparticle properties across a whole range of industrial applications.

An interesting avenue of further investigation would be to conduct a focussed study on tuning the properties of alloy nanoparticles. Furthermore, the core-shell nanoparticles could be fabricated with different shell thicknesses. Comprehensive nanocharacterisation of these nanoparticles utlising the methods deviced and additional magnetic studies could be conducted. In this way— —strain relationships could be identified between the synthesis methods, morphology and magnetic properties of the nanoparticles. Thus, enabling strain-engineering of the nanoparticles for their desired applications in, for example, biomedical nanocatyalytic and mass-transport devices. Furthermore, other important alloys could be analysed such as PtCo, PtNi, AuPd.

Furthermore, the 21st century has seen the emergence of 4th generation radiation sources X-ray Free Electron Lasers (XFEL) which utilise intense femtosecond pulses of coherent x-ray radiation that are shorter than the timescale of radiation damage ($\sim$70 fs) first XFEL—Linac Coherent Light Source (LCLS)—to come on line in 2009 [Jianwei and Ian, 2015] and plans are in place for the UK's first XFEL.

Dedicated XFEL experiments of alloy nanoparticles would enable the structure of the FePt nanoparticles to be probed.

Chapter 9

Appendix

9.1 Methodology

9.1.1 Materials

The reagents adopted in the synthesis of FePt nanoparticles were all supplied by Sigma-Aldrich Ltd, UK, and have the following materials safety data sheet (MSDS) details: *iron(iii)acetylacetonate;$Fe(acac)_3$: Mw = 353.17 g/mol, purity = 99.9 %(GC), m.p = 210 °C, iron(ii)penta-carbonyl;$Fe(CO)_5$, Mw = 195.5 g/mol, purity = 99.99 % (GC), ρ = 1.453 g/cm^3, m.p = -21° C, b.p = 103° C,platinum(ii)acetyl acetonate; $Pt(acac)_2$ Mw = 393.29 g/mol, purity = 97 %(GC), m.p = 249-252 °C, b.p = 194 °C, octa-1-decene; $C_{18}H_{36}$: Mw = 252.48 g/mol, purity = 90 %(GC), ρ = 0.789 g/cm^3, b.p. = 315 °C, olelylamine; $C_{18}H_{35}NH_2$: Mw = 267.49 g/mol, purity = 70 %(GC), ρ = 0.813 g/cm^3, m.p = 21° C, b.p = 348 °C, oleic acid; $C_{18}H_{34}O_2$: Mw = 282.46 g/mol, purity = 90 %(GC), ρ 0.89 =g/cm^3, m.p = 14° C, b.p = 195° C, oleic acid-d34; $C_{18}D_{34}O_2$: Mw = 315.99 g/mol, purity = 99 %(GC), ρ= 0.996g/cm^3, m.p = 13.4° C, b.p = 195° C, hexadecylamine-H; $C_{16}H_{33}NH_2$: Mw = 241.46 g/mol, purity = 98 %(GC), ρ = 0.7821 g/cm^3, b.p = 330 °C, hexadecylamine-d33; $C_{16}D_{33}NH_2$: Mw = 274.66 g/mol, purity = 98 %(CP), ρ = 0.813 g/cm^3, b.p = 322° C, toluene-d8; $C_6D_5CD_3$ Mw = 100.19 g/mol, purity = 99 % atom D contains 0.03 % (v/v) TMS, ρ = 0.943 g/cm^3, b.p = 110° C, toluene-h; $C_6H_5CH_3$: Mw = 100.19 g/mol, purity = 99 % atom D contains 0.03 % (v/v) TMS, ρ = 0.943 g/cm^3, b.p = 110° C; tetraethy-*

lorthosilicate (TEOS); 99.0% (GC) $Si(OC_2H_5)_4$: Mw = 208.33 g/mol, purity = 98 %(CP), ρ = 0.993 g/mL at 20° C, b.p = 168

9.1.2 Schlenk Apparatus

The Schlenk line apparatus was set up as detailed in Fig.9.1, for the nanoparticle synthesis in a glove box. This inert environment is required to prevent any introduction of moisture or oxygen into the reaction during the synthesis procedure. Taps 1 and 2 control the vacuum system, which is run through a liquid nitrogen

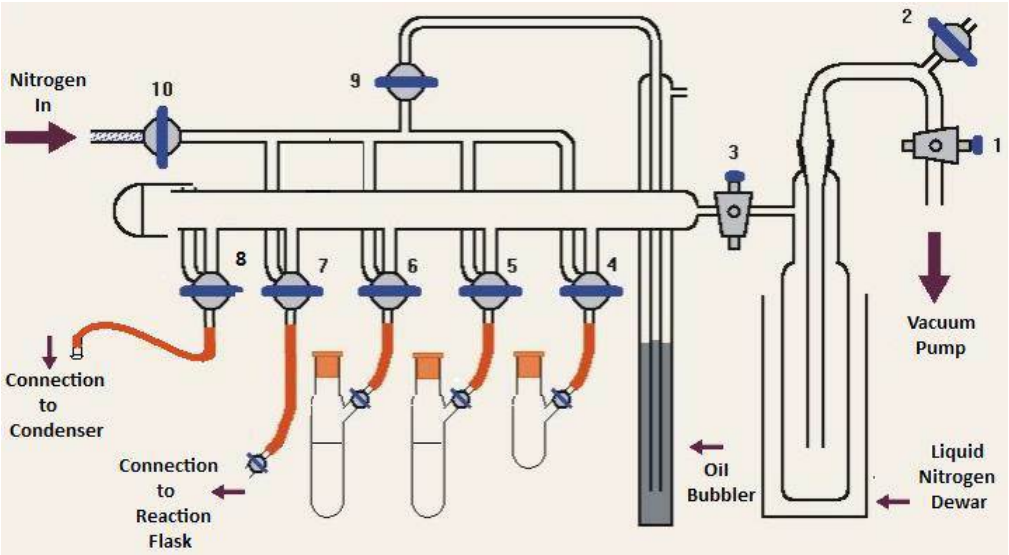

Figure 9.1: *Schematic of Schlenk line set-up with numbered connector taps. Reprinted adaption from Fridgen et al*

dewar. The dewar is a precautionary measure acting as a cold trap condensing any liquid that may have escaped into the system. Once the vacuum had been set to atmospheric pressure the trap was placed in the liquid nitrogen dewar and the vacuum pump was turned on. A vacuum could then be attained in the system by opening tap 3. Taps 4-8 could then be opened to vacuum by turning them horizontally. The other side of the tap would open to the N_2 supply. The N_2 is supplied to the system via tap 10 and tap 9 is always open when on to indicate the strength of the N_2 flow. Tap 4 is the N_2 supply system for purging the gas tight syringes with N_2. Before use, tap 4 is opened and the small flask connected is filled with N_2 and a small needle is inserted to release any air inside. Taps 5 and

6 are for the degassed solvent and ethanol which are supplied with N_2 on removal of any solvents. Tap 7 is connected to the side neck of the reaction flask and Tap 8 is connected to the condenser of the reaction flask as indicated in Fig. 9.2. This three necked round-bottomed flask was used for the synthesis reaction.

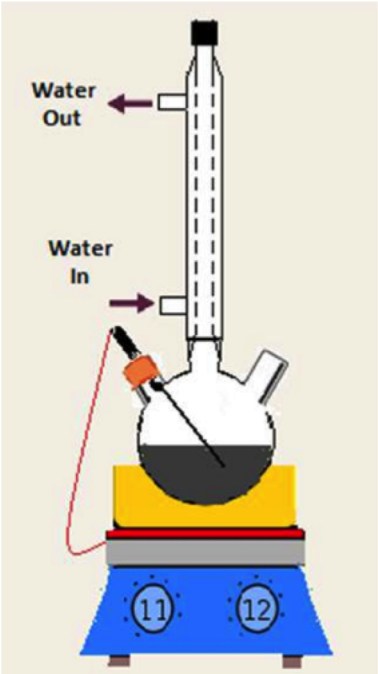

Figure 9.2: *Schematic of round-bottomed reaction flask on heating mantle, with a middle neck connection for the condenser and right neck connection for reagent injection and temperature probe and left neck connection for N_2 flow.*

The left neck opening was used to input the initial metal precursors and the liquid reagents (when sealed with a septum/rubber sealant) and for the insertion of the temperature probe. The centre neck was used for the attachment of the condenser system, which is connected to tube 8 (Fig.9.1). The condenser is required to prevent any reaction gases from escaping out of the flask into the Schlenk line. The right side neck was used to attach connecter tube 7, which can be used to control vacuum to the flask or to fill it with N_2 where required. The flask in Fig.9.2 was situated on top of a heating mantle, which has a variable temperature supply (knob 11) up to 300 °C. The mantle is connected to a temperature probe, which is used to monitor the temperature of the reaction. The variable magnetic stirrer (knob 12) was kept at a constant 500 rpm for each reaction.

9.1.3 Solvent Degassing

The high temperature solvents were required to be de-gassed to remove any possibility of gases from the air contaminating the reaction. Firstly, the solvent was sealed in the Schlenk flask and frozen by immersion into liquid N_2. Once the solvent was completely frozen, the flask was vacuumed for 5-10 minutes, with the flask still immersed. When the vacuum level in the flask reached a suitable level (between 10^{-2}-10^{-4} Bar) the vacuum was closed and gently removed from the liquid N_2 and immersed in warm water (taking care not to jerk the flask) to 'defrost' the solvent. This process was repeated (three times) and after the last cycle the flask was backfilled with an inert gas, in this case nitrogen. A degassed solvent in a sealed Schlenk flask was usually kept and re-used for up to 2-3 days before following the degassing procedure again.

9.2 Quantification and Data Treatment

9.2.1 Powder Diffraction Data Treatment

The diffraction pattern data was treated using the instruments corresponding 'X-pert high score data viewer; program. Firstly, using the software program, the slit data was converted from automatic divergence slit data to fixed divergence slit (ADS to FDS). The background was then defined (ensuring it does not interfere with the peaks and is below the peak baseline) and the peaks were identified by a peak search tool. Each peak was then manually selected and zoomed in (being careful to only zoom in on one peak) and a peak profile fitted. Notably, the first two peaks in an XRD diffractogram measured at the RI for FePt samples have additional background peaks at angles 46.954°, 54.757° and 81.269° due to the required Kapton film these peaks were identified but not fitted using the peak fitting process. With the background applied and all the peaks identified and fitted, a search and match regime was implemented on the treated data in order to identify a reference pattern (stored within a JPCDS) that was representative of the sample.

9.2.2 TEM Beam Direction Calculation

The beam direction, B, can be calculated by taking the cross product of two vectors in the anticlockwise direction in order to calculate the direction up out the page. In this case (200) x (220) = [004], thus $B = [001]$ as denoted in Fig.9.3. The

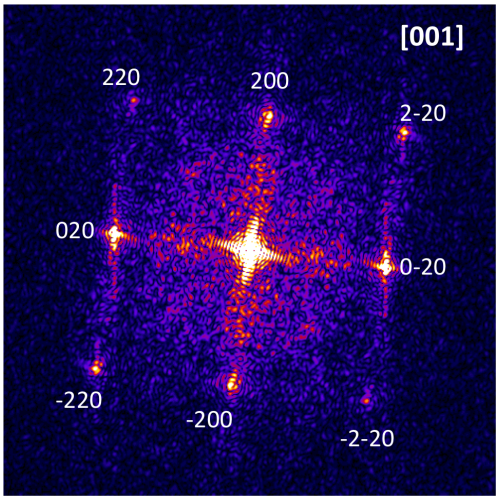

Figure 9.3: *Indexed FFT of nanocube in 5.5 with* $B = [001]$ *pointing out of the page*

indexed FFT from the nanocube, where $B = [001]$, indicates the plane direction 'out of page' and determines the position of the nanocube on the substrate with the (100) facet parallel to the substrate and the (001) facet normal to the substrate surface. From extended analysis of different nanocubes the nanocube orientation of (100), where the cube edge is orientated parallel to the substrate, was identified as the most common over the (110) orientation, where the cube face which was orientated parallel to the substrate. This result is expected to be due to the cube edge parallel being the most energetically favourable orientation.

9.2.3 Matlab Code: Gradient Phase Analysis

9.3 DISCUS Modelling Package

An example of the steps involved in the 3D modelling of a nanoparticle using the sub packages of the DIFFUSE program, detailed in the flow diagram in Fig.7.1 [Page et al., 2011] the sub-programs are described in more detailed below.

```
dir = '/Users/marianneadmin/Desktop/folder/filename';
rname = 'filename_input';
sname = 'filename_output';
% %SAD for spot a
cenX = 389;
cenY = 456;
%data = loadTif3D([dir,'/',rname,'.tiff']);
file = [dir,'/',rname,'.tif'];
ff = imread(file, 'tif');
%ff = imread(file);
data(:,:) = ff(:,:,1); %RBG channels are all the same, so pick R
tot = double(0);
for i=1:49 %from row 1 to 49 background selection
   for j=248:305
      tot = tot + double(data(i,j));
   end
end
avg = tot/50/58;
out = sprintf('Average background is %f', avg);
disp(out);
%
% manually block out aliens
% data(1:100,1:200) = avg;
%
figure;
imagesc(data);
file = [dir,'/',sname,'_d.tif'];
%   Simplified version of Jesse mat2tif function
disp('Saving embed array as .tif file....')
imwrite(uint16(abs(data)),file,'tif');
%
% find centre of mass
i1=double(0); j1=double(0); tot = double(0);
for i=1:size(data,1)
   for j=1:size(data,2)
      i1 = i1 + i*(double(data(i,j))-avg);
      j1 = j1 + j*(double(data(i,j))-avg);
      tot = tot + (double(data(i,j))-avg);
   end
end
i2 = uint16(i1/tot);
j2 = uint16(j1/tot);
out = sprintf('Centre of mass at %d %d', i2, j2);
disp(out);
arraysize = 512
doublearraysize = 2*arraysize
% embed in FFT array
embed(1:doublearraysize,1:doublearraysize) = double(0);
for i=1:size(data,1)
   for j=1:size(data,2)
      embed(arraysize+i-i2,arraysize+j-j2) = data(i,j) - avg;
   end
end
```

Figure 9.4: *Gradient phase analysis Matlab code for 2D strain mapping Part 1 of 3*

The corresponding ‘calculated’ diffraction and PDF data sets can then be extracted from the nanoparticle model, based on the experimental input parameters e.g. in this investigation neutron or X-ray diffraction is specified and the corresponding wavelengths inputted. The arrangement of the atoms in the nanoparticle model is saved as a ‘.cif’ file and can be viewed in ‘vacuum’ using an interac-

```
%
figure;
imagesc(embed);
file = [dir,'/',sname,'_e.tif'];
%   Simplified version of Jesse mat2tif function
disp('Saving embed array as .tif file....')
imwrite(uint16(abs(embed)),file,'tif');
%
recip = ifftshift(fftn(fftshift(embed)));
figure;
imagesc(log(abs(recip)));
%
file = [dir,'/',sname,'_a.tif'];
%   Simplified version of Jesse mat2tif function
disp('Saving amp array as .tif file....')
imwrite(uint16(abs(recip)/2000),file,'tif');
%
file = [dir,'/',sname,'_p.tif'];
%   Simplified version of Jesse mat2tif function
disp('Saving phase array as .tif file....')
imwrite(uint16((angle(recip)+pi)*1000),file,'tif');

%
% crop Bragg peak from manual centre position
cenX; cenY;
reg = 35;   % pixels surrounding Bragg
embed2(1:doublearraysize,1:doublearraysize) =
complex(0+0*i);
for i = -3*reg:3*reg
   for j = -3*reg:3*reg
      % soften edges with Gaussian
      embed2(arraysize+i,arraysize+j) = recip(cenY+i,cenX+j) *
exp(-(i*i+j*j)/2/reg/reg);
   end
end
figure;
imagesc(log(abs(embed2)));
file = [dir,'/',sname,'_e2.tif'];
%   Simplified version of Jesse mat2tif function
disp('Saving embed2 array as .tif file....')
imwrite(uint16(abs(embed2)/100),file,'tif');
%
real = 1000 * fftshift(ifftn(ifftshift(embed2)));
figure;
imagesc(log(abs(real)));
%
file = [dir,'/',sname,'_a2.tif'];
%   Simplified version of Jesse mat2tif function
disp('Saving amp2 array as .tif file....')
imwrite(uint16(abs(real)),file,'tif');
%
file = [dir,'/',sname,'_p2.tif'];
%   Simplified version of Jesse mat2tif function
disp('Saving phase2 array as .tif file....')
phase = angle(real);
% adjust cut to avoid phase wraps
for i = 1:doublearraysize
   for j = 1:doublearraysize
      if phase(i,j) < 0.6
```

Figure 9.5: *Gradient phase analysis Matlab code for 2D strain mapping Part 2 of 3*

tive structure-viewing program. In this investigation both JMOL and VESTA were

```
        phase(i,j) = phase(i,j) + 2*pi;
      end
    end
end
% make positive large number for int16
imwrite(uint16(phase*1000),file,'tif');
%
% display_rec3D(pnm,support,chi,DM_error);
% figure;
% imagesc(abs(fftshift(fft2(pnm))));
% figure; imagesc(phase);
% figure;
% phase = pnm(10:80,5:35);

ax=imagesc(angle(phase));        % generate hsv image of
array
set(ax,'AlphaData',abs(phase)/max(max(abs(phase))));   %
needs to be normalised
set(gca,'Color', [0 0 0]);      % zero colour becomes black
clear
```

Figure 9.6: *Gradient phase analysis Matlab code for 2D strain mapping Part 3 of 3*

used to view the model.

9.3.0.1 KUPLOT Plotting Package

KUPLOT is a data plotting package which enables any data sets to be plotted and allows for comparisons of observed and calculated data sets of the models created in DISCUS.

9.3.0.2 DIFFEV Refinement Package

In order to determine the internal structure of the nanoparticle that is the closest representative (lowest R value) to the nanoparticle that was analysed, the calculated PDF data has to be refined with the experimental PDF data. The nanoparticle-surfactant model can be refined using DIFFEV in order to create a model that best fits the experimental data set, creating a representative nanoparticle system with surfactants attached. There are different algorithms that can be used to interpret the fit results and output a new generation of parameter values that are fed into DISCUS. The three main algorithm fits are: (1) Least squares fit: this is the fastest algorithm and tends to be used when refining de-

fects with very small size difference, it requires an analytical derivable expression. (2) Monte Carlo techniques: e.g. simulated annealing or (3) genetic algorithms: e.g. evolutionary algorithms this is also a slow algorithm which requires an initial experimental concept of the input model, the model is derived from structural parameters. It is used for the refinement of the experimental PDF and calculated PDF data sets over a prescribed range, using a differential evolutionary algorithm to generate the refined parameter values. Generally, an assembly average of 30 individual nanoparticles, is required to be compared and refined from the calculated data in order to obtain a model PDF that effectively represents the observed data.

9.3.1 DISCUS Code

```
#
#   Building ligand-capped nanoparticles
#
################################################################################
#
# ligand molecule structure is defined using the lattice of gold structure,
# oriented with its carbon backbone in the [100], included an attached Au atom
#
################################################################################
variable  integer,nligand
variable real, radius
variable real, small
variable real, separate
variable integer, first
#
radius   = 10.0           ! Sphere radius
small    = radius - 1.0   ! shell thickness
separate =  4.0           ! minimum mdistance between "Po"
separate =  7.0           ! minimum mdistance between "Po"
#
read
   stru  ligand.stru
@plot.cif.mac ligand.stru                 # number of atoms in ligand
#
# Transform the ligand to a cartesian basis
#
@trans_tkl2cart.mac
@symmetry.mac             ! rotate and shift
#                         ! O(19) is places at 2,0,0, chain in positive x-direction
insert ni, 0.1,0.00,0.00, 0.1    ! Add a dummy atom as anchor to NP
nligand = n[1]            !number of atoms in ligand
#
save
   outf ligand_cartesian.stru
   omit all
   sel  all
   run
exit
#
# spherical FePt nanoparticle 20 A
#
read
   cell  fept_fcc_1.cell,6,6,6
replace Fe,Pt,all,0.7
boundary  sphere, radius
purge
################################################################################
#
# a number of atoms at the surface of nanoparticle are selected for ligand attachment
# replacing select Au atoms with Po dummy atoms
#
################################################################################
variable  integer,loop
variable  integer,ncore
#RBN###insert  Po,0,0,0,0.1               # insert dummy Po at origin (remove later)
insert  Po,0,0,0,0.10               # insert dummy Po at origin (remove later)
do  loop  =  1,n[1]-1
#RBN   if (blen(x[loop],y[loop],z[loop]).gt.(7.7)) then  # find atoms more than 7.7A
#RBN   find  env,Po,x[loop],y[loop],z[loop],0.9,2.876        # if no Po within 5A
   if (blen(x[loop],y[loop],z[loop]).gt. small) then  # find atoms more than 7.7A
   find  env,Po,x[loop],y[loop],z[loop],0.9,separate     # if no Po within 5A
      if  (env[0].eq.0)  then                #
      replace  loop,Po                       # atoms replaced with Po
   endif
enddo
remove  n[1]                                        # remove Po(origin)
purge
#
ncore  =  n[1]                                      # sphere is recoreded as ncore
#
# Transform the particle to a cartesian basis
#
@trans_tkl2cart.mac
save
   outfile  surface.stru
   omit  all                                          # controlled format includes..
   dese  all                                          # all atoms of crystal are deselected
   sel  Po
        run
exit
@plot.cif.mac NP_Po_sites
################################################################################
#
# molecules are then attached to the Po atom sites
# all the ligands are parallel to each other and oriented in [100] direction
#
```

Figure 9.7: *DISCUS code written in Fortran with edits added from Prof. Reinhard Neder indicated by 'RBN' Part 1 of 3*

```
################################################################################
domain
   reset
   mode  pseudo
   inputfile  surface.stru
   assign  character,po,fuzzy
   assign  fuzzy,   po,  0.0001 #0.0001
   assign  content, po,  ligand_cartesian.stru
   assign  orient,  po,  1,  1.0,  0.0,  0.0,  0.0
   assign  orient,  po,  2,  0.0,  1.0,  0.0,  0.0
   assign  orient,  po,  3,  0.0,  0.0,  1.0,  0.0
   assign  shape,   po,  1,  1.0,  0.0,  0.0,  0.0
   assign  shape,   po,  2,  0.0,  1.0,  0.0,  0.0
   assign  shape,   po,  3,  0.0,  0.0,  1.0,  0.0
        set remove, none
   show
   run
exit
#
#chem
#   element
#exit
#wait return
#purge
#chem
#   element
#exit
#wait return
@plot.cif.mac straight
#
################################################################################
#
# rotate each molecule parallel to a radial vector
# from the particle center through the connecting ligand atom
#
# The rotation needs to be done in atom Ni, the anchor that sits at (almost) the
# surface Po position. This atom is the last atom in the ligand stucture, i.e.
# within the loop it is atom number (loop + nligand - 1), and referenced by
# label "first", as this is the first atom on the NP surface.
#-------------------------------------------------------------------------------
variable  real,angle
variable  real,length
#
#echo " ncore, n[1],nligand %d  %d  %d ", ncore, n[1], nligand
#wait return
#################################################
do  loop  =  ncore+1,n[1],nligand            # loop over all ligand atoms <loop=start,end,increment>
#
   first   =  loop + nligand - 1
   angle   =  bang(1,0,0,  x[first],y[first],z[first])  # angle btw [100] and radial vector pointing to each ligand
   vprod      1,0,0,  x[first],y[first],z[first],ddd       # vector product of [100] and radial vector
   length  =  blen(res[1],res[2],res[3])           # length of the radial vector
#
   if(angle.ne.0.and.length.ne.0)  then
      vprod  1,0,0,  x[first],y[first],z[first],ddd
#
      symmetry                              # rotates the ligands along the rotation axis
         uvw  res[1],res[2],res[3]
         angle  angle
         trans  0.00,  0.00,  0.00
         origin  x[first],y[first],z[first],crystal
         type  proper
         mode  repl
         power  1
         sel  all
         incl  loop,loop+nligand-1 # symm operation includes atoms <start> to <end>
         run
      exit
   endif
enddo
#
#
replace Po,Fe,all,1.0        ! remove all Po, warning, this makes the surface all
#                            ! Fe terminated , no Pt are attached to a ligand...
replave Ni,void, all, 1.0    ! remove al anchor atoms
purge
#
chem
   elem
exit
#
@plot.cif.mac NP_ligand
#
#        "powder.mac"     calculates the powder pattern according to Debye
#        "output.mac"     writes the intensites to a file in x-y format
#        "plot.cif.mac"   writes the atom coordinates for plotting
#
variable real,   rhozero
rhozero = n[1]/vol[1]
#
```

Figure 9.8: *DISCUS code written in Fortran with edits added from Prof. Reinhard Neder indicated by 'RBN' Part 2 of 3*

```
#################################################################################
variable  real,angle
variable  real,length
#
#echo " ncore, n[1],nligand %d  %d  %d ", ncore, n[1], nligand
#wait return
#################################################
do  loop  =  ncore+1,n[1],nligand            # loop over all ligand atoms <loop=start,end,increment>
#
   first   =  loop + nligand - 1
   angle   =  bang(1,0,0,  x[first],y[first],z[first])  # angle btw [100] and radial vector pointing to each ligand
   vprod     1,0,0,  x[first],y[first],z[first],ddd      # vector product of [100] and radial vector
   length  =  blen(res[1],res[2],res[3])            # length of the radial vector
#
   if(angle.ne.0.and.length.ne.0)  then
      vprod  1,0,0,  x[first],y[first],z[first],ddd
#
      symmetry                                 # rotates the ligands along the rotation axis
         uvw  res[1],res[2],res[3]
         angle  angle
         trans  0.00,  0.00,  0.00
         origin  x[first],y[first],z[first],crystal
         type  proper
         mode  repl
         power  1
         sel  all
         incl  loop,loop+nligand-1 # symm operation includes atoms <start> to <end>
         run
      exit
   endif
enddo
#
#
replace Po,Fe,all,1.0        ! remove all Po, warning, this makes the surface all
#                            ! Fe terminated , no Pt are attached to a ligand...
replave Ni,void, all, 1.0    ! remove al anchor atoms
purge
#
chem
   elem
exit
#
@plot.cif.mac NP_ligand
#
#        "powder.mac"     calculates the powder pattern according to Debye
#        "output.mac"     writes the intensites to a file in x-y format
#        "plot.cif.mac"   writes the atom coordinates for plotting
#
variable real,   rhozero
rhozero = n[1]/vol[1]
#
powder
  neut
  set axis,q
  set calc,debye
  set disp,off
  set delta,0.0
  set qmin,1.1000  #changed from 1.1
  set qmax,20.000  #changed from 7.1
  set dq,  0.0005
  set temp,use
  set wvle, 0.15 #changed from 1.54056
  set four,four
  set lpcor,bragg, 26.58 # 26.58
  #
  output
    form powder,q
    value inte
    outf ligand.q
    run
  exit
  #
  #        "pdf.mac"  calculates the pdf and saves results
  #
  pdf
  #
      ides all
      jdes all
      isel all
      jsel all
  #
      set bound, crystal,exact
      set dens,  0.1966
      set delta, 0.00100
      set gamma, 0.0
      set qalp,  0.0020
      set qsig,  0.0040
      set qmax,  20.0000 #changed from 50
      set rad,   neut
      set range, 2.5*10,0.02
      set srat,  1.0,3.5
      set therm, gauss
  #
      set weight,  1.0
      set finite,sphere, 2.*10
  #
      show
      calc
      save pdf,ligand.grcalc     ! Changed extension to avoid acrobat issues
  exit
```

Figure 9.9: *DISCUS code written in Fortran with edits added from Prof. Reinhard Neder indicated by 'RBN' Part 3 of 3*

```
fept_fcc_1.cell

title FePt (fcc)
spcgr Fm-3m
cell  3.81600   3.81600   3.81600  90.00000  90.00000 90.00000
atoms
FE   0.0000000  0.0000000  0.0000000  0.5
#PT   0.0000000  0.0000000  0.0000000  0.5
```

Figure 9.10: *DISCUS FePt cell input file*

Bibliography

[Abe, 2012] Abe, E. (2012). Electron microscopy of quasicrystals - where are the atoms? *Chem. Soc. Rev.*, 41(20):6787–6798.

[Agarwala, 2014] Agarwala, P. V. (2014). Technical report, Metallurgical and Materials Engineering and IIT Roorkee.

[Akbarzadeh et al., 2012] Akbarzadeh, A., Samiei, M., and Davaran, S. (2012). Magnetic nanoparticles: preparation, physical properties, and applications in biomedicine. *Nanoscale research letters*, 7(1):1–13.

[Allen et al., 1987] Allen, F., Kennard, O., Watson, D., Brammer, L., Orpen, G., and Taylor, R. (1987). Tables of bond lengths determined by x-ray and neutron diffraction. part 1. bond lengths in organic compounds. *J. Chem. Soc., Perkin Trans. 2*, 0(12):S1–S19.

[Als-Nielsen and McMorrow, 2011] Als-Nielsen, J. and McMorrow, D. (2011). *Elements of Modern X-ray Physics*. Wiley, 2nd edition edition.

[Aslam et al., 2005] Aslam, M., Fu, L., Li, S., and Dravid, V. (2005). Silica encapsulation and magnetic properties of fept nanoparticles. *Journal of colloid and interface science*, 290(2):444–449.

[Berenguer et al., 2015] Berenguer, F., Bean, R., Bozec, L., Vila-Comamala, J., Zhang, F., Kewish, C., Bunk, O., Rodenburg, J., and Robinson, I. (2015). Coherent x-ray imaging of collagen fibril distributions within intact tendons. *Biophysical Journal*, 106(2):459–466.

[Bhattarai et al., 2013] Bhattarai, N., Casillas, G., Ponce, A., and Jose-Yacaman, M. (2013). Strain-release mechanisms in bimetallic core–shell nanoparticles as revealed by cs-corrected stem. *Surface Science*, 609:161–166.

[Bian et al., 2014] Bian, B., Du, J., Xia, W., Zhang, J., Liu, P., Li, W., Guo, Z., and Yan, A. (2014). Effect of reaction temperature on the shape of fept nanoparticles. *Magnetics, IEEE Transactions on*, 50(11):1–4.

[Billinge, 2008] Billinge, S. (2008). Nanoscale structural order from the atomic pair distribution function (pdf): There's plenty of room in the middle. *Journal of Solid State Chemistry*, 181(7):1695–1700.

[Bowker, 2002] Bowker, M. (2002). Surface science: The going rate for catalysts. *Nat Mater*, 1(4):205–206.

[Bowron et al., 2010] Bowron, D., Soper, A., Jones, K., Ansell, S., Birch, S., Norris, J., Perrott, L., Riedel, D., Rhodes, N., Wakefield, S., Botti, A., Ricci, M., Grazzi, F., and Zoppi, M. (2010). Nimrod: The near and intermediate range order diffractometer of the isis second target station. *Review of Scientific Instruments*, 81(3).

[Carpenter et al., 2003] Carpenter, E., Calvin, S., Stroud, R., and Harris, V. (2003). Passivated iron as coreâĹŠshell nanoparticles. *Chem. Mater.*, 15(17):3245–3246.

[Cha et al., 2010] Cha, W., Song, S., Jeong, N., Harder, R., Yoon, K., Robinson, I., and Kim, H. (2010). Exploration of crystal strains using coherent x-ray diffraction. *New Journal of Physics*, 12(3):035022.

[Chen et al., 2011] Chen, G.-S., Chen, C.-N., Tseng, T.-T., Wei, M.-H., Hsieh, J., and Tseng, W. (2011). Synthesis, characterization, and antibacterial activity of silver-doped silica nanocomposite particles. *Journal of Nanoscience and Nanotechnology*, pages 90–97.

[Chen et al., 2006] Chen, M., Kim, J., Liu, J., Fan, H., and Sun, S. (2006). Synthesis of fept nanocubes and their oriented self-assembly. *J. Am. Chem. Soc.*, 128(22):7132–7133.

[Chen et al., 2004] Chen, M., Liu, J., and Sun, S. (2004). One-step synthesis of fept nanoparticles with tunable size. *J. Am. Chem. Soc.*, 126(27):8394–8395.

[Chen et al., 2007] Chen, M., Pica, T., Jiang, Y.-B., Li, P., Yano, K., Liu, P., Datye, A., and Fan, H. (2007). Synthesis and self-assembly of fcc phase fept nanorods. *J. Am. Chem. Soc.*, 129(20):6348–6349.

[Chen et al., 2010] Chen, Z., Cui, Z.-M., Niu, F., Jiang, L., and Song, W.-G. (2010). Pd nanoparticles in silica hollow spheres with mesoporous walls: a nanoreactor with extremely high activity. *Chem. Commun.*, 46(35):6524–6526.

[Chiu et al., 2014] Chiu, C.-Y., Yang, M.-Y., Lin, F.-C., Huang, J.-S., and Huang, M. H. (2014). Facile synthesis of Au-Pd core-shell nanocrystals with systematic shape evolution and tunable size for plasmonic property examination. *Nanoscale*, 6(13):7656–7665.

[Chokprasombat, 2011] Chokprasombat, K. (2011). Synthesis of patterned media by self-assembly of fept nanoparticles. *Walailak Journal of Science and Technology (WJST)*.

[Chou et al., 2009] Chou, S.-W., Zhu, C.-L., Neeleshwar, S., Chen, C.-L., Chen, Y.-Y., and Chen, C.-C. (2009). Controlled growth and magnetic property of fept nanostructure: Cuboctahedron, octapod, truncated cube, and cube. *Chem. Mater.*, 21(20):4955–4961.

[Crowther et al., 1970] Crowther, R., DeRosier, D., and Klug, A. (1970). The reconstruction of a three-dimensional structure from projections and its application to electron microscopy. *Proceedings of the Royal Society of London A: Mathematical, Physical and Engineering Sciences*, 317(1530):319–340.

[Darwish et al., 2013] Darwish, T., Luks, E., Moraes, G., Yepuri, N., Holden, P., and James, M. (2013). Synthesis of deuterated [d32]oleic acid and its phospholipid derivative [d64]dioleoyl-sn-glycero-3-phosphocholine. *J. Label Compd. Radiopharm*, 56(9-10):520–529.

[Duan and Wang, 2013] Duan, S. and Wang, R. (2013). Bimetallic nanostructures with magnetic and noble metals and their physicochemical applications. *Progress in Natural Science: Materials International*, 23(2):113–126.

[Edit, 2003] Edit (2003). Small angle neutron and x-ray scattering of dispersions of oleic-acid-coated iron particles. *Journal of Magnetism and Magnetic Materials*, 266(1D2):178–184.

[Ersen et al., 2015] Ersen, O., Florea, I., Hirlimann, C., and Pham-Huu, C. (2015). Exploring nanomaterials with 3d electron microscopy. *Materials Today*, 18(7):395–408.

[Ewald, 1962] Ewald, P. (1962). *Fifty Years of X-Ray Diffraction*. Springer.

[Ewald, 1969] Ewald, P. (1969). Introduction to the dynamical theory of x-ray diffraction. *Acta Crystallographica Section A*, 25:103–108.

[Fan et al., 2004] Fan, H., Yang, K., Boye, D., Sigmon, T., Malloy, K., Xu, H., López, G., and Brinker, J. (2004). Self-assembly of ordered, robust, three-dimensional gold nanocrystal/silica arrays. *Science*, 304(5670):567–571.

[Fienup, 1982] Fienup, J. (1982). Phase retrieval algorithms: A comparison. *Applied Optics*, 21:2758–2769.

[Florea et al., 2012] Florea, I., Demortiere, A., Petit, C., Bulou, H., Hirlimann, C., and Ersen, O. (2012). 3D Quantitative Analysis of Platinum Nanocrystal Superlattices by Electron Tomography. *ACS Nano*, 6(3):2574–2581.

[Friedrich et al., 2009] Friedrich, H., de Jongh, P., Verkleij, A., and de Jong, K. (2009). Electron tomography for heterogeneous catalysts and related nanostructured materials. *Chem. Rev.*, 109(5):1613–1629.

[Fuchigami et al., 2011] Fuchigami, T., Kawamura, R., Kitamoto, Y., Nakagawa, M., and Namiki, Y. (2011). Ferromagnetic fept-nanoparticles/polycation hybrid capsules designed for a magnetically guided drug delivery system. *Langmuir*, 27(6):2923–2928.

[Gan et al., 2012] Gan, L., Yu, R., Luo, J., Cheng, Z., and Zhu, J. (2012). Lattice strain distributions in individual dealloyed pt-fe catalyst nanoparticles. *J. Phys. Chem. Lett.*, 3(7):934–938.

[Green, 2014] Green (2014). High pressure synthesis of fept nanoparticles with controlled morphology and fe content. *Royal Society of Chemistry Advances*, 4:1168–1173.

[Günter Möbus, 2007] Günter Möbus, I. B. (2007). Nanoscale tomography in materials science. *Materials Today*, 10(12):18–25.

[Guo and Sun, 2012] Guo, S. and Sun, S. (2012). Fept nanoparticles assembled on graphene as enhanced catalyst for oxygen reduction reaction. *J. Am. Chem. Soc.*, 134(5):2492–2495.

[Hamidinezhad et al., 2011] Hamidinezhad, H., Wahab, Y., Othaman, Z., and Ismail, A. (2011). Synthesis and analysis of silicon nanowire below si–au eutectic temperatures using very high frequency plasma enhanced chemical vapor deposition. *Applied Surface Science*, 257(21):9188–9192.

[Hergt et al., 2006] Hergt, R., Dutz, S., Müller, R., and Zeisberger, M. (2006). Magnetic particle hyperthermia:nanoparticle magnetism and materials development for cancer therapy. *Journal of Physics: Condensed Matter*, 18(38):S2919–S2934.

[Hytch et al., 2008] Hytch, M., Houdellier, F., Hue, F., and Snoeck, E. (2008). Nanoscale holographic interferometry for strain measurements in electronic devices. *Nature*, 453(7198):1086–1089.

[Hytch et al., 2003] Hytch, M., Putaux, J.-L., and Penisson, J.-M. (2003). Measurement of the displacement field of dislocations to 0.03[thinsp]a by electron microscopy. *Nature*, 423(6937):270–273.

[Jha et al., 2015] Jha, D., Varadarajan, K., Patel, A., and Deb, P. (2015). Direct synthesis of water dispersible superparamagnetic tga capped fept nanoparticles: One pot, one shot. *Materials Chemistry and Physics*, 156:247–253.

[Jianwei and Ian, 2015] Jianwei, M. and Ian, R. (2015). Beyond crystallography: Diffractive imaging using coherent x-ray light sources. *Science*, 348(6234):530–535.

[Jochym et al., 2015] Jochym, P., Łażewski, J., Sternik, M., and Piekarz, P. (2015). Dynamics and stability of icosahedral fe-pt nanoparticles. *Phys. Chem. Chem. Phys.*

[Kalambur et al., 2005] Kalambur, V., Han, B., Hammer, B., Shield, T., and Bischof, J. (2005). In vitro characterization of movement, heating and visualization of magnetic nanoparticles for biomedical applications. *Nanotechnology*, 16(8):1221–1233.

[Kalogirou et al., 2010] Kalogirou, O., Angelakeris, M., Dendrinou-Samara, C., Mourdikoudis, S., Simeonidis, K., Gloystein, K., Vilalta-Clemente, A., and Tsiaoussis, I. (2010). The effect of composition and structural ordering on the magnetism of fept nanoparticles. *Journal of Nanoscince and technology*, 10(9):6017–6023.

[Keen, 2001] Keen, D. (2001). A comparison of various commonly used correlation functions for describing total scattering. *Journal of Applied Crystallography*, 34(2):172–177.

[Kodama et al., 2006] Kodama, K., Iikubo, S., Taguchi, T., and Shamoto, S. (2006). Finite size effects of nanoparticles on the atomic pair distribution functions. *Acta Crystallographica Section A: Foundations of Crystallography*, 62(6):444–453.

[Kuo et al., 2013] Kuo, C.-H., Lamontagne, L., Brodsky, C., Chou, L.-Y., Zhuang, J., Sneed, B., Sheehan, M., and Tsung, C.-K. (2013). The effect of lattice strain on the catalytic properties of pd nanocrystals. *ChemSusChem*, 6(10):1993–2000.

[Lai et al., 2008] Lai, C.-W., Wang, Y.-H., Uttam, B., Chen, Y.-C., Hsiao, J.-K., Liu, C.-L., Liu, H.-M., Chen, C.-Y., and Chou, P.-T. (2008). One-pot solvothermal synthesis of $FePt/Fe_3O_4$ core-shell nanoparticles. *Chem. Commun.*, 42:5342–5344.

[LaMer and Dinegar, 1950] LaMer, V. and Dinegar, R. (1950). Theory, production and mechanism of formation of monodispersed hydrosols. *J. Am. Chem. Soc.*, 72(11):4847–4854.

[Leslie, 2006] Leslie, A. G. W. (2006). The integration of macromolecular diffraction data. *Acta Crystallographica Section D*, 62(1):48–57.

[Liang et al., 2014] Liang, M., Harder, R., and Robinson, I. (2014). Brownian motion studies of viscoelastic colloidal gels by rotational single particle tracking. *IUCrJ*, 1(3):172–178.

[Liang et al., 2015] Liang, S., Zhou, Q., Wang, M., Zhu, Y., Wu, Q., and Yang, X. (2015). Water-soluble l-cysteine-coated fept nanoparticles as dual mri/ct imaging contrast agent for glioma. *International journal of nanomedicine*, 10:2325–2333.

[Liang et al., 2010] Liang, X., Barrett, K., Jiang, Y.-B., and Weimer, A. (2010). Rapid silica atomic layer deposition on large quantities of cohesive nanoparticles. *ACS applied materials and interfaces*, 2(8):2248–2253.

[Liu et al., 2014] Liu, M., Xie, Y., Li, J., Pan, H., Tian, H., and Shi, Y. (2014). Synthesis of optically active deuterated primary amines via reduction of n-tert-butanesulfinyl aldimines. *J. Org. Chem.*, 79(17):8417–8421.

[Lu et al., 2002] Lu, Y., Yin, Y., Mayers, B., and Xia, Y. (2002). Modifying the surface properties of superparamagnetic iron oxide nanoparticles through a solâĹŠgel approach. *Nano Lett.*, 2(3):183–186.

[Luke Green et al., 2014] Luke Green, Thuy, T., Mott, D., Maenosono, S., and Kim Thanh, N. (2014). Multicore magnetic fept nanoparticles: controlled formation and properties. *RSC Adv.*, 4(3):1039–1044.

[Marco et al., 2009] Marco, M. D., Ballirano, P., Port, M., Piscopiello, E., Couvreur, P., Dubernet, C., and Sadun, C. (2009). Atomic pair distribution function (pdf) study of iron oxide nanoparticles in aqueous suspension. *J. Mater. Chem.*, 19(35):6354–6360.

[Matsui et al., 2011] Matsui, I., Ogi, T., Iskandar, F., and Okuyama, K. (2011). Perpendicular easy axis alignment of FePt nanoparticles on a platinum-(001) buffer layer for high-density magnetic recording. *Journal of Applied Physics*, 110(8):083906+.

[Miao et al., 2005] Miao, J., Förster, F., and Levi, O. (2005). Equally sloped tomography with oversampling reconstruction. *Phys. Rev. B*, 72.

[Nandwana et al., 2005] Nandwana, V., Elkins, K., and Liu, J. (2005). Magnetic hardening in ultrafine fept nanoparticle assembled films. *Nanotechnology*, 16(12).

[Nandwana et al., 2007] Nandwana, V., Elkins, K., Poudyal, N., Chaubey, G., and Yano (2007). Size and shape control of monodisperse fept nanoparticles. *J. Phys. Chem. C*, 111(11):4185–4189.

[Newton et al., 2012] Newton, M., Chapman, K., Thompsett, D., and Chupas, P. (2012). Chasing changing nanoparticles with time-resolved pair distribution function methods. *J. Am. Chem. Soc.*, 134(11):5036–5039.

[Newton et al., 2009] Newton, M., Leake, S., Harder, R., and Robinson, I. (2009). Three-dimensional imaging of strain in a single zno nanorod. *Nature Materials*, 9(2):120–124.

[Nguyen et al., 2006] Nguyen, L., Howard, L., Stinton, G., Giblin, S., Tanner, B., Terry, I., Hughes, A., Ross, I., Serres, A., and Evans, J. (2006). Synthesis of size-controlled fcc and fct fept nanoparticles. *Chemistry of Materials*, 18(26):6414–6424.

[Nishino et al., 2009] Nishino, Y., Takahashi, Y., Imamoto, N., Ishikawa, T., and Maeshima, K. (2009). Three-dimensional visualization of a human chromosome using coherent x-ray diffraction. *Physical review letters*, 102(1).

[Norio Baba, 2008] Norio Baba, Katayama, E. (2008). A novel "ghost"-free tomographic image reconstruction method applicable to rotary-shadowed replica specimens. *Ultramicroscopy*, 108(3):239–255.

[Nudelman et al., 2011] Nudelman, F., de With, G., and Sommerdijk, N. (2011). Cryo-electron tomography: 3-dimensional imaging of soft matter. *Soft Matter*, 7(1):17–24.

[Page et al., 2011] Page, K., Hood, T., Proffen, T., and Neder, R. (2011). Building and refining complete nanoparticle structures with total scattering data. *Journal of Applied Crystallography*, 44(2):327–336.

[Page et al., 2010] Page, K., Proffen, T., Niederberger, M., and Seshadri, R. (2010). Probing local dipoles and ligand structure in batio3 nanoparticles. *Chemistry of Materials*, 22(15):4386–4391.

[Palma et al., 2007] Palma, R. D., Peeters, S., Van Bael, M., Van den Rul, H., Bonroy, K., Laureyn, W., Mullens, J., Borghs, G., and Maes, G. (2007). Silane ligand exchange to make hydrophobic superparamagnetic nanoparticles waterdispersible. *Chem. Mater.*, 19(7):1821–1831.

[Pankhurst et al., 2009] Pankhurst, Q., Thanh, N., Jones, S., and Dobson, J. (2009). Progress in applications of magnetic nanoparticles in biomedicine. *Journal of Physics D: Applied Physics*, 42(22):224001.

[Paul Midgley, 2008] Paul Midgley, Matthew Weyland, H. S. (2008). *Advanced Tomographic Methods in Materials Research and Engineering*. Monographs on the Physics and Chemistry of Materials. Oxford University Press.

[Paul Midgley, 2009] Paul Midgley, Dunin-Borkowski, R. (2009). Electron tomography and holography in materials science. *Nat Mater*, 8(4):271–280.

[Pratt et al., 2014] Pratt, A., Lari, L., Hovorka, O., Shah, A., Woffinden, C., Tear, S., Binns, C., and KrÃÂűger, R. (2014). Enhanced oxidation of nanoparticles through strain-mediated ionic transport. *Nat Mater*, 13(1):26–30.

[Proffen and Kim, 2009] Proffen, T. and Kim, H. (2009). Advances in total scattering analysis. *J. Mater. Chem.*, 19(29):5078–5088.

[Proffen and Neder, 1999] Proffen, T. and Neder, R. (1999). Discus, a program for diffuse scattering and defect structure simulations - update. *Journal of Applied Crystallography*, 32(4):838–839.

[Robinson and Harder, 2009] Robinson, I. and Harder, R. (2009). Coherent x-ray diffraction imaging of strain at the nanoscale. *Nature Materials*, 8(4):291–298.

[Rochelle Cornell, 2006] Rochelle Cornell, Schwertmann, U. (2006). *The Iron Oxides: Structure, Properties, Reactions, Occurrences and Uses,*. Wiley, 2nd completely revised and extended edition edition.

[Sahu and Bahadur, 2013] Sahu, N. and Bahadur, D. (2013). Influence of excess fe accumulation over the surface of fept nanoparticles: Structural and magnetic properties. *Journal of Applied Physics*, 113(13):134303.

[Schneider et al., 2012] Schneider, C., Rasband, W., and Eliceiri, K. (2012). Nih image to imagej: 25 years of image analysis. *Nat Meth*, 9(7):671–675.

[Scott et al., 2014] Scott, M., Chen, C., Zeng, H., Ercius, P., and Miao, J. (2014). Atomic resolution tomography of magnetically anisotropic fept nanoparticles. *Microscopy and Microanalysis*, 20:804–805.

[Scott et al., 2012] Scott, M., Chen, C.-C., Mecklenburg, M., Zhu, C., Xu, R., Ercius, P., Dahmen, U., Regan, B., and Miao, J. (2012). Electron tomography at 2.4-angstrom resolution. *Nature*, 483(7390):444–447.

[Sebt et al., 2009] Sebt, S., Parhizgar, S., Farahmandjou, M., Aberomand, P., and Akhavan, M. (2009). The role of ligands in the synthesis of fept nanoparticles. *Journal of Superconductivity and Novel Magnetism*, 22(8):849–854.

[Shemilt, 2014] Shemilt, L. (2014). Coherent diffraction imaging and ptychography of human metaphase chromosomes. Master's thesis, University College London, London Centre for Nanotechnology.

[Shi et al., 2012] Shi, X., Xiong, G., Huang, X., Harder, R., and Robinson, I. (2012). Radiation-induced bending of silicon-on-insulator nanowires probed by coherent x-ray diffractive imaging. *New Journal of Physics*, 14(6):063029.

[Shukla et al., 2003] Shukla, N., Liu, C., Jones, P., and Weller, D. (2003). Ftir study of surfactant bonding to fept nanoparticles. *Journal of Magnetism and Magnetic Materials*, 266(1ÃŘ2):178–184.

[Shukla et al., 2006] Shukla, N., Liu, C., and Roy, A. (2006). Oriented self-assembly of cubic fept nanoparticles. *Materials Letters*, 60(8):995–998.

[Sivia, 2011] Sivia, D. (2011). *Elementary Scattering Theory Elementary Scattering for X-ray and Neutron Users*. Oxford University Press.

[Sneed et al., 2015] Sneed, B., Young, A., and Tsung, C.-K. (2015). Building up strain in colloidal metal nanoparticle catalysts. *Nanoscale*, 7(29):12248–12265.

[Soichiro Saita, 2005] Soichiro Saita, Maenosono, S. (2005). Formation mechanism of fept nanoparticles synthesized via pyrolysis of iron(iii) ethoxide and platinum(ii) acetylacetonate. *Chemistry of Materials*, 17(26):6624–6634.

[Soper, 2009] Soper (2009). Inelasticity corrections for time-of-flight and fixed wavelength neutron diffraction experiments. *Molecular Physics*, 107(16):1667–1684.

[Soper and Barney, 2011] Soper, A. and Barney, E. (2011). Extracting the pair distribution function from white-beam X-ray total scattering data. *Journal of Applied Crystallography*, 44(4):714–726.

[Sousa et al., 2011] Sousa, A., Azari, A., Zhang, G., and Leapman, R. (2011). Dual-axis electron tomography of biological specimens: Extending the limits of specimen thickness with bright-field stem imaging. *Journal of structural biology*, 174(1):107–114.

[Strasser et al., 2010] Strasser, P., Koh, S., Anniyev, T., Greeley, J., More, K., Yu, C., Liu, Z., Kaya, S., Nordlund, D., Ogasawara, H., Toney, M., and Nilsson, A. (2010). Lattice-strain control of the activity in dealloyed core–shell fuel cell catalysts. *Nature Chemistry*, 2(6):454–460.

[Sun, 2006] Sun, S. (2006). Recent advances in chemical synthesis, self-assembly, and applications of fept nanoparticles. *Advanced Materials*, 18(4):393–403.

[Sun et al., 2000] Sun, S., Murray, C. B., Weller, D., Folks, L., and Moser, A. (2000). Monodisperse fept nanoparticles and ferromagnetic fept nanocrystal superlattices. *Science*, 287(5460):1989–1992.

[Tao, 1993] Tao, Y. (1993). Structural comparison of self-assembled monolayers of n-alkanoic acids on the surfaces of silver, copper, and aluminum. *J. Am. Chem. Soc.*, 115(10):4350–4358.

[Thanh and Green, 2010] Thanh, N. and Green, L. (2010). Functionalisation of nanoparticles for biomedical applications. *Nano Today*, 5(3):213–230.

[Tucker et al., 2001] Tucker, M., Dove, M., and Keen, D. (2001). Application of the reverse monte carlo method to crystalline materials. *Journal of Applied Crystallography*, 34(5):630–638.

[Tucker et al., 2007] Tucker, M., Keen, D., Dove, M., Goodwin, A., and Hui, Q. (2007). Rmcprofile: reverse monte carlo for polycrystalline materials. *Journal of Physics: Condensed Matter*, 19(33):335218.

[Ulvestad et al., 2015] Ulvestad, A., Singer, A., Cho, H.-M., Clark, J., Harder, R., Maser, J., Meng, Y., and Shpyrko, O. (2015). Correction to single particle nanomechanics in operando batteries via lensless strain mapping. *Nano Lett.*, 15(5):3654–3654.

[Ung et al., 2009] Ung, D., Tung, L., Caruntu, G., Delaportas, D., Alexandrou, I., Prior, I., and Thanh, N. (2009). Variant shape growth of nanoparticles of metallic fe-pt, fe-pd and fe-pt-pd alloys. *CrystEngComm*, 11(7):1309–1316.

[Usuda et al., 2005] Usuda, K., Numata, T., Irisawa, T., Hirashita, N., and Takagi, S. (2005). Strain characterization in soi and strained-si on sgoi mosfet channel using nano-beam electron diffraction (nbd). *Materials Science and Engineering: B*, 124-125:143–147.

[van Ewijk et al., 2002] van Ewijk, G., Vroege, G., and Philipse, A. (2002). Susceptibility measurements on a fractionated aggregate-free ferrofluid. *Journal of Physics: Condensed Matter*, 14(19).

[Wang et al., 2009] Wang, C., Baer, D. R., Amonette, J. E., Engelhard, M. H., Antony, J., and Qiang, Y. (2009). Morphology and Electronic Structure of the Oxide Shell on the Surface of Iron Nanoparticles. *J. Am. Chem. Soc.*, 131(25):8824–8832.

[Wang et al., 2015] Wang, D.-Y., Chou, H.-L., Cheng, C.-C., Wu, Y.-H., Tsai, C.-M., Lin, H.-Y., Wang, Y.-L., Hwang, B.-J., and Chen, C.-C. (2015). Fept nanodendrites with high-index facets as active electrocatalysts for oxygen reduction reaction. *Nano Energy*, 11:631–639.

[Wang and Xia, 2004] Wang, Y. and Xia, Y. (2004). Bottom-up and top-down approaches to the synthesis of monodispersed spherical colloids of low melting-point metals. *Nano Lett.*, 4(10):2047–2050.

[Watari et al., 2011] Watari, M., McKendry, R., VÃÂűgtli, M., Aeppli, G., Soh, Y.-A., Shi, X., Xiong, G., Huang, X., Harder, R., and Robinson, I. (2011). Differential stress induced by thiol adsorption on facetted nanocrystals. *Nat Mater*, 10(11):862–866.

[Weddemann et al., 2010] Weddemann, A., Ennen, I., Regtmeier, A., Albon, C., Wolff, A., Eckstädt, K., Mill, N., Peter, M. K.-H., Mattay, J., Plattner, C., Sewald, N., and Hütten, A. (2010). Review and outlook: from single nanoparticles to self-assembled monolayers and granular gmr sensors. *Beilstein journal of nanotechnology*, 1:75–93.

[Wetterskog, 2013] Wetterskog, E. (2013). Anomalous magnetic properties of nanoparticles arising from defect structures: Topotaxial oxidation of fe1–xo|fe3âĹŠÎ'o4 core|shell nanocubes to single-phase particles. *ACS Nano*, 7(8):7132–7144.

[Williams et al., 2003] Williams, G., Pfeifer, M., Vartanyants, I., and Robinson, I. (2003). Three-dimensional imaging of microstructure in au nanocrystals. *Phys. Rev. Lett.*, 90.

[Wu et al., 2012] Wu, J., Zhu, J., Zhou, M., Hou, Y., and Gao, S. (2012). Fept concave nanocubes with enhanced methanol oxidation activity. *CrystEngComm*, 14(22):7572–7575.

[Xiong et al., 2014a] Xiong, G., Clark, J., Nicklin, C., Rawle, J., and Robinson, I. (2014a). Atomic diffusion within individual gold nanocrystal. *Scientific Reports*, 4:6765.

[Xiong et al., 2014b] Xiong, G., Moutanabbir, O., Reiche, M., Harder, R., and Robinson, I. (2014b). Coherent x-ray diffraction imaging and characterization of strain in silicon-on-insulator nanostructures. *Advanced materials (Deerfield Beach, Fla.)*, 26(46):7747–7763.

[Yang et al., 2013] Yang, W., Huang, X., Harder, R., Clark, J., Robinson, I., and Mao, H.-k. (2013). Coherent diffraction imaging of nanoscale strain evolution in a single crystal under high pressure. *Nature Communications*, 4:1680.

[Young and Goodwin, 2011] Young, C. and Goodwin, A. (2011). Applications of pair distribution function methods to contemporary problems in materials chemistry. *J. Mater. Chem.*, 21(18):6464–6476.

[Yung et al., 2014] Yung, T.-Y., Huang, L.-Y., Chan, T.-Y., Wang, K.-S., Liu, T.-Y., Chen, P.-T., Chao, C.-Y., and Liu, L.-K. (2014). Synthesis and characterizations of ni-nio nanoparticles on pdda-modified graphene for oxygen reduction reaction. *Nanoscale research letters*, 9(1).

[Zeng et al., 2003] Zeng, H., Li, J., Wang, Z., Liu, J., and Sun, S. (2003). Bimagnetic core/shell $FePt/Fe_3O_4$ nanoparticles. *Nano Lett.*, 4(1):187–190.

[Zhang et al., 2014] Zhang, C., Wang, H., Mu, Y., Zhang, J., and Wang, H. (2014). Structural and compositional evolution of FePt nanocubes in oganometallic synthesis. *Nanoscale research letters*, 9(1).

[Zhang et al., 2006] Zhang, L., He, R., and Gu, H.-C. (2006). Oleic acid coating on the monodisperse magnetite nanoparticles. *Applied Surface Science*, 253(5):2611–2617.

[Zhou et al., 2013] Zhou, M., Li, W., Zhu, M., Zhou, D., and Hou, Y. (2013). Shape-controlled synthesis and magnetic properties of fept nanocubes. *Journal of the Korean Physical Society*, 63(3):302–305.

[Zuo et al., 2003] Zuo, J., Vartanyants, I., Gao, M., Zhang, R., and Nagahara, L. (2003). Atomic resolution imaging of a carbon nanotube from diffraction intensities. *Science*, 300(5624):1419–1421.